Analysis of Energy Balance Components from Flux Measurement Sites near Island Park, Idaho, and the Exploration of Evapotranspiration Rates

A Thesis

Presented in Partial Fulfillment of the Requirements for the

Degree of Master of Science

with a

Major in Biological and Agricultural Engineering

in the

College of Graduate Studies

University of Idaho

by

John W. Stewart

Major Professor: Richard G. Allen

Committee Members: James L. Wright, Ph.D.; Ricardo Trezza, Ph.D.

Department Administrator: Ching-An Peng, Ph.D.

December 2016

Authorization to Submit Thesis

This thesis of John W. Stewart, submitted for the degree of Master of Science with a Major in Biological and Agricultural Engineering and titled "Analysis of Energy Balance Components from Flux Measurement Sites near Island Park, Idaho, and the Exploration of Evapotranspiration Rates," has been reviewed in final form. Permission, as indicated by the signatures and dates below, is now granted to submit final copies to the College of Graduate Studies for approval.

Major Professor: _____ Date: _____
Richard G. Allen Ph.D.

Committee Members: _____ Date: _____
James L. Wright, Ph.D

_____ Date: _____
Ricardo Trezza, Ph.D

Department Administrator: _____ Date: _____
Ching An Peng, Ph.D

Abstract

The surface energy budget at the earth surface describes the partitioning of energy into storage (S), sensible heat (H), and latent heat (LE). The measurement of the surface energy flux provides key insight into processes such as evapotranspiration (ET) and the water budget. However, attempts to measure energy fluxes into these variables often fails to account for all the available energy, referred to as energy balance closure error (EBCE). Available energy (net radiation - R_n) and energy fluxes into storage (S), sensible heat (H), and latent heat (LE) were analyzed for a lodgepole pine forest in eastern Idaho, USA. The EBCE analysis indicated approximately 20% missing energy for the lodgeplole pine forest. The flux pathways were evaluated to identify which were under-measured. Consistent with findings at other flux measurement sites, it is believed that H and LE were under-measured and were largely responsible for most of the error. A novel approach to adjust apparently under-measured H and LE from eddy covariance (EC) systems was developed using independently-measured H from a large aperture scintillometer (LAS) based on the hypothesis that LAS would not be subject to the same errors that affect EC measurements, namely unmeasured fluxes associated with the low frequency part of the turbulent spectra caused by landscape heterogeneity, advection, non-steady state conditions and sonic anemometer limitations. Adjusted data were then used to evaluate ET for the lodgepole pine forest and to develop a cover ET coefficient (ET_c) curve for the forest based on reference ET (ET_r) using meteorological data from a nearby weather station.

Acknowledgements

I would like to express my sincere appreciation to Dr. Rickard Allen, for his willingness to provide this opportunity, and for his mentoring and guidance during my time as a graduate student. I have learned a great deal from his approach to research and admire his ability to see through the data.

I would also like to express my appreciation to my committee members, Dr. Jim Wright and Dr. Ricardo Trezza, who so willingly agreed to serve on my committee and share their expertise and experience. I have benefitted greatly from the vast knowledge and experience of Dr. Wright and Dr Trezza, and their availability, guidance, and willingness to answer questions.

Would like to thank Clarence Robison for his willingness entertain questions and offer guidance, often in the form of another question, and for his assistance statistics. I would like to thank Carlos Kelly for his encouragement and feedback. Wenguang Zhao was also instrumental in setting up the research sites and processing the data. Theresa Albright's assistance with the administrative requirements of my graduate program was most helpful and very much appreciated.

I would like to thank Matt Germino (formerly of Idaho State University, now with the USGS) and Dr. Venkant Sridhar (formerly of Boise State University, now with Virginia Tech), who supported the construction and instrumentation of the Island Park site as part of the EPSCoR team.

The National Science Foundation EPSCoR program provided funding support through NSF EPSCoR Research Infrastructure Improvement (RII) grant EPS 0814387 that supported the construction and instrumentation of the Island Park Research site. The USGS Landsat Science Team contributed funding support to both my research assistantship and to the operation of the research site. The U.S. Forest Service permitted the Island Park Flux research sites on National Forest System lands.

The University of Idaho Kimberly Research and Extension Center, where the research team was based, provided facilities and support. The USDA ARS Northwest Irrigation and Soils Research lab provided office space and a computer during my tenure as a graduate student.

Dedication

As is usually the case, and it certainly is the case here, behind every good man is a better woman. This thesis and my graduate experience would not have been have happened without the considerable vision, sacrifice, and encouragement of my dear wife and better half, Leisa. I truly appreciate her confidence in me to embark on this journey, and to continue on it when I wondered if I would ever make it to the end. Once again, she was right. Thank you sweetheart.

Table of Contents

List of Abbreviations and Symbols

ANCOVA	Analysis of covariance
ANOVA	Analysis of variance
β	Bowen ratio
CNR1	Kipp and Zonen four-way net radiometer
CS	Canopy heat storage
EB	Energy balance
EB Ratio	Energy balance ratio
EBCE	Energy balance closure error
EC	Eddy covariance
EPSCOR	Experimental Program to Stimulate Competitive Research
ET	Evapotranspiration
ET_c	Cover ET coefficient
G	Soil heat flus
H	Sensible Heat
H_{EC}	Sensible heat from EC
H_{LAS}	Sensible heat from the LAS
H_{LASadj}	Sensible heat from EC adjusted by the LAS adjustment
H_o	Null hypothesis
K_c	Crop coefficient
LAS	Large aperture scintillometer
LE	Latent Heat
LE_{EC}	Latent energy from EC
LE_{LASadj}	Latent heat from EC adjusted by the LAS adjustment
NR01	Hukseflux four-way net radiometer
Rn	Net radiation
R_s	Global shortwave radiation
R_{so}	Theoretical global shortwave radiation
u*	Friction velocity
W m^{-2}	Watts per meter square
VWC	Soil volumetric water content

List of Figures

List of Tables

Chapter 1 Introduction

1.1 Overview of Topics

The surface energy budget at the earth surface is a fundamentally important process. It is influenced by many variables and in turn influences or determines many other processes. The surface energy budget describes the partitioning of energy into storage, sensible heat, and latent heat. The measurement of the surface energy flux provides key insight into processes such as evapotranspiration and the water budget. The eddy covariance (EC) method is a direct measure of a turbulent flux density of a scalar process across horizontal wind streamlines (Paw et al. 2000), from which surface energy fluxes may be estimated. However, EC flux measurements usually do not result in energy balance (EB) closure, indicating that some of the energy is not accounted for in the measurements (Foken 2008, Foken et al. 2006, Twine 2000, Wilson et al. 2002,).

The University of Idaho research group at the Kimberly Research and Experiment Center at Kimberly, Idaho, USA, has been operating three EC surface energy flux measurement sites. One site is located near Hollister, Idaho, in a sagebrush steppe community. It was installed in 2009. The second site is located in the Raft River area of southern Idaho in a cheatgrass-crested wheatgrass community, installed in late 2009. The third site is located in Island Park, Idaho, in a lodgepole pine forest community. It was installed in late 2010. Sensors from these sites have provided an extensive sets of energy flux data for their respective communities. More specifically, these data quantify the components of the surface energy flux, namely net radiation (R_n), soil heat flux (G), sensible heat flux (H), latent heat flux (LE), and canopy storage (CS). This work will focus on data collected from the Island Park site and explore the following research topics:

1) The components of the surface EB equation will be analyzed to better understand the behavior of measurements of energy fluxes over a lodgepole pine forest. A primary goal is to provide insight into the relationship among fluxes and relationships with theory to identify any that may be under- or over-estimated and thus require adjustment.

2) Soil heat flux data will be analyzed to understand spatial and temporal variation in soil heat flux in a forest system and to answer basic questions about the best means for its measurement. The Island Park site has a north and a south site, with each site having six subsites with soil heat flux sensors placed at two different depths. The subsites represent variability in the community in terms of shaded vs. sun-exposed, and vegetated vs. less vegetated or varying type of vegetation. This

analysis will explore several topics related to estimating soil heat flux, including: 1) the benefit of using multiple sensors and locations, particularly in heterogeneous sites; 2) the optimal depth of sensor placement; 3) how these considerations may change temporally; and 4) how to represent variability in the community when measuring soil heat flux. This research will increase the understanding of how to increase the accuracy of soil heat flux measurement.

3) One of the products of the energy flux measurements is an evapotranspiration (ET) estimate. ET will be estimated from the from the 30-minute data to analyze the day-to-day behavior of ET in the vegetation. ET will be correlated to the climatic conditions to investigate patterns in temporal variability. This research will increase the understanding of consumptive water use in a nonagricultural forest community.

4) In agricultural settings, crop coefficients are used to predict water requirements from standard weather data sets and reference ET. This method requires that a crop coefficient (K_c) be developed for the specific crop of interest to estimate irrigation requirements. However, this method has had limited application to natural ecosystems, which are fundamentally more complex than a typical single-crop agricultural system. This research will determine if a simple single (or dual) crop coefficient model is able to reproduce the measured ET for the vegetation communities at each flux measurement site. In this case, the objective will be to develop and evaluate K_c values that represent the composite water use of all the species in the community, relative to a reference ET. The data present a unique opportunity to conduct this research because of the multi-year, high-quality ET data set that is available for each site. This research will increase the basic understanding of water use in the natural vegetation communities where the measurement sites are located.

1.2 Problem Statement and Research Objectives

Accurately quantifying the surface energy budget is a complex undertaking due to the number of parameters involved and the challenges in accurately estimating the corresponding fluxes, especially in a natural setting such as within a lodgepole pine forest. This work seeks to provide a better understanding of the energy budget parameters and measurements necessary to quantify their magnitude at the Island Park research site. At the same time this research will provide additional understanding of the specific forested system where the study area is located, particularly in terms of the water budget and consumptive water use. To this end, the following research objectives are identified:

- Investigate the energy balance closure error (EBCE) based on an analysis of the individual fluxes. The EBCE in the Island Park data indicates that fluxes are not fully accounted for by the flux measurements. An analysis of each variable in conjunction with all other variables is necessary to better understand the system and how adjustments or corrections could be applied to achieve closure. Accurate estimation of the fluxes is necessary to understand the consumptive water uses of this forested system through ET.
- Investigate differences in the magnitude of G and the corresponding effect on closure using different combinations of sensor locations, sensor depths, and solar exposure regimes. As a sub category of the previous, quantifying the energy budget requires a good and representative estimation of G. However, estimating G for a complex footprint source area is likely to require a number of sensor locations. Analysis of these factors will increase the understanding of the impact of placement, number of sensors and sensor sites needed to provide a representative estimate of G for the EC energy flux footprint area in a forested setting.
- ET data provide an opportunity to better understand the water budget and time-based trends in a water-limited landscape. Data from the study site will be used to explore the development of reference ET fraction (ET_rF) values for use in a crop coefficient - daily soil water balance model to predict ET. This will allow exploration of how precipitation inputs are evaporated over time and their correlation with climatic patterns.
- A K_c-type crop water use model coupled with a water balance model may be able to quickly predict the water use for a forest site. Information regarding water use would enable more informed decision regarding water and vegetation management. To this end, the feasibility of developing a simple K_c-type crop water use model will be explored by developing ET_rF coefficients.

1.3 Description of Research Site and Instrumentation

This research utilizes the Island Park, Idaho, Experimental Program to Stimulate Competitive Research (EPSCoR) Flux and Energy Balance Site (IFEBS) energy flux data set. The Island Park IFEBS is located in a moderately dense, second-growth (approximately 50 year-old) lodgepole pine forest with thick grass/forbs understory. The mean maximum tree height is 14 to 15 m. The average tree spacing is about 4 m with occasional clearings and meadows.

There are two subsites, referred to as the north and south sites. The north site is located at 44°28'19.7" N, 111°22'24.8"W at 1,977 m elevation. The south site is located at 44°29'15.9 N, 111°22'29.6" W at 1,945 m elevation. Both sites have observation towers constructed of 1.5 m by 2.1 m scaffolding supported by two 18.5-m-tall wooden power poles. The north tower is 24-m tall and the south tower is 22 m tall. Both towers extend above the forest canopy and support EC, net radiation, and a large aperture scintillometer (LAS), and a rain gage on the south tower only. Additional instruments to measure parameters relevant to the calculation of soil heat flux are located within 50 m of the towers. All instruments are connected to data loggers. The net radiometers positioned above the canopy were suspended on long poles extending approximately 4-m from the tower, near the top of the tower. Data were collected by Campbell scientific CR1000 data loggers. The sampling rate for the EC data was 10 Hz.

Figure 1-1 and Figure 1-2 show detailed close-up aerial images of the Island Park north and south sites, respectively. Both sites are forested with relatively uniform stands of lodgepole pine forest that was clear-cut in about 1970, although there are some scattered large trees. Small park-like meadows are more common around the south site than the north site. Figure 1-3 illustrates a typical view of the forest from the ground near the north site. Figure 1-4 shows view of the forest canopy from the observation tower at the south site. Included in the view are the CSAT sonic anemometer and the LICOR 7500 infrared gas analyzes as well as the Huksflux NR01 net radiometer. Figure 1-5 provides another view of the forest canopy from the observation tower at the south site. Figure 1-6 and Figure 1-7 show the understory at soil heat flux measurement sites prior to installation of the instrumentation. Figure 1-8 show an open soil pit with thermocouples and soil heat flux plates. Although this photo is of another site, it illustrates a typical installation of the soil sensors. Figure 1-9 show the IRT camera that measured the temperature of the tree canopies, which was used to estimate CS. Figure 1-10 show the Campbell Scientific TE525SW 8-inch typing range gauge at the north site. A Hukesflux NR01 four-way net radiometer was co-located with the rain gauge. A similar rain gauge was installed on the top of the south tower. Figure 1-11 shows a view from the south tower to the north tower, along the LAS transect.

Figure 1-1. Aerial image showing the Island Park north site.

Figure 1-2. Aerial image showing the Island Park south site.

Figure 1-3. Photo of Island Park north site showing typical vegetation.

Figure 1-4. Photograph from the Island Park south tower showing typical forest canopy and the LI-COR 7500 infrared gas analyzer, CSAT 3-D sonic anemometer, and Hukseflux NR01 net radiometer mounted on the tower.

Figure 1-5. View of the forest canopy from the Island Park south tower looking south east.

Figure 1-6 View of the understory at the north site following the installation of two soil heat flux sites. White tops of Campbell 616 soil moisture probes are visible. These mark the approximate locations of heat flux plates.

Figure 1-7. View of the understory at an Island Park soil heat flux site.

Figure 1-8. View of installation of thermocouples and soil heat flux plates in a soil heat flux subsite. at the Hollister EPSCoR flux site. Installations were similar for the Island Park EPSCoR site. Photo by R.G. Allen

Figure 1-9. View of the infrared camera at the south site used to measure the canopy temperature to estimate canopy heat storage.

Figure 1-10. View of the Campbell Scientific TE 525WS 8-inch tipping rain gauge at the Island Park north site. A Hukseflux NR01 four-way net radiometer is also visible.

Figure 1-11. View of the Lodgepole pine forest from the south tower looking north toward the north tower along the LAS transect.

Long-term climatic data for the Island Park area from the National Weather Service Island Park Cooperative Weather Station are shown in Table 1-1 (Western Region Climate Center 2016). This weather station is located approximately 27.4 km south southeast of the Island Park research sites at an elevation of 1,925 m. This climate summary is based on weather data from 02/01/1937 to 05/31/2016. Figure 1-12 shows a graphical summary of the long-term climate data presented in Table 1-1. Precipitation is bimodal with a winter peak and a secondary peak in early summer. Winter precipitation comes as snowfall. Winter snow accumulation does not melt until June, and new snow accumulation begins in October.

	Average Max. Temperature (C)	Average Min. Temperature (C)	Average Total Precipitation (cm)	Average Total Snow Fall (cm)	Average Snow Depth (cm)
Jan	-3.1	-16.1	9.7	123.4	96.5
Feb	-0.2	-15.1	7.4	95.3	119.4
Mar	3.6	-11.9	6.3	74.4	119.4
Apr	9.1	-5.8	5.2	35.3	71.1
May	15.4	-0.5	6.3	10.4	7.6
Jun	20.5	3.2	6.9	1.0	0.0
Jul	26.1	6.1	3.2	0.0	0.0
Aug	25.8	4.8	3.7	0.3	0.0
Sep	20.4	0.4	3.8	2.5	0.0
Oct	12.7	-3.8	4.8	16.8	2.5
Nov	2.9	-9.5	6.5	64.3	17.8
Dec	-2.4	-14.7	9.0	121.7	58.4
Annual Total	10.9	-5.2	72.8	545.6	40.6

Table 1-1. Summary of long-term climatic parameters for the Island Park area. Data are from the National Weather Service Island Park Cooperative Weather Station. Data retrieved from http://www.wrcc.dri.edu/cgi-bin/cliMAIN.pl?id4598 on Oct. 10, 2016.

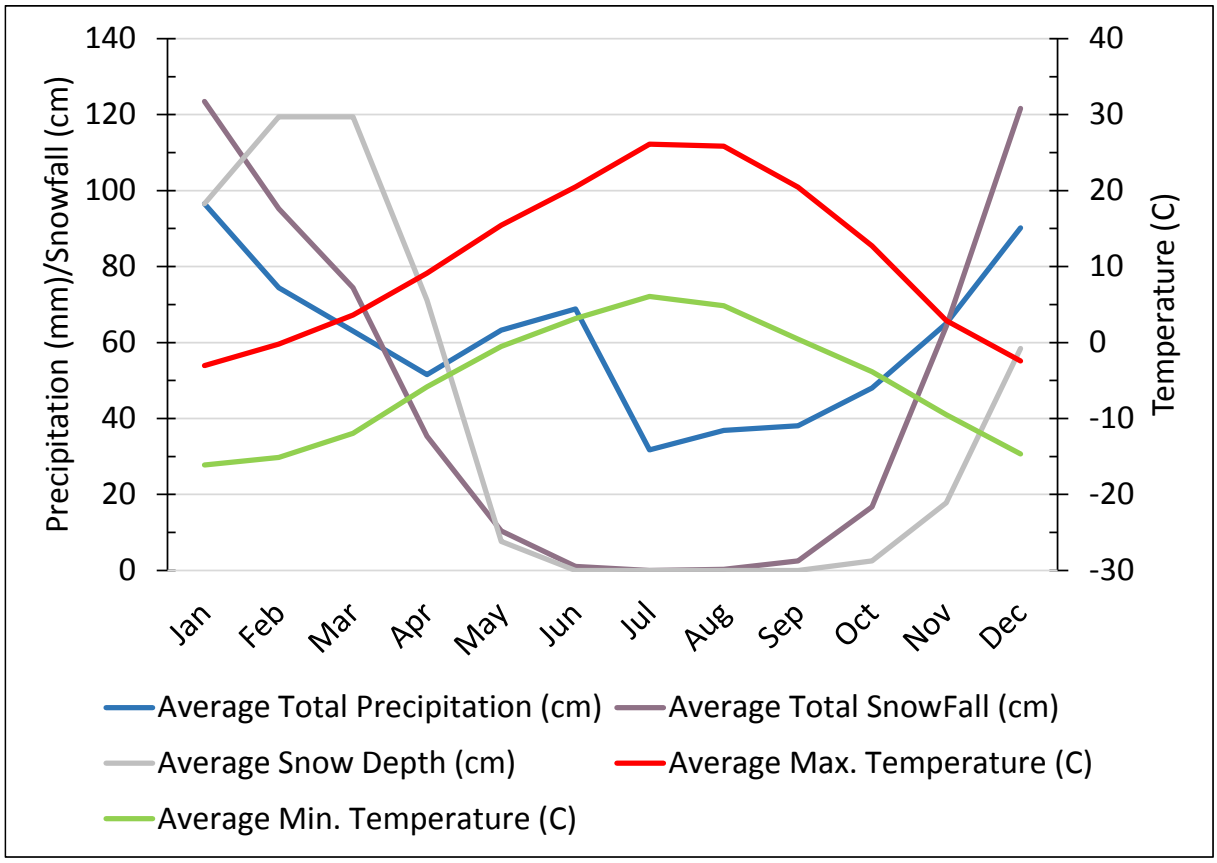

Figure 1-12. Graphical summary of the long-term climatic data in Table 1-1 from the National Weather Service Island Park Cooperative Weather Station.

Site maintenance and data retrieval were performed approximately every 59 days, a time frame determined by the data storage capacity limitation of the EC data loggers. Site maintenance activities included checking all instruments and making repairs and adjustments as necessary. Radiometers were cleaned and releveled if necessary. Retrieved data were processed in Excel spreadsheets.

Below is a list of instruments at each site. A detailed list of sensors at each site and their placement is included in Appendix A.

<u>North Site</u>

- LiCor 7500 infrared gas analyzer
- RM Young 3D sonic anemometer

- Two Hukseflux NR01 four component net radiometers, one suspended above the canopy on the observation tower and one below the canopy, Apogee SP110 pyranometer, and REBS Q7 net radiometer

- Scintec BLS 900 large aperture scintillometer transmitter

- Campbell Scientific TE 525WS 8-inch tipping rain gauge at 3 m above the ground in a small clearing

- Vaisalla humidity-temperature sensor at 2 m above the ground

- Soil Measurement Sites (10 soil measurement sites). In total there were 24 thermocouples, 12 REBS soil heat flux plates, 1 Hukseflux self-calibrating soil heat flux plate, 4 Decagon Echo 5 soil water content sensors (Figure 1-13), and 15 Campbell Scientific CS616 soil water content sensors (Figure 1-14) between the sites.

  Of particular interest to this work were the 6 soil measurement sites used to estimate G, which were instrumented to measure heat flux, volumetric water content (VWC), and soil temperature. Each of these soil site was instrumented with 2 REBS soil heat flux plates, one at 6 cm depth and the other at 12 cm depth. A CS616 was inserted at an angle so as to measure a slab of soil approximately 12 cm thick. Four thermocouples were inserted at 2, 4, 9, and 15 cm depth to measure a temperature profile. An Echo 5 probes was also placed to measure VWC at 1 – 5 cm depth at site 5.

  Additional soil moisture sensors were places at deeper depths in the other four soil sites to provide information of the VWC in the deeper soil profile.

- Campbell Scientific CR1000 data logger and multiplexer (3)

<u>South Site</u>

- EC: LiCor 7500 infrared gas analyzer

- Campbell Scientific CSAT 3-D sonic anemometer

- Two Hukseflux NR01 four component net radiometers, one suspended above the canopy on the observation tower and one below the canopy, one Kipp and Zonen CNR01 four-

component net radiometer suspended above the forest canopy on the observation tower, one Eppley PSP pyranometer, and one REBS Q7 net radiometer

- Scintec BLS 900 large aperture scintillometer receiver
- Two Apogee infrared thermometers (IRT)
- Campbell Scientific TE 525WS 8-inch tipping rain gauge at 22 m height
- Vaisalla humidity-temperature sensor at 2 m above the ground
- Soil Measurement Sites (10 soil measurement sites). In total there were 24 thermocouples, 12 REBS soil heat flux plates, 1 Hukseflux self-calibrating soil heat flux plate, 8 Decagon Echo 5 soil water content sensors (Figure 1-13), which measure the VWC over a 5-cm length, and 14 Campbell Scientific CS616 soil water content sensors (Figure 1-14), which measure the VWC over a 30-cm length, between the sites.

  Of particular interest to this work were the 6 soil measurement sites used to estimate G, which were instrumented to measure heat flux, volumetric water content (VWC), and soil temperature. Each of these soil site was instrumented with 2 REBS soil heat flux plates, one at 6 cm depth and the other at 12 cm depth. A CS616 was inserted at an angle so as to measure a slab of soil approximately 12 cm thick. Four thermocouples were inserted at 1.5, 3, 4.5, and 9 cm depth to measure a temperature profile. An Echo 5 probes was also placed to measure VWC at 1 – 5 cm depth at sites 1, and 3.

  Additional soil moisture sensors were places at deeper depths in the other four soil sites to provide information of the VWC in the deeper soil profile.

- Campbell Scientific CR1000 data logger and multiplexer (3)

Figure 1-13. Decagon EC-5 soil moisture probe. Probe length = 5 cm. Source https://www.decagon.com/en/soils/volumetric-water-content-sensors/ec-5-lowest-cost-vwc/.

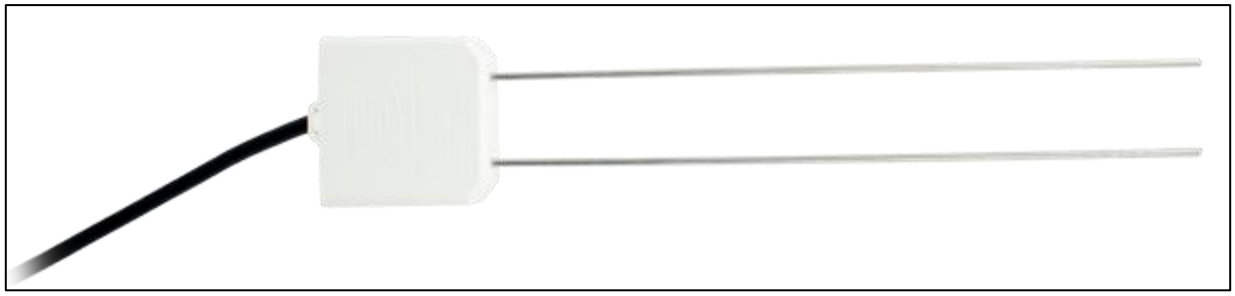

Figure 1-14. Campbell Scientific CS616 soil moisture probe. Probe length = 30 cm. Source: https://www.campbellsci.com/cs616-reflectomer.

1.4 Document Overview.

This document includes 6 chapters. Chapter 1 contains the Introduction, Problem Statement and Research Objective, and study area description. Chapter 2 provides a review of relevant literature. Chapter 3 details the data preparation methodology, including QA/QC and initial assessment of EBCE. Chapter 3 is a particularly important chapter because it discusses approaches to deal with under-measurement of turbulent fluxes as a preparatory step to subsequent use of the data to explore other topics. Chapter 4 looks at a number of questions relating to the estimation of G. Chapter 5 explores topics relating to the turbulent fluxes. Chapter 6 explores the development of a K_c/ET_rF factor for lodgepole pine forest surrounding the study area based on the evapotranspiration (ET) measured by the Island Park EC system.

Chapter 2 Literature Review

2.1 Energy Balance Closure Error

The use of the eddy covariance (EC) method to measure energy fluxes at the earth's surface has become relatively common (Wilson et al. 2002). Principles of conservation of mass and energy require that the energy source terms balance the energy output terms, referred to as EB closure. The absence of closure is referred to as the EBCE (EBCE=R_n - G - CS - LE – H). EBCE may be used to evaluate the accuracy or quality of the scalar flux estimates (Allen 2008, Barr et al. 2006, Michel et al. 2008, Wilson et al. 2002). Systems that have a lower EBCE suggest more accurate measurement of the energy flux components. However, most sites experience an EBCE ranging from 10 to 30 percent (Wilson et al. 2002, Finnigan et al. 2003, Twine et al. 2000, Foken 2008, Stoy et al. 2013).

Many researchers have studied the EBCE to identify factors which contribute to this error (Twine et al. 2000, Wilson et al. 2002, Foken et al. 2006). Foken (2008) noted that the EBCE is not solely due to statistically-distributed measurement error. Instead, Foken (2008) found that underestimation of turbulent fluxes or the over estimation of available energy are responsible for much of the EBCE. Wilson el al. (2002) suggested that the surface energy fluxes (latent and sensible heat) are often underestimated relative to the available energy, which includes R_n, G, and heat storage in the air and biomass. Stoy et al. (2013) and others (Foken 2008, Panin and Bernhofer 2008) found that landscape level heterogeneity in vegetation and topography may play an important role in the EBCE.

Foken (2008) provided a review of research into the EB closure problem. The typical EB residual in the daytime was 50 - 300 W m^{-2}, and was characterized by low turbulent fluxes. Foken noted that past assumptions as to the cause of the lack of EB closure, mismatch of measure areas for different components of the EB equation (i.e. net radiation is dependent on the angle of view of the radiometer and is dependent on the height of the radiometer, while the EC foot print varies based on wind conditions) and measurement errors, do not fully account for the closure error. Recently, these factors have been diminished by increased data quality and accuracy. He suggested that better closure by extension of the averaging period indicates that larger turbulence structures may have a significant influence on closure. These structures are functions of the structure of the underlying surface. Heterogeneous surfaces give rise to large scale eddies and tend to have larger closure errors. Turbulent fluxes are comprised of small eddies that can be measured by the EC method and larger eddies which the EC method, when positioned only tens of meters above the surface, does not measure well. Foken noted that closure in heterogeneous environments may only be possible on the

landscape scale with the measurement of small-scale eddies with the classical EC method in combination with an area averaging measuring system, such as a LAS, to measure the large eddies.

In an earlier paper, Foken et al. (2006) used the ogive function to assess EC methods, specifically to determine if the 30-minute averaging time typically used in the EC method was adequate. The authors found that the main reason for the EBCE was the low frequency part of the turbulent spectra caused by landscape heterogeneity, advection, and non-steady state conditions. However, they also observed cases when the 30-minute averaging periods were too long and fluxes were reduced due to non-steady state conditions or longwave trends. They suggested that in some cases it would be appropriate to implement the EC method with variable integration periods, with the length determined by the ogive function.

Wilson et al. (2002) evaluated the EBCE at 22 sites in the FLUXNET system. They found a general lack of closure at most sites, averaging around 20 percent. They noted that EB closure increased with turbulence intensity, and that the imbalance was greatest at night. The authors used OLS regression to evaluate EB closure, where an intercept of 0 and a slope of 1 would indicate ideal closure. They discussed contributing factors to lack of EB closure, including advection.

Twine et al. (2000) discussed the need to ensure conservation of energy in the surface energy budget. They noted that Rn would typically be the most accurate measurement, and that closure is most reasonable forced by assuming Rn - G is representative of the EC footprint. The authors suggested that the Bowen ratio closure method may be the most appropriate approach to force closure

Stoy et al. (2013) reviewed the closure for 173 ecosystems in the FLUXNET database to explore the relationship between EB closure and landscape heterogeneity. The authors speculated that heterogeneous landscape conditions may result in exchange processes and turbulent motions at large spatial and temporal scales that are not well measured by the EC method, and is likely the primary source of the error at well-installed and maintained sites. They utilized MODIS products to develop an index of landscape heterogeneity based on the enhanced vegetation index (EVI). They found that EB closure was significantly related to MODIS plant functional types and EVI in the nine 250-m pixels immediately surrounding the tower, as well as mean precipitation, site-level Bowen ratio, and landscape elevational variety. The EBCE error due to landscape heterogeneity may be compounded by other factors, such as sonic anemometer limitations, including uncorrected physical

impedance of vertical components of eddies by transducers and frame (Frank et al. 2016), inaccurate measurements of R_n, biological energy assimilation, energy storage, and incorrect measurement practices, including appropriate site selection for making the flux measurements.

Barr et al. (2006) evaluated surface energy balance closure for three boreal forest sites in Canada. Closure imbalances ranged from 11 to 15 percent. Improving energy balance was correlated with increasing friction velocity u*. Closure improved to near 1 as u* increased to 0.35 ms^{-1}. Anderson and Wang (2014) found a similar improvement in EB closure with increasing turbulence/u* in a paired EC experiment over sugarcane in Hawaii. They also noted significant improvements in closure using daily sums as opposed to 30-minute data, emphasizing the importance of storage terms. Franssen et al. (2010) analyzed the data from over 20 sites and found that EBCE increased for very unstable conditions. However, for a given u*, EBCE decreased for increasing instability. Moderow et al. (2007) studied the effects of advection on the estimation of H in a tall forest. They found that neglecting advective fluxes may lead to incorrect results, and if advective fluxes are taken into account, the sensible heat budget based on vertical turbulent flux only was reduced by approximately 30 percent.

Alfieri et al. (2012) compared surface flux measurements between EC and lysimeter-based systems in a pair of irrigated cotton fields in Bushland, Texas, under strongly advective conditions. Substantial differences were found between the two methods, with daytime mean differences exceeding 200 W m^{-2}. The reasons for these discrepancies were found to include: (1) the failure of the EC systems to balance the surface energy budget, (2) flux divergence due to local advection of warm, dry air, and (3) the failure of the lysimeters to accurately represent the actual field conditions. The first two reasons for the discrepancies have application to the Island Park research site and are addressed in subsequent sections of this thesis.

Alfieri and Blacken (2012) compared the energy flux measurements from two EC systems in close proximity to each other. One EC system location was fixed, and the second system was moved around the first in the cardinal directions, but was always within 16 to 32 m of the stationary station. Statistically significant variation in H, LE, and G were found. These differences were correlated to small changes in the near surface soil moisture content and leaf area index. The authors discussed the uncertainty regarding using a single point to process over larger area. The Island Park research site has two sites approximately 1750 meters apart so differences in the flux measurement from the two sites may be anticipated.

Zeri and Sa (2010) analyzed the dependence of energy balance closure and carbon balance on data gaps resulting from screening for high-quality data or turbulent conditions. They found that the level of closure was dependent on the amount of data filtered out according to the data quality flag. A compromise between moderate data quality and good sampling of the daytime period resulted in the best energy balance closure.

Kessomkiat et al. (2013) describe an approach for estimating uncertainty in EC flux measurements. The uncertainty is comprised of systematic error (related to EB closure) and random error, which can be determined on the bases of differences between simultaneous flux measurements from EC sites in very similar conditions. They describe the adaption of the two-tower approach so that it may be applied if more heterogeneous conditions exist between the two sites. They also found that atmospheric stability was an interesting alternative explanatory variable for the random error in the fluxes.

Data collected by the EC system requires complex calculations and a series of corrections to estimate H and LE. Pearman and Leuning (1980) discussed corrections that may need to be applied to EC data for variations in the constituent's density due to the presence of a flux of heat and/or water vapor. Paw et al. (2000) presented equations to correct EC data for fluctuation in density and non-zero mean advection. Massman and Lee (2002) discussed the handling of EC data in a summary paper, particularly the corrections that need to be applied to the data to calculate H and LE. Differences in how data are handled can affect the estimated fluxes and complicate cross-sites and long-term comparisons of the data. Papale et al. (2006) propose a new standardized set of corrections and discussed the uncertainties introduced by these corrections.

2.2 Net Radiation

R_n is generally considered to be the most reliable term in the EB equation (Kohsiek et al. 2007, Allen 2008, Twine et. al 2000), but is difficult to measure accurately (Blonquist et al. 2009). Allen (2008) noted non-representative measuring of R_n can create bias as a component of the EBCE. Michel et al. (2008) noted that there is a surprising paucity of information in the literature evaluating the uncertainty of R_n instruments given the importance of R_n in the EB closure evaluation. They evaluated the Kipp & Zonen CNR1 net radiometer and found rather large root-mean-square (rms), up to 26 percent on daily averages for the original sensitivity coefficients without field calibration. The uncertainty was larger in shortwave components versus longwave components, and larger in incoming versus outgoing components. The 10 percent rms uncertainty claimed by the manufacture

was only obtained after field calibration with high-standard reference radiometers and when the radiometer was installed with a ventilation and heating system (Michel et al. 2008).

Brotzge and Duchon (2000) conducted a field inter-comparison of Kipp and Zonen NR-Lite net all-wave radiometers by comparing differences between the mean daily variation of individual sensor and the mean daily variation of the group, and by comparing sensors to higher-standard instruments. They noted a range of variation among sensors as well as the need for a calibration factor to standardize the radiometers.

Blonquist et al. 2009 evaluated the accuracy of five different types of net radiometers. They found that the Hukseflux NR01 and Kipp and Zonen CNR1 that independently measure the four components of R_n were typically the most accurate. The difference between the reference pyranometer and the surface temperature was typically less than 2 percent, while the difference in incoming longwave was approximately 5 percent. This difference was attributed to differences in calibration and emphasized the need for a standardized calibration method and reference. Instruments that do not separate shortwave and longwave radiation (Kipp and Zone NR-Lite, REBS Q*7.1) component measurements were generally less accurate.

Kohsiek et al. (2007) discussed the importance of using multiple radiometers to measure R_n over non-homogeneous terrain. Kohsiek et al. (2007) and Bloquist et al. (2009) recommended that R_n be calculated from its four components, rather than from a net radiometer. Kjaersgaard et al. (2009) noted that R_n is not always part of the data collected by weather stations. They evaluated several physically-and empirically-based models that can be used to estimate R_n based on other parameters when it is not available. They concluded that the empirically-based models were easier to calibrate and use and could be used when meteorological data is limited. Allen (2008) outlined a procedure to evaluate and correct solar radiation when values are consistently above or below theoretical values.

Intercomparisons and calibrations were made by Zhao and Allen (2010, 2012, unpublished data) for more than 20 four-component R_n sensors using both Kipp and Zonen CNR1 and Kipp and Zonen high precision CG4 pyrgeometer and CM21 pyranometer as a reference and calibration biases a preliminary evaluation for the Island Park research. Most instruments were found to measure within 5% of the references.

2.3 Sensible Heat

Hoedjes et al. (2002) compared H measured by a LAS vs an EC system for a homogeneous irrigated area subject to advection in northwest Mexico. They found that areally averaged H and LE can be predicted by LAS measurements during daytime periods when R_n is greater than 0. The authors concluded that LAS-measured fluxes were in reasonable agreement compared to the EC derived fluxes.

Alferi and Blanken (2012) found that the heterogeneity in a semi-arid sagebrush ecosystem resulted in significant variation in surface energy fluxes as large a 35 to 40 W m^{-2} over only a few tens of meters, due to relatively small changes in near surface soil moisture content and leaf area index (LAI)

In light of the variables that can influence the surface energy flux, Allen (2008) outlined the use of ordinary least-squares (OLS) linear regression to identify the terms having the most likelihood of having systematic effect on EBCE. Similarly, Wilson et al. (2002) used OLS regression to derive linear regression coefficients for half-hourly estimates of dependent flux variables (LE + H) versus independently derived available energy (R_n-G-S). Greth (2013) used OLS regression to analyze the components of surface energy flux and select best combination of soil heat flux sensors at the EPSCoR sagebrush site near Hollister, Idaho.

2.4 Soil Heat Flux

G is an important component in surface EB (Stoy et al. 2013, Hsieh et al. 2009, Heusinkveld et al. 2002, Ogee et al. 2009), especially in hot desert sites (Hsieh et al. 2009). Ogee et al. (2009) noted that G is a major term in the night time energy budget in a coastal pine forest in Southern France, and a significant term during the daytime periods where it can be 50 percent of midday R_n. Hsieh et al. (2009) found that G can be of the same order of magnitude as H for bare soils, and for dry soil conditions, up to 50 percent of the R_n. G may be under-estimated in many instances (Stoy 2013). The measured G may also be non-representative of the variability of the environment (Allen 2008), or mismatched with the source areas of EC measurements (Wilson 2002). Inaccurate measurement of soil heat flux may have a significant influence on the EBCE (Foken 2008). Higgens (2012) conducted an analysis of surface energy budget closure for a research site at the Utah Salt Flats and noted the importance of G in the EBCE. The author found that 89 percent of the EBCE was attributable to the under measurement of energy storage in the soil and soil heat flux. They noted the importance of correctly developing an experimental design that would accurately capture all fluxes, and in their specific case, G.

Ogee et al. (2009) noted that on a 24-hour basis G is usually small or even negligible because heat stored during the day is released at night. They found daily sums of soil heat flux ranged from -1 to 1.5 MJ m^{-2}. However, for longer term energy budgets of a month or more, neglecting G contributes to an imbalance between turbulent fluxes and R_n due to gradual warming or cooling of the soil profile. They found the cumulative value of soil heat flux to be -70 MJ m^{-2} for the September to March period. W m^{-2} are converted to MJ m^{-2} as follows:

$$\frac{W}{m^2} = \frac{J}{s\,m^2} \rightarrow \frac{J}{s\,m^2} * \frac{60s}{1\,min} * 30\ min/(30\ min\ period) = \frac{1800J}{m^2\ \cdot\ 30\,min\,period}$$

$$= \frac{0.0018MJ}{m^2\ \cdot 30\,min\,period}$$

Oliphant et al. (2004) reviewed the equation describing the calculation of G using the traditional flux – heat storage change combination method:

$$\Delta Q_g = Q_{g(z)} + C_s \frac{T_s}{\Delta t} z \qquad \textbf{(2-1)}$$

where Q_g is the soil heat flux at the ground surface, $Q_{g(z)}$ is the measured soil heat flux at depth z (m), T_s is the average soil temperature (K) above the heat flux plate, t is time, and C_s is the soil heat capacity, calculated as:

$$C_s = \rho_b c_{sd} + \theta_v c_{sw} + w_{OM} c_{OM} \qquad \textbf{(2-2)}$$

Where ρ_b is the bulk density of the soil, c_{sd} c_{sw}, and c_{OM} are the specific heats of the dry mineral soil soil water, and organic matter, θ_v is the volumetric water content and w is the percent organic matter in the soil. G for the Island park data set is calculated as described using equation 2-1. Separate calculations are made for the mineral, organic matter, and water fractions of the soil, and the contribution of each is summed. A polynomial extension of the temperature data developed by Zhao and Allen to estimate surface temperature (unpublished) was used to calculate Δt. Details of the calculations are provided in Appendix B.

2.5 Evapotranspiration (ET) Modeling

ET is an energy and mass transfer process involving radiation, conduction, diffusion, convection, and surface-atmospheric interactions (Liu et al. 2012). The magnitude is dependent on a suite of environmental and climatic variables, including radiation, air temperature, air vapor pressure deficits, and plant-soil water stresses (Gharsallah et al. 2013). Therefore, ET may vary spatially and temporally based on unique combinations of these variables. ET has been extensively studied in agricultural settings and numerous models have been developed to estimate water use and irrigation requirements (Gharsallah et al. 2013). However, ET is less intensively studied in non-agricultural plant communities.

Because of the complexity in measuring ET, a number of models to estimate ET have been developed, including "direct" and "indirect" methods (Gharsallah et al. 2013, Zhu et al. 2014). Direct methods refer to the use of the Penman-Monteith equation to estimate ET based on measured or estimated environmental and climatic parameters and the corresponding plant response. The Penman-Monteith equation estimates ET for standard reference crops of cool season clipped grass and alfalfa. Application to other crops or settings requires the development of specific, variable, and generally unknown resistance terms (Gharsallah et al. 2013, Zhu et al. 2014). Indirect methods use an empirically-determined crop-specific "K_c" factor to adjust the ET for a well-watered reference ET (ET_o) to ET of the crop of interest, as outlined in FAO 56 (Allen et al. 1998, Gharsallah et al. 2013). K_c is the ratio of ET of any specific crop or soil surface to reference ET as determined by weather station data for reference conditions (Allen et al. 2005).

Allen et al (1998, 2005) describe the calculation of crop ET using a single K_c of FOA-24 (Doorenbos and Pruitt 1977) to represent the evaporation and transpiration. The authors also describe a dual K_c approach:

$$K_c = K_{cb} + K_e \qquad \textbf{(2-3)}$$

where K_c is "actual" crop coefficient that includes any effects of environmental stress, K_{cb} is the basal crop coefficient, and K_e is evaporation from the soil surface. The dual K_c method was found to estimate ET as measured by a lysimeter relatively well for periods of bare soil and partial and full vegetative cover. Wright (1982) noted that irrigation methods, frequency, soil characteristics, weather factors, and agronomic techniques affect K_c values, which typically vary by region (Kang et

al. 2003, Allen et al. 1998). K_c estimates suggested in the literature should be adjusted to reflect local conditions as outlined in Allen et al. (1998).

However, even after adjusting K_c values proposed in Allen et al. (1998) to account for local conditions, crop water requirements may not be accurately estimated (Facchi et al. 2013), or may not be available in the first place (Ghamarnia et al 2014). Researchers have worked to determine local K_c coefficients through site specific measurements, using a variety of techniques to estimate crop water use (Facchi et al. 2013). For example, Ghamarnia et al. (2014) described the use of lysimeters to develop K_c coefficients for black cumin in Iran. Facchi et al. (2013) describe the use of the EC method to estimate crop water use for corn in northern Italy and develop local K_c coefficients.

High-quality weather station data are needed to calculate reference ET (ET_o or ET_r) for use with the K_c method. Weather station data range widely in the data actually available and the quality of that data. Allen (2008) describes QA/QC evaluations of weather station data that should be completed prior to utilizing the data, and methods that can be used if the weather station data is found to be faulty. Allen (2016) has developed a computer program that calculates reference ET based on weather station data. The software includes a module that assists with the QA/QC process that should be performed before using weather station data in the calculation of ET_r.

Because of the importance of accurate measurement of the basic energy flux components, the data from individual sensors at a measurement site should be evaluated. Corrections should be made, if necessary, to ensure the accurate measurement of the energy flux components (Allen 2008). Sensors calibration, orientation, contamination, and electrical problems can affect data quality.

Chapter 3 Data Assurance Review

The data used in this analysis were collected at the Island Park energy flux measurement sites. Data from the dataloggers were processed to compute H and LE from the EC system, R_n from the radiometers, CS from the IRT, G from the soil sensors, and H_{LAS} from the scintillometer. The original data were then archived in Excel spreadsheets by month. The QA/QC process utilized the original data archived in the Excel spreadsheets. A description of the processing is given in Appendix C, including the standard corrections made to the EC data that included frequency correction, density correction, and coordinate rotation.

This chapter discusses steps taken during the data preparation phase. These included a review of site maintenance records and an assessment of data quality for H, LE, R_n, CS, and G. EBCE was used as a tool to evaluate the fluxes, and OLS regression was used to assess the behavior of individual components of the EB equation. R_n, G, CS, H, and LE have strong diurnal variation, with each component having a unique characteristic shape. This uniqueness among diurnal variation and magnitudes of variation allow the use of regression analysis to indicate corrections to individual components that are reasonable in that they tend to improve correlation among the components. Allen (2008) explored this approach for estimating adjustments to soil heat flux during EB closure. He noted however, that sometimes this approach can indicate the wrong component and magnitude of adjustment when some components are much larger than others. In those situations, the weaker components can be wrongly used to 'tune' time-oriented biases in the stronger components. In this study, all EB components appear to be strong enough in magnitude to enable the use of regression analysis to indicate the more likely corrections to make on individual components. The analyses are not definitive, but do provide an opportunity to explore behavior of the individual components and potential systematic adjustments. It became apparent as the fluxes were evaluated that the turbulent fluxes were likely under-measured at the study site. Consequently, approaches to adjust the turbulent fluxes for under-measurement were explored and this became a major topic of investigation.

3.1 Review of Site Maintenance Records

The maintenance logs for the Island Park sites for 2011 and 2013 were reviewed to identify any reported problems with a sensor that could affect data quality or accuracy. If a period could be identified when a problem with a sensor would affect data quality, such as a dirty or out of level sensor, i.e., a radiation sensor, then it may be possible to calculate a correction as a linear

adjustment to the data back to the time of the prior site visit when the instrument did not have the reported problem. Alternatively, the data from that period may be excluded from the analysis if a correction was not possible. It was noted, however, that the maintenance log did not record all the site visits during the periods of data collection for this analysis.

A review of the site maintenance log for 2011 did not indicate dirty radiation sensors that would affect the estimates. However, on May 19, 2011, the maintenance log did indicate that the NR01 on the north tower was 2 to 3 degrees out of level to the west, and that it was re-leveled. The days preceding and following the adjustment were partly cloudy. Thus any changes in the magnitude of the radiation estimates before and after the adjustment were confounded by variable cloud cover. Therefore, no correction was calculated and the effect of the out-of-level sensor on data quality was judged to be minimal. Figure 3-1 and Figure 3-2 show graphs of the data from the radiometers for the date when the maintenance was performed and the following day. R_n and longwave recordings were similar among the five radiometers, especially among the Hukseflux NR01s suspended above the canopy, with the Q7 and CNR1 and the south site reading 5 to 10 percent higher than the other sensors during midday. These sensors had been inter-compared and calibrated to accurate references by Zhao and Allen (2010 and 2012, unpublished data) prior to deployment, as previously described.

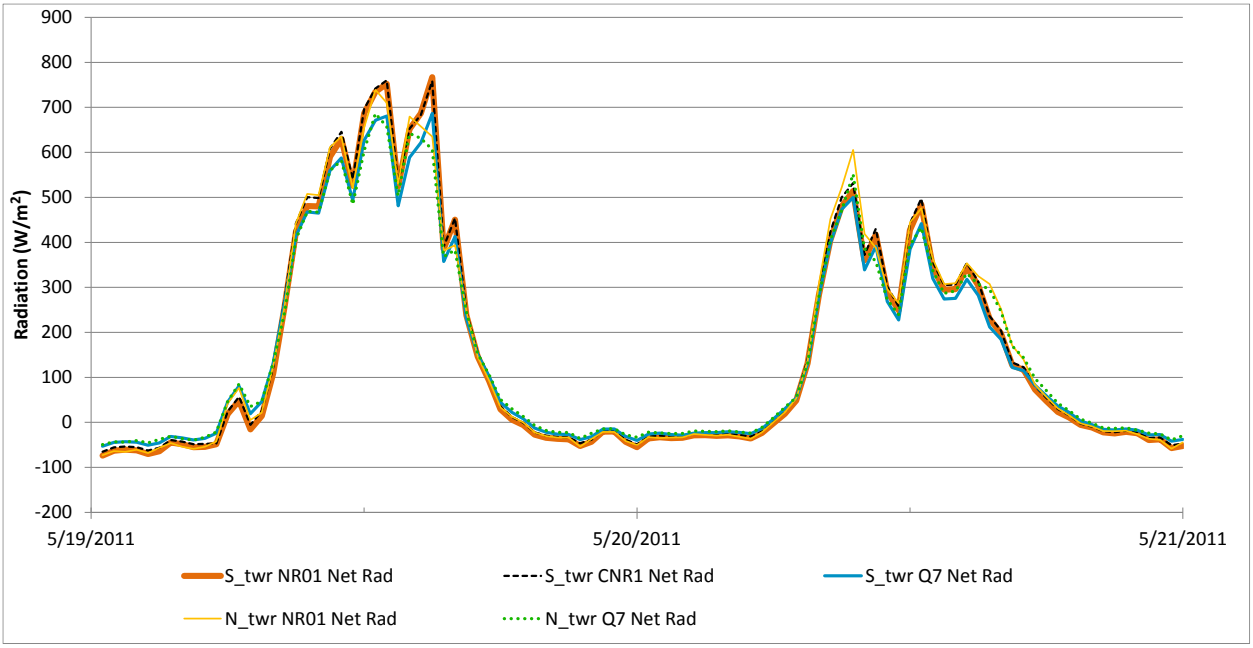

Figure 3-1. Graph of net radiation for a two-day period corresponding to the day the NR01 on north tower was releveled (5/19/2011) and the following day. Island_Park_monthly_data_and_flag_output8_2011-05

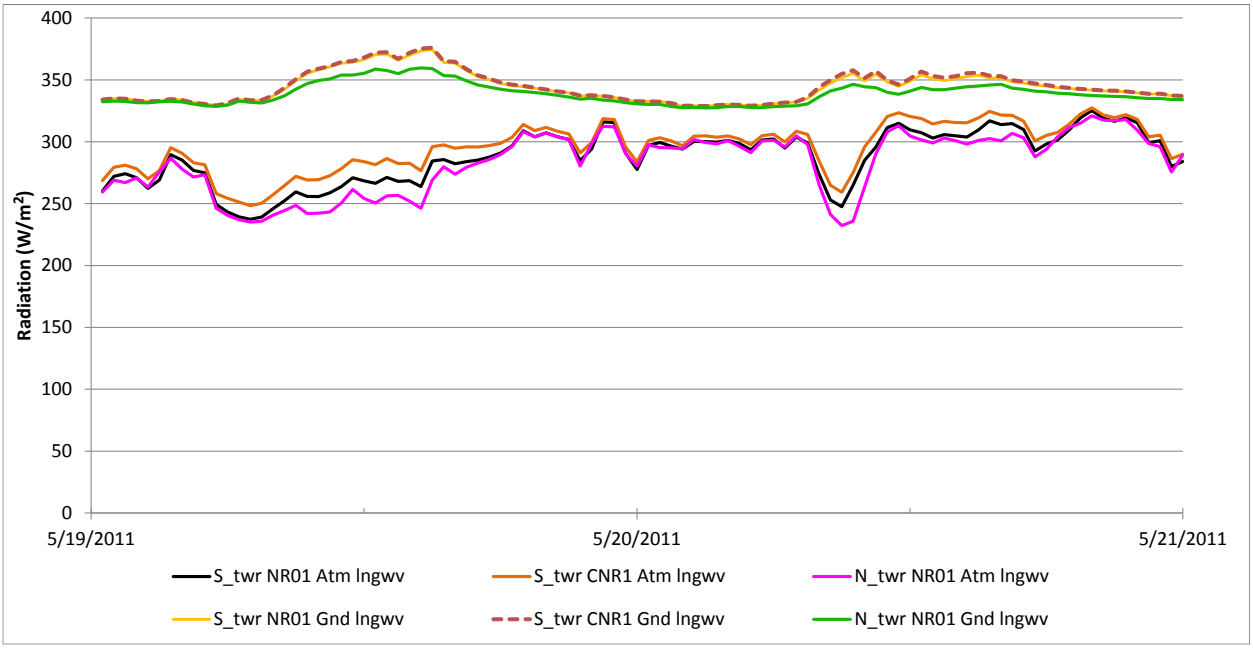

Figure 3-2. Graph of atmospheric longwave and ground longwave radiation for a two-day period corresponding to the day the NR01 on north tower was releveled (5/19/2011) and the following day.

A review of the maintenance log indicated that on September 11, 2013, the NR01 longwave sensor on the north tower was 30 percent dirty. The shortwave sensor was clean, and the instrument level was good. The sensor was pulled in to the tower, cleaned, the pole re-extended, and the instrument re-leveled. The data from the period were analyzed to determine if the dirty sensor affected the radiation estimates. However, no changes in the magnitude of the radiation estimates due to the cleaning were detected, as shown in Figure 3-3 and Figure 3-4. Variable cloud cover was also present during the days preceding and following the adjustment, which could mask some effects of the cleaning.

3.2 Data Quality Assessment and Data Preparation

The analysis in this work utilized data from 2011, primarily for the months when snow was not present (June – September). Data from the Island Park north and south sites were periodically retrieved from the data loggers, approximately every 60 days. Visual Basic (VBA) macros in Excel were used to process the data and calculate R_n, H, LE, G, CS, and other parameters for half-hour time intervals. The processing included a data quality review. Numeric data quality flags were assigned for each data element for each half hour time step (Table 3-1). Multiple data flags may be assigned to a particular data element and time step, in which case the flags are numerically summed. Processed data were stored in Excel workbooks with a separate workbook for each month.

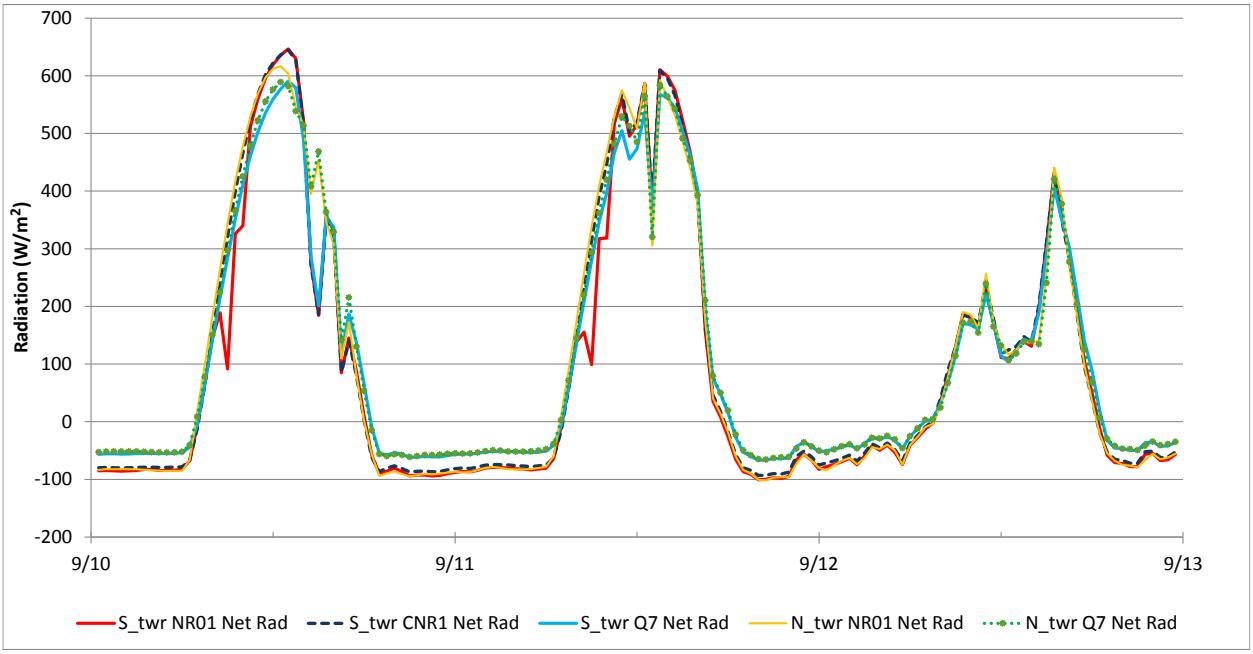

Figure 3-3. Graph of net radiation for a three-day period corresponding to the day the NR01 on north tower was cleaned (9/11/2013) and the preceding and following days.

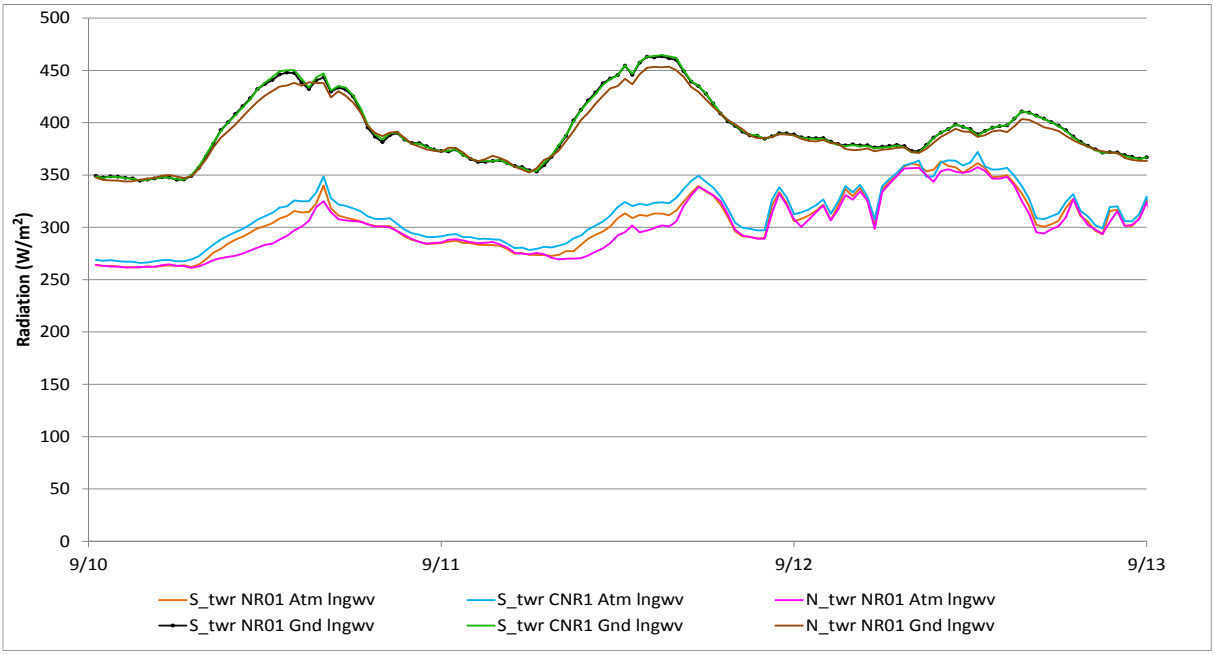

Figure 3-4. Graph of atmospheric longwave and ground longwave radiation for a three-day period corresponding to the day the NR01 on north tower was cleaned (9/11/2013) and the preceding and following days.

Data Flag	Flag Description
0	Good data.
1	Data deviated from same data from a different instrument (+/- 50 W m^{-2} for turbulent fluxes).
2	Wind direction was from the "rear" of the CSAT 3 (42-72 degrees); interference with the frame could affect readings (south site).
4	Precipitation was recorded by the rain gage.
8	Data out of normal range (varies by data element).
16	Data error, i.e., NAN, DIV/0, no data.
32	Voltage too low for dependable functioning of instruments (< 10 volts).

Table 3-1. Data error flags used in the Island Park data set during initial data processing and their corresponding error description.

Data were screened for problematic data, i.e., outliers and spikes to prepare the data for use in this analysis. This process was accomplished using the flagging system described previously in conjunction with graphs of the data. Figure 3-5 illustrates the data graph used in the data screening process for a few days in July 2011. Figure 3-6 illustrates a graph of the error flags for the same period. Precipitation can interfere with accurate senor performance, and data spikes were often associated with precipitation events. Time steps with an error flag of 4, corresponding to precipitation, or greater were identified and excluded from the analysis, which removed most of the spikes from the data sets. Review of the data indicated that conditions that resulted in data being assigned error flags typically affected both towers. Thus data from both the north and south sites usually carried the same error flag, particularly in the case of the flag for precipitation. Turbulent flux data from the EC system was most often problematic due to conditions relating to the flag. A decision was made to exclude all data in the time step with an error flag of 4 or greater, even though G or CS may not have been affected by the error. Retaining some of the data was not warranted for the purposes of this work if reliable data from the EC systems were not available. Occasionally only turbulent flux data from one site was affected, however, due the amount of data involved and the time required to review individual data elements, as well as associated uncertainty, no data from time steps with the error flag of 4 or greater were retained for use in the analysis. VBA macros were developed in Excel to automate the data screening process. The use of the data screening macros is described in Appendix C.

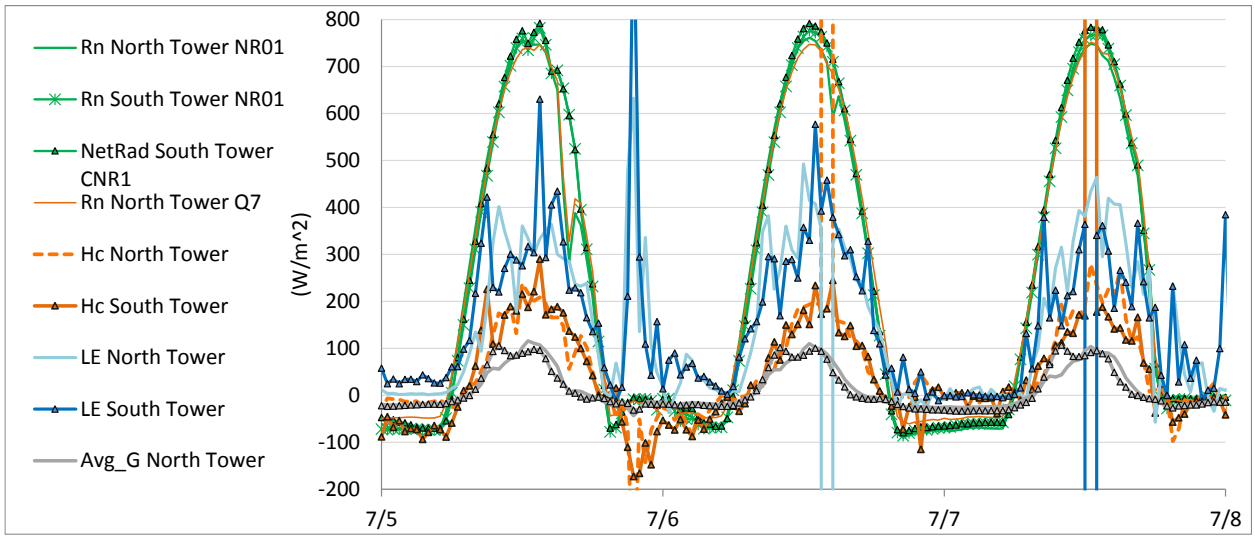

Figure 3-5. Example of the data graphs used for data quality review for a 3-day period in July 2011 showing the original data. Data spikes were present in the data and were typically flagged with an error code.

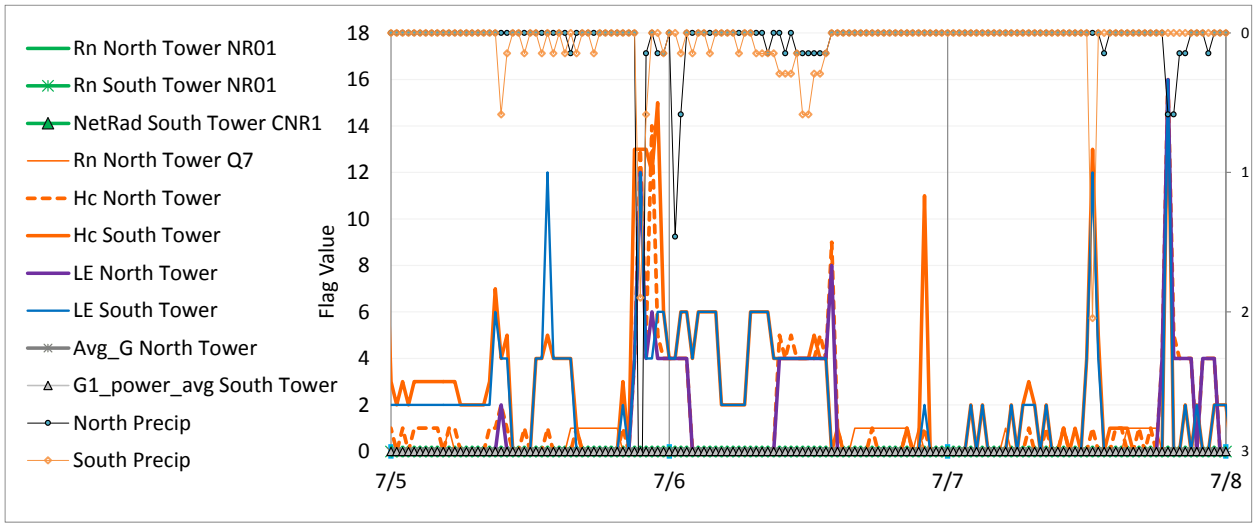

Figure 3-6 Example of the error flag graph used in the data quality review for a 3-day period in July.

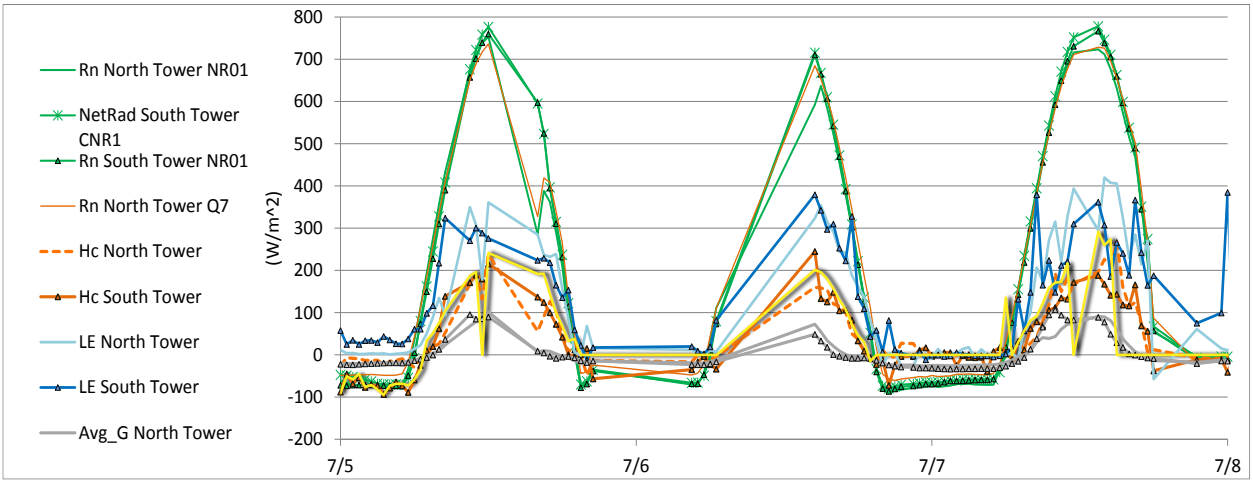

Figure 3-7. Example of the data graph after the QA/QC process for a 3-day period in July 2011. Time steps with data with an error flag of 4 or greater were excluded because they were considered to be potentially unreliable, as explained in the text.

The data flagging system was evaluated as part of the data screening process. The error flag for rain was based on data from the tipping rain gauge at the site to indicate the occurrence of precipitation. The relationship between the error flags and data from the rain gages, radiometers, and EC systems were analyzed. Inconsistency between registered precipitation by the rain gage and data from the radiometers regarding the presence of clouds suggested a problem in the rain gage data and the associated error flag for rain (Figure 3-5 and Figure 3-6). Many error flags for rain flags were set when the rain gauge registered a single tip in a half-hour period (Each tip of the rain gage bucket corresponded to 0.254 mm of precipitation). In addition, the precipitation flagging procedure bracketed the precipitation event by ½ hour on either side. However, in some cases the data from the radiometers for the same time step indicated clear, or predominantly clear, skies. Further, the data from the EC instruments was well-behaved without the spikes that usually accompanied precipitation events. This combination of variables seemed to indicate “false tips”. The “false tips” may have been caused by the wind triggering a tip of a nearly full bucket, or during a site visit as part of a test.

Setting a precipitation flag based solely on the rain gauge indicating precipitation resulted in some data being unnecessarily flagged for precipitation. To address these problems, additional criteria for setting the precipitation flag were developed. Suggested additional criterial for the error flag for precipitation included calculating R_{so} and comparing it to R_s. If this ratio were within a predetermined range that indicated minimal cloudiness, and if the rain flag was associated with the minimum precipitation registration (one tip, equal to 0.254 mm), and if the precipitation was only

registered at one of the sites, it was judged likely that the tip did not reflect actual precipitation and the data should not be flagged. The inclusion of these additional parameters to the error flagging system reduced unnecessary data fall out due to erroneous error flags for precipitation.

The evaluation of the data flagging system also identified a problem with the setting of the bad wind direction flag for the sonic anemometer, particularly in the case of the CSAT3 sonic anemometer at the south site. Due to instrument design and orientation, eddies with a bearing of 42 to 72 degrees could reflect interference from the mast due to the orientation of the CSAT3 facing about 235 degrees west. Wind with a bearing of 42 to 72 degrees most often occurred at night when wind velocity was typically low. However, this flag was not set when the wind was from this direction. Recommended improvements to the criteria for this flag include a wind velocity component, since very low wind speeds could be less affected by the mast.

The data were reprocessed to correct the error flagging issues described above and the data screening process was repeated to develop the data sets used in the analysis. Fewer times steps were unnecessarily skipped with the revised error flagging system.

The following sections describe the systematic evaluation of data from the Island Park energy flux site for turbulent fluxes H and LE, R_n, CS, G, and H_{LAS}. EC data used in the following sections were the original, unadjusted data, which included corrections for frequency, air density and coordinate rotation, unless otherwise noted. In this context, “unadjusted” means that no regression-based or LAS-based multipliers or additional corrections were applied to H and LE to improve EBCE. H and LE data have had the standard corrections applied to the raw data to calculate the turbulent fluxes.

3.2.1 Assessment of H and LE

An Initial assessment of the original Island Park data was completed to explore the behavior of the dataset in terms of EBCE. EBCE, defined as,

$$EBCE = R_n - G - CS - H - LE \quad \textbf{(3-1)}$$

and EB ratio, defined as

$$EB\ ratio = \frac{H + LE}{R_n - G - CS} \quad \textbf{(3-2)}$$

were graphically assessed. Figure 3-8 shows a graph of EBCE and EB ratios for a 3-day period in July 2011. The EB ratio varied throughout the day, ranging from less than 0.5 in the morning to near 1.0 in the afternoon. Beginning with sunrise, the closure ratio quickly increased to about 0.8. During the day the EB ratio fluctuated, but remained relatively high, approximately 0.9. As evening approached, the EB ratio quickly decreased to less than 0.5 and demonstrated more spikes at night than during the day. This daytime-nighttime EB closure behavior followed the pattern identified by Stoy et al. (2013) in their analysis of 173 FLUXNET sites. They found that EB closure increased more slowly in the morning than the corresponding decrease in the evening. In the Island Park data, the magnitude of the EBCE, in W m^{-2}, actually increased to its maximum as the EB ratio approached 1 in the afternoon. Conversely, at night the magnitude of the EBCE became small while the EB ratio decreased to near 0, due in part to the small magnitude of the H and LE fluxes at night. In addition, horizontal flux of energy below the forest canopy, and below the EC sensors, can also contribute to inaccurate flux measurements at night. The magnitude of the fluxes in play in the daytime relative to the night-time periods was responsible for the dichotomy of the behavior of EBEC and EB ratio during daytime vs nighttime periods. This pattern was typical for the Island Park data set, and has been observed by others (Franssen et al. 2010). The behavior of the EBCE was spikey, particularly at night, reflecting the spikey nature of the original EC data. We also note that the EB ratio was typically, but not always, about 0.15 less at the south site relative to the north site during daytime periods. Figure 3-9 and Figure 3-10 show a frequency distribution analysis of the EBCE residuals for the north and south sites using original EC data from July 2011. The EBCE residual had a distribution with a right-side skewing centered on approximately 0 W m^{-2}, with negative values occurring mostly during nighttime and positive values during daytime

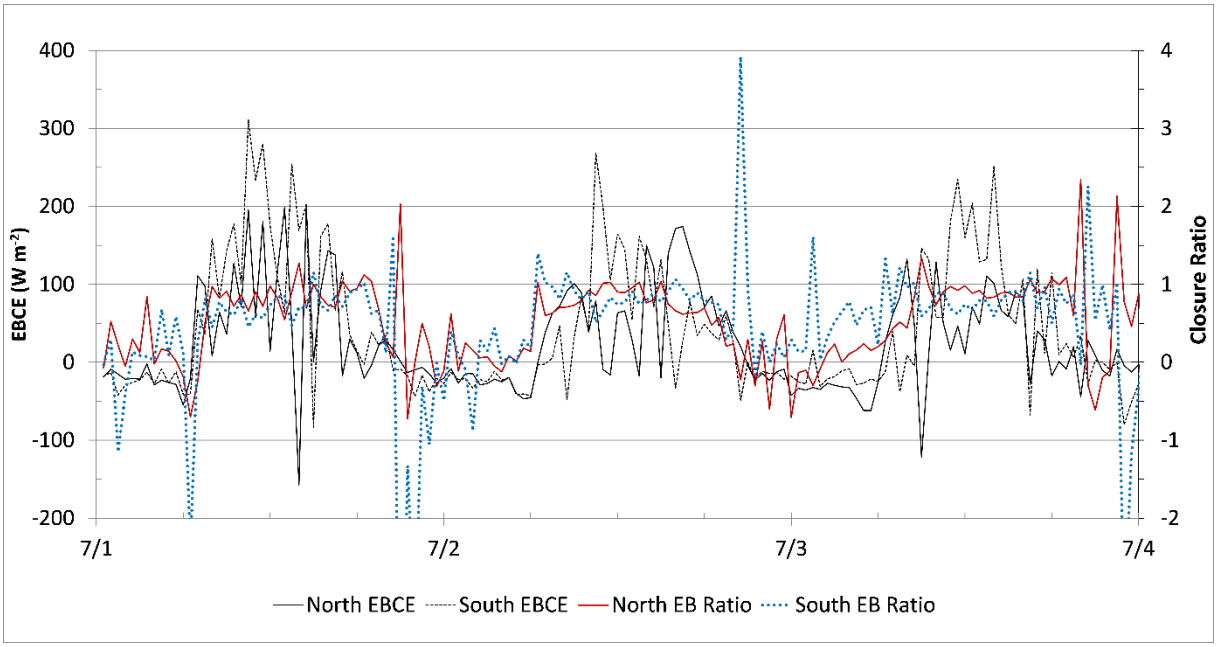

Figure 3-8. Comparison on EBCE and EB ratio for north and south sites for a typical 3-day period, July 2011. This graph shows the behavior of the original data. The date labels mark the occurrence of midnight.

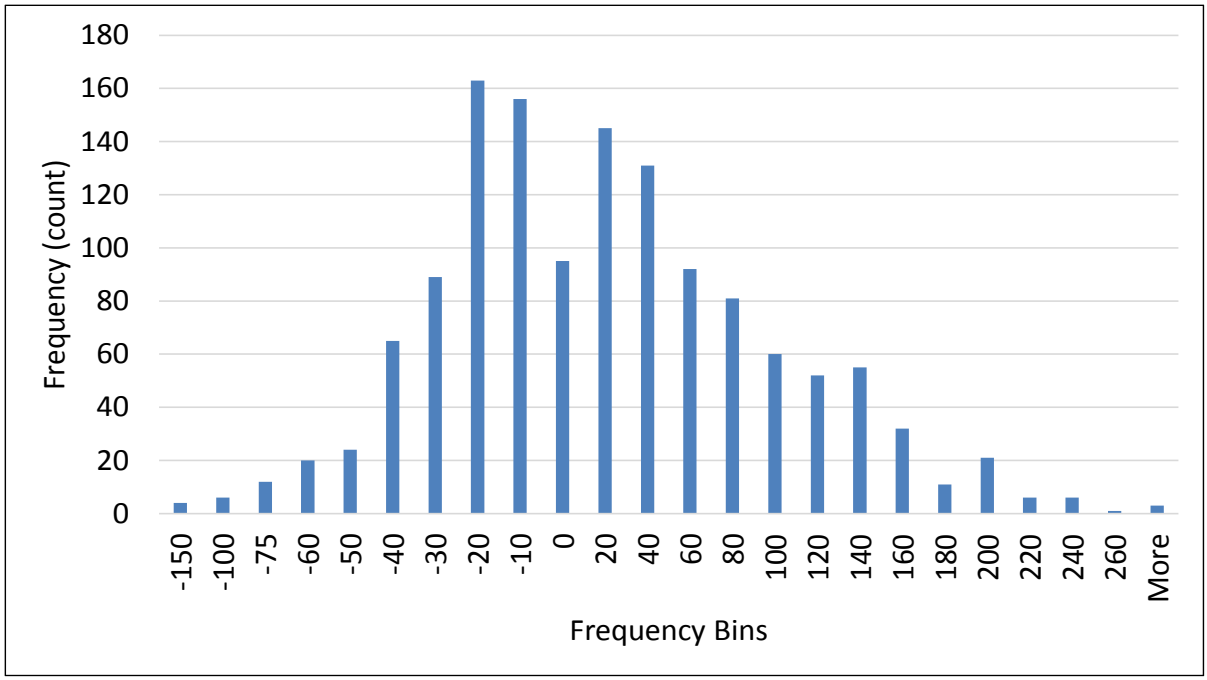

Figure 3-9. Analysis of the frequency distribution of the EBCE residual based on the original EC data for the north site, July 2011, n = 1329. .

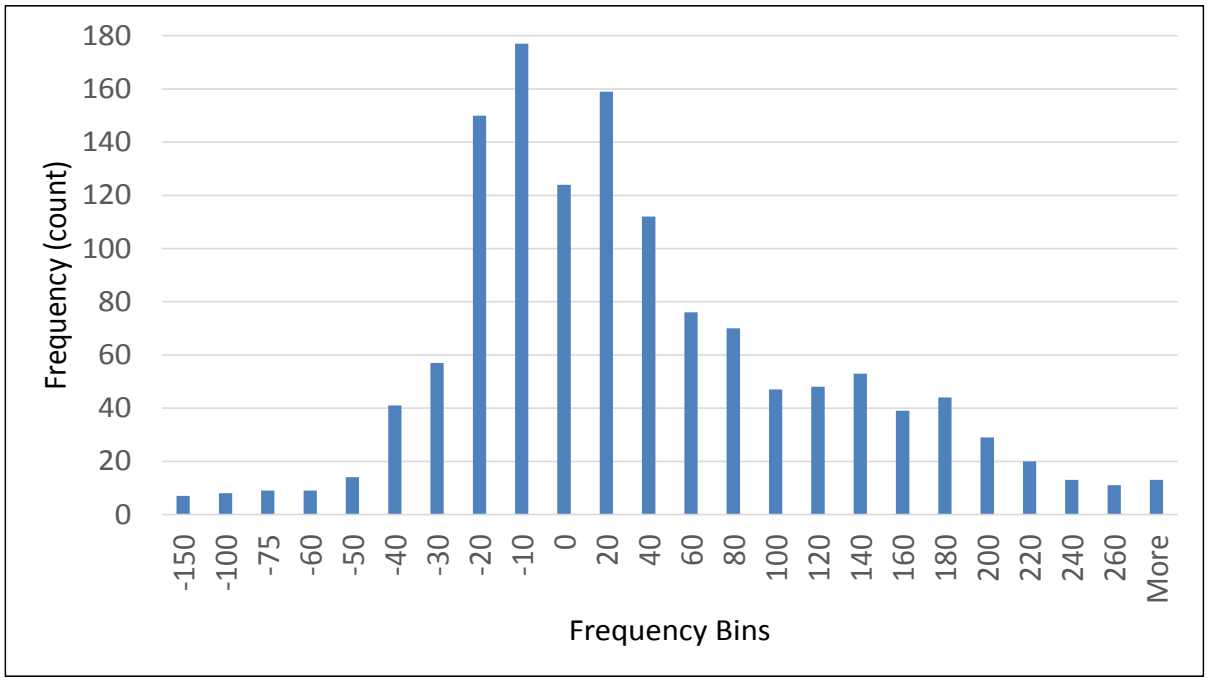

Figure 3-10. Analysis of the frequency distribution of the EBCE residual based on the original EC data for the south site, July 2011, n =1329.

A regression analysis was used to assess the relationship of R_n, G, and CS vs the turbulent fluxes H and LE. R_n - G - CS were the dependent variables and H + LE were the independent variable. This regression model assumed that R_n, G, and CS were "good" for the purpose of understanding the effect of the turbulent fluxes in the EBCE. Subsequent sections assess R_n, G, and CS in detail. In this regression model, R_n was the average of the three four-component net radiometers (two at the south tower and one at the north tower). G was the average from 10 soil heat flux subsites from both the north and south sites (see section 3.2.4). CS was estimated from the IRT on the south tower. H and LE were the original unadjusted turbulent flux estimates from the EC systems. The regression coefficients of 1.12 and 1.31 for LE and H in Table 3-2 suggested that both LE and H were under-measured. This is consistent with the literature that indicate that turbulent fluxes are typically under-measured by EC systems, particularly in complex environments (Foken 2008, Wilson et al. 2002). This conclusion assumes that measurements and estimates for R_n, G, and CS were "good" and that most of the EBCE resided in the turbulent fluxes. Subsequent sections support this assumption.

Independent Variables:	LE	H		
Coefficient	1.12	1.31	-3.70	Y Intercept
Standard Error of Coefficient	0.02	0.03	1.63	Standard Error of Intercept
R^2	0.97		42	Standard Error of Regression
F Value	20618		1288	Degrees of Freedom
Regression Sum of Squares	74044551		2312814	Residual Sum of Squares

Table 3-2. Results of a regression model analyzing dependent variables R_n-G-CS vs independent variables H+LE, where H and LE were the original data from the EC system. Data are from July 2011.

Graphical regression models were prepared to explore the EBCE and the relationship between Rn - G - CS vs H + LE. Separate models were prepared for the Island Park north and south sites using all half-hourly data. All data (both daytime and nighttime) were included. Data removed in the QA/QC process due to error flagging were not included. R_n - G - CS was the dependent variable as described above. H + LE was the independent variable and utilized the corrected, but unadjusted EC data. In this context, 'unadjusted' means that no multipliers or adjustments based on regression or LAS data had yet been applied.

Figure 3-11 and Figure 3-12 show the OLS regression graphs for June 2011 datasets. Figure 3-13 and Figure 3-14 show the OLS regression graphs for July 2011 datasets. Night time data are clustered at the bottoms of the graphs. Data points falling below the 1:1 line represent time steps where R_n - G - CS was greater than H + LE, i.e., when EBCE was greater than 0. The graphs show that this is the most common characteristic of the Island Park data set. It can also be seen in these graphs that the turbulent fluxes H and LE from the north site were between 2 – 7 percent higher relative to the turbulent fluxes at the south site for the months shown, resulting in the better closure at the north sites, as noted above. The relationship between the turbulent fluxes at the north and south sites is explored in Section 4.

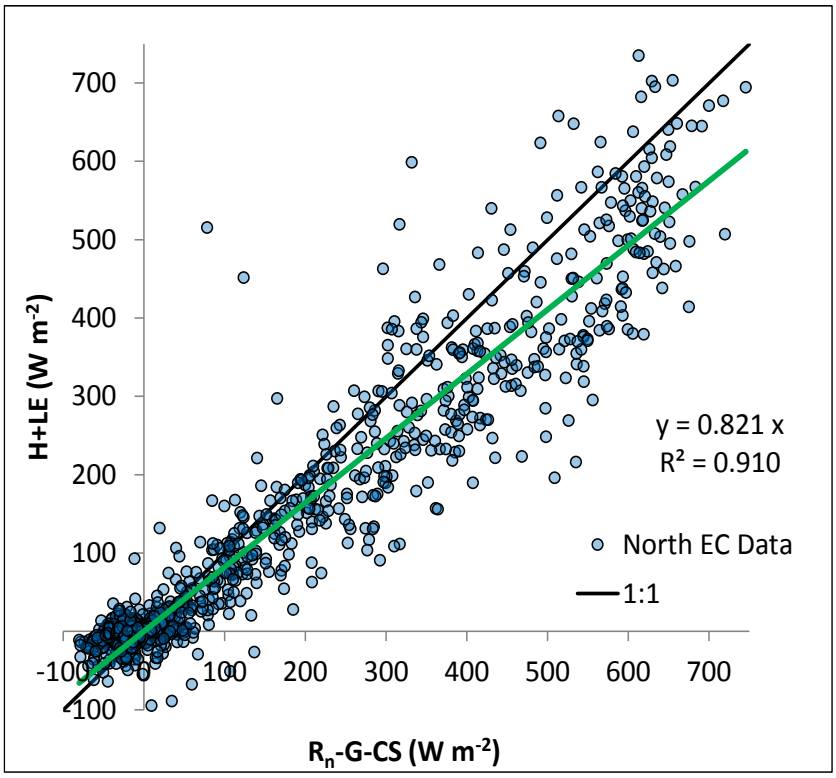

Figure 3-11. EB ratio for the north site, using unadjusted H and LE from the EC system. Data from June 2011, n = 1093.

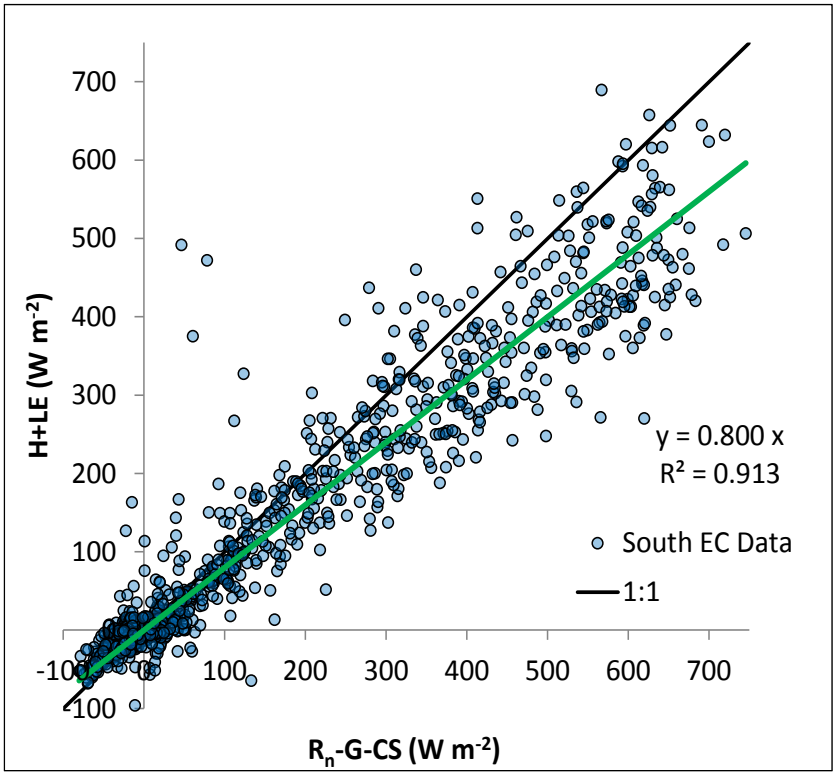

Figure 3-12. EB ratio for the south site, using unadjusted H and LE from the EC system. Data from June 2011, n = 1093.

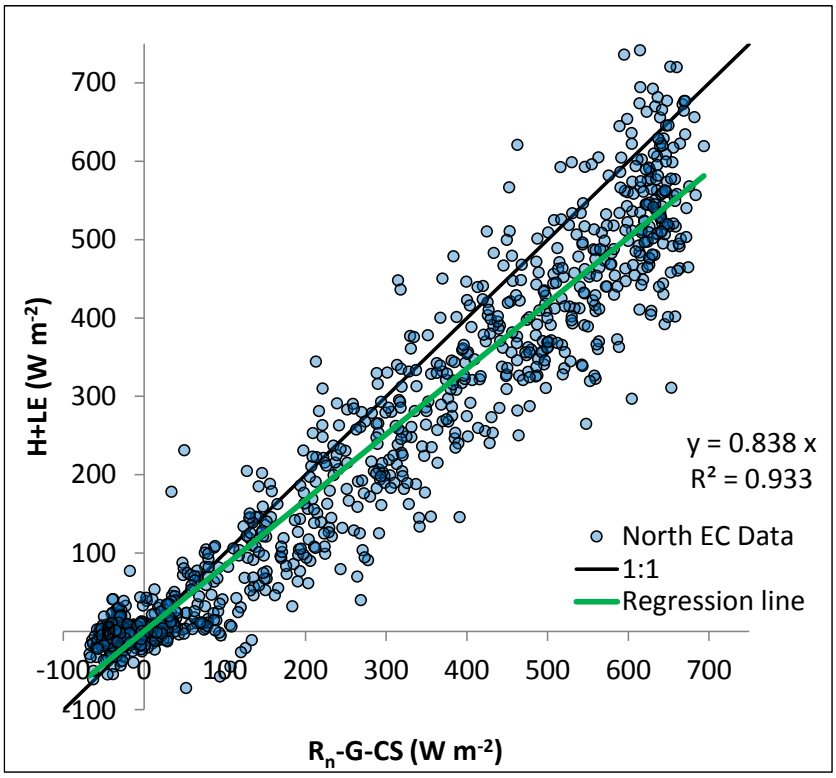

Figure 3-13. EB ratio for the north site, using unadjusted H and LE from the EC system. Data from July 2011, n = 1329.

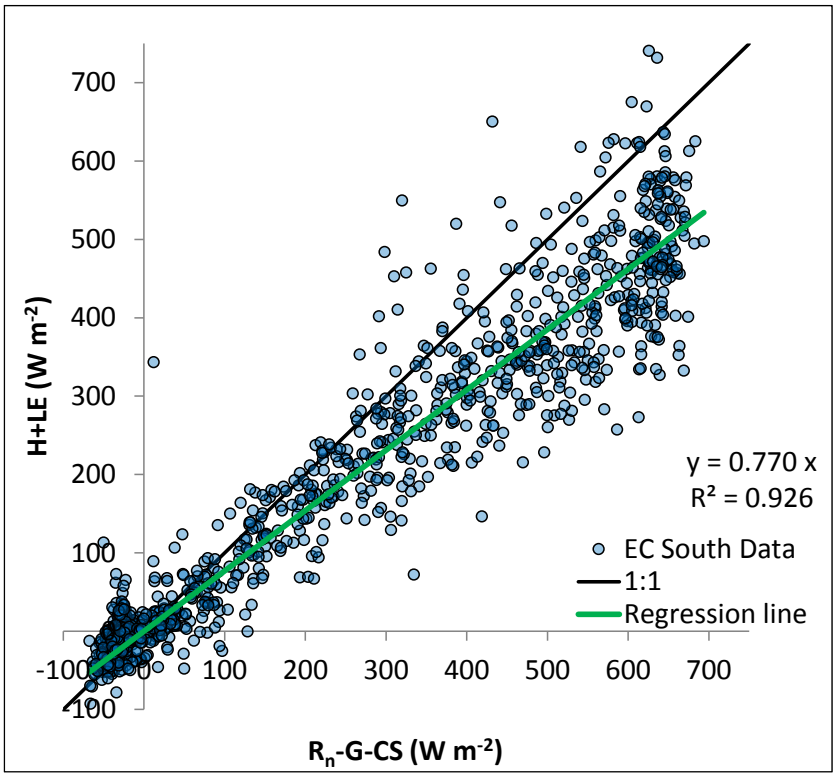

Figure 3-14. EB ratio for the south site, using unadjusted H and LE from the EC system. Data from July 2011, n = 1329.

Analyses of EBCE were also conducted on a monthly and daily time step basis to determine if general systematic biases in the data were relatively similar over different lengths of time periods. Monthly and daily sums were calculated for R_n, G, CS, and unadjusted H and LE from the July 2011 dataset because this month had the fewest time steps that were dropped due to error flagging. R_n, G, CS were as described above. Monthly and daily sums included all ½-hour time steps not excluded due to error flagging. The north and south sites were analyzed separately. The monthly sums were calculated for the entire 24-hour period and for the daytime fractions of each 24-hour period. The daytime fraction was defined as time steps with R_n at the north site greater than 25 W m^{-2}. The results of the monthly analysis are shown in Table 3-3. The EB ratio $((H_{EC}+LE_{EC})/(R_n-G-CS))$ for the daytime group was smaller than the 24-hour group due the strength of the relative cumulative magnitude of R_n during the day. Figure 3-15 and Figure 3-16 show the daily EB ratio for the north and south sites. The same patterns noted previously of better EB closure at the north site are evident in the daily data.

	R_n-G-CS (W m^{-2})	H_{EC} (W m^{-2})	LE_{EC} (W m^{-2})	EBCE (W m^{-2})	$(H_{EC}+LE_{EC})/(R_n-G-CS)$	H_{LAS} (W m^{-2})	H_{LAS}/H_{EC}
North All Data	187	53	112	23	**0.88**	67	**1.26**
North Daytime Only Data	387	114	208	65	**0.83**	129	**1.13**
South All Data	187	48	104	35	**0.81**	67	**1.39**
South Daytime Only Data	387	110	192	85	**0.78**	129	**1.17**

Table 3-3. Summary of monthly EBCE analysis using 24 hour and daytime only average data from the July 2011 dataset. This table also shows the EB ratio for the month of July 2011 for both nighttime and day time data, daytime only data, and the H_{LAS}/H_{EC} ratio. Rn-G-CS is based on the average of the three net radiometers (1 at the north site and 2 at the south site), a single estimate of CS for both sites (see section 3.2.3), and the average of the G sites at the north and south sites, n = 1329 for all data, n = 506 for daytime only.

Graphs of OLS regression between the H_{LAS} and H_{EC} were prepared using both nighttime and daytime data for the north and south sites (Figure 3-17 and Figure 3-18). Points that fall above the 1:1 line represent time steps when H_{LAS} was greater than H_{EC}, which is the most common relationship in the dataset. Data from time steps when the LAS was off line plots along the X axis.

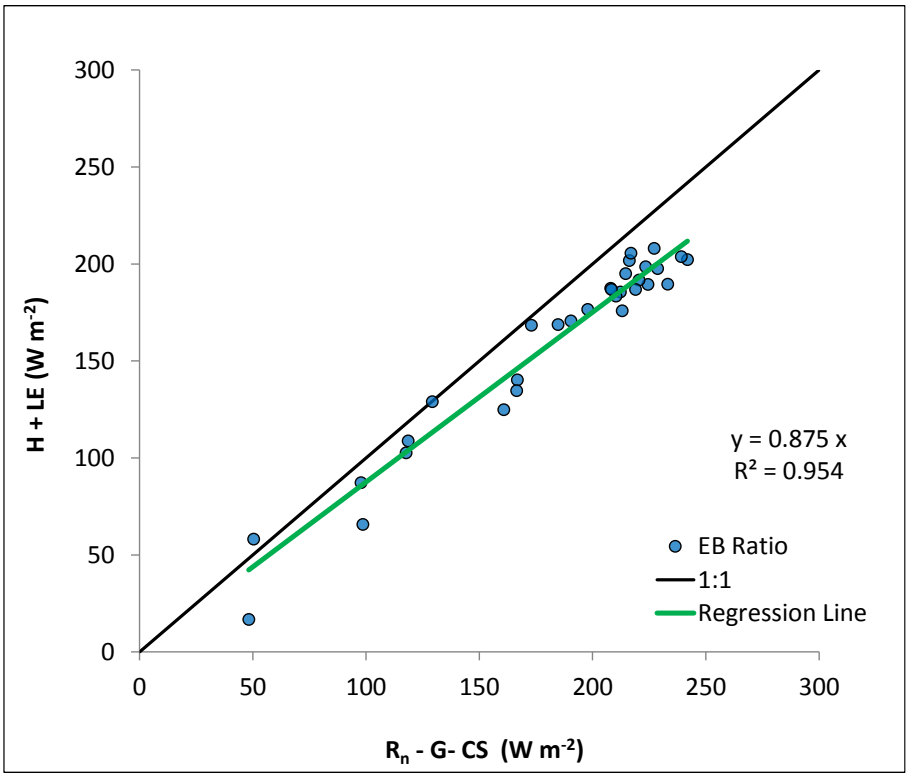

Figure 3-15. Graph of OLS regression between R_n - G - CS and H + LE based on 24-hour average fluxes for the Island Park north site. H and LE are unadjusted data from the EC system. Data from July 2011, n = 1329.

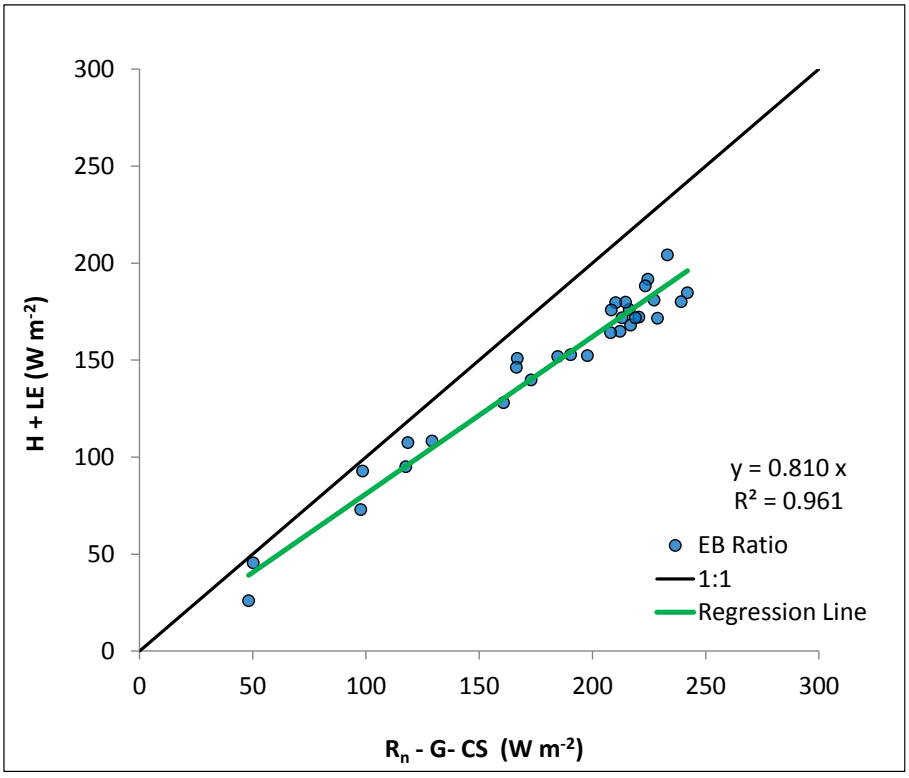

Figure 3-16. Graph of OLS regression between R_n - G - CS and H + LE based on 24-hour average fluxes for the Island Park south site. H and LE are unadjusted data from the EC system. Data from July 2011, , n = 1329.

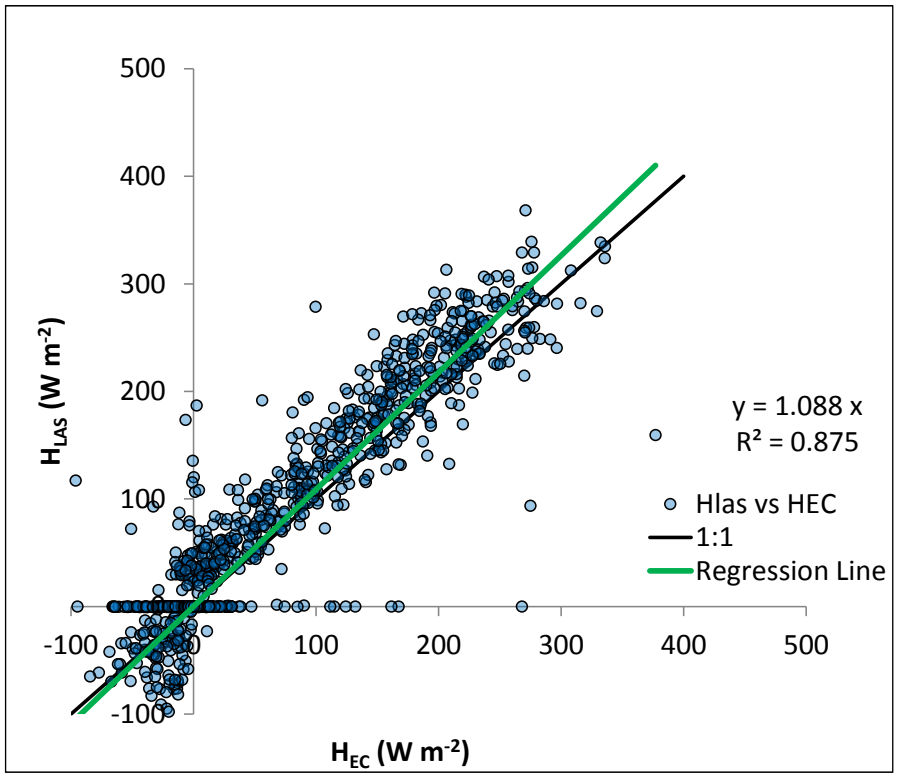

Figure 3-17. Graph for H_{LAS} vs H_{EC} for the Island Park north site. H_{EC} represents data from the EC system following standard corrections, prior to any regression or LAS adjustment. Data from July 2011, n = 1329.

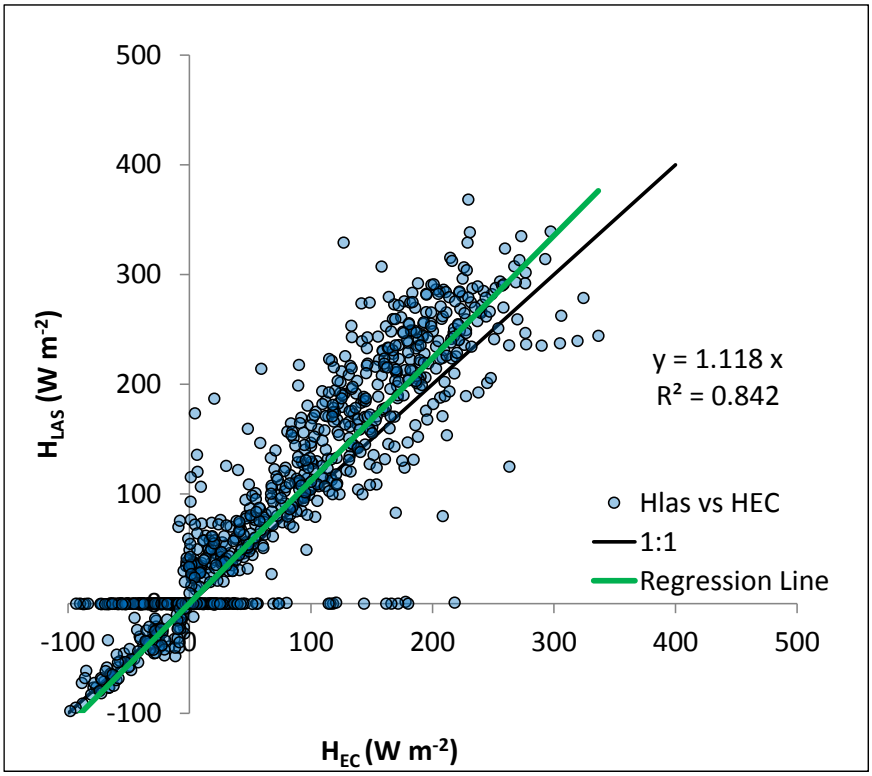

Figure 3-18. Graph for H_{Las} vs H_{EC} for the Island Park south site. H_{EC} represents data from the EC system following standard corrections, prior to any regression or LAS adjustment. Data from July 2011, n = 1329.

The 24-hour sums for R_n, G, CS, H_{EC}, LE_{EC}, and H_{LAS}, and the corresponding EB ratio $(H_{EC}+LE_{EC})/(R_n-G-CS)$ and H_{LAS}/H_{EC} are shown in Table 3-4 and Table 3-5 for the north and south sites for July 2011. Days 12 and 13 were uncharacteristic due to rain/cloud events that affected those days. Figure 3-19 and Figure 3-20 provide a visual overview of the EB ratio. The 24-hour ratios were consistently less than 1, reflecting EBCE greater than 0 for the Island Park data set. The graphs also shows that while there is not an exact match between the north and south sites in terms of EBCE, they are similar. Factors that could contribute to the differences between the sites include differences in the vegetation, soil moisture, and instruments.

Three additional routine calibrations of the longwave sensors have been performed since the radiometers were installed on the observation towers. The calibrations were completed on 12/08/2011, 08/09/2012, and 08/26/2014. The calibrations used two Hukseflux IR02 sensors, which are radiation sensors without the solar blind filter (Zhao et. al 2014). The IR02 sensors measure both shortwave and longwave radiation without any unknown filter effects. The IR02 can be used to calibrate the longwave radiation measurement of the NR01 and CNR1 4-way net radiometers since there is no shortwave radiation at night.

The 2011 calibration showed that the three 4-way net radiometers in use at Island Park measured atmospheric long wave radiation to within 5 W m^{-2} of one another and most of the time were within the range of the two "standard" IR02s, which showed about 7 to 8 W m^{-2} of difference. The 2012 calibration showed that the three 4-way net radiometers in use at the Island Park site measured atmospheric long wave radiation to within 8 W m^{-2} compared to the "standard" IR02. During the 2014 calibration, the IR02 was again used as a standard. In addition a Kipp and Zonen CG4 pyrgeometer that was reconditioned and recalibrated by Kipp and Zonen in 2012 was used. During the nighttime, the three 4-way net radiometers in use at Island Park measured atmospheric long wave radiation usually within 5 W m^{-2} of the standards. However, during the day, comparison to the CG4 showed that the longwave measurement of the NR01s had a slight dependency on the intensity of the shortwave radiation, as documented by Zhao et al. (2014). A correction factor was incorporated into the data processing to account for this shortwave "seepage". The CNR1 did not demonstrate a short wave dependency.

Day	Num. of 30-minute Time Steps	R_n-G-CS (W m^{-2})	H_{EC} (W m^{-2})	LE_{EC} (W m^{-2})	EBCE (W m^{-2})	$H_{EC}+LE_{EC}$/ (Rn-G-CS)	H_{LAS} (W m^{-2})	H_{LAS}/H_{EC}
1	47	229	96	102	31	**0.86**	0	0.00
2	48	224	82	108	35	**0.84**	92	1.12
3	48	216	61	141	14	**0.93**	74	1.22
4	40	233	66	124	44	**0.81**	88	1.33
5	32	161	32	93	36	**0.78**	22	0.69
6	23	167	39	101	27	**0.84**	48	1.23
7	36	242	64	138	40	**0.84**	57	0.89
8	28	99	9	57	33	**0.67**	31	3.65
9	44	190	43	128	20	**0.90**	60	1.40
10	48	212	67	118	27	**0.87**	80	1.18
11	40	239	70	134	35	**0.85**	88	1.26
12	22	48	-15	32	32	**0.35**	-27	1.78
13	31	50	-1	59	-8	**1.15**	0	-0.73
14	38	118	28	75	15	**0.87**	44	1.60
15	48	220	72	119	29	**0.87**	87	1.20
16	39	119	25	84	10	**0.92**	34	1.34
17	48	215	54	141	20	**0.91**	66	1.21
18	48	217	69	137	11	**0.95**	79	1.14
19	48	129	9	120	0	**1.00**	29	3.16
20	48	227	101	107	19	**0.92**	112	1.11
21	48	198	64	112	21	**0.89**	81	1.26
22	48	173	55	114	5	**0.97**	59	1.08
23	48	219	76	111	32	**0.85**	98	1.28
24	48	210	57	127	27	**0.87**	77	1.36
25	48	185	33	135	16	**0.91**	54	1.62
26	46	223	72	127	25	**0.89**	85	1.19
27	48	213	79	97	37	**0.83**	102	1.30
28	48	208	78	109	21	**0.90**	92	1.18
29	48	208	63	124	22	**0.90**	83	1.31
30	48	166	30	105	32	**0.81**	56	1.89
31	48	98	16	71	11	**0.89**	27	1.67

Table 3-4. North site 24-hour sums of R_n G, CS H_{EC}, LE_{EC}, and H_{LAS} using all time steps in each 24-hour period, excluding error-flagged time steps. Daily EBCE ratio (R_n-G-CS/(H_{EC}+LE_{EC})) and H_{LAS}/H_{EC} are also shown. Data from July 2011.

Day	Num. of Time Steps	R_n-G-CS (W m^{-2})	H_{EC} (W m^{-2})	LE_{EC} (W m^{-2})	EBCE (W m^{-2})	$H_{EC}+LE_{EC}$/ (Rn-G-CS)	H_{LAS} (W m^{-2})	H_{LAS}/H_{EC}
1	47	229	89	82	57	0.75	0	0.00
2	48	224	78	114	33	0.85	92	1.18
3	48	216	52	124	40	0.81	74	1.42
4	40	233	67	137	29	0.88	88	1.32
5	32	161	14	114	33	0.80	22	1.53
6	23	167	33	118	16	0.90	48	1.45
7	36	242	55	130	57	0.76	57	1.05
8	28	99	16	77	6	0.94	31	2.01
9	44	190	41	112	38	0.80	60	1.48
10	48	212	57	108	47	0.78	80	1.40
11	40	239	65	115	59	0.75	88	1.34
12	22	48	-37	63	22	0.54	-27	0.73
13	31	50	-12	57	5	0.91	0	-0.04
14	38	118	21	74	23	0.81	44	2.08
15	48	220	60	112	48	0.78	87	1.44
16	39	119	13	94	11	0.91	34	2.55
17	48	215	44	136	35	0.84	66	1.49
18	48	217	50	118	49	0.77	79	1.58
19	48	129	6	102	21	0.84	29	5.00
20	48	227	92	89	46	0.80	112	1.23
21	48	198	58	94	45	0.77	81	1.40
22	48	173	46	94	33	0.81	59	1.30
23	48	219	74	98	47	0.78	98	1.31
24	48	210	60	119	31	0.85	77	1.29
25	48	185	32	119	33	0.82	54	1.67
26	46	223	76	113	35	0.84	85	1.13
27	48	213	81	91	41	0.81	102	1.26
28	48	208	63	101	44	0.79	92	1.46
29	48	208	69	107	33	0.84	83	1.20
30	48	166	46	100	20	0.88	56	1.21
31	48	98	15	58	25	0.75	27	1.77

Table 3-5. South site daily sums of R_n G, CS H_{EC}, LE_{EC}, and H_{LAS} using all time steps in each 24-hour period, excluding error flagged time steps. Daily EBCE ratio (R_n-G-CS/($H_{EC}+LE_{EC}$)) and HLAS/HEC are also shown. Data from July 2011.

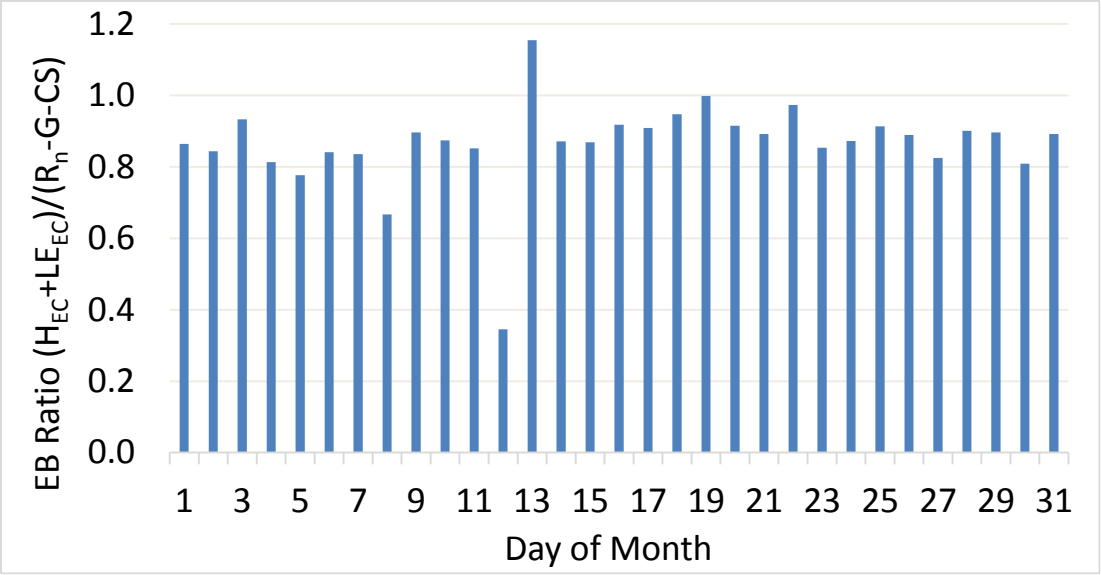

Figure 3-19. 24-hour EB ratios ($(H_{EC}+LE_{EC})/(R_n-G-CS/)$) for the Island Park north site. Data from July 2011.

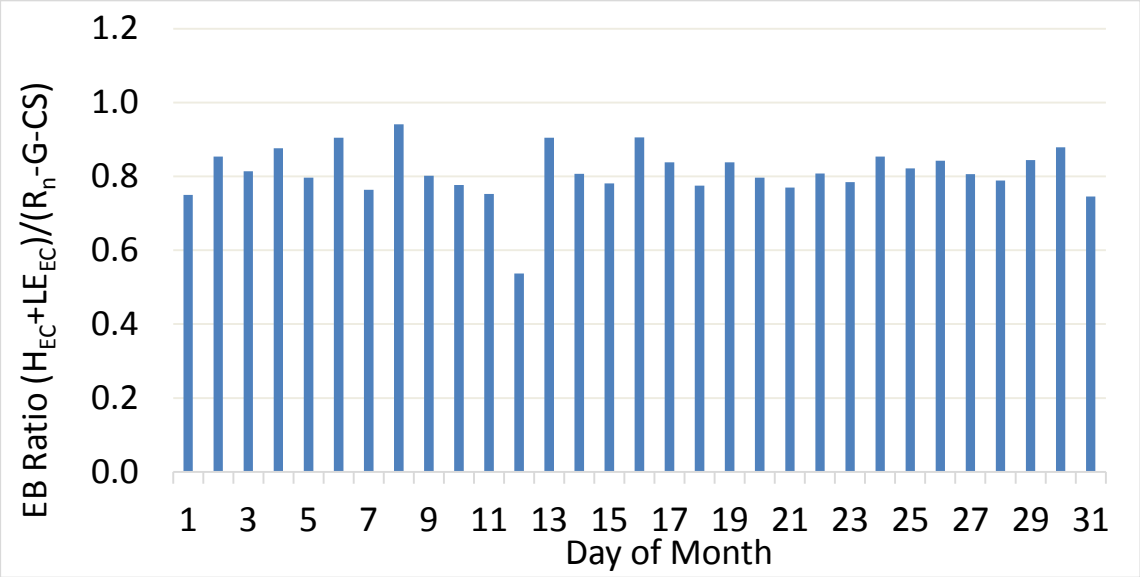

Figure 3-20. 24-hour EB ratios ($(H_{EC}+LE_{EC})/(R_n-G-CS/)$) for the Island Park south site. Data from July 2011.

3.2.2 Assessment of R_n

This section assess the reliability of the R_n measurements from the Island Park site. R_n was based on three net radiometers mounted on the observation towers. As noted in Section 1.3, the south tower was equipped with a CNR1 and an NR01. The north tower was equipped with an NR01. This section documents the work that was done to ensure good estimates of R_n. Before installation, the 4-way net radiometers were inter-calibrated as previously described, and the calibration coefficients were programmed into the data logger programs.

An analysis was conducted to evaluate the sensitivity of the EBCE to which radiometer, or combination of radiometers, were used to estimate R_n. Figure 3-21, Figure 3-22, Figure 3-23, and Figure 3-24 show regression between north and south average unadjusted H + LE, as measured by the EC systems, and R_n - G - CS, for day time periods for July 2011. R_n was the average of the NR01 at the north site, and the NR01 and CNR1 at the south site. G was the average of the soil sites at the north and south sites. CS was based on an IRT at the south tower, as described in Section 2.2.3. The regression models in the graphs explored the effects of different weightings of the three radiometers to explore how the magnitude of R_n was affected due to instrument bias or differences in location. Figure 3-21 shows the regression model with R_n calculated as the average of the three radiometers (the NR01 at the north site and the NR01 and CNR1 at the south site). Figure 3-22 shows the regression model when only R_n from the NR01 at the North Tower was used. Figure 3-23 shows the regression model when only R_n from the NR01 at the South Tower was used. Figure 3-24 shows the regression model when only R_n from the CNR1 at the south tower was used. An evaluation of the regression plots showed that the NR01 radiometers performed similarly in terms of EBCE. The slopes of the EBC for the two NR01s were within 1 percent of each other. The CNR1-based estimate for R_n was 2 to 3 percent higher than with the two NR01s. This difference could be due to calibration differences, or it could be due to real difference in the mix of sky, trees, and ground within the field of view of the radiometers.

At Island Park, all the radiometers were suspended above tree canopies, but had different fractions of understory views, including some sunlit areas in off-nadir directions. Based on the close behavior of the three net radiometers at Island Park, using an average R_n comprised of the three radiometers seems valid and is a means to reduce some impact of any sporadic behavior in any one sensor. In addition, multiple radiometers would better represent the diverse conditions present in the flux footprint area, as each instrument “sees” a different mix of tree canopy and understory and using instruments from different manufactures could help offset instrument biases. Using radiometers at the North and South Towers provides estimates of R_n at each end of the 1.6 km LAS transect.

As a trial approach to close the EB equation, the average R_n of the three radiometers was multiplied by 0.84, which resulted in a slope of the regression line of 1 (Figure 3-25). This approach would be applicable if it was believed that the R_n was over-measured and was the source of the EBCE. Although this method would result in closure, it is believed that the measured values of R_n are reliable, and therefore no adjustment to R_n is recommended for the Island Park data.

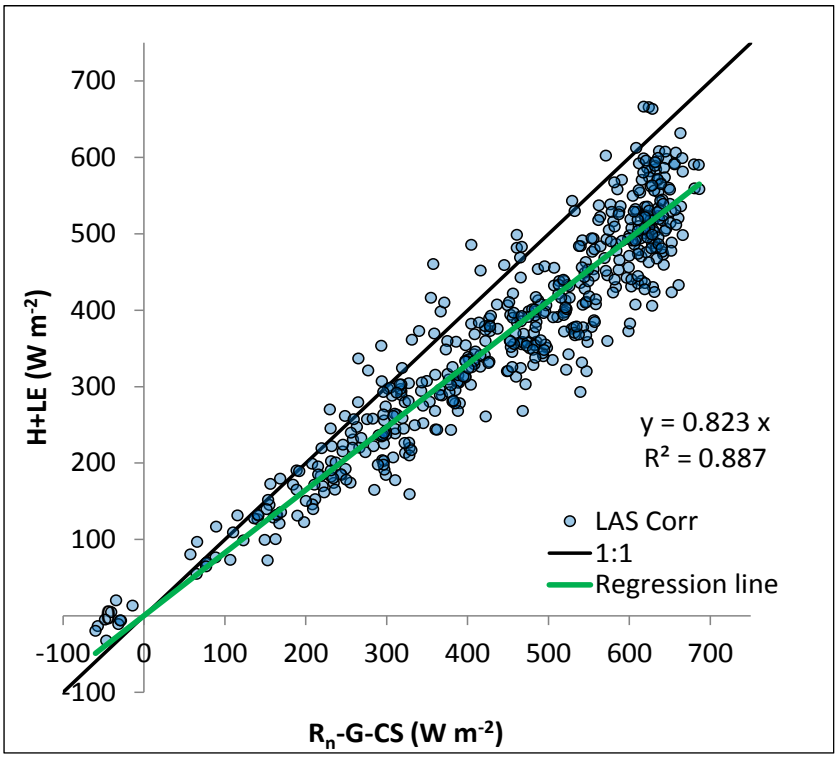

Figure 3-21. Regression between unadjusted, averaged north and south H + LE and R_n - G - CS. R_n was calculated as the average R_n from the three net radiometers. Data are from the Island Park July 2011 dataset, n = 506.

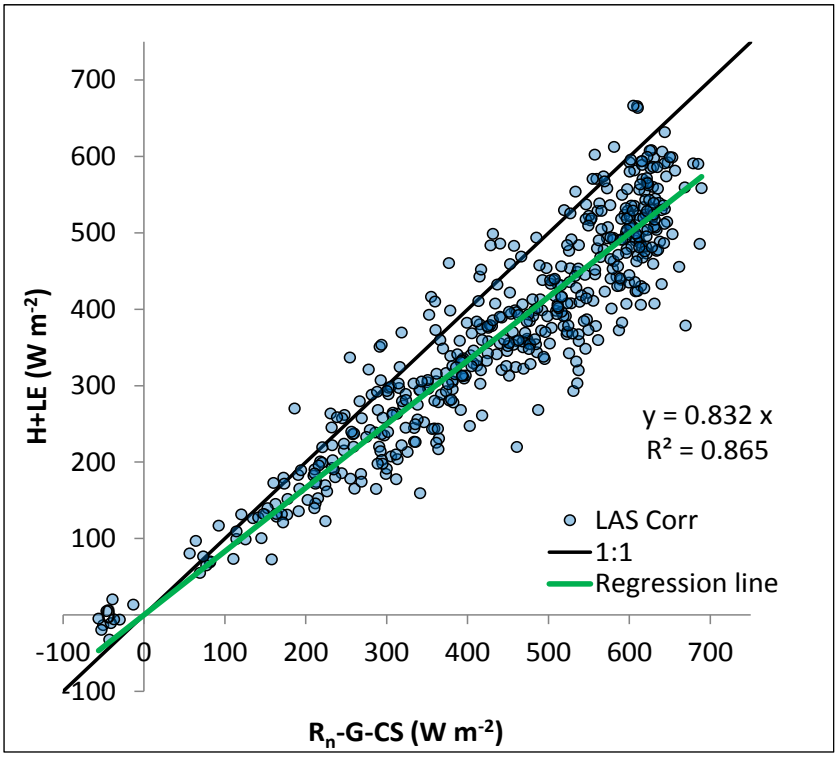

Figure 3-22. Regression between unadjusted, averaged north and south H + LE and R_n - G - CS. R_n is from the NR01 at the north tower. Data are from the Island Park July 2011 dataset, n = 506.

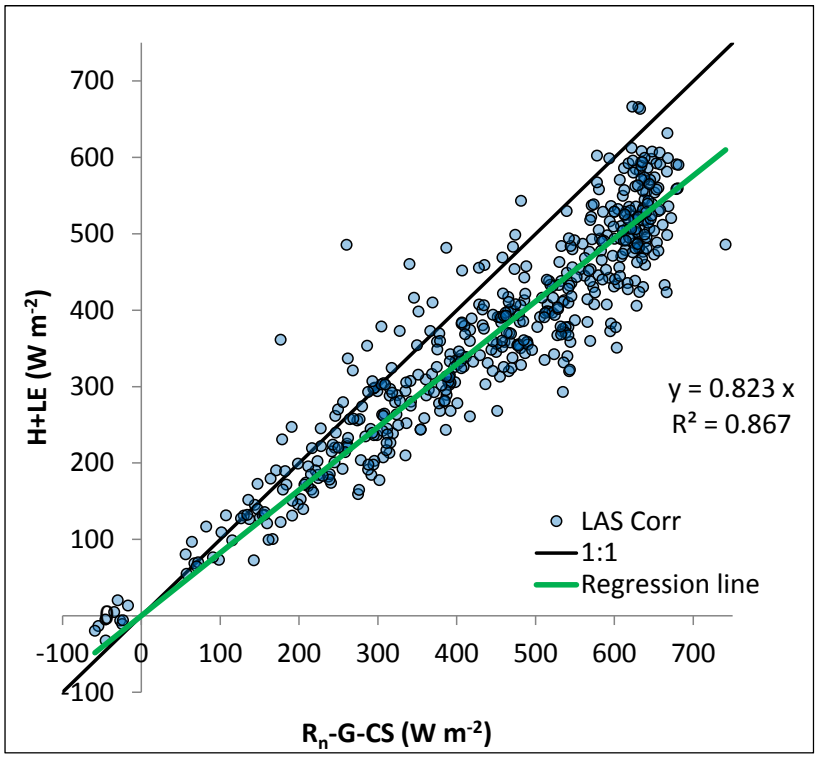

Figure 3-23. Regression between unadjusted, averaged north and south H + LE and R_n - G - CS. R_n is from the NR01 at the south tower. Data are from the Island Park July 2011 dataset, n = 506.

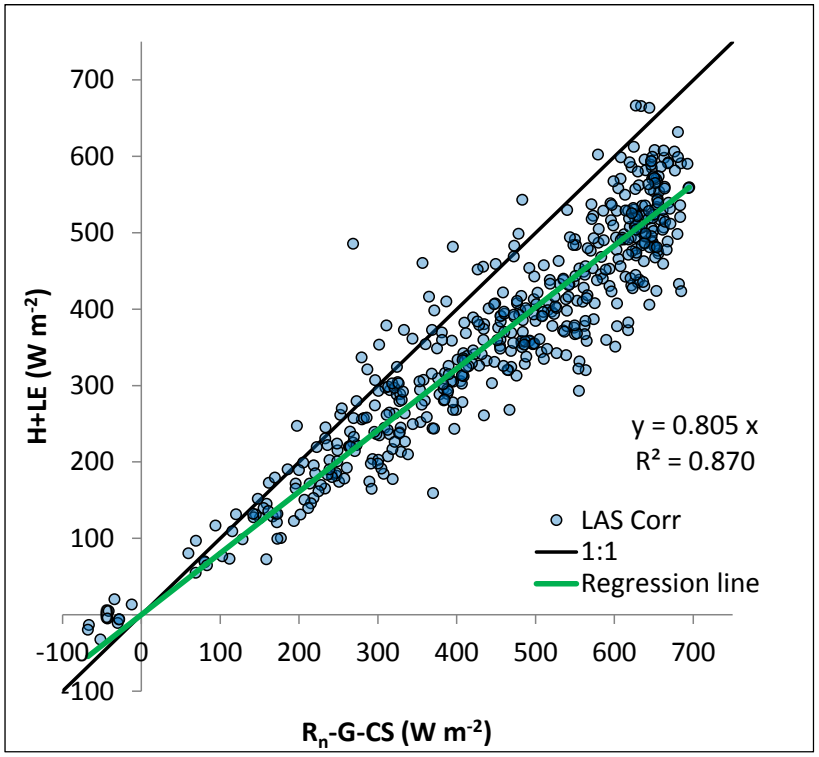

Figure 3-24. Regression between unadjusted, averaged north and south H + LE and R_n - G - CS. R_n is from the CNR1 at the south tower. Data are from the Island Park July 2011 dataset, n = 506.

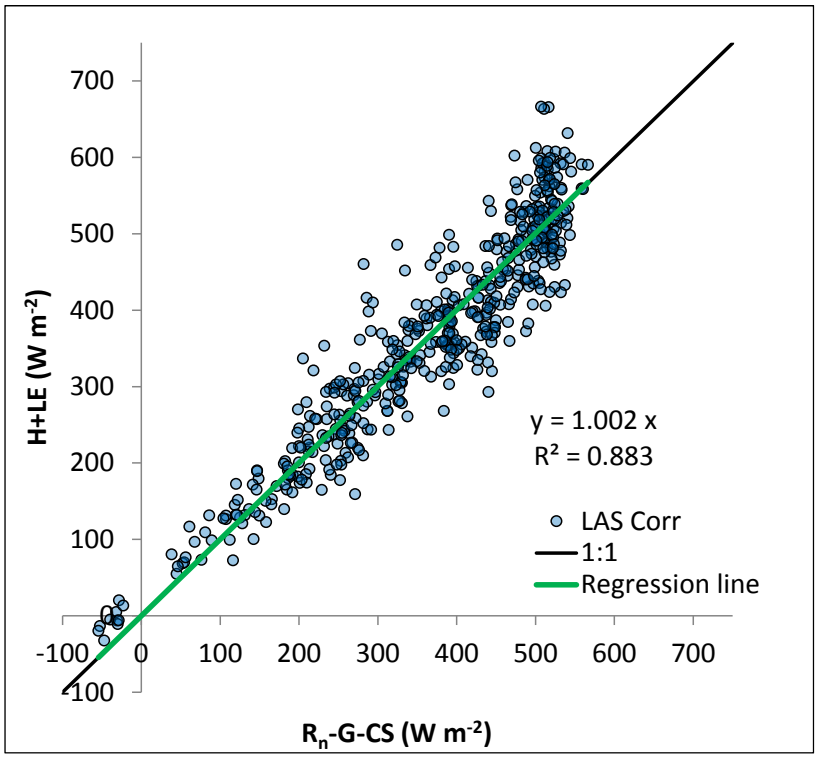

Figure 3-25. Regression between unadjusted, averaged north and south H + LE and R_n - G - CS. R_n, calculated as the average R_n from the three net radiometers, was multiplied by 0.83 as a trial approach to balance the EB equation, if it were believed that R_n was over-estimated. Data from Island Park July 2011 dataset, n = 506.

3.2.3 Assessment of Canopy Storage Change

Canopy Storage Change (CS) represents the energy flux into and out of the biomass, specifically the heating of stems, branches, trunks, and needles during the day. Energy flux into and out of the Lodgepole pine forest represents most of the CS at Island Park. CS can be an important component of an energy flux system, particularly if substantial biomass is present (Haverd et al. 2007, Michiles and Gielow 2008). Wilson et al. (2002) found canopy storage to represent seven percent of the energy budget in forested systems. Michiles and Gielow (2008) measured above-ground energy storage rates (including the storage in the air) in a "terra firme" tropical rain forest site in central Amazonia, Brazil, that were usually between of 30 to 70 W m^{-2}, but with maxima that could exceed 90 W m^{-2} and minima as low as -200 W m^{-2} during rain events. The trunk, branch, twig, and leaf components had maximum values of 30, 20, 20, and 5 W m^{-2}, respectively. Haverd et al. (2007) found hourly biomass heat storage values in trunks in a 40 m-tall Australian temperate Eucalyptus forest peaked at 61 W m^{-2}. Oliphant et al. (2004) found canopy (biomass) storage in a deciduous forest in south central Indiana peaked in mid-spring just before leaf emergence at about 20 W m^{-2}. Garai et al. (2010) found that tree biomass storage in a walnut orchard near Davis, California varied from 12 W m^{-2} to -6 W m^{-2}, constituting 1% of daytime and 9% of nighttime net radiation in late May

and early June. Meesters and Vugts estimated the biomass heat flux in a pine plantation on Fiji to range from 7 to -16 W m^{-2}. Moderow et al. (2009) assessed available energy at four coniferous sites across Europe. They found that the heat storage in biomass ranged from a high of 18 W m^{-2} during the day to a low of -15 W m^{-2} during the night.

CS was estimated in this study using an approximate heat balance method based on canopy temperature measured by a narrow field IRT mounted on the south tower that measured the temperature on the southeast-facing side of the canopies of a group of lodgepole pine trees. Figure 1-9 shows of photo of the IRT mounted on the south tower. CS was estimated by a relationship developed by Zhao (2014, email communication, 7/10/2014).

$$CS = C * (IRT_{before} - IRT_{after}) \quad \textbf{(3-3)}$$

where CS has units of W m^{-2}, IRT has units of ^{o}C, and C is an empirically determined constant, determined to be 31.1 W m^{-2} $^{o}C^{-1}$, for the Island Park study area. IRT is the measured canopy temperature. The change in canopy temperature for the time step of interest was calculated by subtracting the temperature of the tree canopy for the time period following the time step of interest from the temperature of the canopy for the time step preceding the time step of interest. The value of the constant C (31.1) was determined by statistical methods.

The canopy heat flux estimate was unique among the data collected at Island Park because there were not multiple, independent sensors to confirm the estimate, nor direct measurement of CS. The CS estimate for the Island Park site ranged from daily maxima of 80 to 100+ W m^{-2} to daily minima of -60 to -80 W m^{-2}. These estimates are both higher and lower than the values reported in the literature.

Several options were explored to modify the CS function of Eq. 3-3, including the use a time-lag term and the use of an R_s-dependent function. However, none were found that gave satisfactory results. In particular, strengthening the CS function resulted in unreasonably high CS estimates relative to the values reported in the literature and were inconsistent in improvements to EBCE. The results of increasing or decreasing CS through the use of a weighting factor in the regression model between H + LE and R_n - G - CS are shown in Figure 3-26, Figure 3-27, Figure 3-28 and Figure 3-29. Figure 3-26 shows the regression model when a weighting factor of 1 was applied to CS, meaning no adjustment to the original CS function. Figure 3-27 shows the regression when a weighting factor of 2 was applied to the CS term. Doubling CS resulted in slightly lower R^2 values and only small changes in the

slope of the regression line due to the small magnitude of the CS relative to R_n. In addition, the use of the multiplier 2 caused the estimated H + LE to substantially exceed R_n – G – CS at low flux values when the impact of CS is relatively large (Fig. 3-24) Figure 3-28 shows the regression when a weighting factor of 0.5 was applied to the CS term. Again there was little effect on EBCE, indicating that the standardized form of Eq. 3-3 and magnitude of CS was appropriate and sufficient. Figure 3-29 shows regression when a weighting factor of 0 was applied to the CS term, meaning that CS was not assigned any energy. This resulted in approximately 2 percent less closure.

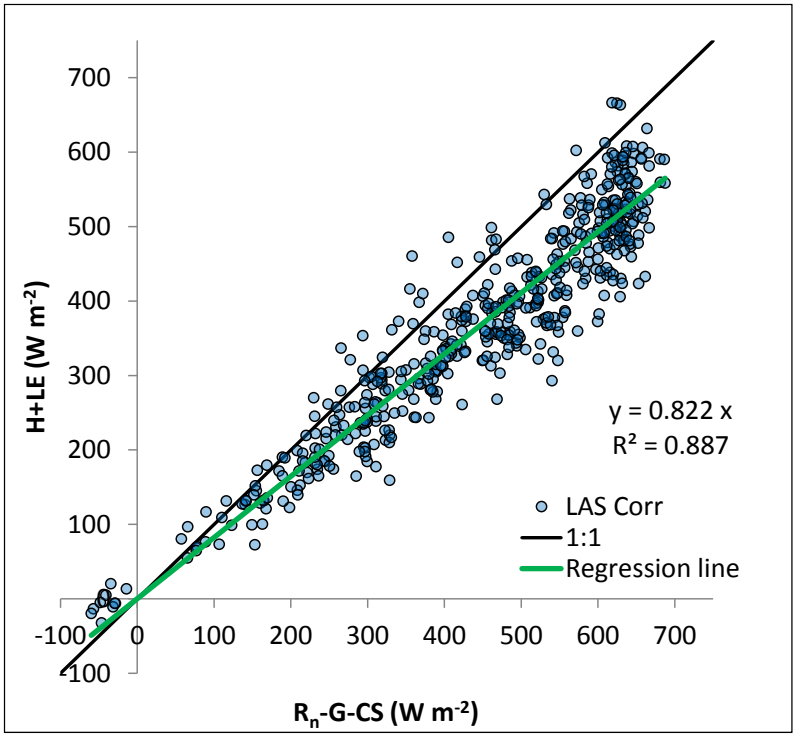

Figure 3-26. Regression between unadjusted, averaged north and south H + LE and R_n - G - CS exploring various weighting factors for the CS term. This regression used a CS weighting factor of 1. Data are from July 2011, n = 506.

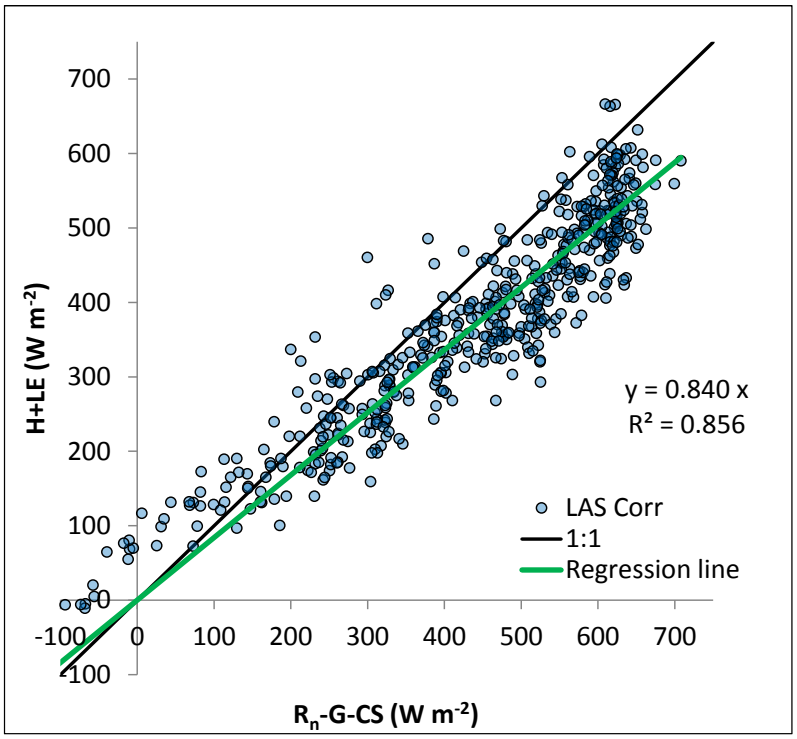

Figure 3-27. Regression between unadjusted, averaged north and south H + LE and R_n - G - CS exploring various weighting factors for the CS term. This regression used a CS weighting factor of 2. Data are from July 2011, n = 506.

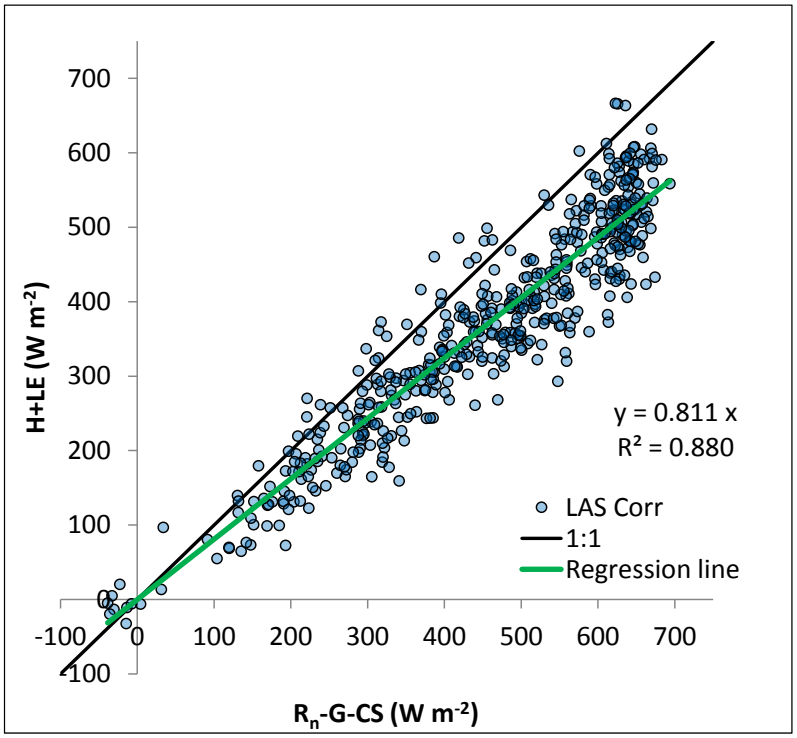

Figure 3-28. Regression between unadjusted, averaged north and south H + LE and R_n - G - CS exploring various weighting factors for the CS term. This regression used a CS weighting factor of 0.5. Data are from July 2011, n = 506.

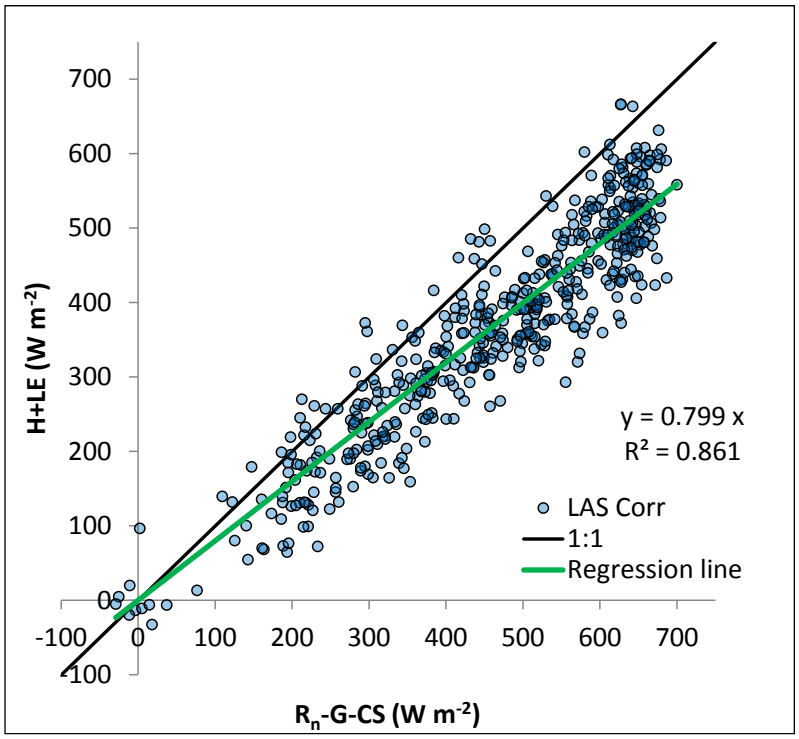

Figure 3-29. Regression between unadjusted, averaged north and south H + LE and Rn - G - CS exploring various weighting factors for the CS term. This regression used a CS weighting factor of 0. Data are from July 2011, n = 506.

3.2.4 Assessment of G

Measurement of Soil heat flux at the surface includes the flux of energy past a soil heat flux plate plus the change in heat storage above that plate (Eq. 3.4). G was calculated using data from thermocouples, soil heat flux plates, and soil water content sensors placed in the soil profile. The thermocouples were placed at four depths above the heat flux plates to provide a soil temperature profile. The soil temperature at each of the soil subsites was a function of the subsite's relative ratio of sun vs shade, with sunny sites having a warmer soil profile. Table 3-6 describes the solar exposure conditions at each of the soil subsites at the Island Park north and south sites. Each site had heat flux plates at 6 and 12 cm depths and thermocouples at 1.5, 3, 4.5, and 9 cm at the south site and 2, 4, 9, and 15 cm at the north site. Figure 3-30 and Figure 3-31 show the average soil temperature at each of the soil subsites for a seven-day period in June 2011. Note that at the north site, the sub sites were relatively similar in terms of soil temperature, while at the south site, there were subsites having strong sun exposure due to locations in open clearing with varying amounts of ground cover density and vegetation cover types (S3 and S4). Figure 3-32 and Figure 3-33 show graphs of the temperature profile for a seven-day period in January, when the sites were under approximately 1 m of snow cover. Snow cover tends to insulate the soil profile from diurnal temperature cycles and

allows the soil to approach an equi-temperture state. The temperature traces indicate a much smaller diurnal temperature cycle compared to the snow free period shown in Figure 3-30 and Figure 3-31. The graph for the north site does suggest that the thermocouple calibration and behavior is better than at the south site, although temperatures at all subsites are within 1 ^{o}C of one another. Moreover, in the context of calculation of G, the relative change in temperature is required. Consequently, the estimation of G should not be affected by incorrect calibrations of the thermocouples.

$$G_{sur} = G_{plate} + \Delta H_{Storage} \quad \textbf{(3-4)}$$

where G_{sur} is the soil heat flux at the soil surface, G_{plate} is heat flux measured by the soil heat flux plate at the depth it was installed, and $H_{Storage}$ is heat storage in the soil profile above the heat flux plate. The four thermocouples were used to fit a 2nd-degree polynomial curve of the soil temperature, and the equation of the curve was integrated over the depth corresponding to the heat flux plate to estimate the heat storage in that slab of soil. Additional detail regarding the calculation of G is provided in Appendix B.

Site	Sun/Shade exposure
N1	Under trees; morning sun, shade, afternoon sun
N2	Under trees; shade
N3	In small clearing; noon-time sun
N4	In small clearing; early afternoon sun
N5	Patchy trees; strong a.m. sun
N6	Patchy trees; morning sun
S1	Near trees at edge of meadow; shade with a period of afternoon sun
S2	Near trees at edge of meadow; shade with a period of afternoon sun
S3	In meadow; strong morning sun
S4	In meadow; strong morning sun
S5	In a patch of trees; patchy a.m. sun
S6	In a patch of trees; early morning sun, with afternoon sun as well

Table 3-6. Description of the solar exposure regimes at the Island Parks soil sub-sites.

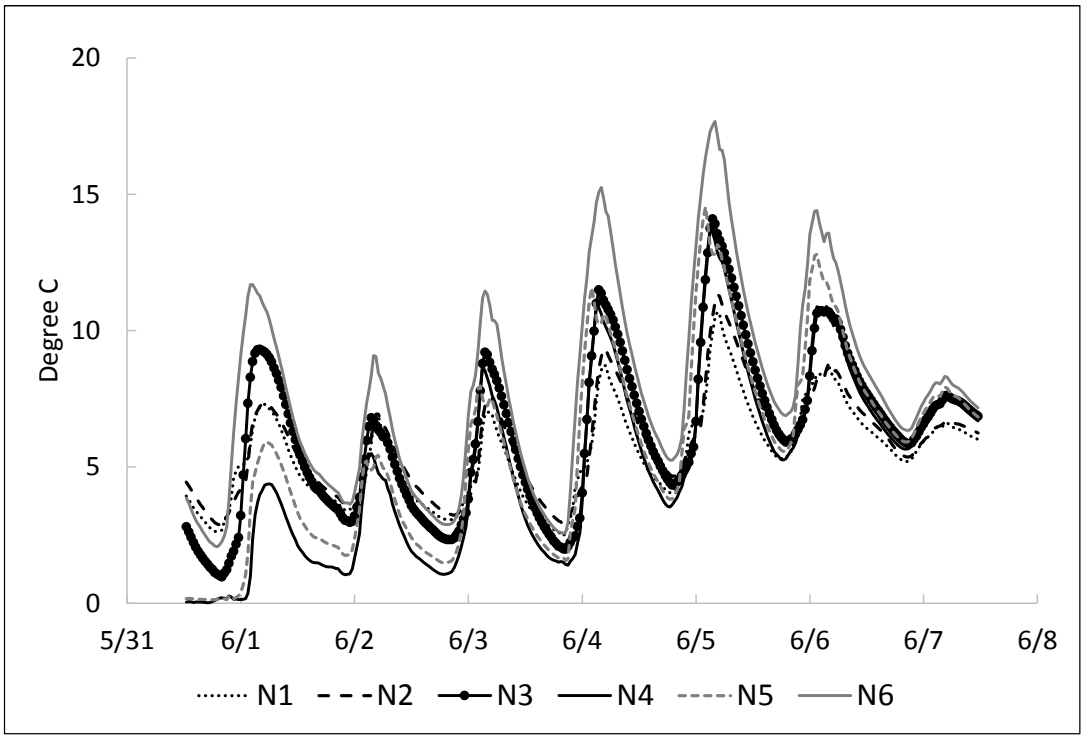

Figure 3-30. Graph of average soil temperature at six subsites for the Island Park north site for a seven-day period in June 2011. Soil temperature was the average of the four thermocouples placed at 2, 4, 9, and 15 cm depths in the soil profile.

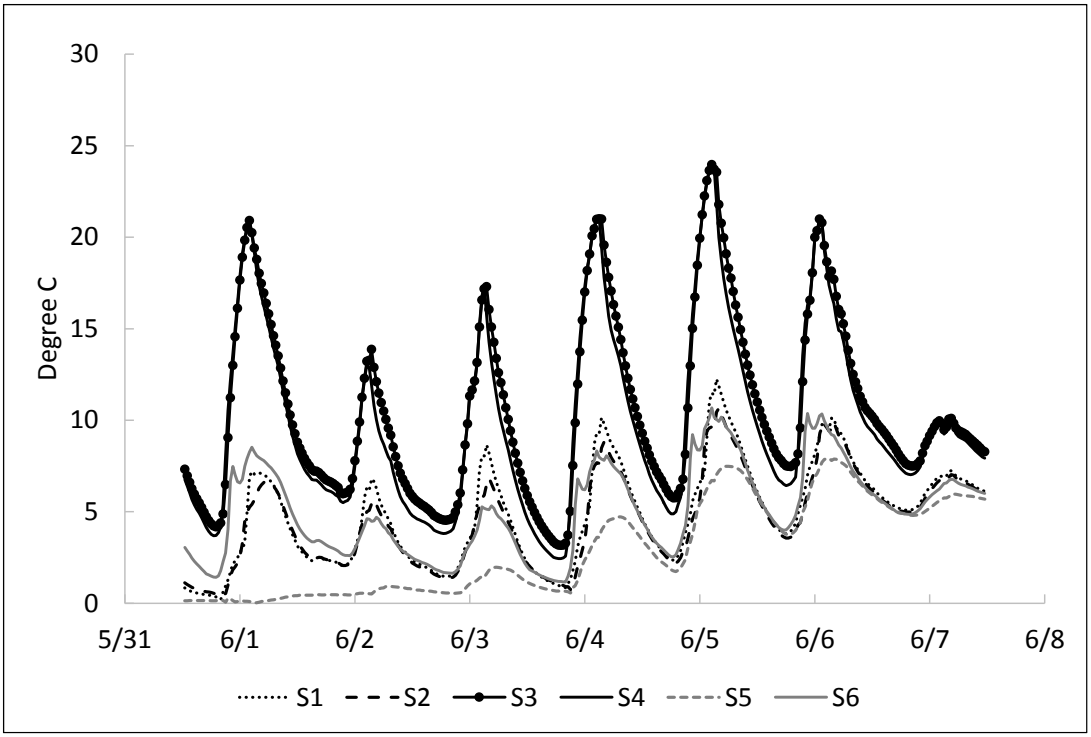

Figure 3-31. Graph of average soil temperature for six soil subsites at the Island Park south site for a seven-day period in June 2011. Soil temperature is the average of the four thermocouples placed at 1.5, 3, 4.5, and 9 cm depths in the soil profile.

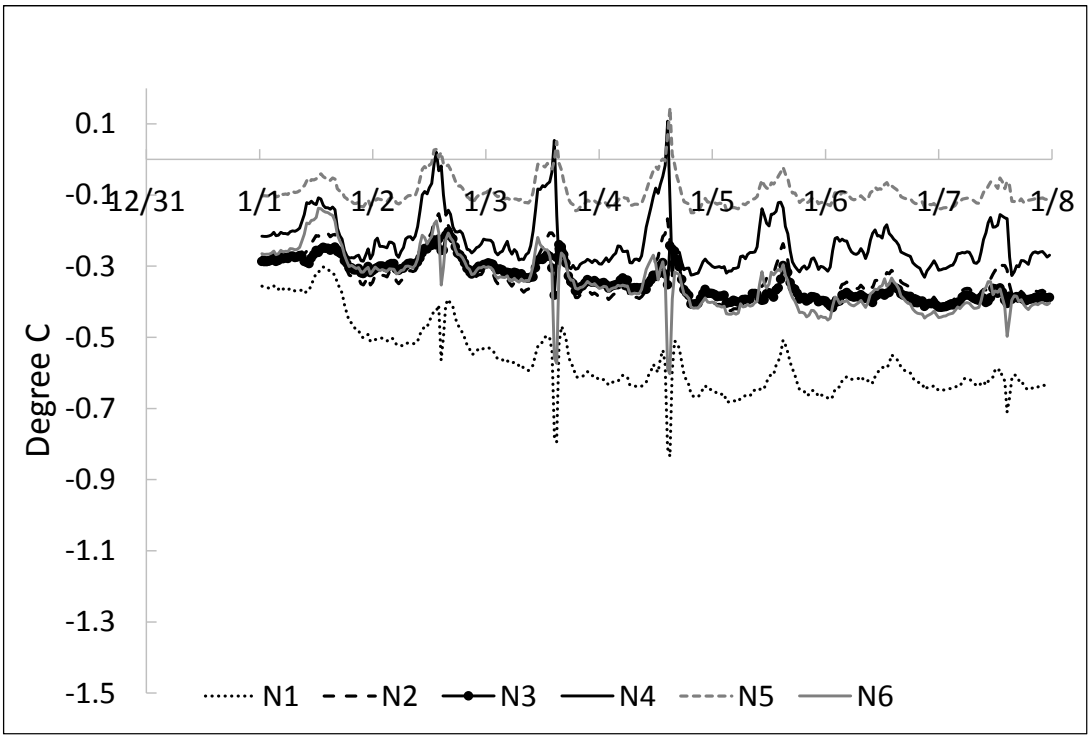

Figure 3-32. Graph of average soil temperature at six subsites for the Island Park north site for a seven-day period in January 2011. Soil temperature was the average of the four thermocouples placed at 2, 4, 9, and 15 cm depths in the soil profile.

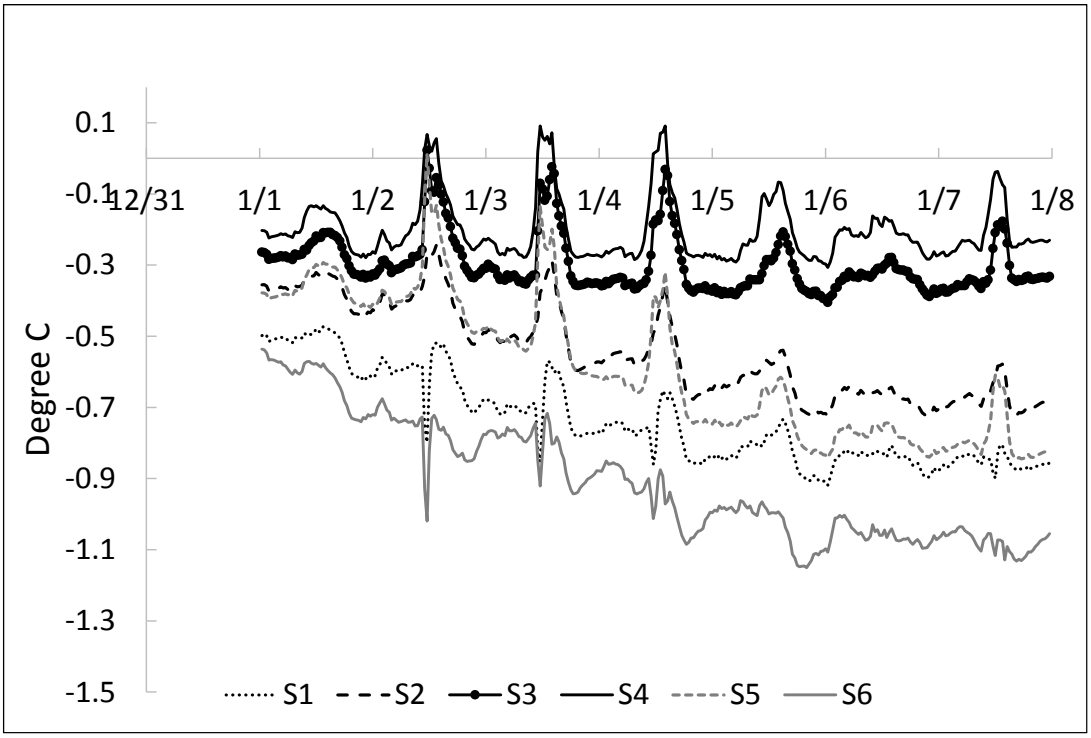

Figure 3-33. Graph of average soil temperature for six soil subsites at the Island Park south site for a seven-day period in January 2011. Soil temperature is the average of the four thermocouples placed at 1.5, 3, 4.5, and 9 cm depths in the soil profile.

The soil heat flux data were evaluated to assess their quality. Figure 3-34, Figure 3-35, and Figure 3-36 display data from the Island Park data set on July 24 and 25, 2011 and illustrate the relationship between total soil heat flux (G), heat flux as measured by the soil heat flux plate, and heat storage change in the soil profile. Figure 3-34 shows G at the surface; Figure 3-35 shows G at the soil heat flux plate; and Figure 3-36 shows heat storage change in the soil between the heat flux plate and the soil surface. Thus Figure 3-34, soil heat flux, is the sum of Figure 3-35, heat flux at the specified depth, and Figure 3-36, heat storage change in the soil profile above the sensor to the soil surface. Several points regarding the behavior of soil heat flux can be observed in these graphs. Soil subsites had heat flux plates at 6 and 12 cm depth. Figure 3-35 shows that the flux was dampened with depth, as expected. Figure 3-36 shows that more heat was stored in the thicker soil profile associated with the heat flux plate placed at 12-cm depth. The effects of shading and sensor depth can be seen in the graphs as well, with different sensors peaking at different times of the day, and reaching different magnitudes corresponding to the micro environment. Figure 3-34 also shows much smaller differences in surface soil heat flux computed using the two plate depths at each subsite than among subsites. This occurred, even though fluxes measured at 6 cm were much stronger than fluxes at 12 cm. This tends to confirm that 1) the procedure and coefficients used to estimate soil heat storage change were valid and 2) the placement depth of plates (6 and 12 cm) did not have substantial impact on the accuracy of estimated G at the surface. More important in EB closure is the sampling of multiple locations to represent the wide range of vegetation cover and exposure to sun or shade. This is discussed in more detail in a later section.

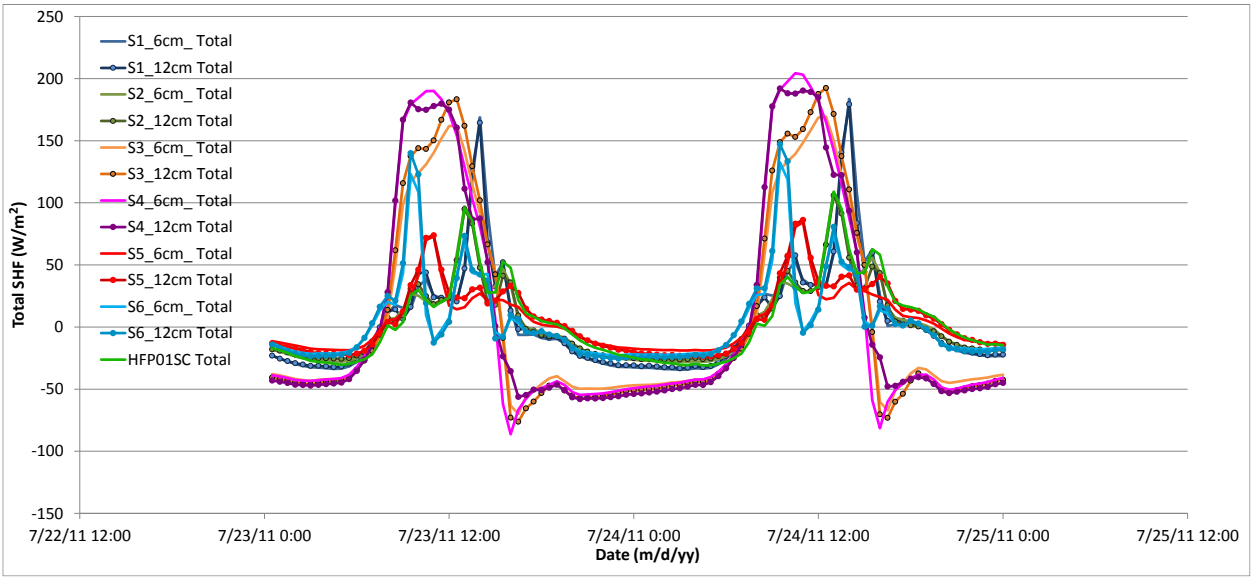

Figure 3-34. Graph of soil heat flux at the soil surface at the six soil subsites at Island Park south site for a typical two-day period in July 2011.

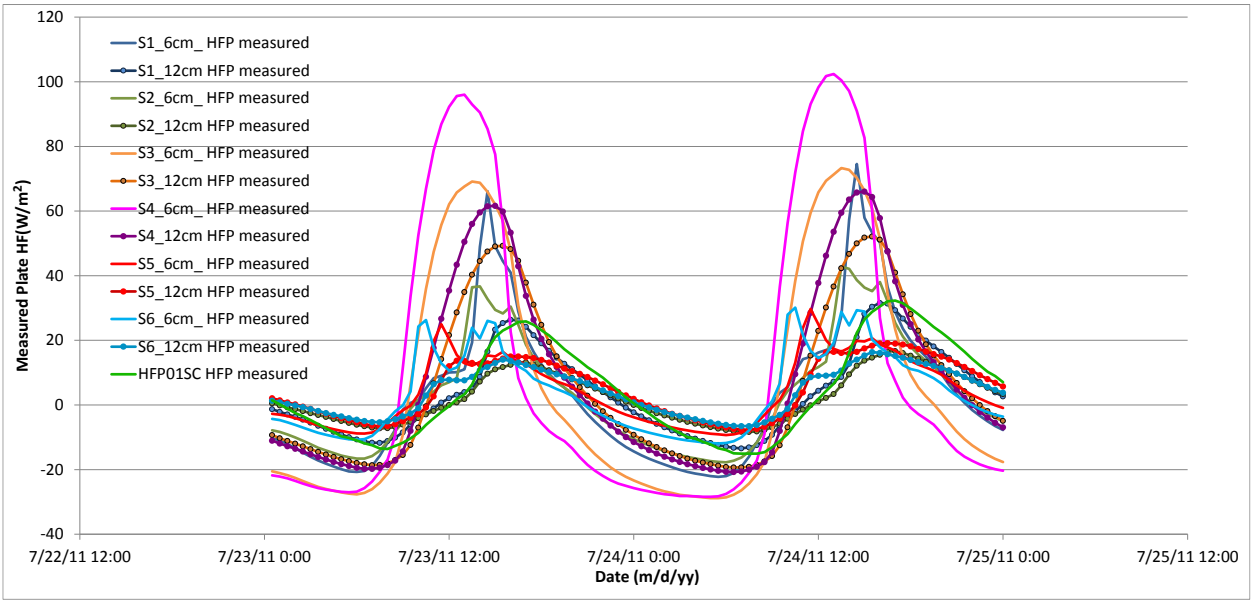

Figure 3-35. Heat flux at sensors placed at 6- and 12-cm depth from the surface at the six soil subsites at Island Park south site for a typical two-day period in July 2011.

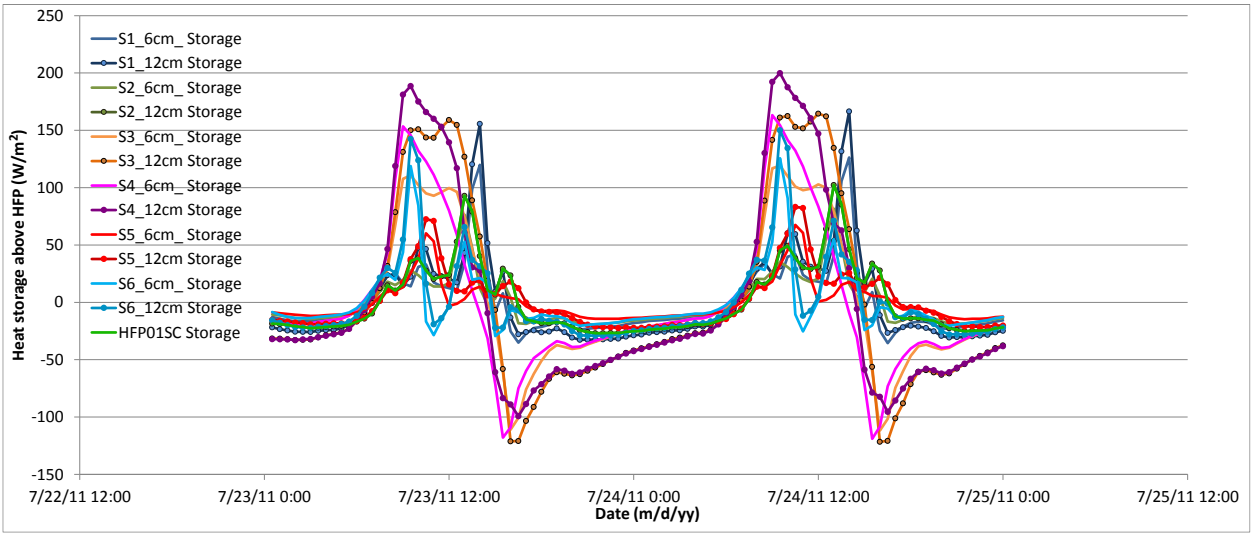

Figure 3-36. Heat storage change in the soil above the heat flux sensors at the six soil subsites at Island Park south site for a typical two-day period in July 2011.

Annual Soil Heat Flux

Over a period of time, net G tends to be 0 (Wright 1982, Ogee 2009). As an overall assessment of the estimate of G, the annual soil heat flux balance was analyzed. An annual budget that approached 0 would suggest confidence in the estimated G.

The annual soil heat flux balance for the Island Park north and south sites was assessed by analyzing the running totals for 2011. The running total was based on the average G for each site. The average of soil temperatures at subsites better represented the complex conditions of the study areas. Specifically, sensors sites were placed in shady, sunny, and partially sunny sites characteristic of the flux footprint. The average G for each site was calculated using data from both the 6- and 12-cm depth soil heat flux plates. Thus a total of 12 estimates of G comprised each site average. The analysis of annual soil heat flux balance used all data, including time steps with error flags associated with the turbulent fluxes. This was done because the error flags did not indicate errors in G, and this analysis only used the G data. Missing data from one site were filled with data from corresponding times from the other site, if available. If no data were available from either site, missing data were filled by taking the average of the day preceding and following the missing data.

The south site had an annual balance of 4.9 MJ m^{-2}, while the north site had a balance of 13.7 MJ m^{-2} at the end of 2011, corresponding to 0.15 W m^{-2} and 0.43 W m^{-2} respectively. These values are relatively small. Daily balances ranged between -1.6 MJ m^{-2} day^{-1} in early October when the soil was cooling quickly to 1.7 MJ m^{-2} day^{-1} in early June when the soil was warming quickly. More typical daily values once isothermal conditions were reached in the soil profile ranged between -0.3 and 0.3

MJ m^{-2} day^{-1}. These values compare favorably with the expected average annual value of 0 (Wright 1982, Ogee 2009) and suggest that the estimated G does not have obvious bias or other measurement problems.

Figure 3-37 shows the annual cumulative G for each Island Park soil subsite for 2011. Comparison of the annual cumulative G for each of the sensors shows that all of the north soil subsites had a positive EB at the end of the year. At the south site two of the soil sites had a positive EB at the end of the year. One would expect the balance to be near 0. Taken on average, the 12 cm heat flux plate produced a stronger estimate of G than the 6 cm heat flux plate. This could suggest that the plate at 12 cm depth gives a higher estimate because more of the flux was accounted for by the storage term, which was measured by thermocouples. Thus any under-measurement by a heat flux plate at 12 cm depth was less pronounced than with the plate at a 6 cm. Conversely, any over-measurement of water content would cause higher estimates for heat storage change, which would impact the 12 cm depth more than the 6 cm depth due to the thicker slab, so that G based on the 12 cm depth would tend to estimate higher than that based on the 6 cm depth.

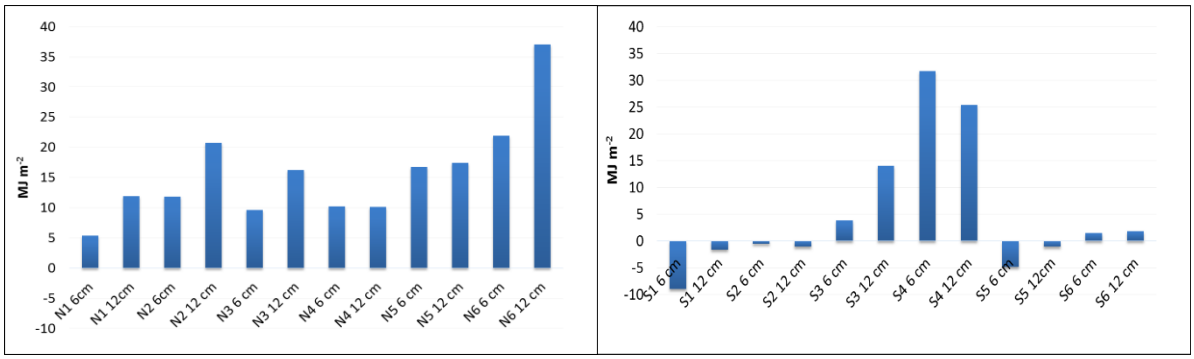

Figure 3-37. Comparison of the annual cumulative soil heat flux of the individual north and south soil sites.

Evaluation of Sensor Performance

Regression models were prepared to assess the correlation between G estimated by the HFP at 6 cm and 12 cm. The graph for each of the paired soil heat flux sites is shown in Figure 3-38 . G based on the 6-cm soil heat flux plate is plotted on the x axis and the paired estimate from G based on the 12-cm heat flux plate is plotted on the y axis. Data that are equivalent would produce a line having a slope near 1 and a high R^2 value.

With the exception of N2, there is a high correlation between G based on the 6 cm depth and G based on the 12 cm depth, with the R^2 being over 0.94. The graph of G from N2 suggests that one of the sensors was not performing well. The regression coefficients ranged from 0.93 to 1.27. Five of

the six pairs from the north site had a coefficient greater than 1, while three of the pairs from the south site had a coefficient greater than 1. A coefficient greater than 1 indicates that the deeper heat flux plates tended to produce a higher estimate of G. The performance of the thermocouples at each of the soil subsites was evaluated by preparing plots of each group of thermocouples for a representative month. Figure 3-40 shows plots for a representative 7-day period in June 2011. Evaluation of these graphs indicated that thermocouples were switched at N2, resulting in the poor performance of this site noted in Figure 3-38. As a result, N2 was not included in the calculation of global G estimates.

The performance of the soil moisture probes was also evaluated by preparing plots of the soil volumetric water content. Soil moisture content is an important variable needed to estimate G because it affects heat storage and heat transmissivity within the soil profile. Soil water content varies over time based on precipitation, percolation, evaporation, and transpiration. The Island Park site utilized two different soil moisture probes to estimate soil moisture content: the Campbell Scientific 616 (CS616), and the Decagon EC5. The CS616 is a time domain transmissivity sensor, and the EC5 is a capacitance type sensor. Using different sensors that use different measurement methodologies helps to identify sensor bias. The CS616 is also a large sensor and integrates the measurement over a larger distance. Figure 3-41 shows the behavior of the soil moisture probes for a representative seven-day period in June 2011. The CS6 sensors at 0 -12 cm depth are of primary interest in the context of G because they were used to estimate soil water content used to calculate G. Because the soil moisture sensors were located in close proximity at the north and south sites, it was expected that sensors at similar depths would have similar soil moisture readings. The sensors were responsive to precipitation events, with deeper sensors showing a lag relative to the shallower sensors. The graph of the soil moisture content indicates that at N5 an EC5 probe at the 1 to 5 cm depth range may have a calibration problem. Two other sensors EC5 sensors at N7 and N8 indicate negative water content, indicating sensor malfunction or calibration problems. These sensors are not shown on the graph due to scale and were not used in the calculation of G.

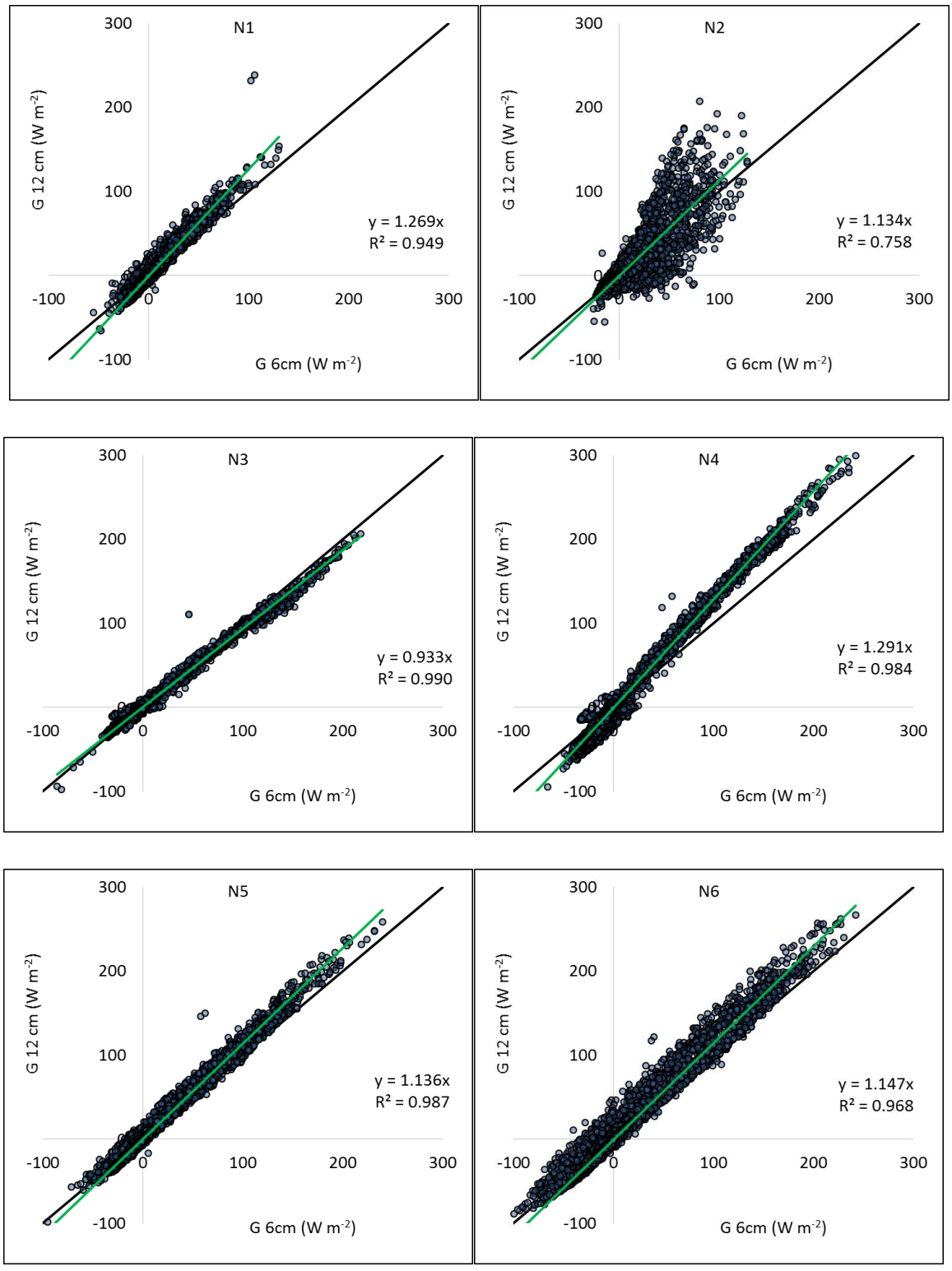

Figure 3-38. Graph showing the regression between G based on the sensors at 6 cm depth vs G calculated from sensors placed at 12 cm depth for the north site. All plots show good data behavior and correlation except for N2. The graph N2 suggest the subsite is not reliable.

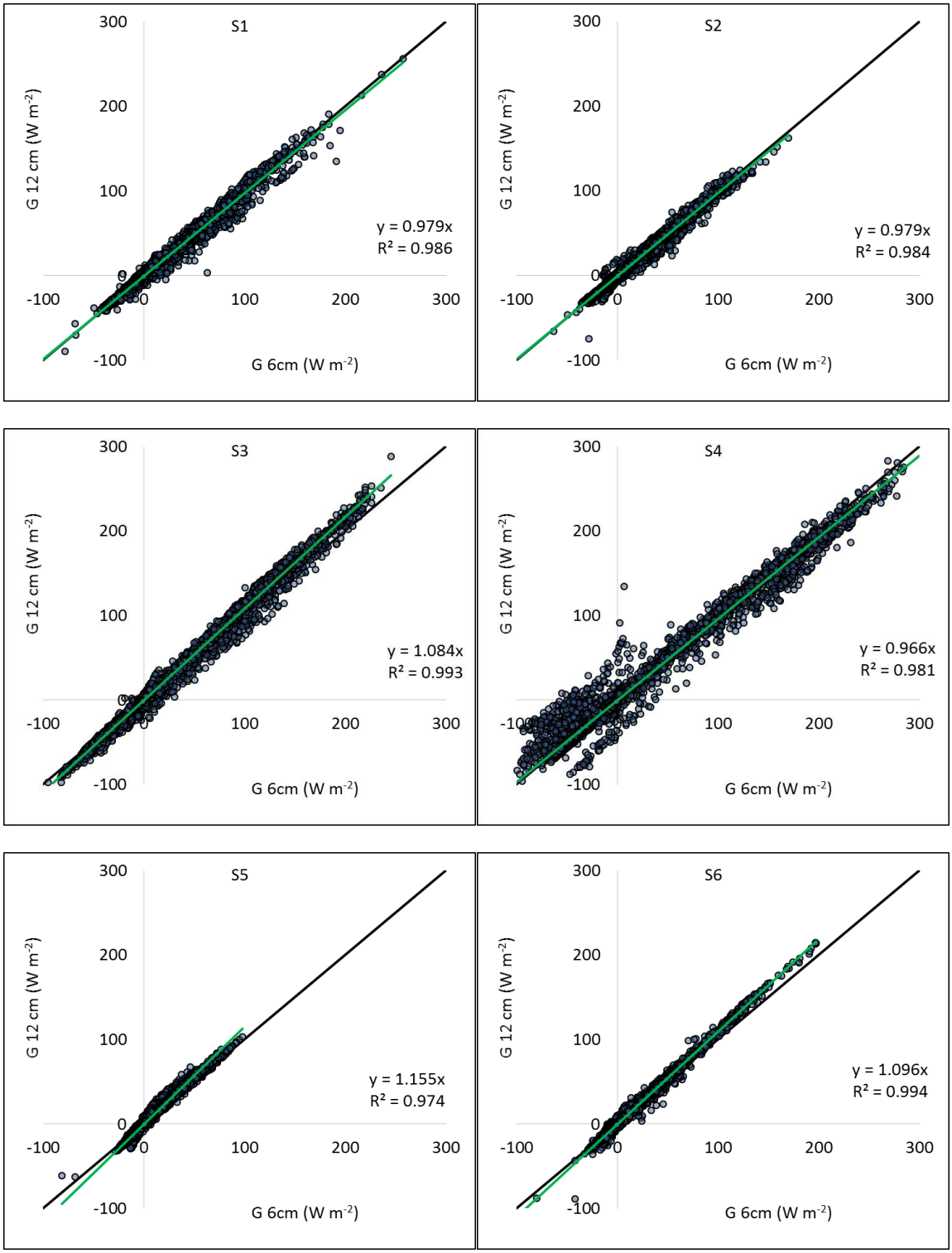

Figure 3-39. Graph showing the regression between G based on the sensors at 6 cm depth vs G calculated from sensors placed at 12 cm depth for the south site. All plots show good data behavior and correlation.

North Soils 1

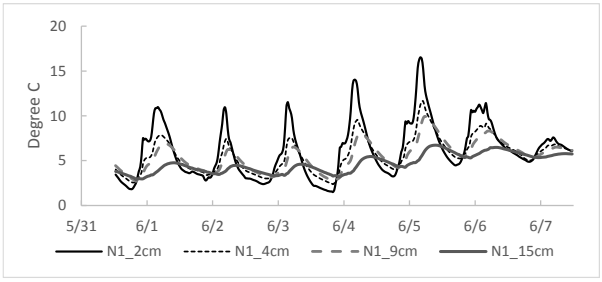

North Soils 2

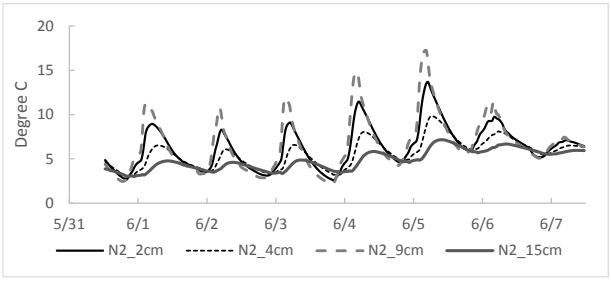

North Soils 3

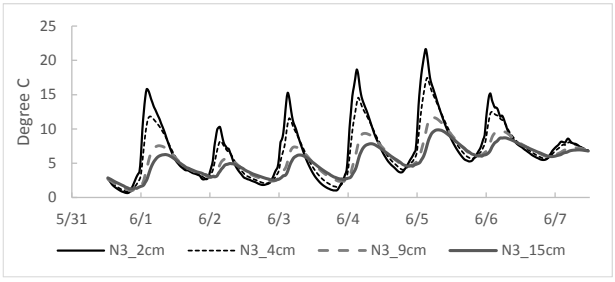

North Soils 4

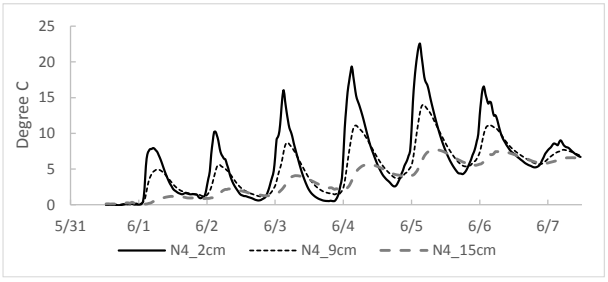

North Soils 5

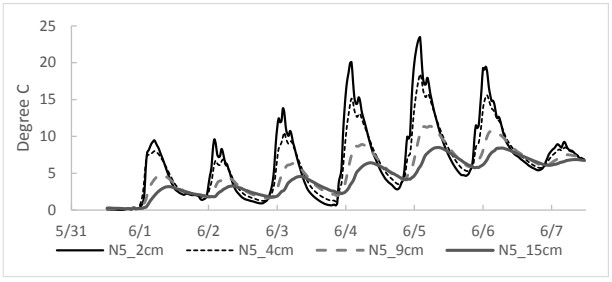

North Soils 6

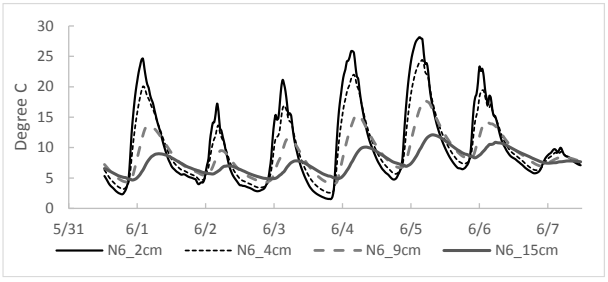

South Soils 1

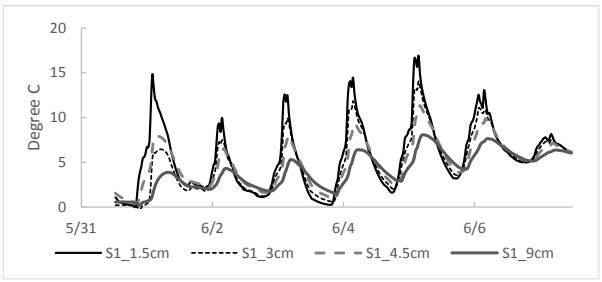

South Soils 2

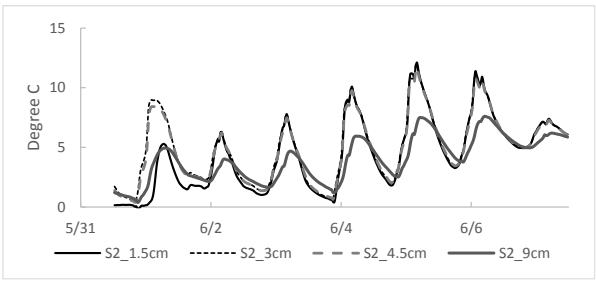

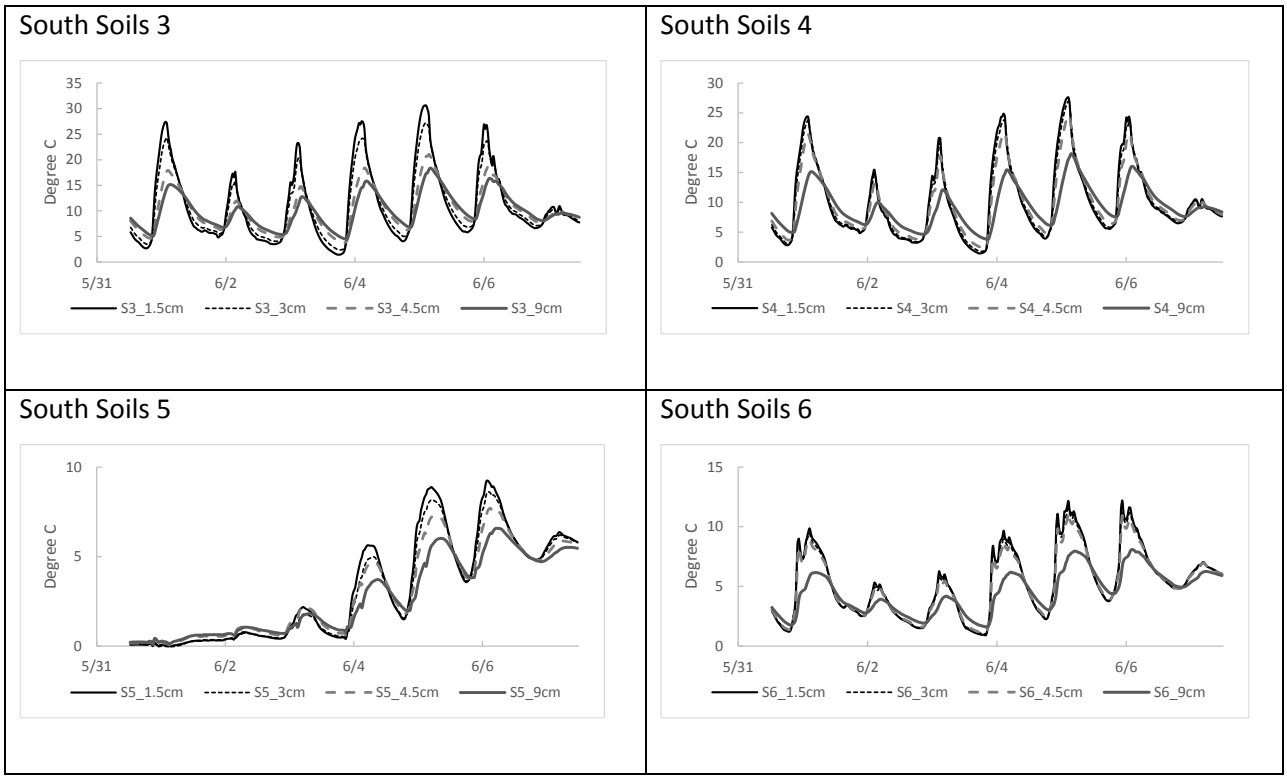

Figure 3-40. Plots of the thermocouple performance for each of the Island Park soil subsites for a seven-day period in June 2011.

Another evaluation to assess G was in terms of EBCE. Different weighting factors were applied to G and their effect evaluated based on regression line slope and the R^2 value for plots of Rn - G - CS vs H+LE, using original EC data. Table 3-7 shows how the slope and R^2 value changes for weighting factors of 1, 2 and 0.5 for the June 2011 dataset. Table 3-7 shows that the slope of the regression line increased to nearly 1.00, indicating that a doubling of G would 'close' the EB. However, with a weighting factor of 2, the R^2 value decreased, suggesting that EB closure was not due to a strong underestimation of G. The 0.5 weighting factor decreased both the regression coefficient and the R^2 value. This analysis suggests that attempting to improve the EBCE by substantially increasing or decreasing the estimated G has the undesirable effect of amplifying variability in the differences between LE + H and R_n - G - CS estimates. This suggests that modification of G is not the proper solution to EB closure.

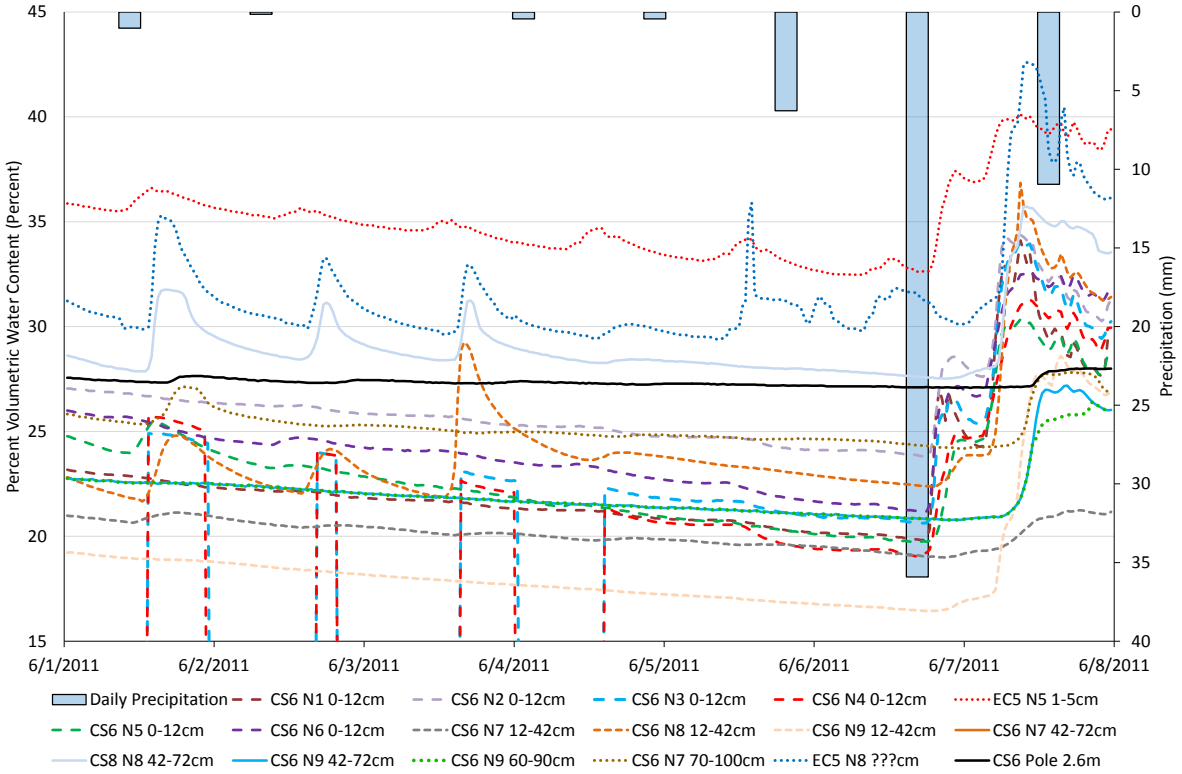

Figure 3-41. Volumetric water content and precipitation for a seven-day period in June 2011 for the north site to evaluate sensor performance. Note that two CS616 N3 and N4 demonstrate faulty performance for part of the period.

Weighting Factor on G	1	2	0.5
North			
Slope of regression line	0.82	0.93	0.77
R^2	0.910	0.899	0.905
South			
Slope of regression line	0.80	0.91	0.75
R^2	0.913	0.903	0.908

Table 3-7. Analysis of the sensitivity of EBCE to different weighting factors for G. This table shows how the slope of the regression line and R^2 values for a regression using H + LE and R_n-G-CS. Data are from June 2011.

3.2.5 Assessment of the Large Aperture Scintillometer

Data from the Large Aperture Scintillometer (LAS), specifically sensible heat (H_{LAS}) were utilized in an EBCE and QA/QC procedure for this study. The original H_{LAS} data that were evaluated were characterized by spikiness, particularly at night (Figure 3-42). The reason for the spikiness of the data was related to the calculation procedure (W. Zhao, per comm. with J Stewart, 9/8/2016). The H_{LAS}

calculation routine is different under stable and unstable atmospheric conditions. Notably, the H_{LAS} data do not indicate atmospheric stability. During the iterative calculation process required for H_{LAS}, once the calculation goes to unstable conditions (L<0) from neutral, the calculation assumes that it will remain unstable and cannot return to the stable side conditions, even at night. An artifact of this phenomena is that the H_{LAS} calculation can become a large positive number, rather than a small negative one due to incorrect adjustment for stability condition. In order to correct this problem, the Penman-Monteith equation was used to compute ET, where the value for r_s was based on a running average for the previous 24 hours. H was then estimated from EB. The estimated H was used to assign a starting atmospheric stability condition (stable or unstable). The stability estimate was then used to improve the PM estimate and estimate for H. This method resolved the spikiness in the original H_{LAS} dataset, particularly at night (Figure 3-43).

During the day, the H_{LAS} data were generally of the same magnitude as the H from the EC system. H_{LAS}, was often in between the H_{EC} from the north site and the H_{EC} from the south site. This suggests that the LAS system was functioning well across the 1.6 km transect. The differences in magnitude between H_{EC} and H_{LAS} presented a potential opportunity to adjust H_{EC} using an independent measure of H to improve EBCE, as discussed in section 3.3.

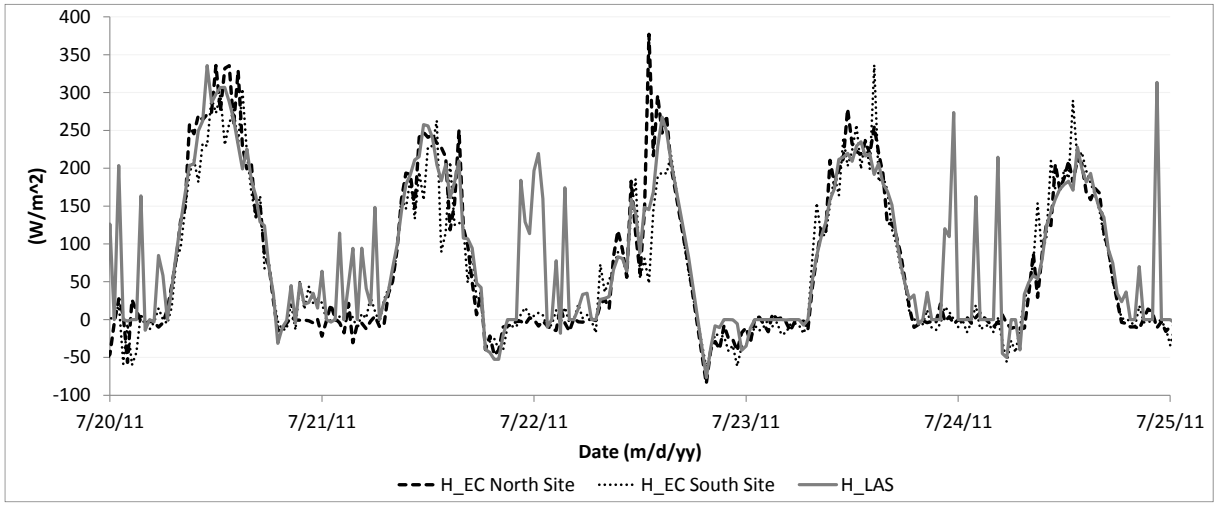

Figure 3-42. Graph showing relationship between H_{EC} for the north and south sites and the original H_{LAS} data for the Island Park site. The spikiness of the H_{LAS} data at night is evident.

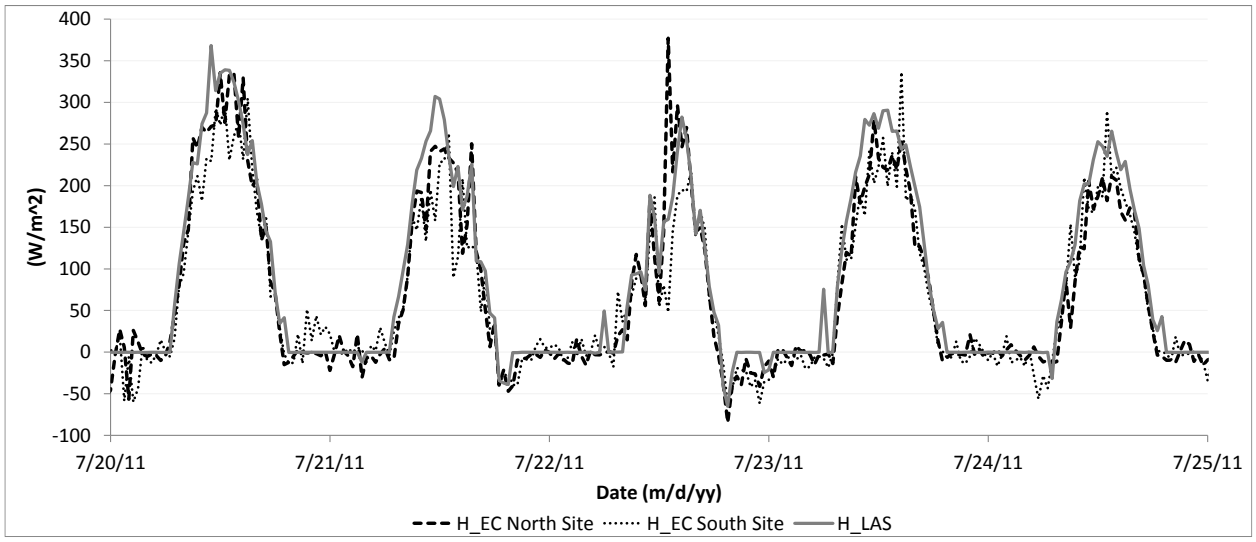

Figure 3-43. Graph show the relationship between the H_{EC} data from the north and south sites and the reprocessed H_{LAS} data. The spikiness of the H_{LAS} data has been greatly reduced.

3.3. Development of an Adjustment Method to Compensate for Under-measurement of Turbulent Fluxes

Options to adjust the turbulent fluxes for under-measurement errors were explored because there was an underlying EBCE in the Island Park data set. An adjustment to compensate for under-measurement of turbulent fluxes prior to additional analysis of other EB variables would improve results from regression models. The premise underlying the work to explore an adjustment for the turbulent fluxes includes the assumption that R_n was the most reliable component of the EB equation (Kohsiek et al. 2007, Allen 2008, Twine et. al 2000). Further, the G estimate also appears to be robust based on the assessment of G (section 3.2.4), and the magnitude of this parameter and CS is relatively small compared to R_n and the turbulent fluxes. Turbulent fluxes are often under-measured (Foken 2008, Wilson el al. 2002), particularly during stable atmospheric conditions that are common at night, indicated by lower friction velocity (u*) (Oliphant et al. 2004) and in heterogeneous sites. The following sections outline approaches that were explored and the methodology that resulted to produce what are considered to be the best estimates of an adjusted H and LE to account for the apparent under-measurement of turbulent fluxes.

3.3.1 Bowen Ratio Correction

One method to adjust the turbulent fluxes utilizes the Bowen ratio to force closure, as described by Twine et al. (2000) and Oliphant et al. (2004) where H and LE are multiplied by a common multiplier, thus preserving the Bowen ratio. This method was investigated for its usefulness in preparing the data for regression analysis. The premise of this approach is that the energy imbalance is due to a

systematic under-measurement of both turbulent fluxes, for example, due to impacts of sonic transducers on disrupting vertical flow lines and small eddies (Frank et al. 2016). The Bowen ratio (β), is defined as

$$\beta = \frac{H}{LE} \quad \textbf{(3-5)}$$

where H is sensible heat and LE is latent heat. The Bowen ratio describes the relative strength of the turbulent fluxes, and is used in the Bowen ratio correction to partition the residual energy to H and LE according to the following equations (Oliphant et al. 2004):

$$LE_{BRadj} = \frac{R_n - G - CS}{1 + \beta} \quad \textbf{(3-6)}$$

$$H_{BRadj} = \beta \cdot LE_{BRadj} \quad \textbf{(3-7)}$$

Where LE_{BRadj} is the Bowen ratio adjusted LE and H_{BRadj} is the Bowen ratio adjusted H. G is the average of G estimated using the 6- and 12-cm depth heat flux plates for the 6 subsites. Oliphant et al. (2004) noted that when fluxes are very small (within +/-5 W m^{-2}) or when β approaches-1, these equations result in large diverging corrections of opposing sign and they recommend partitioning the residual energy equally between H and LE. For this analysis, the criteria for partitioning the residual energy equally between H and LE is set as $-2 < \beta < 0$ or -5 W $m^{-2} < H \; or \; LE < 5 \; m^{-2}$, as described in Oliphant et al. (2004).

The Bowen ratio-based correction was applied to July 2011 Island Park data on a half hourly basis, resulting in EB closure. Adjusted daytime H values were typically increased, while night time values had less adjustment, but were sometimes slightly decreased (Figure 3-45). Bowen ratio adjusted H was compared to H from the LAS. Adjusted H was in better agreement with H for the LAS than was unadjusted H.

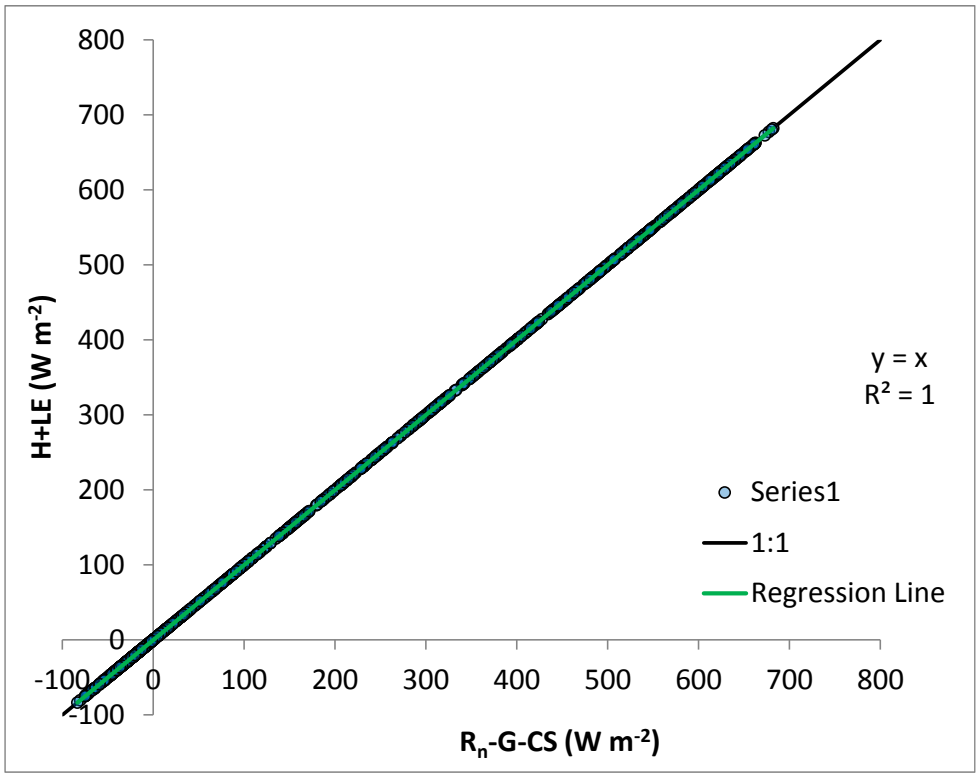

Figure 3-44. Graph illustrating regression between Rn-G-CS vs H + LE adjusted by the Bowen ratio correction. H+LE is the average of the north and south sites, July 2011, n = 1329.

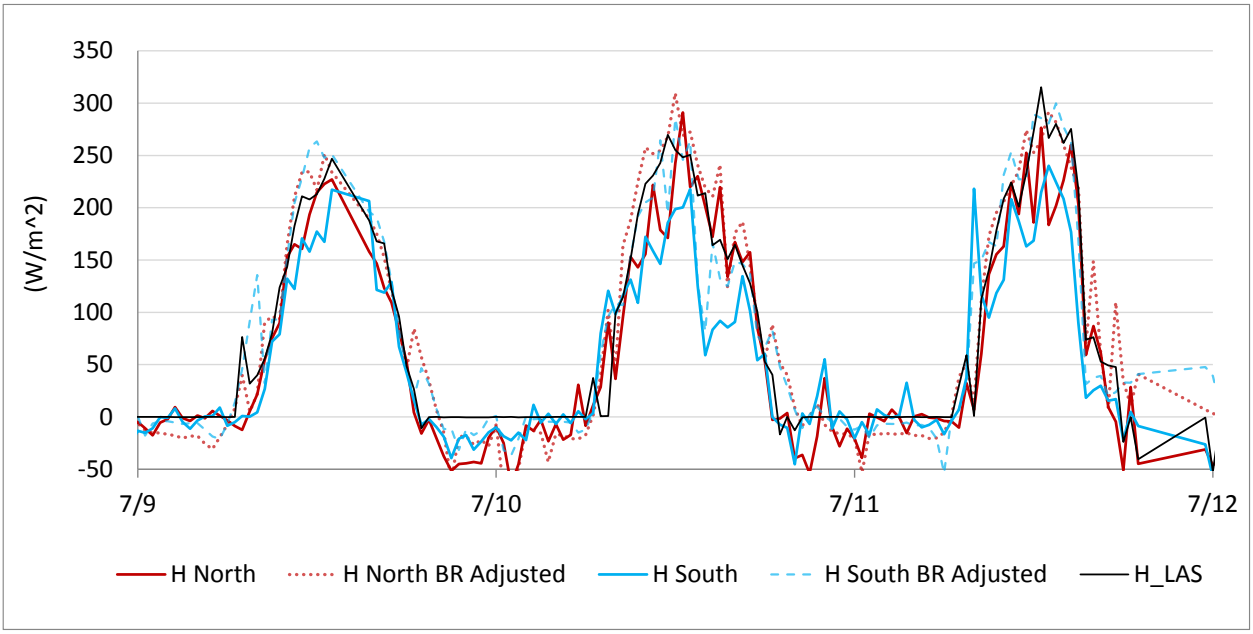

Figure 3-45. Comparison of measured and Bowen ratio adjusted H and H from the LAS for a typical period in July 2011.

Bowen ratio adjusted LE followed a similar pattern. The Bowen ratio adjustment typically increased LE during the day, but at night, the adjustment was minimal, as shown in Figure 3-46. In many cases

the adjusted H and LE from the two sites were brought closer to one another than prior to adjustment. This is a good indication that the adjustment based on the Bowen ratio for both H and LE is in the right direction and is appropriate.

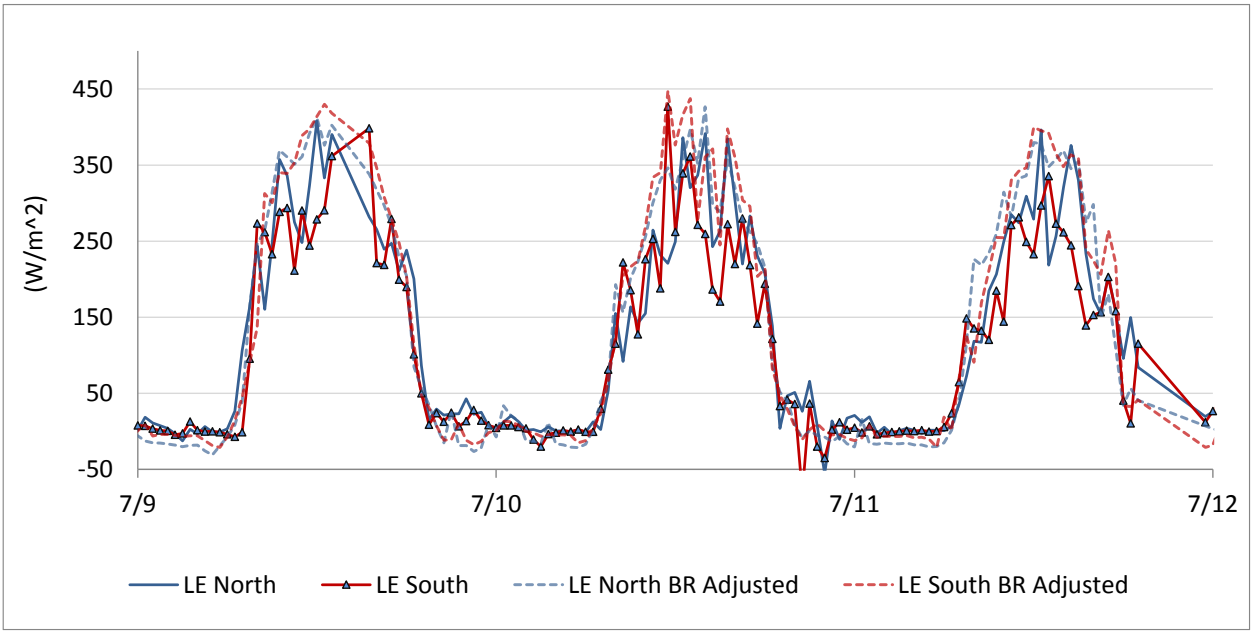

Figure 3-46. Comparison of measured and Bowen ration adjusted LE for a typical period in July 2011.

The Bowen ratio correction uses the Bowen ratio to maintain the relationship between H and LE as the correction is applied. The Bowen ratio correction can be implement by calculating the Bowen ratio based on the desired time interval, i.e., half-hour, daily, or monthly time steps. The choice of a basis for the Bowen ratio does affect its value. Regardless of the Bowen ratio basis used in the correction, the closure is the same as shown in Figure 3-44, specifically EBCE = 0. However, the choice of the basis upon which to implement the Bowen ratio correction does affect the magnitude of adjusted H and LE. Figure 3-47 illustrates the effect of using half hourly and daily Bowen ratio for in the correction. In the case of H, the use of a daily Bowen ratio results in 15 percent lower adjusted H relative to the correction if a Bowen ratio from a half hour basis were used. Conversely, the use of a daily Bowen ratio results in an adjusted LE that that is about 7 percent lower than LE adjusted with half-hourly Bowen ratios. Similar relationships were found when the monthly Bowen ratio was used. The preference of which basis to use to calculate the Bowen ratio could depend on the purpose to which the data would be used, how variable the Bowen ratio might be for the site, and which time basis is of most interest.

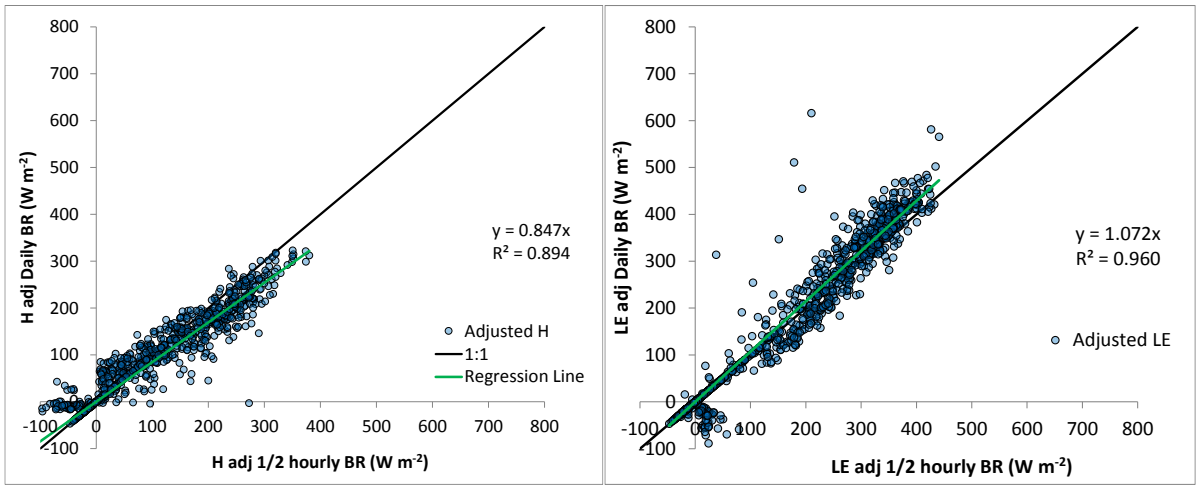

Figure 3-47. Comparison of H and LE from the Island Park north site, where H (left) and LE (right) have the Bowen ratio correction applied. These graphs illustrate the effect of using Bowen ratio calculated on a half-hourly basis (x axis), and daily bases (y axis). July 2011, n =1329.

While the Bowen ratio adjustment closed the EB equation, it was not useful in adjusting H and LE to improve the regression analysis-based adjustment of G for the following reason. Because the G used in the Bowen ratio closure method was G averaged from the heat flux plates at 6- and 12-cm depths, and H and LE were adjusted via Equations 2.5 and 2.6, regression analysis with R_n - CS as the dependent variable and H_{BRadj} + LE_{BRadj} + G as the independent variables resulted in the regression model identifying the G grouping closest to the G average used in the Bowen ratio adjustment equations. For example, the regression analysis comparing the 6- and the 12-cm depths for the Island Park North site indicated that there is essentially no preference between the two depths since they comprised the G average. Regression results are summarized in Table 3-8. This regression model is included to illustrate the interdependence of the parameters once the Bowen ratio adjustment was applied.

	Coefficient H+LE	Coefficient for G	R^2	Intercept
$G_{ave\ all}$	1.00	1.00	1	1
$G_{ave\ 6\ cm}$	0.99	1.13	0.99	0.65
$G_{ave\ 12\ cm}$	1.00	0.89	0.99	-0.64

Table 3-8. OLS Regression results from analysis of G using Bowen ratio adjusted H and LE, with R_n-CS as the dependent variable and Bowen ratio adjusted (H+LE) and G average as the independent variables. The regression model compares G average calculated with both 6 and 12 cm G, 6 cm only data, and 12 cm only data. Data from July 2011, Island Park North site. In this model, the y-intercept was not set to 0.

Weighting Factor Adjustment

Two other options were also investigated to adjust the parameters in the EB equation in preparation for further analysis. The first was a graphical solution. R_n - G - CS was plotted on the X axis and H+LE

was plotted on the Y axis. Coefficients were used to "tune" the parameters, i.e., to increase or decrease them. The graphical solution was defined as set of coefficients that caused the slope of the regression line to approach 1 and R^2 was at a maximum. The R_n-G-CS term was calculated as

$$R_n - G - CS = R_{n\,NR01\,n} * c1 + R_{n\,NR01\,s} * c2 + R_{n\,CNR1\,s} * c3 + G_{ave\,all\,n} * c4 + G_{ave\,all\,s} * c5 + CS * c6 \quad \textbf{(3-8)}$$

where c1, c2, c3, c4, c5 and c6 are weighting coefficients that can be independently adjusted to explore graphical solutions. The R_n terms included the three radiometers on the towers: the NR01 on the north tower and the NR01 and the CNR1 on the south tower. Since the three radiometers saw a different mix of vegetation and ground, the three radiometers were included to better represent the diverse landscape of the study area. $G_{ave\,all\,n}$ and $G_{ave\,all\,s}$ were the average G of the north and south soil sites, which included six 6-cm and six 12-cm G estimates at each site. All G terms were included to represent the diversity of the study site. CS was the canopy storage based on the IRT sensor on the south tower.

H+LE was calculated as:

$$H + LE = H_{ECn} * c6 + H_{ECs} * c7 + H_{LAS} * c8 + LE_{ECn} * c9 + LE_{ECs} * c10 \quad \textbf{(3-9)}$$

where c6, c7, c8, c9, c10 are weighting coefficients that can be independently adjusted to explore graphical solutions. H_{ECn} and H_{ECS} were the EC systems at the north and south sites, respectively. H_{LAS} was from the LAS. LE_{ECn} and LE_{ECs} were from the EC systems at the north and south sites, respectively.

The values assigned to the weighting factors was based on the perceived reliability of the parameter. Reliable parameters were weighted with a 1. R_n was considered to be the most reliable parameter. Thus the R_n weighting factors for the three radiometers were set to sum 1, and each was weighted equally to use the average of the R_n measurements. G was also assumed to be a relatively robust parameter due in part to the number of independent measurements that comprise the average G. The weighting factors for G also summed to 1 and were equally weighted to use the average between the north and south sites. The canopy storage parameter was also set to 1. As noted above, turbulent fluxes H and LE are often under-measured by the EC system, and this under-measurement was most likely responsible for much of the EBCE in the data. To explore adjustments

to H and LE to reduce the EBCE, H and LE were increased by setting the weighting factors to sum to greater than 1.

Figure 3-48 shows graphs of R_n - G - CS vs H + LE for the north and south sites where original EC H and LE have not been adjusted by weighting factors. Note that the weighting factors in Table 3-9 sum to 1 for each parameter. The slope of the regression line for the north site is 0.85, suggesting a 15 percent under-measurement of H+LE, while R^2 is 0.94, indicating a good correlation between the data. The slope of the regression line for the south site is 0.78, suggesting a 22 percent under-measurement of H+LE, while R^2 is 0.93, also indicating a good correlation between the data.

Parameter	Weight	Description
Rn:	0.33	NR01 North
	0.33	NR01 South
	0.33	CNR1 South
LE	0.5	North RMY
	0.5	South CSAT
H	0.5	North RMY
	0.5	South CSAT
	0	Scintech LAS
G	0.5	North
	0.5	South
CS	1	One value for all

Table 3-9. Parameter weighting for graphical solution. This run has parameters adjusted to show the measured values for each parameter. For parameters with multiple instruments, estimated values were averaged.

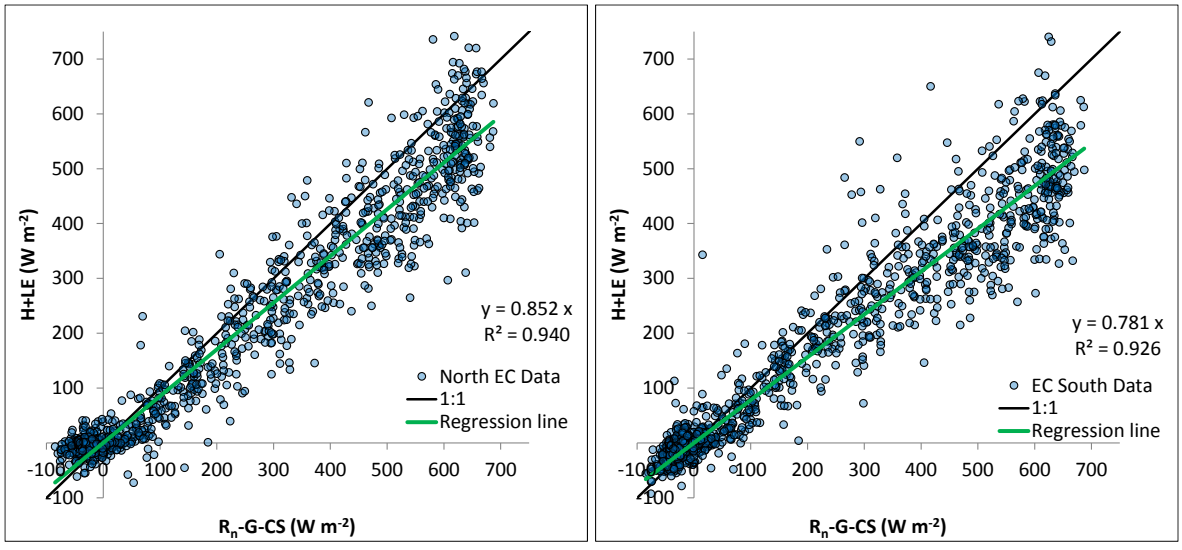

Figure 3-48. Regression of R_n – G - CS vs H+LE using original data for the Island park north site (left) and south site (right). Parameters are as measured with equal representation by all three net radiometers, EC systems

and all working G subsystems. The slope of the regression line indicates about 14 percent EBCE for the north site and about 21 percent closure for the south site. Data are from July 2011. n = 1,329.

Trials were conducted to find appropriate coefficients for H and LE that would increase the slope of the best fit line through the data towards 1 and maximize R^2. Figure 3-49 shows the results for the north and south sites using data from July 2011 when H and LE are increased by 18 and 28 percent for the north and south sites, respectively. The weighting factors used in Figure 3-49 are shown in Table 3-10. The slope of the best fit line had increased to 1.0, while the R^2 value remained unchanged.

The graphical solution effectively closed the EB for the Island Park site. However, it is not based on any real measure of the parameters, and it is possible that some of the unmeasured energy should be portioned to other parameters. None-the-less, the graphical solution provides a bench mark to compare the performance of other methods to adjust the fluxes to address the EBCE.

Parameter	Weight	Description
R_n	0.33	NR01 North
	0.33	NR01 South
	0.33	CNR1 South
LE	0.59	North RMY
	0.64	South CSAT
H	0.59	North RMY
	0.64	South CSAT
	0	LAS
G	0.5	North
	0.5	South
CS	1	CS is calculated from 1 IRT

Table 3-10. Parameter weighting for graphical solution. In this run the turbulent fluxes are weighted 20 percent greater than the measured value.

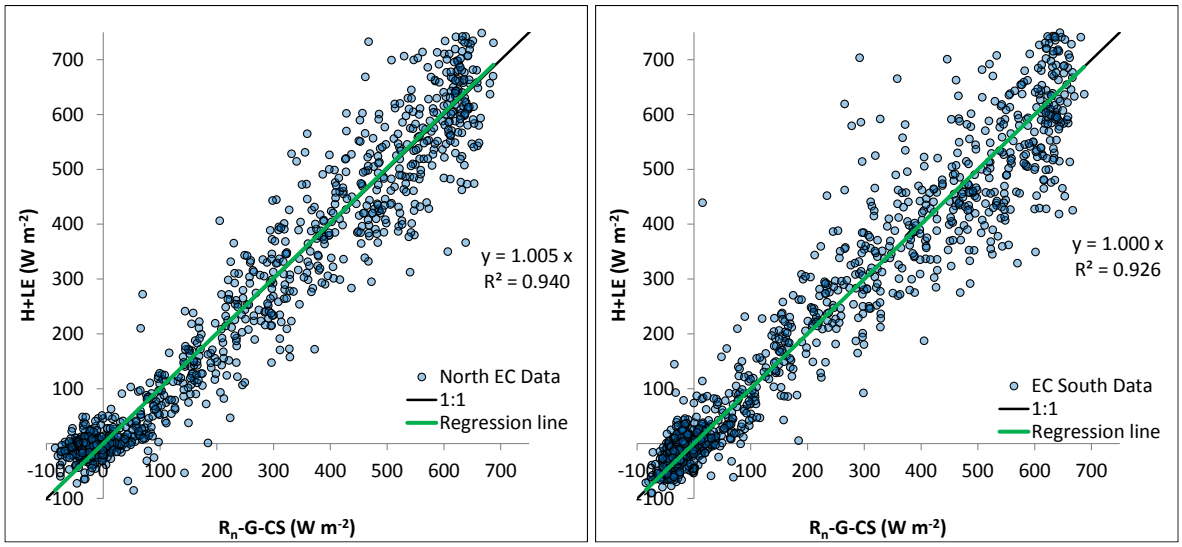

Figure 3-49. Results of graphical solution to EB equation showing the Island park north site (left) and south site (right). These graphs shows the results when the turbulent fluxes H and LE are weighted 1.18 for the north site and 1.28 for the south site. Weighting factors are shown in Table 3-10. Data are from July 2011. n = 1,329.

3.3.2 Adjustment of Turbulent Fluxes with H_{LAS} (LAS Adjustment)

While evaluating the flux data, it was noted that the constant Bowen ratio-based adjustment increased H_{EC} to near the magnitude of H_{LAS} during the day time (buoyant EBL conditions). It was theorized that H_{LAS} may be less affected by phenomena that cause the EC method to under-estimate H and LE, such as low frequency eddies, some transducer flow line disruption, regional advection, and landscape heterogeneity, etc. A method to adjust H_{EC} and LE_{EC} based on the H_{LAS} was devised and evaluated. The basic adjustment utilizes the following:

$$\text{If } H_{LAS} > H_{EC,} \text{ then } H_{ECadj} = H_{LAS}, \text{ otherwise } H_{ECadj} = H_{EC} \quad \textbf{(3-10)}$$

$$\text{If } H_{LAS} > H_{EC} \text{ then } LE_{ECadj} = LE_{EC} * \frac{H_{LAS}}{H_{EC}}, \text{ otherwise } LE_{adj} = LE_{EC} \quad \textbf{(3-11)}$$

This method was explored using the Island Park data for July 2011. H_{EC} and LE_{EC} were adjusted according to the equations. The correction was applied to data from the north and south site separately. Regression between R_n - G - CS and H_{ECadj} + LE_{ECadj} was used to evaluate how well the adjustment performed. R_n-G-CS was plotted on the x axis and H_{ECadj} + LE_{ECadj} was plotted along the y axis. R_n was the average estimate of the three radiometers and G was the average of the soil heat flux estimates from each of the soil sites using the 6 and 12-cm depth heat flux plates at the north and south sites. When data from all time steps (stable and buoyant EBL conditions) were treated the same, the regression coefficient was 0.999, but the R^2 value was very low at 0.06, as shown in Figure

3-50. Data from time steps with stable atmospheric conditions, which occurred primarily during the night time, were responsible for most of the scatter in the data, indicating the low dependability of LAS measurements during stable, low H conditions. Other outliers were produced when R_n - G - CS was between 100 and 300 W m^{-2}.

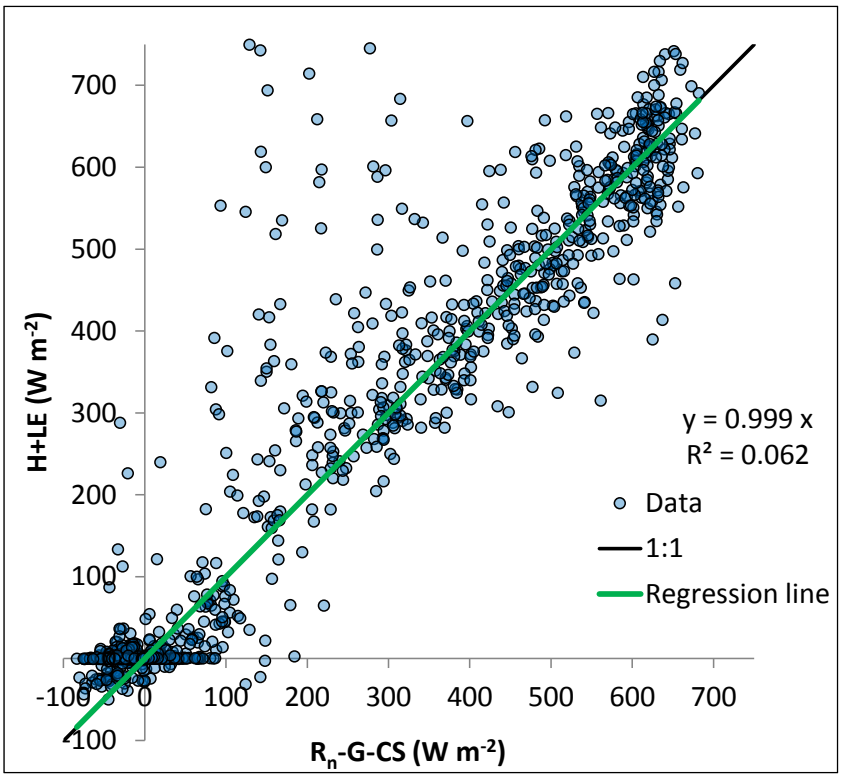

Figure 3-50. Relationship between R_n-G-CS and adjusted H+LE. H and LE from the eddy covariance system are adjusted with the LAS correction. Data from time steps with stable and buoyant conditions are adjusted with the same correction. The slope of the regression is almost 1.0, but the R^2 value indicates poor correlation. Data from July 2011, n = 1329.

A hybrid methodology was explored to address closure during stable periods. This approach only applied the H_{LAS} adjustment during buoyant periods, typically during the day. During unstable periods, typically during the night, residual energy was partitioned equally between H and LE, as described by Oliphant et al. (2004). Stable periods were defined as when H < 0. While the LAS correction being explored here is distinct from the Bowen ratio method described by Oliphant et al. (2004), the criteria they described for determining when the adjustment could be successfully applied is used. Specifically, the criteria for partitioning the residual energy equally between H and LE was initially set as $-2 < \beta < 0$ or $-5 < H < 5$ W m^{-2} or $-5 < LE < 5$ W m^{-2}.

Including these provisions to handle data from stable time steps greatly improved the results. R_n-G-CS was again plotted on the x axis and H + LE was plotted along the y axis. The regression coefficient increased to 1.04, while the R^2 value increased substantially to 0.89 (Figure 3-51). In the graph, points below about 150 W m^2 on the x axis tend to fall on the 1:1 line. These points correlate with predominately stable conditions when the residual was partitioned equally between H and LE. The number of outliers occurring when R_n - G - CS > 200 W m^{-2} were substantially reduced as well.

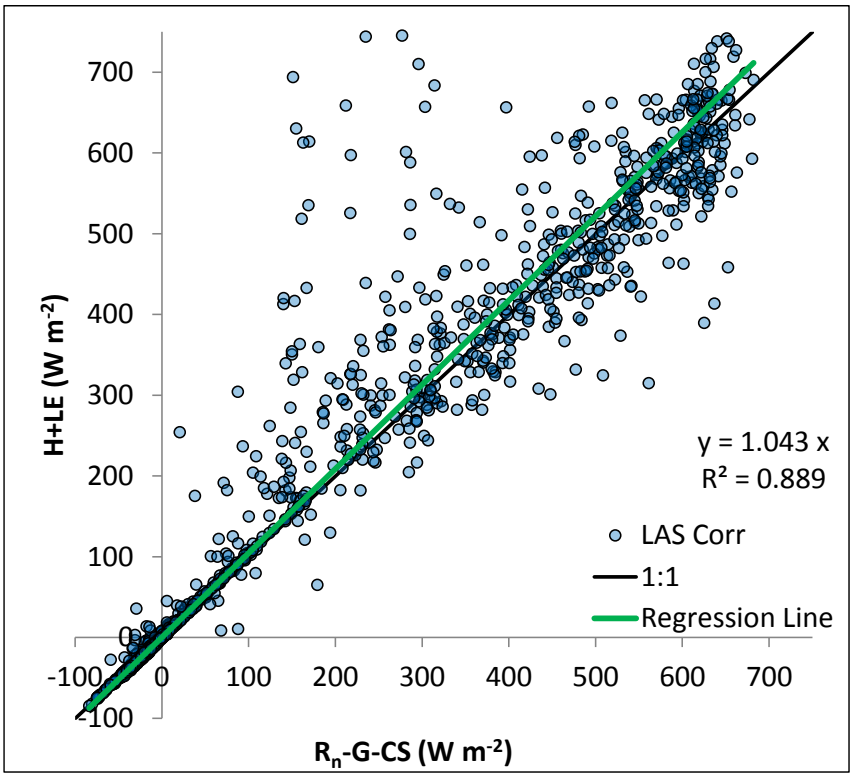

Figure 3-51. Relationship between Rn-G-CS and adjusted H+LE. H and LE from the eddy covariance system are adjusted with the LAS adjustment. Data from time steps with stable conditions are adjusted by partitioning the residual equally between H and LE and cluster along the lower section 1:1 line. Data from July 2011, n = 1329.

The outliers on the graph Figure 3-51 which fall above the 1:1 line were investigated. These outliers tended to be associated with time steps in the morning as the sun was coming up, and in the evening as the sun was going down. These outliers seemed to be associated with problematic data from the EC system. The outliers came from LE_{adj} being adjusted too high, rather than from H_{adj}, indicating the problem came from multiplying LE by the adjustment ratio ($LE_{ECadj} = LE_{mea}*(H_{LAS}/H_{EC})$) when the Bowen ratio associated with these outliers was positive but very small (low H to LE ratios) and the EBL was in strong transition from buoyant to stable conditions. A sensitivity analysis of the Bowen ratio filter parameter showed that by increasing the Bowen ratio threshold in the filter very slightly,

the outliers associated with time steps when the earth boundary layer (EBL) is in strong transition were eliminated by partitioning the residual energy equally between H and LE, as was done for the nighttime during stable conditions. Raising the threshold in the Bowen ratio filter from 0 to 0.1 eliminated many of the outliers, resulting in a regression coefficient of 1.02 and an R^2 value of 0.95. Increasing the Bowen ratio threshold to 0.2 further reduced the number of outliers, resulting in a regression coefficient of 1.01 and an R^2 value of 0.97. Graphs a, b, and c in Figure 3-52 illustrate the data behavior as the Bowen ratio threshold was incrementally increased.

An analysis of the relationship between the Bowen ratio and the ratio H_{LAS}/H_{EC} was conducted for the July 2011 dataset. The average ratio H_{LAS}/H_{EC} was calculated for all time steps with a Bowen ratio < 0, and for time steps with Bowen ratio > 0, in categories based on the Bowen ratio in increments of 0.1 up to Bowen ratio = 2. The results are shown in Table 3-11. Initially, as the Bowen ratio increased, the ratio H_{LAS}/H_{EC} decreased, and became somewhat stable at around 1.1 to 1.2 at Bowen ratio > 0.3. At Bowen ratio >1.0, the H_{LAS}/H_{EC} varied again, possibly due to the low number of observations. The H_{LAS}/H_{EC} ratio tends to decrease as the BR increase. This could reflect a tendency for the localized increases in H_{EC} while LE_{EC} remains relatively stable. Conversely, H_{LAS}, which is an area averaged estimate of H, could be less affected by localized increases in H. Most of the time steps when the LAS adjustment was applied had a Bowen ratio between 0.1 and 1. It seems reasonable that setting the Bowen ratio threshold at 0.1 would be sufficient to reduce the number of outliers without excluding too many time steps from the LAS adjustment. The ratio of H_{LAS}/H_{EC} of 1.16 to 1.2 follows the correction required by Frank et al. (2016) to account for transducer shadowing of eddy components.

An additional filter parameter was evaluated to check for the EBL becoming stable (Bowen ratio < 0) during the afternoon on an advective, wet day, for example, when a wet canopy is present and substantial advection of heat from outside the area may be occurring. The filter was expanded such that the LAS correction would be used unless the Bowen ratio < 0.1 and LE < 100 W m^{-2}. In cases of a wet canopy and advection, LE should be well over 100 W m^{-2}. The Bowen ratio threshold was maintained at 0.1 based on the previous analysis. The logic for this filter parameter is

> If β < 0.1 AND LE < 100 W m^{-2}, then partition residual energy equally between H and LE; otherwise H_{ECadj} = the greater of H_{LAS} or H_{EC} and $LE_{ECadj} = LE_{EC}$ if $H_{EC} > H_{LAS}$ otherwise $LE = LE_{EC} * H_{LAS}/H_{EC}$.

	Count	Ave H_{LAS}/H_{EC}
NORTH TOWER		
BR < 0	607	0.55
0 <= BR <= 0.1	42	4.40
0.1 < BR <= 0.2	35	2.36
0.2 < BR <= 0.3	53	1.52
0.3 < BR <= 0.4	60	1.20
0.4 < BR <= 0.5	76	1.13
0.5 < BR <= 0.6	91	1.18
0.6 < BR <= 0.7	74	1.11
0.7 < BR <= 0.8	60	1.09
0.8 < BR <= 0.9	48	1.07
0.9 < BR <= 1.0	28	1.00
1.0 < BR <= 1.1	15	0.81
1.1 < BR <= 1.2	12	1.01
1.2 < BR <= 1.3	10	0.61
1.3 < BR <= 1.4	9	0.46
1.4 < BR <= 1.5	7	0.40
1.5 < BR <= 1.6	1	1.36
1.6 < BR <= 1.7	5	0.85
1.7 < BR <= 1.8	2	1.28
1.8 < BR <= 1.9	0	N/A
1.9 < BR <= 2.0	4	-18.61
BR > 2.0	78	1.62
SOUTH TOWER		
BR < 0	587	0.34
0 <= BR <= 0.1	43	5.47
0.1 < BR <= 0.2	39	1.98
0.2 < BR <= 0.3	45	1.45
0.3 < BR <= 0.4	50	1.29
0.4 < BR <= 0.5	78	1.27
0.5 < BR <= 0.6	84	1.17
0.6 < BR <= 0.7	81	1.16
0.7 < BR <= 0.8	67	1.18
0.8 < BR <= 0.9	45	1.18
0.9 < BR <= 1.0	37	0.98
1.0 < BR <= 1.1	27	0.95
1.1 < BR <= 1.2	11	1.00
1.2 < BR <= 1.3	9	0.83
1.3 < BR <= 1.4	11	1.04
1.4 < BR <= 1.5	7	0.32
1.5 < BR <= 1.6	1	3.46
1.6 < BR <= 1.7	2	0.00
1.7 < BR <= 1.8	1	1.18

	Count	Ave H_{LAS}/H_{EC}
1.8 < BR <= 1.9	2	0.03
1.9 < BR <= 2.0	3	-0.01
BR > 2.0	100	-3.09

Table 3-11. Analysis of the relationship between Bowen ratio and H_{LAS}/H_{EC}. Data from July 2011.

A sensitivity analysis for the LE filter was conducted, graphs d, e, f in Figure 3-52. The data were not sensitive to the magnitude of the LE threshold, within reasonable ranges (0 to 150 W m^{-2}). The inclusion of the LE parameter had little effect on the regression coefficient and decreased the R^2 value slightly. The inclusion of the LE filter parameter allowed a few more time steps to be adjusted with the LAS adjustment during time steps when the process was becoming stable, i.e., when Bowen ratio was small – less than 0.1 – while the LE remained relatively high. Typically this relationship persists for a few time steps in the morning and the evening, but resulted in a few outliers and reduce the R^2 value. EC data from stable, or near stable, periods tends to be more problematic and errors in LE or H estimates may be magnified by the correction ratios, producing the outliers. Specifically, the addition of an LE filter allows near stable conditions that occur late in the day on a typical day to be processed with the LAS correction, which may produce outliers, rather than identifying data associated with a wet canopy and advection. Therefore, the use of the LE parameters is not recommended.

Another filter method using a shortwave radiation threshold was explored to handle the time steps when the EBL is stable or in strong transition to stable conditions. This filter took the form of:

> If $\beta < 0.1$ OR $R_s <$ "x" W m^{-2} then partition the residual equally between H and LE; otherwise H = the greater of H_{LAS} or H_{EC} and LE = LE_{EC} if $H_{EC} > H_{LAS}$ otherwise LE = $LE_{EC}*H_{LAS}/HEC$.

In terms of the R_s filter, there was minimal effect on the LAS adjustment for the July 2011 data (graphs a, g, h, and i, Figure 3-52). However, as noted below, the R_s filter did improve the LAS adjustment in September when there was a tendency for the BR become positive for a few times during the night. The data associated with those periods was spikey and did not correct well with LAS adjustment. Therefore the R_s threshold was retained.

In summary, the effectiveness of BR, LE, and, R_s filters were evaluated by testing various combinations of thresholds for those parameters. The results are shown in Figure 3-52. Based on this analysis, the inclusion of the LE parameter decreased the performance of the LAS adjustment, and the R_s filter does not overcome these short comings. The LE filter parameter allows data from time steps when the EBL is in strong transition, when estimated values of H and LE can become problematic, to be processed

with the LAS adjustment. In practice, the LE filter parameter did not preserve data from time steps when the process becomes stable during the afternoon on very wet days. Such conditions are not common in the timeframe of the dataset. The best results were obtained using only the Bowen ratio filter. The LAS adjustment method does not obtain as "perfect" of a closure as the graphical solution method where a 1.2 multiplier on H and LE was used for the July dataset, as shown in Figure 3-49, produced the highest R^2 and with a slope near 1.0. However, the multiplier is different for the north and the south sites, and also varies by month. It also assumes that all EBCE resides in the turbulent fluxes.

The EBCE of the LAS adjusted data was analyzed to evaluate the performance of the LAS correction. EBCE was analyzed using both

$$EBCE = R_n - G - CS - H_{ECadj} - LE_{ECadj} \quad \textbf{(3-12)}$$

to look at absolute closure in terms of W m^{-2}, and

$$EB\ closure\ ratio = \frac{H_{ECadj}+LE_{ECadj}}{R_n-G-CS} \quad \textbf{(3-13)}$$

to look at the closure ratio. Figure 3-53 illustrates the EB closure analysis for a typical three-day period in July 2011. Note that data from the LAS were not available on 7/1 so the EBCE on that day illustrates EBCE for unadjusted EC data while 7/2 and 7/3 shows EC data that has been adjusted with the LAS adjustment.

This analysis indicates that 1) the LAS adjustment tends to make H and LE too strong, resulting in negative energy balances. 2) The EBCE residual is spikey. This is primarily a result of LE correction, where LE_{EC} is multiplied by the H_{LAS}/H_{EC} ratio. LE becomes large when the H_{LAS}/H_{EC} ratio is large, especially when LE_{EC} is also large. 3) The largest spikes in the closure ratio data occur in the morning and evening, when EBL is in strong transition from buoyant to stable conditions. 4) A review of the H and LE data from the time steps on either side of the spikes in the EBCE did not indicate that the data itself was problematic, i.e., the data typically seemed to fit with the data from the adjacent time steps. The spikes were the result of phenomena that combine to make the LE multiplier too great. The graph shows that the south side typically had poorer EBCE due to lower estimated turbulent fluxes.

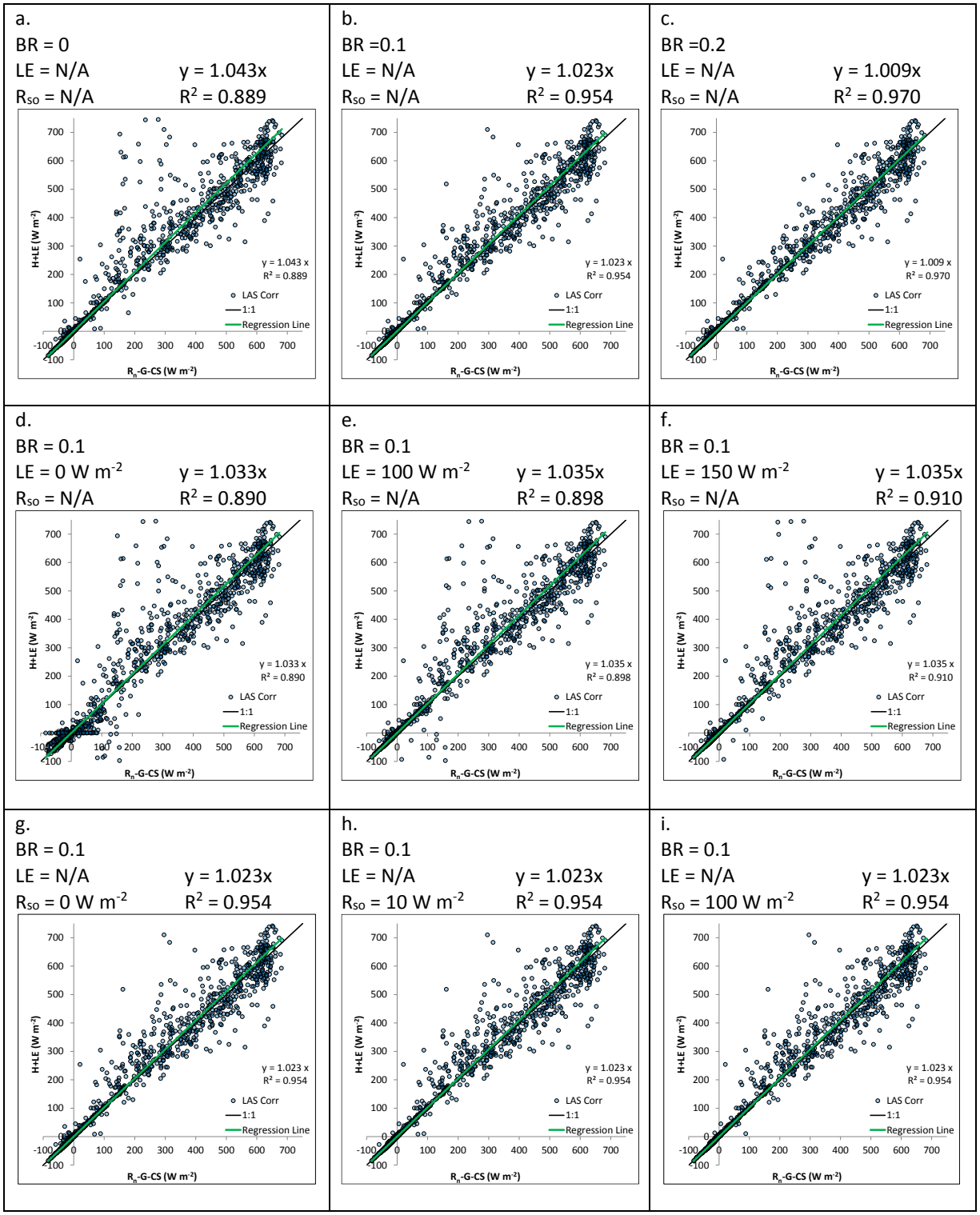

Figure 3-52. Behavior of LAS adjustment, with analysis of various combinations of thresholds for the BR, LE and R_s filter parameters for determining when to apply the LAS adjustment. H+LE is average of the north and south sites. The data are from the Island Park July 2011 data set, n = 1329.

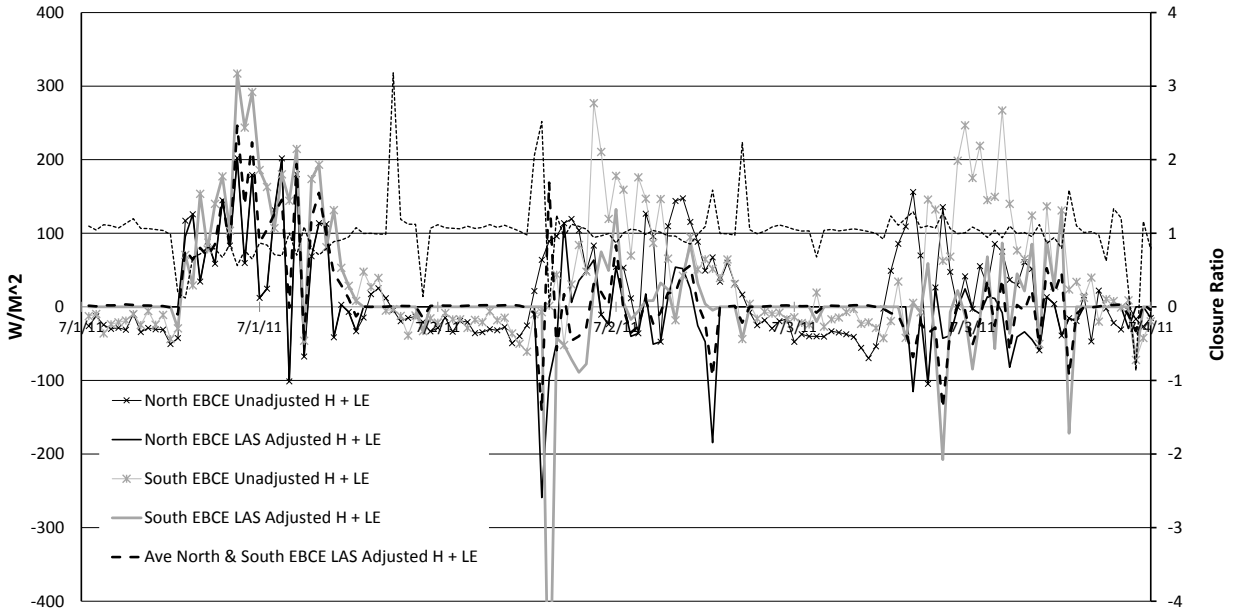

Figure 3-53. Comparison EBCE using original EC (unadjusted) and LAS-adjusted data for the north and south Sites, and average of both north and south H+LE. Data are from July 2011.

Analysis of the behavior of the LAS adjustment indicated that it can make H_{ECadj} and LE_{ECadj} too strong. Therefore it was modified so that it could not over-adjust the turbulent fluxes. For time steps when EBCE (R_n-G-CS-LE_{EC}-H_{EC}) is positive and H_{LAS} is greater than H_{Ec}, H_{LAS} may provide a more valid indication of H. LE_{EC} is increased by the same proportion as H_{LAS}/H_{EC} to preserve the Bowen ratio. This adjustment is warranted under the premise that common and perhaps unknown factors impact both turbulent fluxes equally. However, we limited the LAS adjustment to only allow it to increase the turbulent fluxes to the point where EBCE becomes 0.0. The adjustment is allowed to go no further, i.e., make H and LE even greater even though the measured H_{LAS} may be greater, since the purpose of using H_{LAS} in the LAS adjustment is to provide indication that the true H "could" be greater than the value measured by H_{EC}, as indicated by $H_{LAS} > H_{EC}$. However, the LAS adjustment should not be obligated to use the entire difference between H_{LAS} and H_{EC} when the use of H_{LAS} and associated correction to LE_{EC} would make EBCE negative. At that point, it is concluded that the H_{LAS} measurement overshoots true H, just as H_{EC} apparently undershoots true H.

Therefore the adjustment utilizes what we conclude are our most valid estimates for R_n, G and CS to establish adjustments to H_{EC} and LE_{EC} in the same proportion (i.e., Bowen ratio = constant) so that EBCE improves, i.e., becomes closer to 0.0 but does not go negative. When R_n - G - (H_{EC} +

LE_{EC})*H_{LAS}/H_{EC} - CS > 0, the H_{LAS} measurement is accepted as being the better measurement, and both H_{EC} and LE_{EC} are adjusted according to H_{LAS}/H_{EC}. EBCE remains positive, but less positive than it was. The benefit is that the adjustment does not "speculate" past the measurement of H_{LAS} on what the true H flux is.

When $H_{LAS} < H_{EC}$ and the EBCE is > 0, the LAS adjustment ((H_{EC} + LE_{EC})*H_{LAS}/H_{EC}) would cause the EBCE to deviate further from 0.0. In those cases, it is assumed that H_{EC} is the better measurement and no adjustments are made to EC data.

This was explored in Excel by calculating an adjustment factor to H_{EC} and LE_{EC} using the following coding:

IF(($H_{LAS} < H_{EC}$ OR EBCE < 0) ,1, IF($EBCE_{adj}$ <> 0,MIN((1 + ($EBCE_{adj}$ / (H_{ECadj} + LE_{ECadj})),1),1)

where EBCE was calculated with H_{EC} and LE_{EC} (unadjusted), $EBCE_{adj}$ is the EBCE calculated with the H and LE adjusted by the LAS without any limit on the amount of correction that is allowed to adjust H and LE. H_{adj} and LE_{adj} are the LAS adjusted H and LE without any limit on the amount the correction. This equation first checks if $H_{LAS}<H_{EC}$ or if the EBCE calculated with H_{EC} and LE_{EC} is < 0; if it is, then no adjustment is made because either the LAS-based adjustment either did not adjust the EC data (because H_{LAS} is smaller than H_{EC}), or because EBCE with H_{EC} and LE_{EC} is already negative. The equation then checks to see if the $EBCE_{adj}$ is other that 0.0. If it is, then the LAS-based adjustment may be too strong and an adjustment factor is calculated such that EBCE = 0. The correction factor is 1+$EBCE_{adj}/(H_{ECadj}$ + LE_{ECadj}). The equation then takes on the value of the adjustment factor or 1, whichever is smaller. The adjustment factor is < 1 if H_{ECadj} and LE_{ECadj} are too strong, resulting in $EBCE_{adj}$ < 0, and both H and LE are adjusted equally via the adjustment factor to preserve the Bowen ratio such that EBCE = 0. If the adjustment factor is > 1 ($EBCE_{adj}$ > 0), then the LAS-based adjustment used all the available power of the measured H_{LAS} to increase H_{EC} and LE_{EC} and no additional adjustment is made to H and LE; the equation returns the value of 1. If $EBCE_{adj}$ = 0, then the adjustment was good and no additional adjustment is made to H and LE.

The improvements to the LAS adjustment appear to perform well. Figure 3-54 shows a scatter plot of H_{ECadj} + LE_{ECadj} vs Rn- G- CS for time steps with buoyant EBL conditions for July 2011. The R^2 is 0.95 and the coefficient is 0.95. The points above the 1:1 line (Figure 3-51) due to the over-adjustment of the turbulent fluxes by the LAS adjustment are now on the 1:1 line and the EB ratio is near 1, as shown in Figure 3-55.

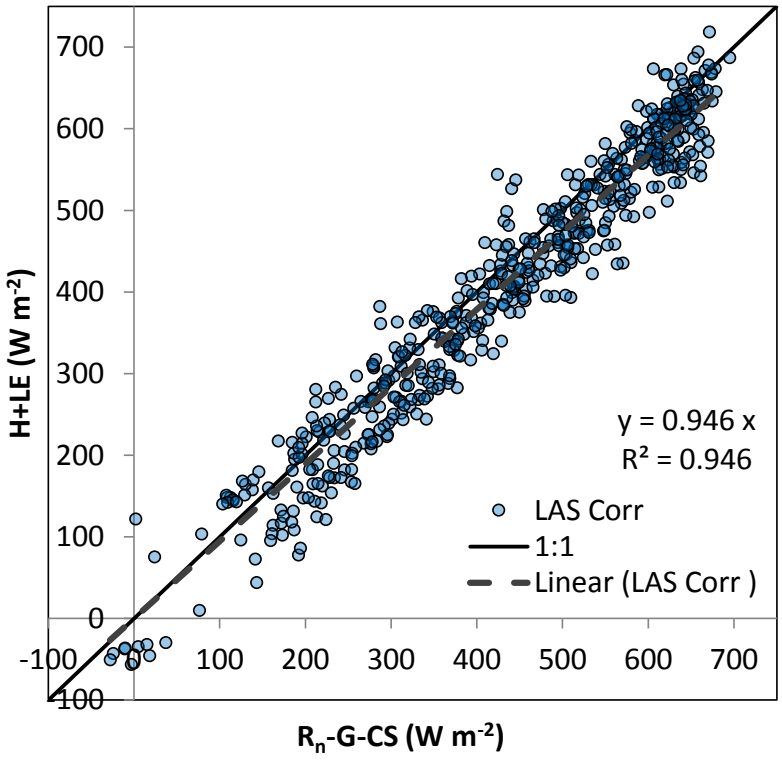

Figure 3-54. Graph showing the behavior of the LAS adjustment when the adjustment is constrained so that the change to H and LE is limited so that EBCE does not go negative as a result of the adjustment. Data from July 2011, n = 506.

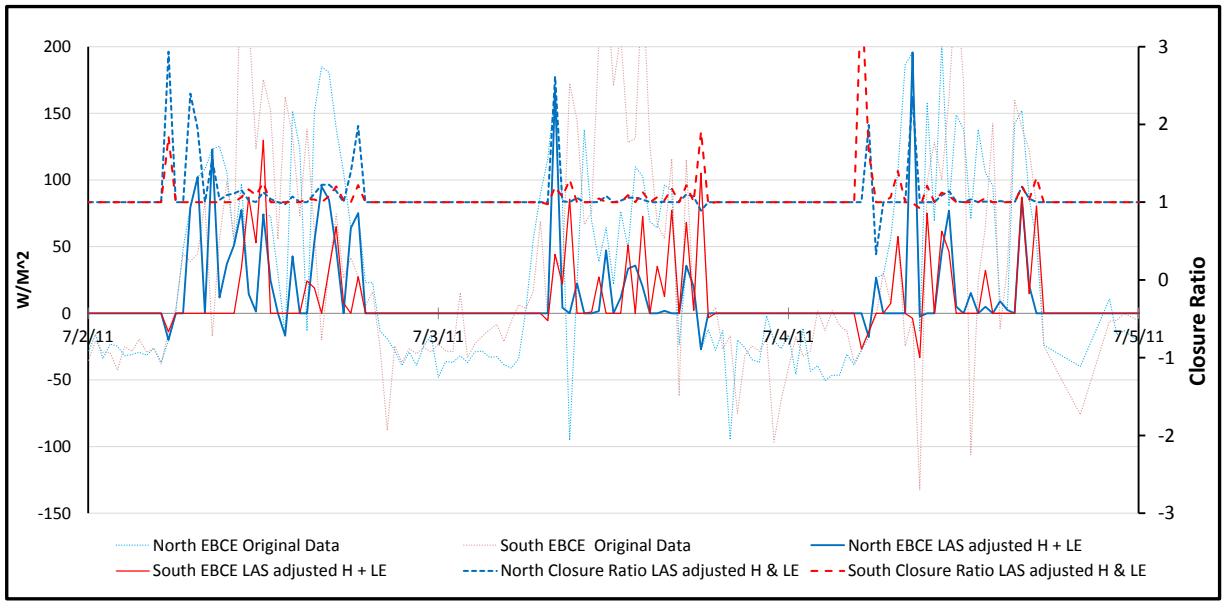

Figure 3-55. Graph of EBCE and closure ratio when the LAS adjustment is constrained so that H_{adj} and LE_{adj} are less than or equal to Rn - G - for the North and South Sites. Data from July 2011.

The LAS adjustment method was tested on the September 2011 data set. For time steps when the EBL is buoyant and there were LAS data available, the correction performed well, as shown in Figure 3-56. The regression coefficient was 0.96 and R^2 was 0.93. Several points were noted about the September data set relative to the LAS adjustment. First, the LAS was frequently offline during September, so there were many time steps that could not be processed with the LAS adjustment. Second, the strength of H_{LAS} relative to H_{EC} was lower than during July. Thus, even though EBCE > 0, H and LE may not be strengthened if $H_{LAS}<H_{EC}$.

The use of the shortwave radiation filter with the Bowen ratio filter became more important with the September data set due to the frequency of buoyant conditions, as indicated by BR>0, during the night. Buoyant night time conditions were associated with both H and LE becoming negative. The LAS-based adjustment does not work well with negative turbulent fluxes.

It was desirable to also adjust the H_{EC} and LE_{EC} data from time steps that met the filter criteria of Bowen ratio > 0.1 and R_{SO} > 10 W m^{-2}even though there was no H_{LAS} data available for a particular time. Although all months were affected by this problem to a limited degree, this was more of an issue in September due to the number of time steps that fall in this category. An adjustment was explored using a graphically-determined multiplier for the H_{EC} and LE_{EC} data for time steps without H_{LAS} data, but that otherwise met the filter criteria for the LAS adjustment, to approximate the LAS adjustment. The "target" was determined by regression between $H_{ECLASadj}$ + $LE_{ECLASadj}$ and R_n - G - CS for time steps when LAS adjustment was applied (Figure 3-56, north site). The equation of the regression line was noted.

On a second graph the relationship between H_{EC} + LE_{EC} and R_n - G - CS for time steps meeting the filter criteria for the LAS adjustment, but for which LAS data were not available, were plotted (Figure 3-57, north site). H_{EC} + LE_{EC} were assigned weighting factors by trial and error such that the regression line equation had the same slope as the regression line in Figure 3-56. H and LE were weighted equally. The same process was repeated for the south site (Figure 3-58 and Figure 3-59). The required weighting factor was about 1.28 for the north site and 1.09 for the south site. This method provided a correction such that the slope of the regression line matched the slope of the regression line for the LAS-adjusted data. However, it was noted that the R^2 value for this method was lower (R^2=0.76). The north site required a stronger weighting factor than the south site because north site had higher LE than the south site in September 2011, as discussed in Chapter 5. Consequently H at the north site was lower than at the south site, so the H_{LAS}/H_{EC} ratio was higher at the north site than the south

site. Therefore, the LAS adjustment had more “power” to adjust the turbulent fluxes at the north site, and a larger weighting factor was required to match the LAS-adjusted data.

As discussed, the LAS adjustment utilizes H_{LAS} to increase H_{EC} and LE_{EC} when $H_{LAS} > H_{EC}$ to minimize the EBCE when the turbulent fluxes are under-estimated. However, turbulent fluxes may also be overestimated by the EC method as well, resulting in EBCE < 0. Data from these time steps plot above the 1:1 line in the scatter plots. In these cases, if $H_{LAS} < H_{EC}$, H_{LAS} can be used to decrease H_{EC} and LE_{EC} and improve the EBCE. The LAS adjustment was modified so that if $R_n - G - CS - H_{EC} - LE_{EC} < 0$, then the turbulent fluxes would be reduced by H_{LAS}/H_{EC}, The adjustment would only be allowed to decrease the turbulent fluxes until EBCE = 0. The result of also using the LAS adjustment to decrease H_{EC} and LE_{EC} when H_{LAS} indicated they are too strong is shown in Figure 3-60 and Figure 3-61 for the June and July 2011 datasets. Notably, many of the points that were previously above the 1:1 line now plot closer to or on the line and the EBCE is reduced. Figure 3-62 and Figure 3-63 show the unadjusted data for June and July 2011 for comparison.

OLS regression graphs showing the relationship between Rn - G - CS and H + LE for the north site and the south site are included in Figure 3-60 and Figure 3-61 for original data without the LAS adjustment for June and July 2011. Figure 3-62 and Figure 3-63 show the same graphs, but with LAS-adjusted data. In June, the unadjusted turbulent fluxes for the north and south sites, as measured by the EC systems, had regression coefficients of 0.83 and 0.80 and R^2 values of 0.81, respectively. In July, the unadjusted turbulent fluxes for the north and south sites, as measured by the EC systems, had regression coefficients of 0.85 and 0.78 and R^2 values of 0.80 and 0.74, respectively. The turbulent fluxes adjusted by the LAS adjustment method for June 2011 had regression coefficients of 0.90 and 0.92 and R2 values of 0.93 and 0.95, respectively. In July, the unadjusted turbulent fluxes for the north and south sites, as measured by the EC systems, had regression coefficients of 0.96 and 0.94 and R2 values of 0.95 and 0.94, respectively.

The unadjusted June and July 2011 datasets had similar EBCE as measured by the slope of the regression line. The LAS adjustment increased the regression coefficient and the R^2 value for both the June and July data and closed 50 to 70% of the EBCE. The LAS adjustment improved the EBCE by adjusting turbulent fluxes if they were over-estimated as well as the under-estimated, although time steps where the fluxes needed to be increased were by far the more common case.

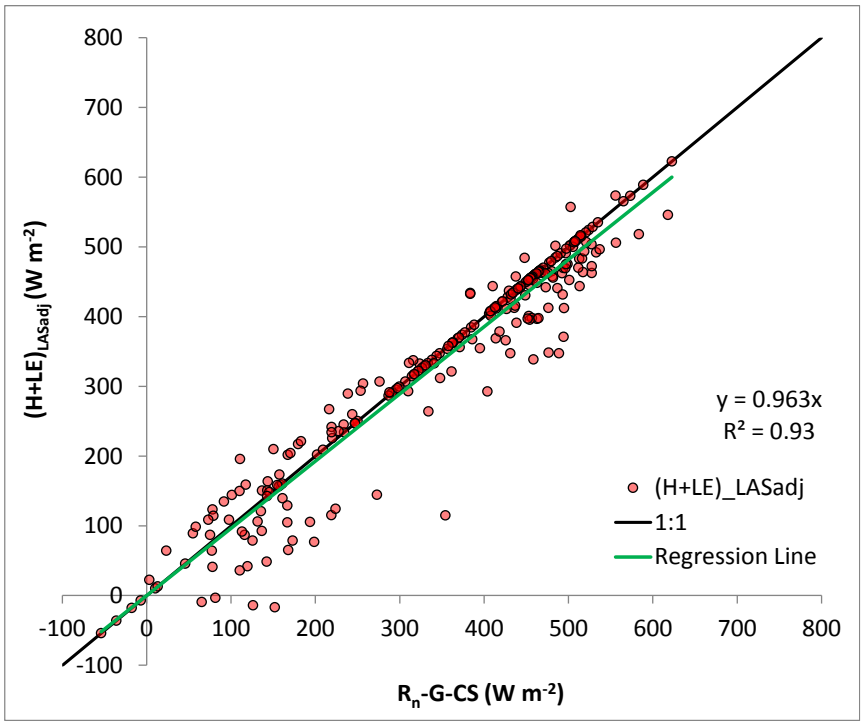

Figure 3-56. Regression relationship between north site LAS-adjusted H+LE and Rn-G-CS. The LAS adjustment was only applied to day-time time steps with buoyant EBL time steps that have LAS data available. Data are from September 2011, n = 275.

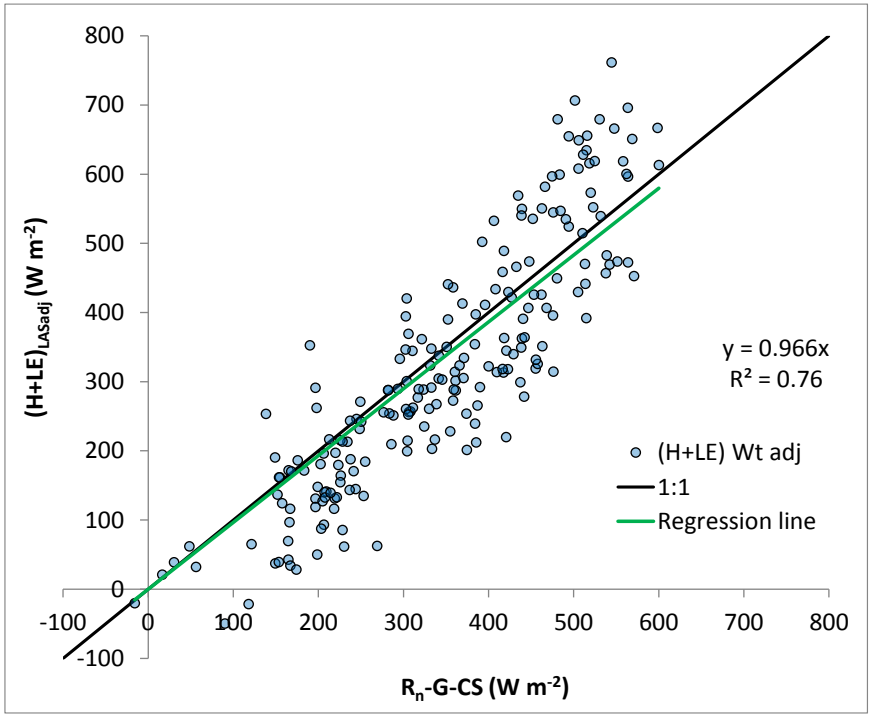

Figure 3-57. Regression relationship between north site weighted H+LE and Rn-G-CS for time step with buoyant EBL but no LAS data. The weighting factor was selected so that the slope of the regression line was the same as the regression line in Figure 3-56. The required weighting factor was 1.28. Data are from September 2011, n = 210.

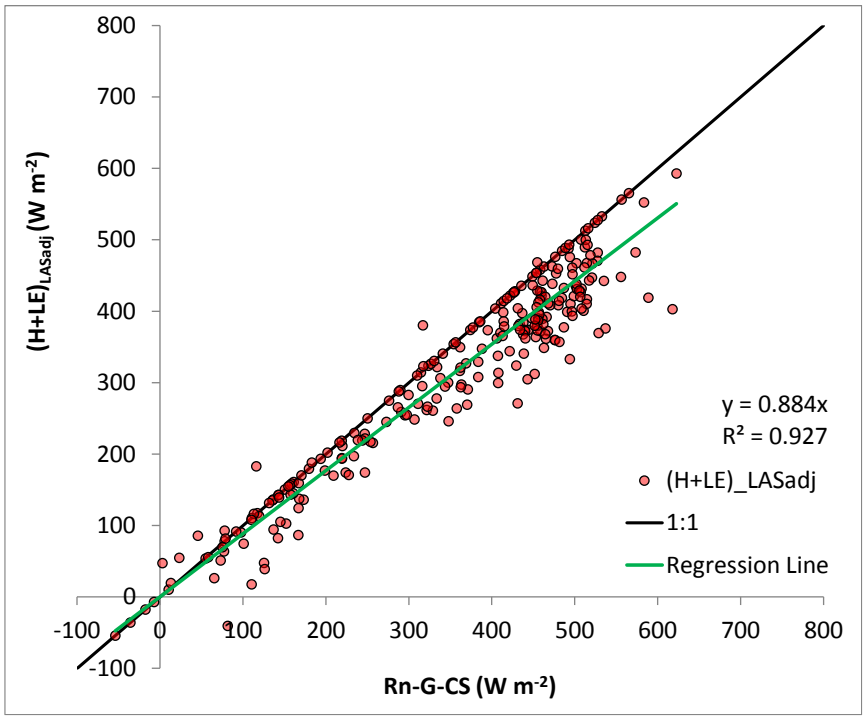

Figure 3-58. Regression relationship between south site LAS-adjusted H+LE and Rn-G-CS. The LAS adjustment was only applied to day-time time steps with buoyant EBL time steps that have LAS data available. Data are from September 2011, n = 275.

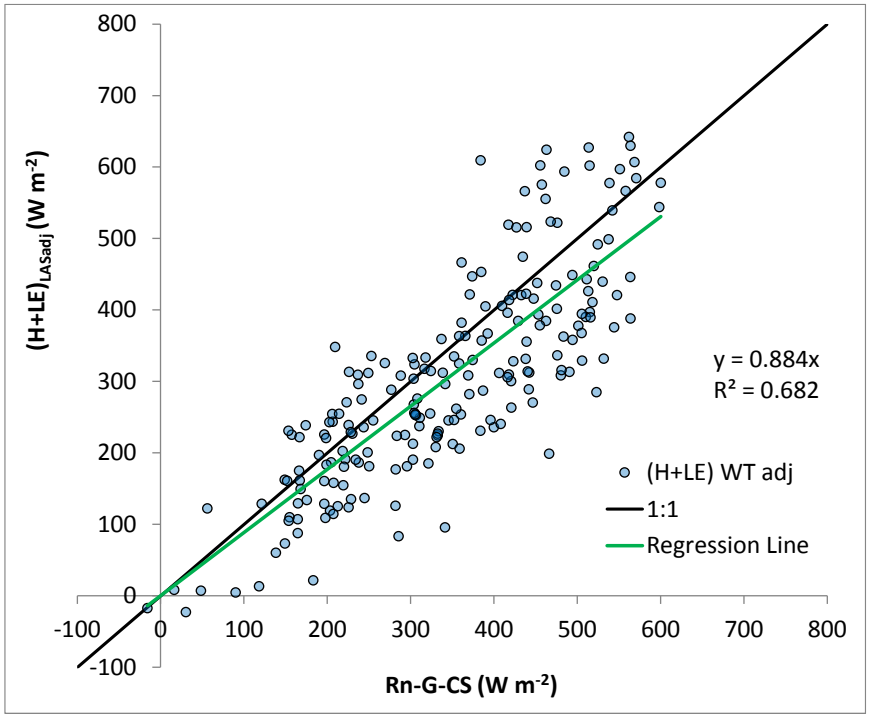

Figure 3-59. Regression relationship between south site weighted H+LE and Rn-G-CS for time step with buoyant EBL but no LAS data. The weighting factor was selected so that the slope of the regression line was the same as the regression line in Figure 2 43. The required weighting factor was 1.09. Data are from September 2011, n = 210.

As a summary of how the LAS adjustment was applied to the data, statistics were calculated for the July 2011 dataset (Table 3-12). EBCE was improved for a majority of time steps by applying the LAS adjustment. The analysis suggest that the LAS adjustment is a valid approach to improving EBCE. It is supported theoretically because the H_{LAS} is an area averaging measuring system capable of measuring energy flux of larger eddies linked to the heterogeneous landscape that the EC method may not measure well, as discussed by Foken (2008).

Condition	Number of Time Steps
North Tower	
H_{LAS} is higher than H_{EC} and has more than enough energy for closure.	138
H_{LAS} is higher than H_{EC} but is not high enough for closure.	238
H_{LAS} is lower than H_{EC} and EBCE<0 so H & LE were decreased; H_{LAS} was low enough for closure.	21
H_{LAS} is lower than H_{EC} and EBCE<0 so H & LE were decreased; EBCE was improved but H_{LAS} was not low enough for closure.	28
H_{LAS} is higher than H_{EC} but EBCE < 0 so no adjustment was made.	33
H_{LAS} is lower than H_{EC} and EBCE > 0 so no adjustment was applied.	49
Total number of time steps eligible for LAS adjustment (R_s > 10, BR > 0.1, H > 50, LE > 0)	507
Percent of total time steps eligible for LAS adjustment	38%
Number of eligible time steps missing LAS data (no adjustment made)	33
South Tower	
H_{LAS} is higher than H_{EC} and has more than enough energy for closure	143
H_{LAS} is higher than H_{EC} but is not high enough for closure	222
H_{LAS} is lower than H_{EC} and EBCE<0 so H & LE were decreased; HLAS was low enough for closure	16
H_{LAS} is lower than H_{EC} and EBCE<0 so H & LE were decreased; EBCE was improved but HLAS was not low enough for closure	12
H_{LAS} is higher than H_{EC} but EBCE < 0 so no adjustment was made	49
H_{LAS} is lower than H_{EC} and EBCE > 0 so no adjustment was applied	65
Total number of time steps eligible for LAS adjustment (R_s > 10, BR > 0.1, H > 50, LE > 0)	507
Percent of total time steps eligible for LAS adjustment	38%
Number of eligible time steps missing LAS data (no adjustment made)	33

Table 3-12. Statistics for the LAS adjustment for July 2011.

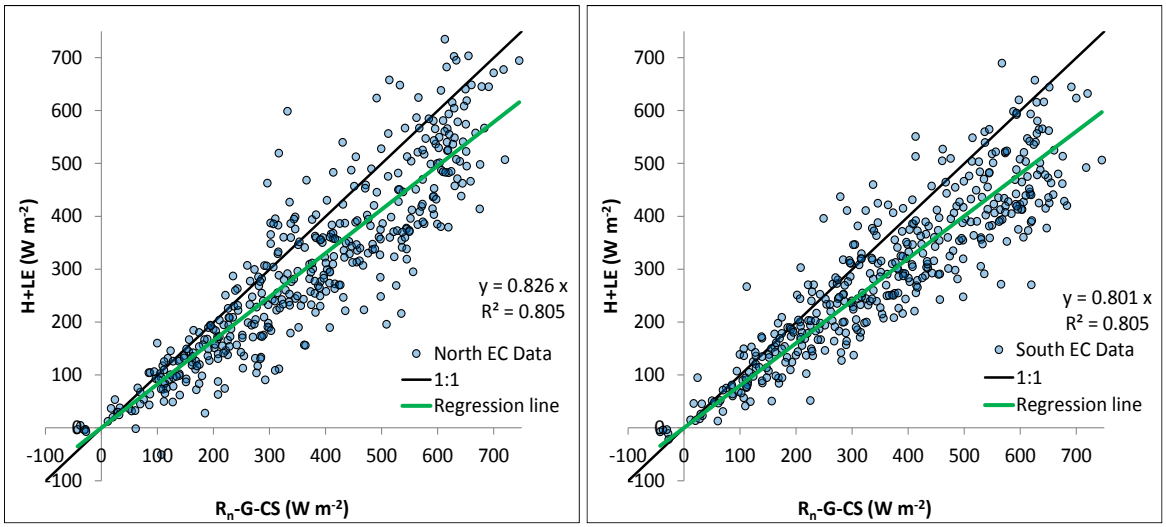

Figure 3-60. Unadjusted H + LE vs Rn - G – CS for the north site (left) and south site (right), June 2011 for time steps with R_s > 10 W m^{-2} and BR > 0.1, n = 420.

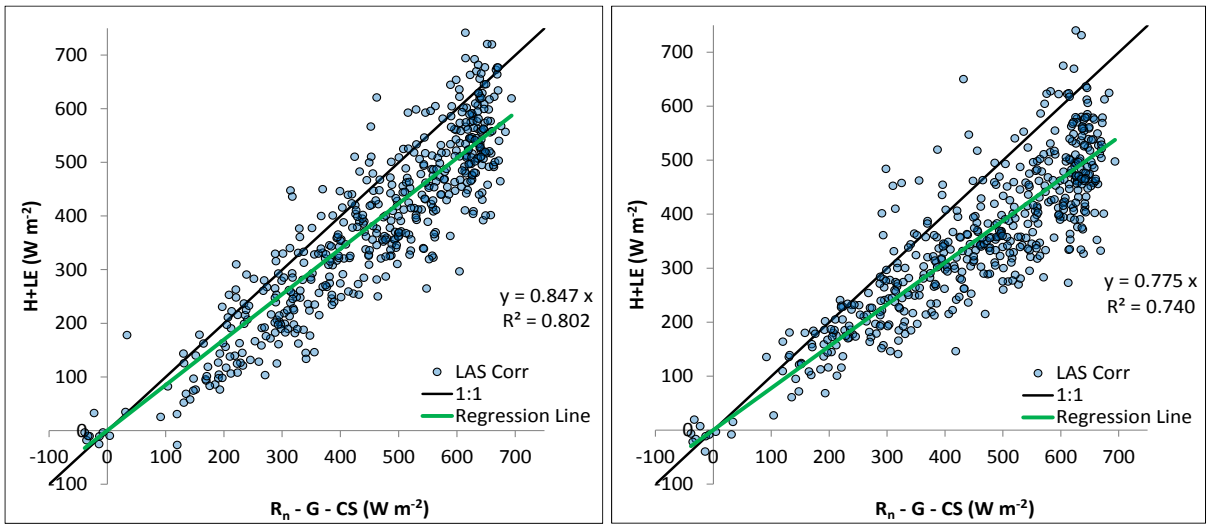

Figure 3-61. Unadjusted H + LE vs Rn - G – CS for the north site (left) and south site (right), July 2011 for time steps with R_s > 10 W m^{-2} and BR > 0.1, n = 506 .

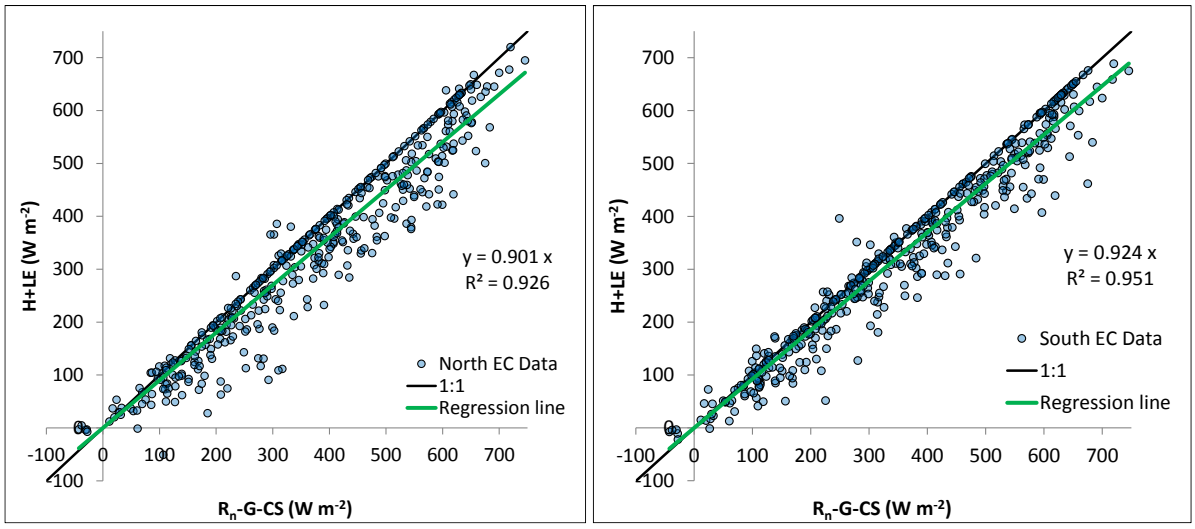

Figure 3-62. Plot showing the results of applying the fully-developed LAS adjustment to the June 2011 dataset for the north site (left graph) and the south site (right graph). H_{LAS} is also used to decrease turbulent fluxes if they are too large from the perspective of EBCE. Note that points above 1:1 have been adjusted toward the 1:1 line, n = 420.

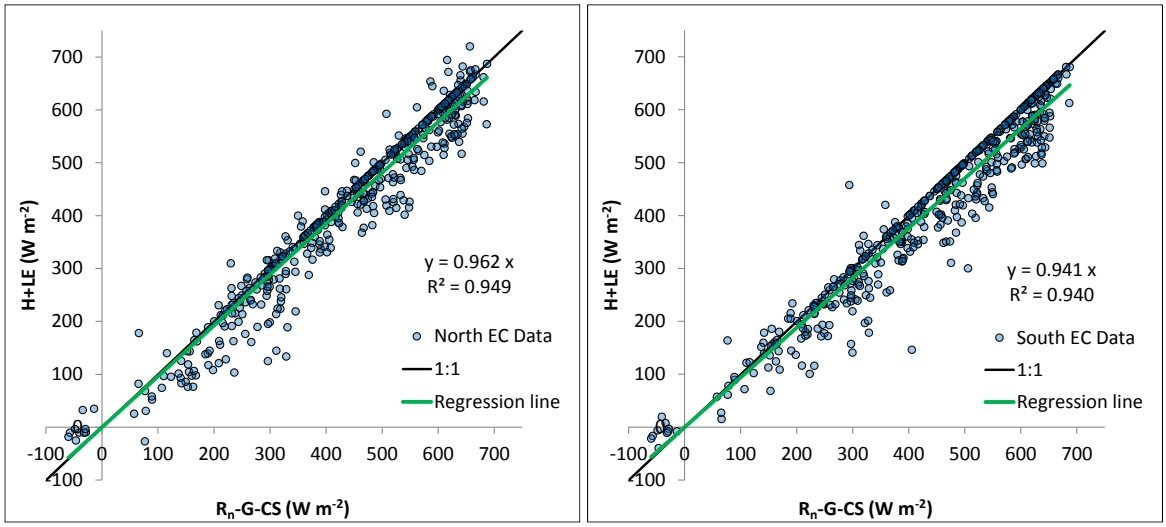

Figure 3-63. Plot showing the results of applying the fully-developed LAS adjustment to the July 2011 dataset for the north site (left) and the south site (right). H_{LAS} is also used to decrease turbulent fluxes if they are too large from the perspective of EBCE. Note that points above 1:1 have been adjusted as well, n = 506.

3.3.2.1 Use of Regression to "Finish" Adjustment of Fluxes

The LAS adjustment reduces the EBCE by adjusting the original H and LE from the EC system for time steps when EBCE and H_{LAS} suggests that H and LE were under-estimated by the EC system. However, the EBCE is not completely resolved by this adjustment. This section evaluates the use of OLS regression to "finish" the adjustment of the flux terms to achieve closure of the EB equation, and at the same time demonstrates the use of the LAS adjustment to limit the freedom of the regression model to use coefficients of the flux terms that might be unreasonable. The form of this regression model was R_n vs G, CS, and (H+LE). Coefficients from the regression were used make the final adjustment of the fluxes necessary for closure.

Two datasets from July 2011 were used in the regression model. R_n, G, and CS were the same in both datasets. The first dataset used LAS-adjusted H and LE, while the second data set used the original H and LE from the EC system. The Excel linest function was used to run the regression models. The results of the regression models are shown in Table 3-13. The regression coefficients for H + LE from dataset 1 are similar to dataset 2, however, it is important to remember that the coefficients for dataset 1 reflect LAS adjustment increase. The coefficients for G and CS are also smaller for data set 1.

Figure 3-64 shows graphs of the regression for the first dataset, with slope and R^2 values of essentially 1. Figure 3-65 shows graphs of the regression for the second dataset. The slope of the regression line for the second data set was about 4 percent lower and the R^2 values were 10 to 15 percent lower than for the first dataset.

The effect of the LAS adjustment on H and LE was evaluated by comparing the magnitude of the regression-adjusted H + LE previously adjusted by the LAS adjustment with the magnitude of regression-adjusted original EC H + LE (Figure 3-66). The H + LE fluxes with the LAS adjustment were about 6 percent higher for the north site and about 12 percent higher for the south site. These results show the value of using the LAS adjustment to first achieve the best estimate possible of the fluxes based on an independent measurement of H before using regression to achieve closure. Doing so constrained the regression model to better reflect actual system behavior and the corresponding coefficients on the fluxes in Table 3-13 are preferred for the LAS-adjusted dataset.

	H+LE	CS	G	Intercept	R2
North LAS- Adjusted H and LE					
Coefficient	1.03	1.30	0.92	0	0.99
Standard Error	0.01	0.06	0.06		
South LAS-Adjusted H and LE					
Coefficient	1.07	0.89	0.87	0	.99
Standard Error	0.01	0.06	0.07		
North H and LE Original EC					
Coefficient	1.07	1.26	1.49	0	0.98
Standard Error	0.01	0.11	0.12		
South H and LE Original EC					
Coefficient	1.12	0.46	2.03	0	0.97
Standard Error	0.02	0.12	0.12		

Table 3-13. Comparison of OLS regression results for the regression model R_n vs G, CS, and (H +LE). The first two runs show the results when H and LE had the LAS adjustment applied, while the second two runs show the results when H and LE were the original data from the EC system. July 2011, n = 506.

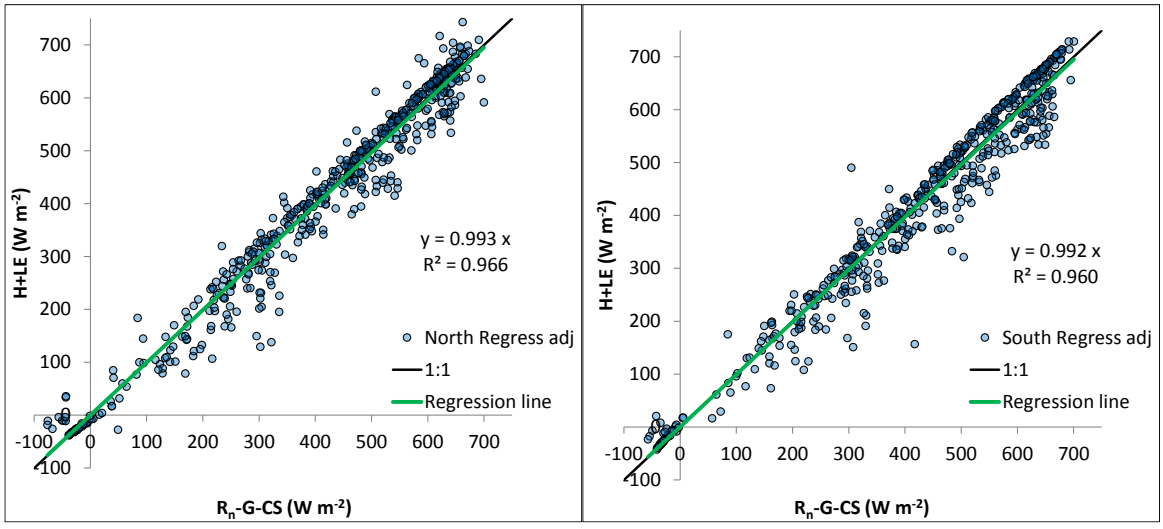

Figure 3-64. Evaluation of the use of OLS regression to "finish" the LAS adjustment. The regression model was R_n vs G, CS, and (H+LE), where H and LE were LAS-adjusted data. These graphs show the behavior the

EBC ratio when G, CS, and $(H + LE)_{LASadj}$ were adjusted by the regression coefficients for the Island Park north site (left) and south site (right). July 2011, n = 506.

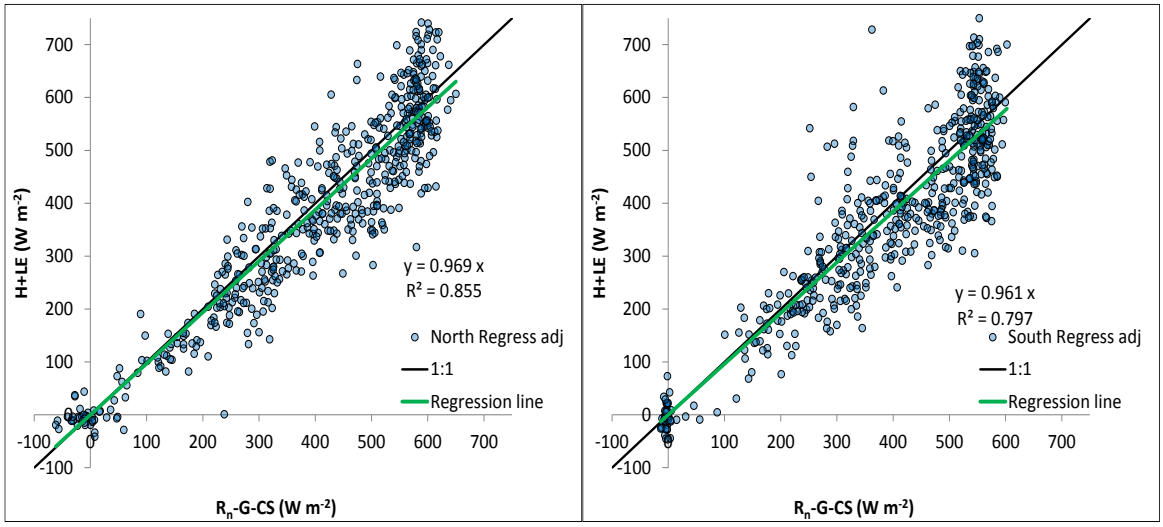

Figure 3-65. Evaluation of the use of OLS regression to adjust the fluxes to address the EBCE. The regression model was R_n vs G, CS, and (H+LE), where H and LE were original EC data. These graphs show the behavior the EBC ratio when G, CS, and $(H + LE)_{EC}$ were adjusted by the regression coefficients for the Island Park north site (left) and south site (right). July 2012, n = 506.

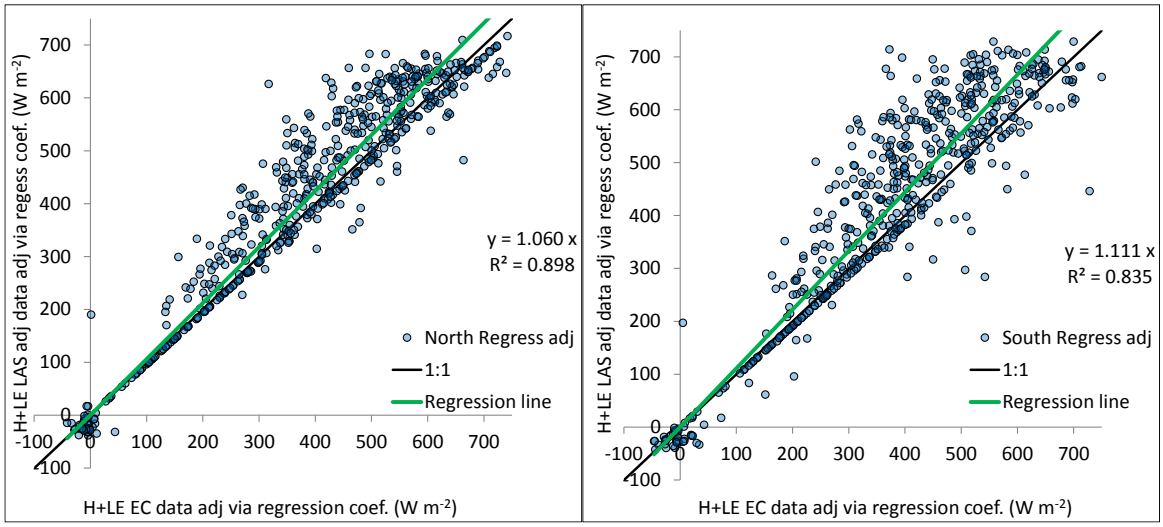

Figure 3-66. Comparison of the effect of the LAS adjustment on the magnitude of H and LE when regression was used to "finish" the EBC for the Island Park north site (left) and south site (right). The original EC H + LE were plotted on the x-axis and the LAS-adjusted H + LE were plotted on the y-axis. Coefficients determined by regression of R_n vs G, CS, and H + LE were used to adjust G, CS, H, and LE. July 2011, n = 506.

3.3.3 Summary of the LAS Adjustment (Method 1)

The preceding section documented the development of the LAS adjustment method. This section providers a concise summary of the equations that are used to apply the LAS adjustment to the data.

After the development and exploration of the LAS adjustment, the adjustment can be accomplished with the following set of equations which make use of an adjustment factor K to adjust H_{EC} and LE_{EC}.

$$R_n - G - CS - K(LE + H) = 0 \quad \textbf{(3-14)}$$

Where

$$K = \frac{R_n - G - CS}{LE + H} \quad \textbf{(3-15)}$$

$$IF\ \frac{R_n - G - CS}{LE_{EC} + H_{EC}} > 1\ then\ K = min\left(\frac{R_n - G - CS}{LE_{EC} + H_{EC}}, \max\left(\frac{H_{LAS}}{H_{EC}}, 1\right)\right) \quad \textbf{(3-16)}$$

$$IF\ \frac{R_n - G - CS}{LE_{EC} + H_{EC}} \leq 1\ then\ K = max\left(\frac{R_n - G - CS}{LE_{EC} + H_{EC}}, \min\left(\frac{H_{LAS}}{H_{EC}}, 1\right)\right) \quad \textbf{(3-17)}$$

$$H_{adj} = H_{EC} * K \quad \textbf{(3-18)}$$

$$LE_{adj} = LE_{EC} * K \quad \textbf{(3-19)}$$

With the following filter conditions:

$$R_{so} > 10\ W\ m^{-2} \quad \textbf{(3-20)}$$

$$BR > 0.1 \quad \textbf{(3-21)}$$

$$H_{EC}\ >\ 50\ and\ LE_{EC} > 0 \quad \textbf{(3-22)}$$

The inclusion of requirement for $H_{EC} > 50$ and $LE_{EC} > 0$ is to ensure that these fluxes are large enough that we have enough confidence in using them as a basis in the first place to apply the LAS adjustment.

3.3.4 Exploration of Alternate Approaches to Adjust Turbulent Fluxes (Method 2)

An alternative approach to adjusting the EC turbulent fluxes using the LAS data was evaluated. In this method, if $R_n - G - CS - H_{EC} - LE_{EC} > 0$, H_{EC} is adjusted up to H_{LAS}, up to the amount needed for closure. LE_{EC} is also adjusted, up to the amount needed for closure after H has been adjusted or by ratio H_{LAS}/H_{EC}, whichever is less.

$$IF\ H_{LAS} > H_{EC}\ then \quad \textbf{(3-23)}$$

$$H_{ECadj} = min(H_{LAS}, R_n - G - CS - LE) \quad \textbf{(3-24)}$$

$$LE_{adj} = min(R_n - G - CS - H_{ECadj}, LE\left(\frac{H_{LAS}}{H_{EC}}\right) \quad \textbf{(3-25)}$$

Method 1 and Method 2 were evaluated by comparing $|LE_{adjST}\text{-}LE_{adjNT}|$. LE_{adjST} and LE_{adjNT} are adjusted LE estimates from the South Tower and the North Tower, respectively, calculated using both Method 1 and Method 2. Regression results comparing Method 1 and Method 2 are shown in Figure 3-67 and Figure 3-68. Both methods produce similar regression results. Method 1 has a regression coefficient that is essentially 1, but has a little greater scatter relative to method 2. Although both methods give similar results, Method 1 is preferred because it uses the LAS to adjust the turbulent flux either up or down when such adjustment appears to better reflect the actually process, and it preserves the Bowen ratio as measured with the EC systems.

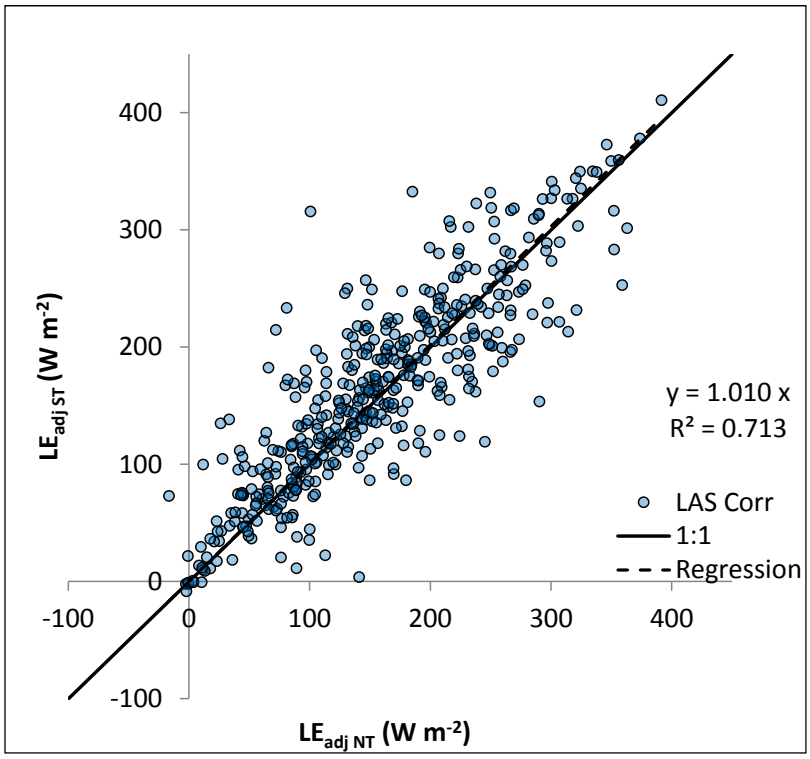

Figure 3-67. Regression between LE_{adj} North Tower and LE_{adj} South Tower. LE_{adj} was calculated by Method 1. Data from June 2011, n = 420.

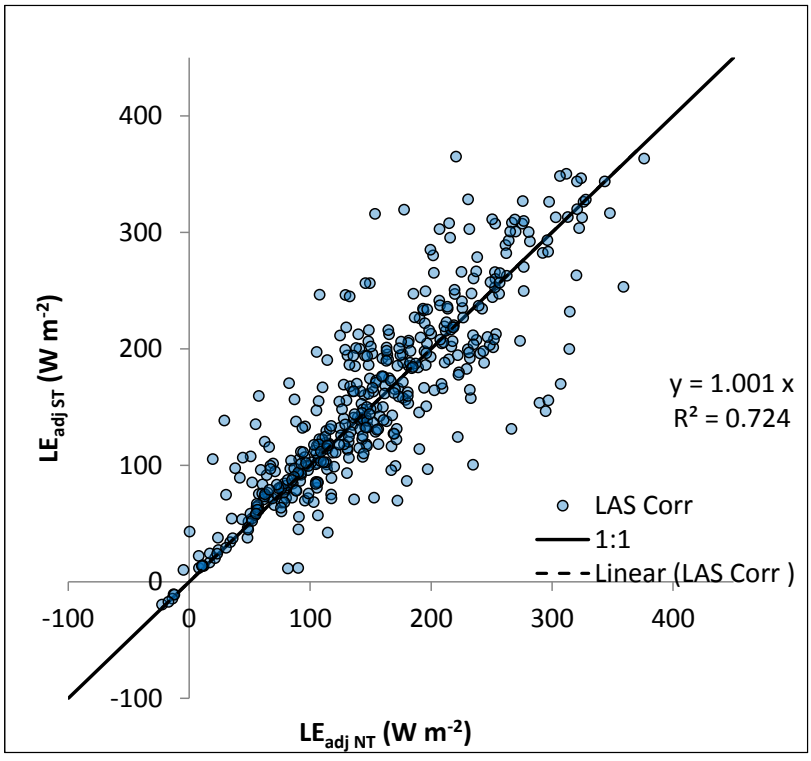

Figure 3-68. Regression between LE_{adj} North Tower and LE_{adj} South Tower. LE_{adj} was calculated by Method 2. Data from June 2011, n = 420.

Chapter 4 Analysis of Soil Heat Flux Estimates

Soil Heat Flux (G) was estimated at the Island Park north and south sites using six soil measurement subsites at each site to represent a variety of sun exposure, vegetation, and soil conditions present in the study area. Subsites were located in and near open meadow and at the edge of a meadow among trees with grass and forb understories, and under a dense lodgepole pine with primarily needle litter on the soil surface. Each subsite had different amounts and timing of sun exposure. Soil heat flux plates were placed at 6 and 12 cm depth at each subsite, and thermocouples were placed at 2, 4, 9, and 15 cm at the north site, and at 1.5, 3, 4.5, and 9 cm at the south site. Data for the four temperature depths were put into a 2nd degree polynomial regression equation to extend the temperature to the surface (Zhao and Allen 2013), and mean temperature for each soil slab above the plate was determined through integration of the 2nd degree polynomial equation between the limits of the soil profile of interest. . Appendix B provides additional detail on the calculation of G. Data from each subsite were used to calculate two estimates for G at the ground surface, one for the 6-cm heat flux plate depth, and one for the 12-cm heat flux plate depth. This chapter explores the effect of sensor placement, temporal variables, and number of sensors on the estimate of G, particularly in terms of EBCE.

4.1 Assessment of Soil Heat Flux Estimate Sensitivity to Sensor Depth

G is the estimate of soil heat flux at the surface measured by sensors located in the soil profile. G estimated from soil heat flux plates placed at different depths in the soil should be similar, within the margin of error of the instruments. Each Island Park site (north site and south site) had six soil subsites that collected data necessary to estimate G. Each soil subsite had two heat flux plates, one at 6 cm and one at 12 cm below the surface. The plates were offset from each other by about 10 cm. This section explores whether the estimate of G based on the 6 cm plate-depth is the same as that based on the 12 cm plate-depth, and, if G from the two depths is different, which one is the better estimate. Advantages to using a shallow plate depth are reduced dependency on estimating mean temperature change and specific heat capacity of the soil layer above the plate. That capacity changes with soil water content and organic material densities, which are generally not known with certainty. Disadvantages are that shallow plates can block vertical flow of rain and upward capillary water flow or vapor flow, changing soil water content above and below the plate from the natural surroundings. Deeper placement allows for better recovery of vertical flowlines of both heat and water around the plate.

4.1.1 Methodology

The sensitivity of the G estimate to sensor depth was investigated by evaluating the estimates from the 6-cm versus the 12-cm HFP. An ANOVA analysis was used to test whether G_{6cm} is the same as G_{12cm}. The null hypothesis is H_o:$\bar{\mu}_{G6cm}$=$\bar{\mu}G_{12cm}$. The alternative hypothesis is that means are different, indicating G estimated from the two depths was different. The statistical software SYSTAT was used to conduct the ANOVA.

The ANOVA used data from June 2011 following filtering of data as described in Chapter 3. The ANOVA tested two groups: G_{6cm} and G_{12cm}. The average of the 10 sensors, four from the north site and six from the south site, were used to calculate G_{6cm} and G_{12cm} (N2 and N4 were not used because of problems with the sensors, as explained in Chapter 3). The average of all subsites was used on the premise that the average of the 10 subsites would result in G representative of the diverse conditions within the turbulent flux footprints. In the ANOVA, G was used as the dependent variable and the two depths were independent (categorical) variables. Two ANOVA runs were made. The first used G corresponding to the times steps that had LAS-adjusted turbulent fluxes. For the June 2011 data set, there were 421 LAS-adjusted time steps. This run was included to guide the use of G in the EBCE analysis using LAS-adjusted H and LE (Section 5). Specifically, should G be averaged, or should one of the depths be selected for use in the EBCE analysis. The second run included all time steps from the month, on the basis that the events that cause a time step to carry error flags primarily affect the turbulent fluxes and sensors that collect data to estimate G are not likely to be affected by these phenomena, i.e., rain. The inclusion of more observations in the second steps gave the ANOVA more power to identify differences in the estimates of G between the two depths. Run 2 also included night-time data, whereas run 1 only included data from daytime periods with buoyant EBL, the same time steps that were included in the LAS adjustment.

4.1.2 Results

The ANOVA results are shown in Table 4-1. The F test indicated that the difference between the means of G estimated from the 6-cm and 12-cm data were not statistically significant ($F(1,840) = 1.004$, $p = 0.317$). The results were stronger for run 2 ($F(1,2880) = 0.123$, $p = 0.726$). This supports the premise outlined above that G estimated from different depth should be, and was, the same, assuming that proper field techniques were followed, temperature profiles were adequately measured, and estimates of parameters of the soil slab were accurate. Thus we expected that the differences seen in the data were due to measurement error or random error. The sum of squares

value for run 1 was larger than for run 2 because run 2 included daytime and nighttime data, resulting in a lower average. Figure 4-1 graphically depict the ANOVA results. The mean G was 41 W m^{-2} and 44 W m^{-2} for the 6-cm and 12 cm depths, respectively, for run 1. For run 2 the mean for the 6-cm data was 8.6 W m^{-2} vs 9.4 W m^{-2} for the 12-cm data. The means were larger for run 1 because only data from time steps associated with a buoyant EBL were included, while run 2 included all data from both daytime and nighttime. The means from both run 1 and run 2 were positive because the summer sun was warming the soil profile in June.

Because the estimate of G from sensors placed at the two depths was not significantly different, there was not a strong indication that one depth was better than the other. In terms of EBCE, G from the 12-cm depth sensor was generally larger and would reduce the EBCE, as illustrated in Figure 4-2. However, the improvement in EBCE would be small and would not offset the benefit of using G derived from both the 6-cm and 12-cm depth sensors as a means of developing an estimate of G that would be more robust in terms of random error or individual sensor malfunction. Further, it is not known which G most closely represented the actual G for the flux footprints. Therefore, the use of an average G based on the 6-cm and 12-cm data is adopted and was used in all analyses in this work. Several possible reasons for the non-statistically significant differences between the 6 and 12 cm depths include the following. If the soil heat storage above the soil heat flux plate was over-estimated, then the deeper plate would tend to produce a higher estimate of G. Conversely, if the soil heat flux plate were underestimating the flux, then the deeper plate would be less affected because there is less flux at the deeper depth.

Source	Type III SS	df	Mean Squares	F-ratio	p-value
RUN 1: Depth of G estimate, LAS adjusted time steps only	1,764	1	1,764.030	1.004	0.317
Error	1,475,811	840	1,756.918		
RUN 2: Depth of G estimate, all time steps	237	1	237.803	0.123	0.726
Error	5,562,707	2880	1,931.496		

Table 4-1. ANOVA table comparing G estimated from soil heat flux plates placed at 6 cm and 12 cm at the north and south sites. Run 1 used only time steps corresponding to LAS adjusted turbulent fluxes. Run 2 used all data. Data from June 2011, n = 420 run 1, , n = 1093 run 2.

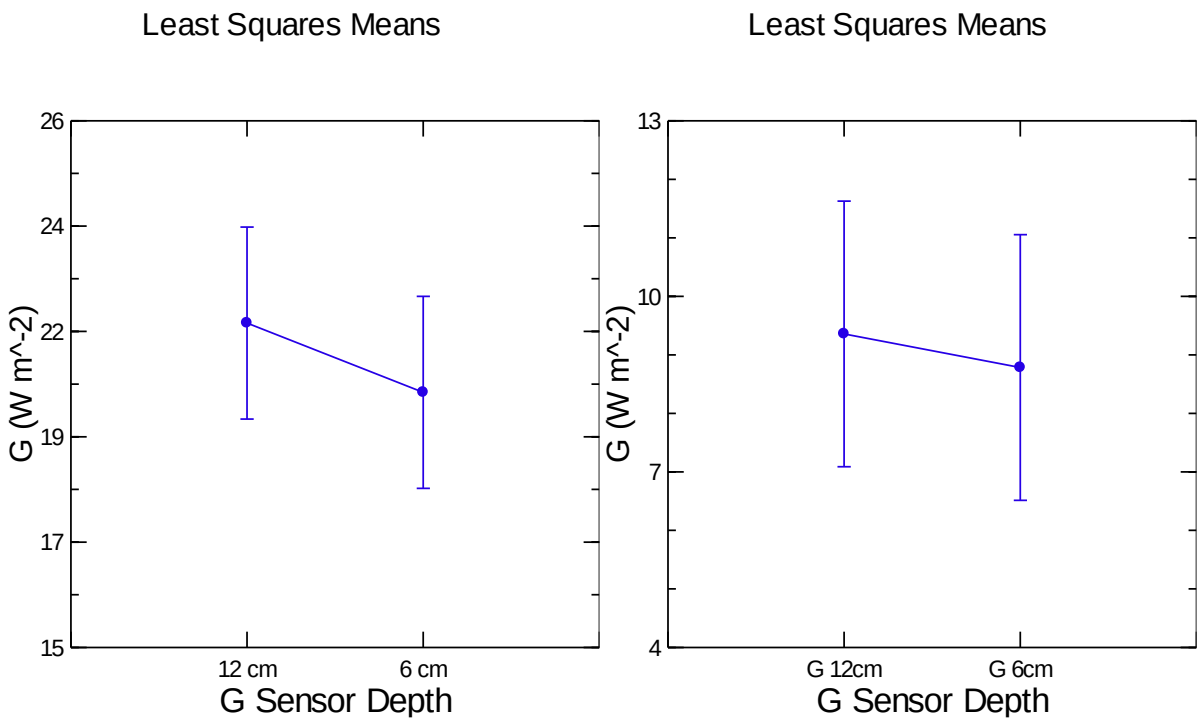

Figure 4-1. Graph from ANOVA testing the similarity of the G estimate from the 6 cm and 12 cm HFP depths. Run 1 (left) uses data from only time steps corresponding to LAS adjusted turbulent fluxes. Run 2 (right) uses data from all time steps. June 2011, n = 420.

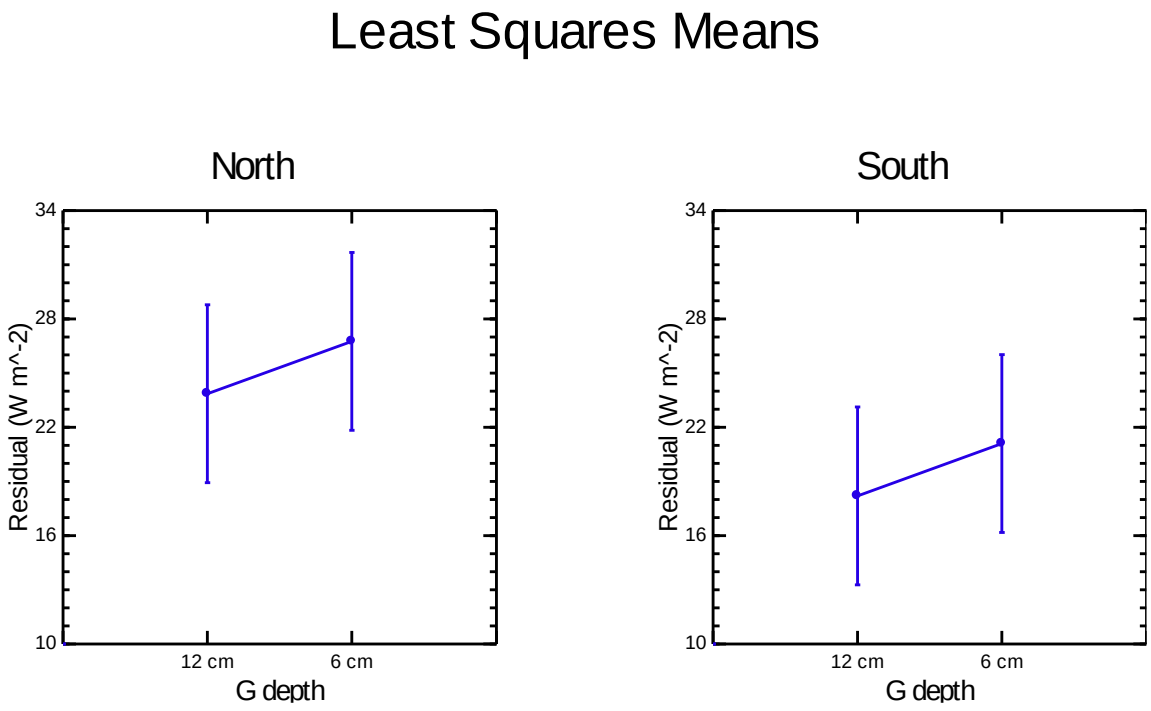

Figure 4-2. Comparison of how EBCE at the north and south sites was affected by the use of G estimated from the 6 cm vs the 12-cm HFP. The G is the average from both the north and south sites, while the H and LE in the residual is LAS-adjusted data from the respective sites. Data from June 2011, n = 420.

4.2. Exploration of Temporal Effects on the Behavior of G

This section evaluates the seasonal behavior of G as a component of the EBCE. The relationship between G and EBCE was explored to determine if it was consistent or if it changed temporally. If a consistent bias could be identified in G, then a multiplier could be calculated to improve the EBCE.

4.2.1 Methodology

Regression was used to evaluate the temporal relationship of G in terms of EBCE. The LINEST function in Excel was used to evaluate the relationship between R_n - CS - H_{ECadj} - LE_{ECadj} as the dependent variable and G_{ave} as the independent variables. R_n was the average of the three net radiometers. H_{ECadj} and LE_{ECadj} were the LAS-adjusted turbulent fluxes for each tower. The LAS-adjusted H and LE were used in the regression rather than the original EC H and LE because the original EC data under-estimated H and LE. The amount of under-measurement varied by site and by month. Use of the original EC data for H and LE would have resulted in the regression model accounting for this error in H and LE in the coefficient for G, whereas the use of LAS-adjusted data addressed this issue by using the best estimate of H and LE available. However, it is recognized that using the LAS-adjusted data introduced a dependency into the data because the LAS adjustment used G in R_n - G - CS in limiting the LAS adjustment when there was more than enough H for closure, or when H and LE were decreased if there was negative closure, as explained in section 3.3.3. It is estimated that this was the case in about 30 percent of the time steps eligible for the LAS adjustments in July 2011. G_{ave} was the average G, comprised of the G estimates from the north and south sites (20 independent estimates of G from the heat flux plates at 6 and 12 cm depths). The regression model was run for June, July, August, and September 2011 on a month by month basis using only data from time steps when buoyant EBL conditions existed.

The average daily G was calculated on a 24-hour basis and on a 0900 to 1500 hour basis for the snow-free months of June-September. The ratio G_{24hr}:$G_{9\text{-}15hr}$ was calculated to understand the relationship between the two.

4.2.2 Results

The Island Park data set showed that G was seasonally dependent, meaning that the relationship between EBCE and G changed with time. Table 4-2 shows the regression coefficients for the regression analysis. The relationship between G and EBCE was not consistent from month to month. The coefficient for both the north and south sites first showed a decreasing trend from June to August, then increased in September to near June levels. Since there was not a consistent

relationship between the G and the ECBE, it is not possible to develop a constant multiplier for this parameter. Factors that could contribute to the changing relationship between G and EBCE could include changing solar angle and changing ground cover and litter. More research is needed to better understand how these and other variables may be involved.

Figure 4-3 shows average daily G calculated on a 24-hour basis and on a 900 to 1500 hour basis for the snow-free months of June-September. There was a consistent decreasing trend in average G for the 4 month period. 24-hour G decreased more quickly, as can be seen in the ratio G_{24hr}:$G_{9\text{-}15hr}$. This decrease is likely a function of the same variables noted above, i.e., shorter days and longer nights, lower solar angles, and more ground cover as the season progressed.

Month	Tower	Number of Ob. n	Regression Coefficient for G	R^2
June	North Tower	420	1.46	0.71
	South Tower	420	1.35	0.74
July	North Tower	506	1.24	0.70
	South Tower	506	1.34	0.72
August	North Tower	482	0.99	0.46
	South Tower	482	1.15	0.61
September	North Tower	485	1.30	0.47
	South Tower	485	1.49	0.82

Table 4-2. Regression coefficients exploring the temporal relationship of G with EBCE on a monthly basis. Data from 2011.

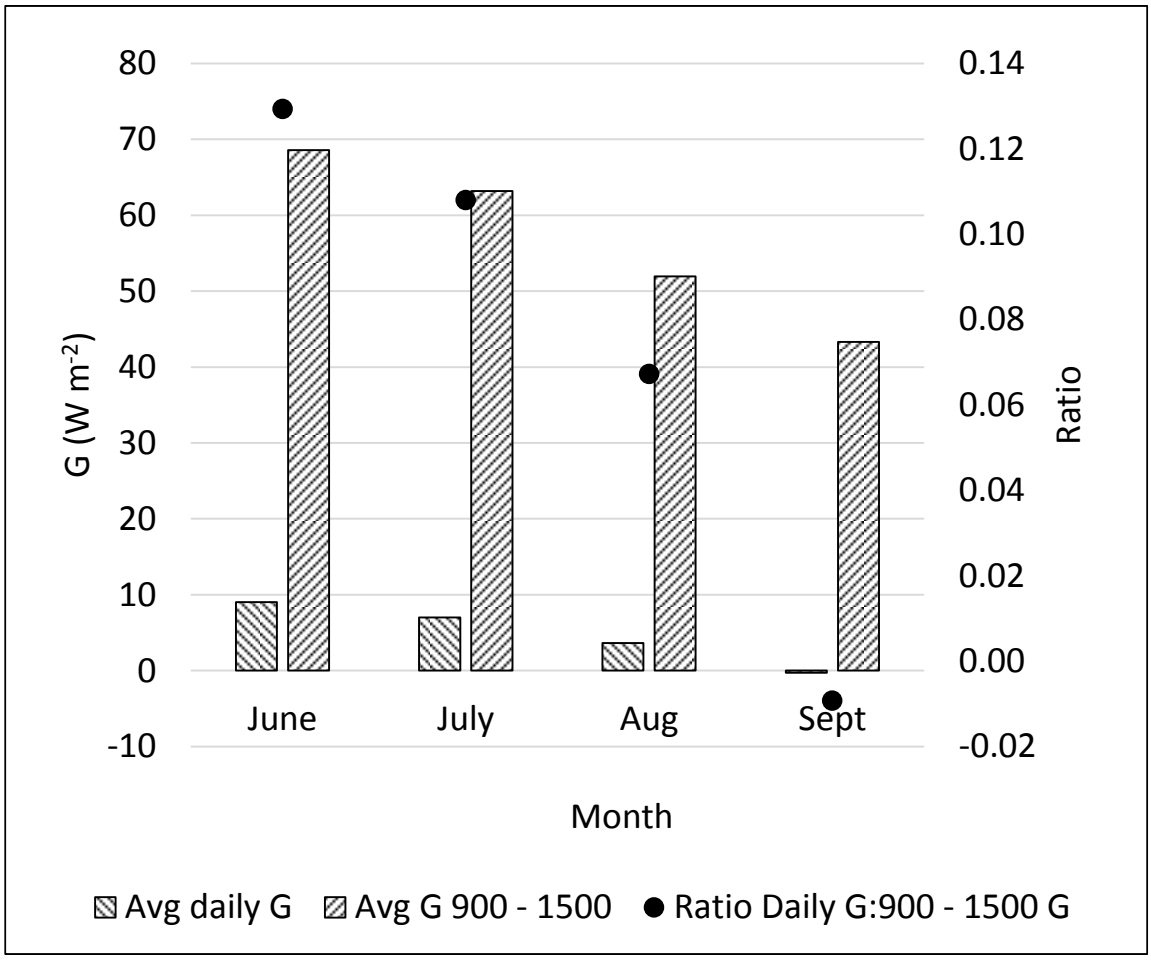

Figure 4-3. Average daily G by month for four snow-free months comparing average G on a 24-hour basis vs average G on the basis of the restricted time frame of hours 0900 to 1500. Data from 2011.

4.3 Assessment of Sensor Location on Soil Heat Flux Estimates

Developing a representative estimate of G for the Island Park study site is difficult because of the heterogeneous nature of the study site and the number of variables that affect energy flux into and out of the soil profile. Heterogeneous conditions exist due to differences in forest canopy, understory, soil surface litter, soil moisture, and sun/shadow exposure. These parameters vary spatially and temporally. Six G subsites were selected at the north and south sites (for a total of 12 subsites)to represent the variety of conditions present at the study site. These sites were placed in small meadows, park-like areas with scattered trees, and in thick stands of trees.

EBCE analyses, as well as extensive literature, showed that there was a tendency to under-estimate the turbulent energy fluxes at the Island Park site. However, under-measurement of G could also contribute to to EBCE. One approach that was explored to reduce the EBCE was the use of different groupings of the soil sites to estimate G. For example, could G estimated from a group of soil

subsites having strong solar exposure be preferred over a group with less solar exposure? A preliminary question was whether different groups of the G sites based on solar exposure were statistically different. Statistical analysis was used to explore whether 1) the soil sites (their estimate of G) were statistically different, and 2) what was the effect of time, through changes in shading and solar angle, on the estimates of G. This analysis used the 2011 Island Park data set to investigate how sensitive the estimate of G is to sensor location and how to best represent the variability in the system in determining an estimate of G, i.e., shade vs. sun, bare ground vs. cover.

4.3.1 Methodology

To explore whether the estimate of G derived from different soil sites was statistically different in terms of their effect on EBCE, five groups of soil sites were created based on their location in the environment and their response to heat transfer as the sun angle and intensity changes throughout the day. These groups are listed in Table 4-3. Group AVE, which is the mean of the 5 groups was also included. ANOVA was used to test if the groupings were statistically the same. Null hypothesis:

$H_o: \bar{\mu}_{GGroup1} = \bar{\mu}_{Ggroup2} = \bar{\mu}_{GGroup3} = \bar{\mu}_{Ggroup4} = \bar{\mu}_{GGroup5} = \bar{\mu}_{GgroupAve}$

The alternative hypothesis was that means were different, indicating that G from at least one of the groups was different. The statistical software SYSTAT was used to conduct the analysis.

The ANOVA used EBCE as the dependent variable and the G groups listed in Table 4-3 as the independent variable. EBCE was calculated as R_n - CS - $H_{ECLASadj}$ - $LE_{ECLASadj}$ - G. R_n was the average R_n from the 3 four-way net radiometers, one at the north tower and two at the south tower. CS was estimated using the IRT on the south tower. The turbulent fluxes H and LE were LAS-adjusted fluxes. G included the groups listed in Table 4-3. Data from 421 time steps from June 2011 were included in the ANOVA, corresponding to time steps with buoyant EBL and LAS data to implement the LAS adjustment for the turbulent fluxes.

G Groups	Soil Flux Site	Site Characteristic	Soil Heat Flux Characteristic
Group 1	S3, S4	Small meadow	Strong daylong solar
Group 2	S6, N6	Patchy trees	AM and PM peaks
Group 3	S5, N5	Patchy trees	Late morning peak
Group 4	S1, S2, N3	Patchy trees	PM peaks
Group 5	N1	Thick stand of trees	Subdued response
Group AVE	Average of all G	-	-

Table 4-3. Grouping used in the ANOVA to explore the effect of G groups on the EBCE.

4.3.2 Results

The ANOVA results are shown in Table 4-4. There was a statistically significant difference between groups as determined by one-way ANOVA ($F(5,7560) = 100.814$, $p = 0.000$). A Tukey post hoc test revealed that there was statistically significant differences between all groups except Group 3 and Group 4 ($p = 0.998$), and between Group 2 and Group AVE ($p = 0.830$), Group 3 and Group AVE ($p = 0.561$), and Group 4 and Group AVE ($p = 0.289$) (Table 4-5). Figure 4-4 provides a graphical interpretation of the ANOVA.

EBCE could be decreased by –25 - 45 W m^{-2} relative to the other groups in Figure 4-4 for the north site and south sites. However, Group 1 was not representative of the heterogeneity of the study site. Group 1 was also too strong and would result in negative EBCE. Groups 2, 3, and 4 were similar in terms of their effects on EBCE. Given these results and considerations, it is most supportable to develop an average G using some weighted average of all of the valid soil subsites because this value is most likely to reflect the actual G of the site.

Source	Type III SS	Df	Mean Squares	F-ratio	p-value
G Groups	1,660,661	5	332,13	100.814	0.000
Sites	58,598	2	29,299	8.893	0.000
G Groups*Sites	10,598	10	1,060	0.322	0.976
Error	24,906,374	7,560	3,294		

Table 4-4. ANOVA results exploring whether the G groups are the same. Data from June 2011, n = 420.

G Group (i)	G Group (j)	Difference Between Groups	p-value	95% Confidence Interval	
				Upper	Lower
Group 1	Group 2	-27.6	0.000	-35.9	-19.3
Group 1	Group 3	-35.9	0.000	-44.2	-27.7
Group 1	Group 4	-37.2	0.000	-45.5	-28.9
Group 1	Group 5	-47.5	0.000	-55.8	-39.2
Group 1	Group AVE	-31.1	0.000	-39.4	-22.8
Group 2	Group 3	-8.3	0.047	-6.6	-0.1
Group 2	Group 4	-9.6	0.012	-17.9	-1.3
Group 2	Group 5	-19.9	0.000	-28.2	-11.6
Group 2	Group AVE	-3.5	**0.830**	-11.8	4.8
Group 3	**Group 4**	-1.3	**0.998**	-9.6	7.0
Group 3	Group 5	-11.5	0.001	-19.8	-3.3
Group 3	Group AVE	4.9	**0.561**	-3.5	13.1
Group 4	Group 5	-10.3	0.006	-18.5	-2.0
Group 4	Group AVE	6.1	**0.289**	-2.2	14.4
Group 5	Group AVE	16.4	0.000	8.1	24.6

Table 4-5. Results of a Post Hoc test identifying differences and similarities among G groups. There was no statistically significant difference among groups with their p-value highlighted in bold font at the $\alpha = 0.05$ level. Units are W m^{-2}.

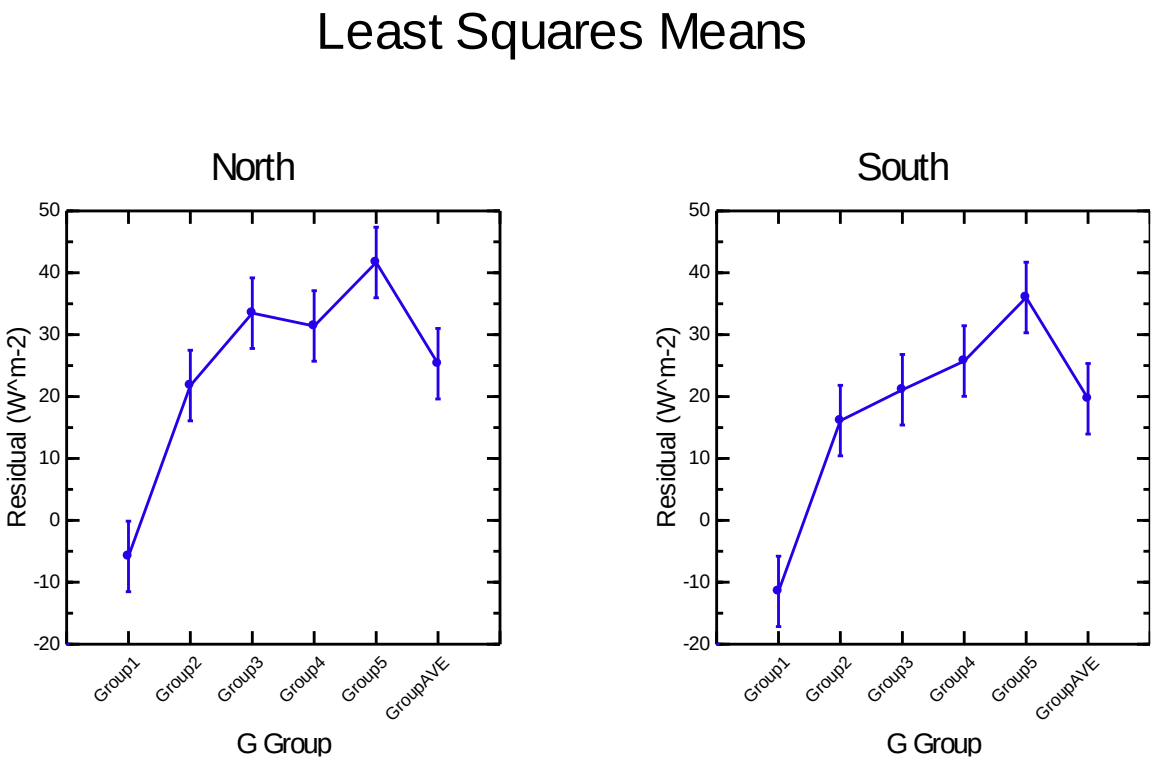

Figure 4-4. Graphical interpretation of the ANOVA of the G Groups. Data from June 2011, n = 420.

The G groups analyzed above are artificial, comprised of the average of several soil subsites with similar environmental settings. These groups were developed to explore whether a specific group, receiving more of less solar exposure than the average of all sites, could improve the EBCE. As a step back to better understand the effect of the local environment on the estimates from the soil subsites, ANOVA was used to explore the similarity between the individual estimates of G from each soil subsite. . Data for the analysis consisted of the G estimates from all time steps in the June 2011 dataset that did not have error flagging.

The results of the ANOVA are shown Table 4-6. The difference between the G estimates on a monthly timeframe from the 12 sites was not statistically significant ($F(11, 17{,}268 = 1.455$, $p = 0.141$)). Figure 4-5 shows a graphical representation of the ANOVA. The conclusion that the differences between the G estimates was not statistically significant is counter-intuitive considering the differences in solar exposure between soil sub sites, which range from all-day sun exposure to all-day shade. These results suggest that on a 24-hour basis the net G converges toward a similar value whether G is measured in a sun-exposed site, a shade site, or a site that has a mix of sun and shade.

Source	Type III SS	df	Mean Squares	F-ratio	p-value
G Sites	42,934.380	11	3,903.125	1.455	0.141
Error	46,329,670.627	17,268	2,682.978		

Table 4-6. ANOVA table for the Island Park G sites. Data from June 2011, n = 1093.

On shorter time intervals, time of day affected the estimate of G. Time of day operates through solar intensity, solar angle, and shading to influence the magnitude of G. As a result of the interaction of these factors, G at a particular subsite can vary substantially relative to itself, and relative to other subsites with different time-dependent solar exposure. To better understand the effect of time on the estimation of G, an ANOVA of G by time of day was completed. To account for the effects of time of day on G, a time code was assigned to each time step. The timecode consisted of the following time categories: 0 - 600 = "A", 600 -1200 = "B", 1200 - 1800 = "C", and 1800 - 2400 = "D". The ANOVA analysis was run using the time codes as groups.

Table 4-7 shows the ANOVA table for the analysis of G by the time code groups. The ANOVA results indicate that there were significant differences between the groups for each time code period. Figure 4-6 shows a graphical interpretation of the results. The graphs also show that the relationship between the various soil subsites is dynamic throughout the day due to changes in solar exposure.

These results demonstrate the importance of solar angle, solar exposure, and ground cover at the soil subsites. Because turbulent flux footprints include a variety of site conditions that affect G, it is important to ensure that the study design includes sufficient robustness in the number and placement of sensors to develop a representative G. On shorter analysis periods, such as the ½ hour time steps, the effect of sensor placement is significant. Over longer time periods, sensor placement is less important because the estimates from the individual sites converge. The use of regression on shorter time steps to select soil sites for use in the EBCE becomes problematic because of the time-dependence of G and the tendency of G from a site to increase or decrease in phase or out of phase with other sites. Regression with half-hourly data, represents the average for the period. As a general guide regarding the number of soil measurement sites required, heterogeneous sites would benefit from the use of more soil sites to estimate G so that all the microsite conditions are represented.

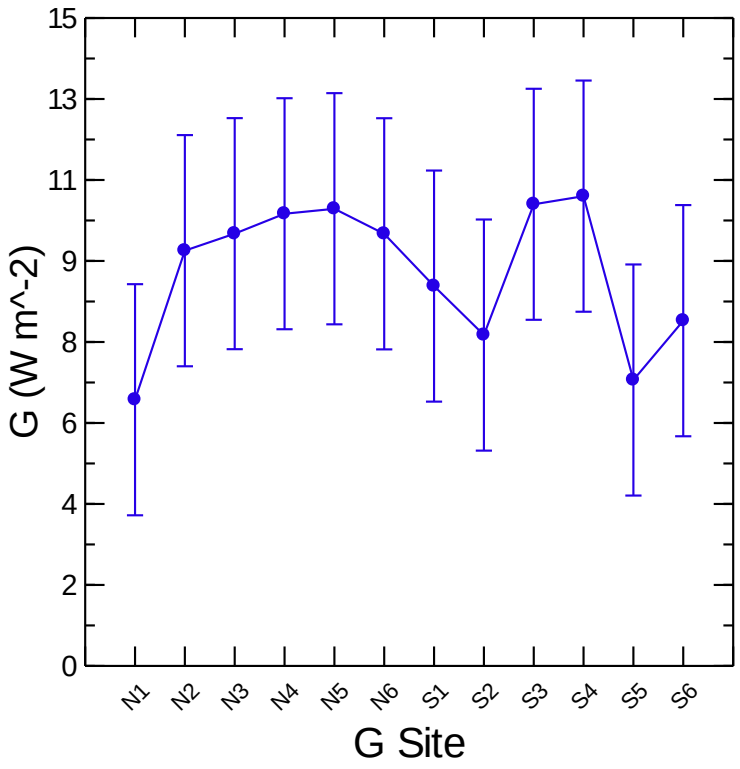

Figure 4-5. Results of ANOVA for the 12 soil subsites. Data from June 2011, n = 1093.

	Type III SS	df	Mean Squares	F-ratio	p-value
G Time Code A	366,433	11	33,312	432.993	0.000
Error	331,434	4,308	76		
G Time Code B	2,477,302	11	225,209	86.192	0.000
Error	11,256,313	4,308	2,612		
G Time Code C	2,477,302	11	225,209	86.192	0.000
Error	11,256,313	4,308	2,612		
G Time Code D	831,439	11	75,585	587.723	0.000
Error	554,040	4,308	128		

Table 4-7. ANOVA table for comparison of similarity of the G from the 12 soil subsites by time code group. Data from June 2011, n = 1093.

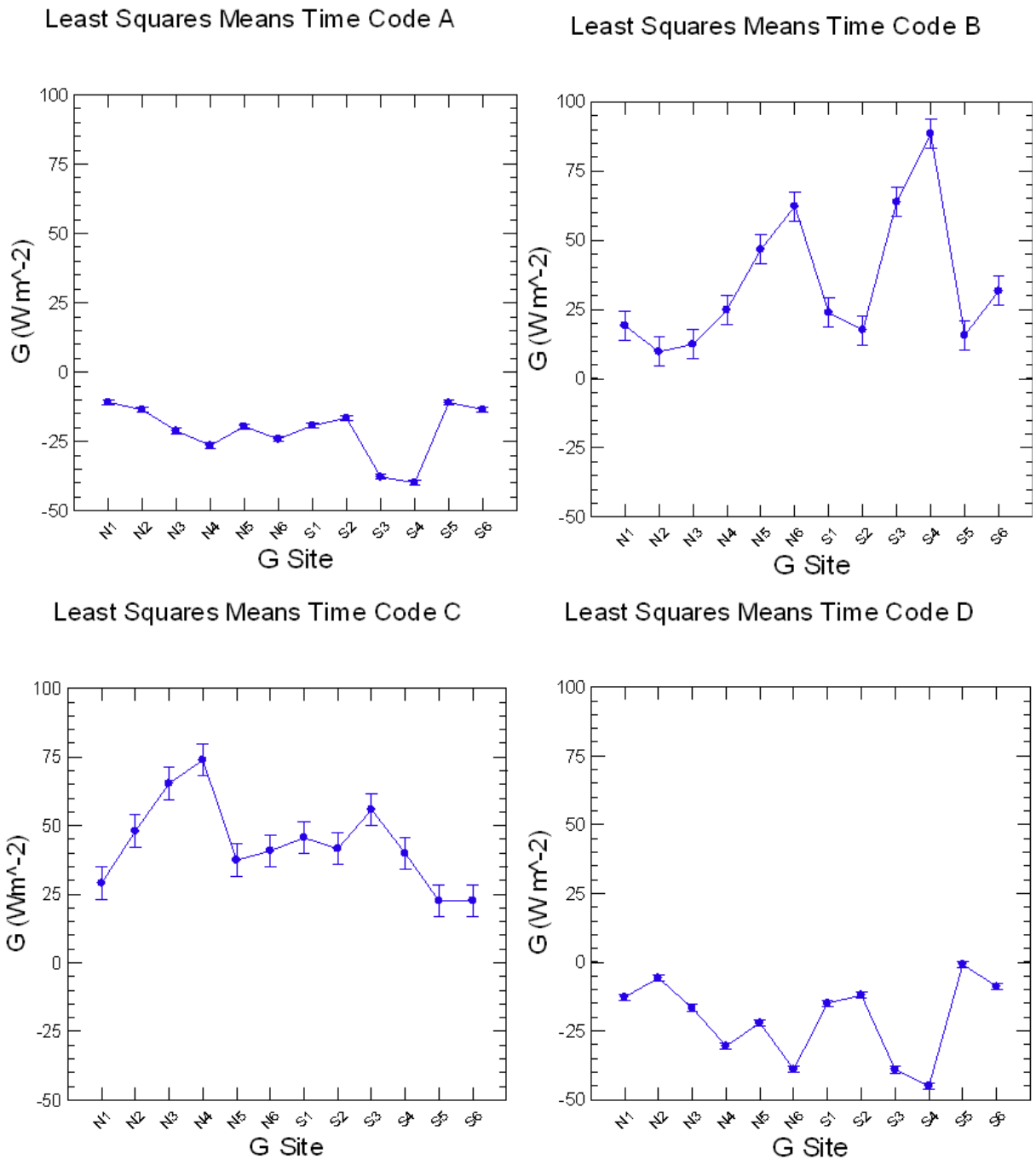

Figure 4-6. ANOVA results for G estimates comparing sites by time code group. Data from July 2011, n = 1093.

Chapter 5 Evaluation of Energy Balance Components and Closure

5.1. Turbulent Fluxes from the North and South Towers: Two Measurements of the Same System or Two Different Systems?

Review of H and LE from the north and south sites showed that they are often not in close agreement, varying by up to 50 to 100 W m^{-2}, and sometimes more. Discrepancies between H and LE between the two sites was not unique to a particular month or season, but agreement was generally better in the summer than in the fall.

Although all of the EB terms may contribute to the EBCE, as noted in section 2.2.5, the turbulent fluxes are often identified as a major component of the closure error. At Island Park, the north and south sites provide two estimates for H and LE. The question is whether these sites are part of the same forest with similar energy fluxes, or are they located in different forests in terms of energy fluxes.

This section explores whether the turbulent flux estimates from the north and south sites represent estimates for the same system, or do they represent essentially different systems due to differences in vegetation, soils, soil moisture content, air flow patterns, etc.? If the north and south sites are measuring the same system, then the turbulent fluxes could be averaged together. If they are separate systems, then the turbulent fluxes should be kept separate.

5.1.1 Methodology

ANOVA was used to explore whether the turbulent fluxes H and LE from the north and south sites are measurements of the same system or if they are different. The null hypothesis was:

H_o: $\bar{\mu}_{H\_ECLASadj\_N} = \bar{\mu}_{HE\_LASadj\_S}$

and

H_o: $\bar{\mu}_{LE\_ECLASadj\_N} = \bar{\mu}_{LE\_LASadj\_S}$

The alternate hypothesis, H_a, would indicate that there was a statistically significant difference between the turbulent fluxes at the north and south sites.

Two ANOVA tests were run using the June 2011 Island Park dataset. The first test used LAS-adjusted H and LE from the north and south sites and was therefore limited to time steps with buoyant EBL. The second ANOVA test used uncorrected H_{EC} and LE_{EC} from the north and south towers. This data set included all time steps that did not have error flagging (nighttime and daytime data). The second

test was included to validate the first ANOVA results that used only the LAS-adjusted data because it is recognized that the LAS adjustment tends to make the data more similar. SYSTAT was used to perform the ANOVA analysis. The ANOVA tests were repeated with the August 2011 dataset to investigate if the same results occurred later in the summer when a drier soil profile was present. Because of differences between the June and August ANOVA results, the ANOVA analysis was also done for the July and September datasets.

5.1.2 Results

The ANOVA results for the June 2011 dataset are shown in Table 5-1. There was no statistically significant difference between $H_{ECLASadj}$ north and south ($p = 0.949$) and $LE_{ECLASadj}$ north and south ($p = 0.287$) using the June 2011 LAS-adjusted data. These results were confirmed with the June 2011 uncorrected H and LE: there was no statistically significant difference between H_{EC} north and south ($p = 0.379$) and LE_{EC} north and south ($p = 0.442$). Figure 5-1, and Figure 5-2, show graphical representations of the ANOVA results. Note that the means for LAS-adjusted data were higher because they included only daytime time steps when the turbulent fluxes were positive.

Source	Type III SS	df	Mean Squares	F-ratio	p-value
Test I: $H_{ECLASadj}$	46	1	46	0.004	0.949
Error	9,609,066	840	11,439		
Test I: $LE_{ECLASadj}$	7,904	1	7,904	1.136	0.287
Error	5,845,487	840	6,958		
Test II: H_{EC} unadjusted	8,168	1	8,168	0.776	0.379
Error	23,019,871	2,186	10,530		
Test II: LE_{EC} unadjusted	4,365	1	4,365	0.591	0.442
Error	16,148,085	2,186	7,387		

Table 5-1. ANOVA table showing the results for testing for statistically significant differences between H north vs H South and LE north and LE south. Test 1 used LAS-adjusted data and Test II used all data for the month that did not have error flagging. June 2011, n = 420.

The ANOVA results for the August 2011 dataset are shown in Table 5-2. The ANOVA shows there was a statistically significant difference between LAS-adjusted H ($F(1, 964) = 19.790$, $p = 0.000$) and $LE_{ECLASadj}$ north and south ($F(1, 964) = 111.548$, $p = 0.000$). These results were confirmed with the uncorrected dataset: there was a statistically significant difference between H_{EC} north and south ($F(1, 2750) = 16.380$, $p = 0.000$) and LE_{EC} north and south ($F(1, 2750) = 16.786$, $p = 0.000$). Figure 5-3 and Figure 5-4 show graphical representations of the ANOVA results.

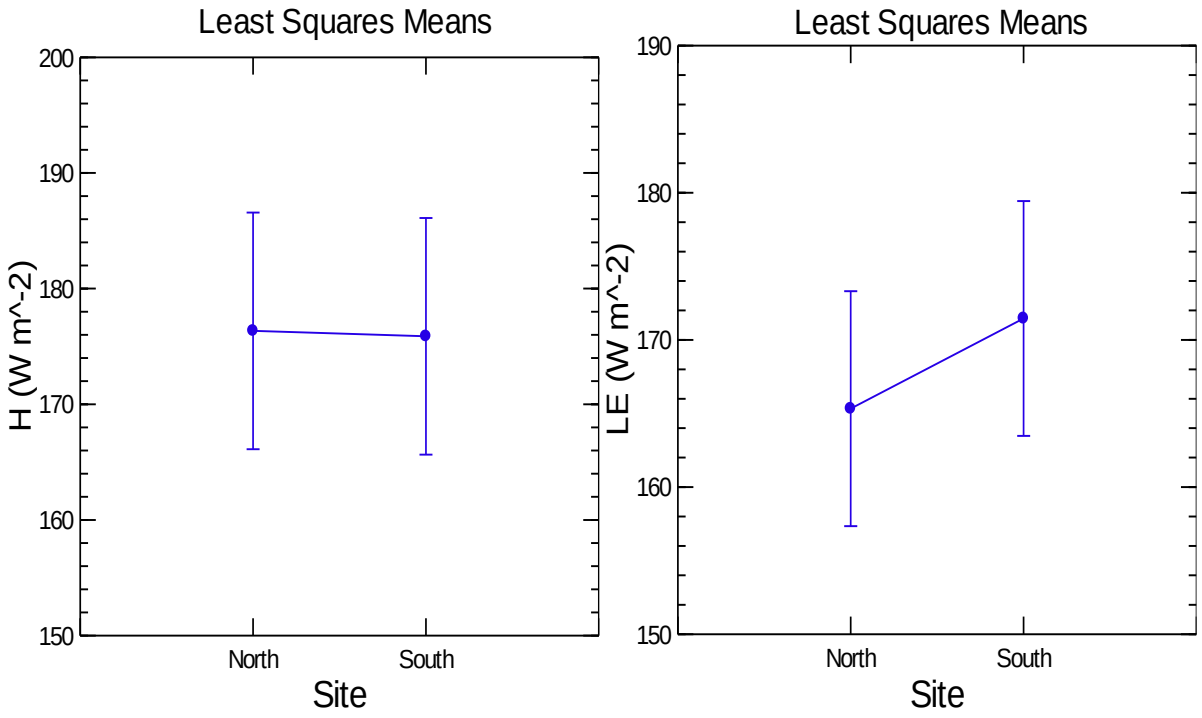

Figure 5-1. Graphical results for ANOVA test for statistically significant differences between LAS-adjusted H (left) and LAS-adjusted LE (right) from the north and south sites. Data from June 2011, n = 420.

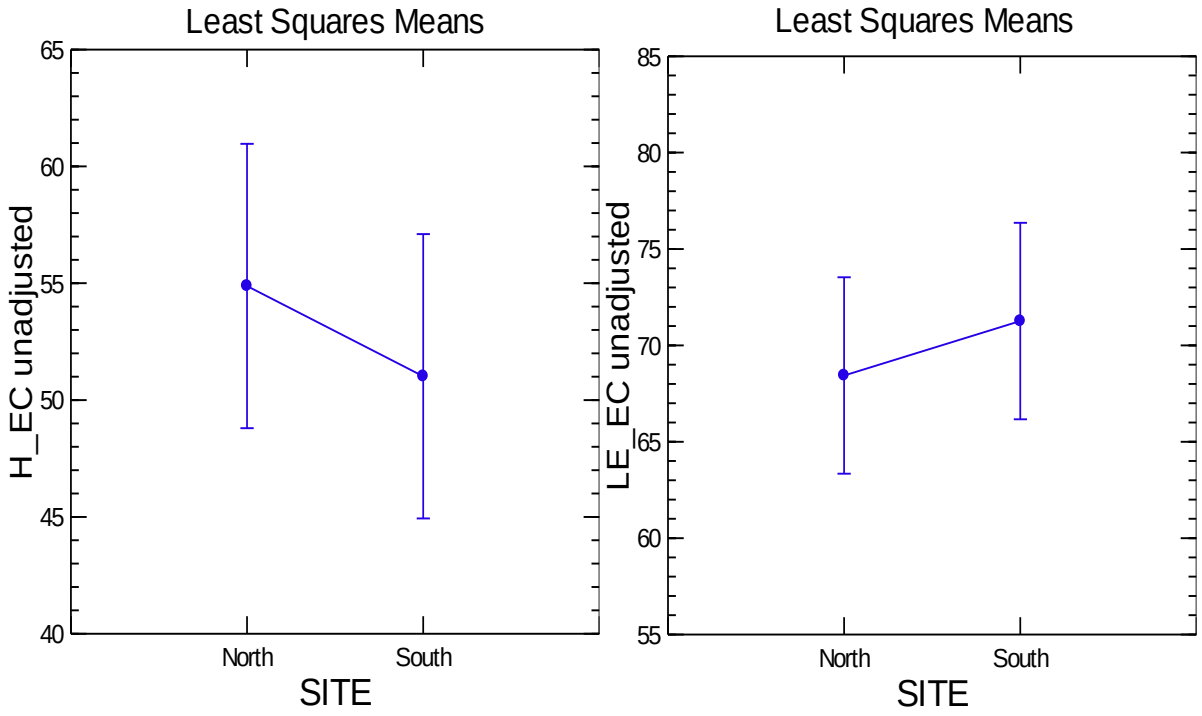

Figure 5-2. Graphical results for ANOVA test for statistically significant difference between original EC H (left) and EC LE (right) for the north and south sites. Data from June 2011, n = 420.

Source	Type III SS	df	Mean Squares	F-ratio	p-value
Test I: $H_{ECLASadj}$	133,965	1	133,965	19.790	0.000
Error	6,525,591	964	6,769		
Test I: $LE_{ECLASadj}$	1,876,439	1	1,876,439	111.543	0.000
Error	16,216,919	964	16,822		
Test II: H_{EC} unadjusted	158,062	1	158,062	16.380	0.000
Error	26,537,466	2,750	9,650		
Test II: LE_{EC} unadjusted	176,775	1	176,775	16.786	0.000
Error	29,961,144	2,750	10,531		

Table 5-2. ANOVA table showing the results for testing for statistically significant differences between H north vs H South and LE north and LE south. Test 1 used LAS-adjusted data and Test II used all data for the month that did not have error flagging. August 2011, n =482.

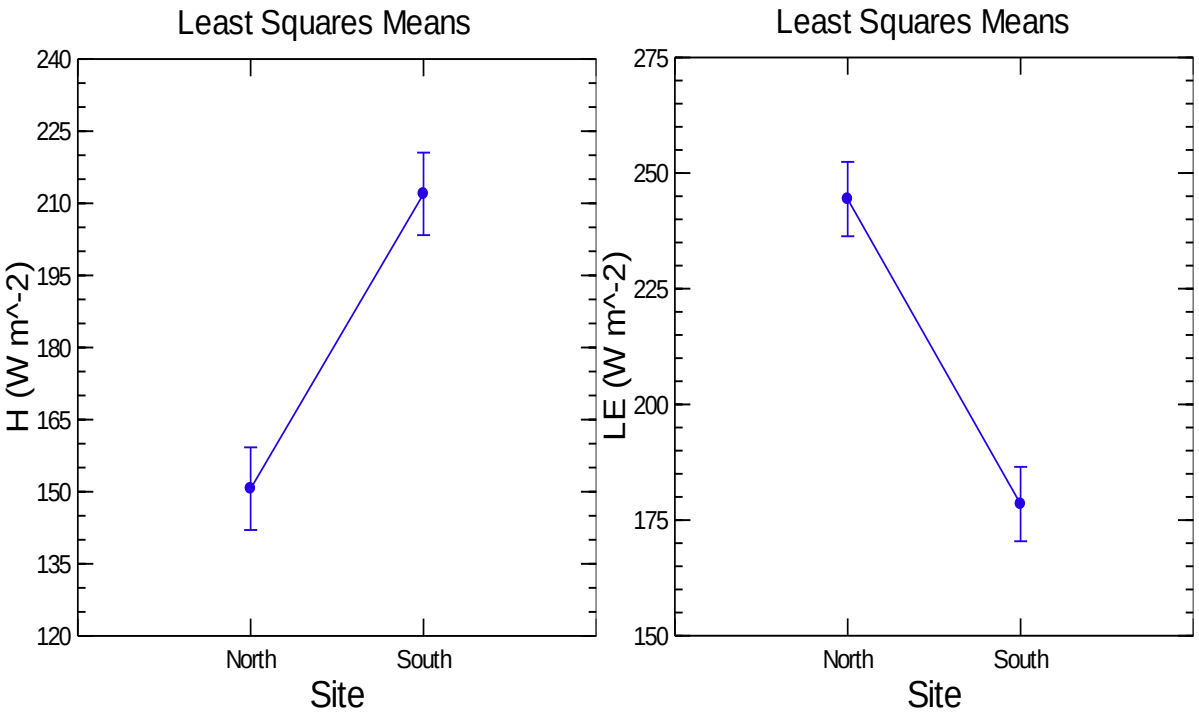

Figure 5-3. Graphical results for ANOVA test for statistically significant difference between LAS-adjusted H (left) and LAS-adjusted LE (right) from the north and south sites. Data from August 2011, n = 482.

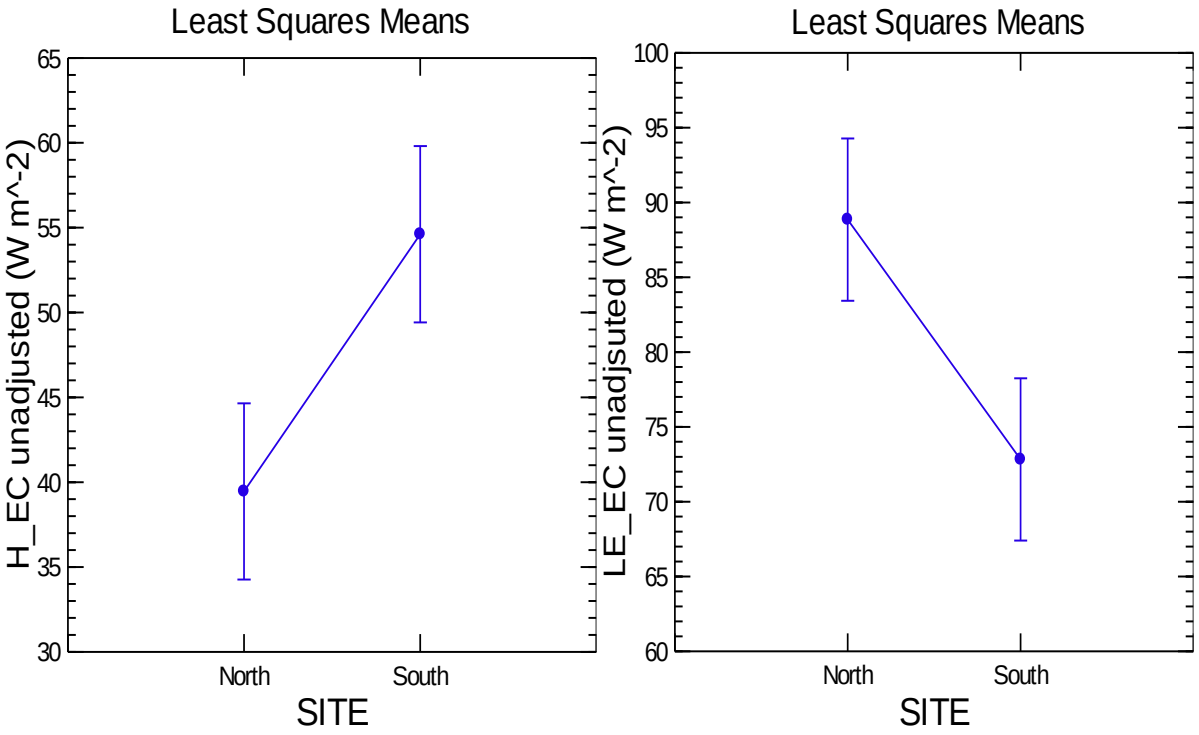

Figure 5-4. Graphical results for ANOVA test for statistically significant difference between original EC H (left) and original EC LE (right) for the north and south sites. Data from August 2011, n = 482.

The ANOVA results for the August 2011 dataset were in contrast with June 2011 dataset. Specifically, the differences between H from the north and south sites and LE from the north and south sites were not statistically significant for the June dataset, but the differences were statistically significant in August 2011. Regression plots of LAS-adjusted H north and south and LE north and south were prepared for the June and August 2011 datasets to better understand the relationship between the turbulent fluxes from the north and south sites (Figure 5-5, Figure 5-6, Figure 5-7, Figure 5-8). Each figure in this series of graphs shows two regression models, one using LAS-adjusted data and the other using original EC data for comparison. The effect of the LAS adjustment on the slope of the regression line and the R^2 value is evident compared to the regression with the original EC data. The regression using the data from August illustrates that H was higher at the south site, while LE was lower, relative to the north site. As discussed below, lower VWC at the south site likely reduced LE and caused a corresponding increase in the energy portioned into H. The regression models used H or LE from the north site as the independent variable while H or LE from the south site was the dependent variable. The regression plots for the June data had a regression slope coefficient near 1 and a high R^2 value. However, the regression plots for the August had a regression slope coefficient that diverged from 1 and a lower R^2, particular in the case of LE. The ANOVA results indicated the

difference between H and LE for the north and south sites was not statistically significant in June, but the difference between the north and south sites was statistically significant in August. The statistically significant difference in the August data set confirms the delinked fluxes in August. This may be due to differences in soil characteristics during drying conditions. The delinking is reflected in the August regression plots.

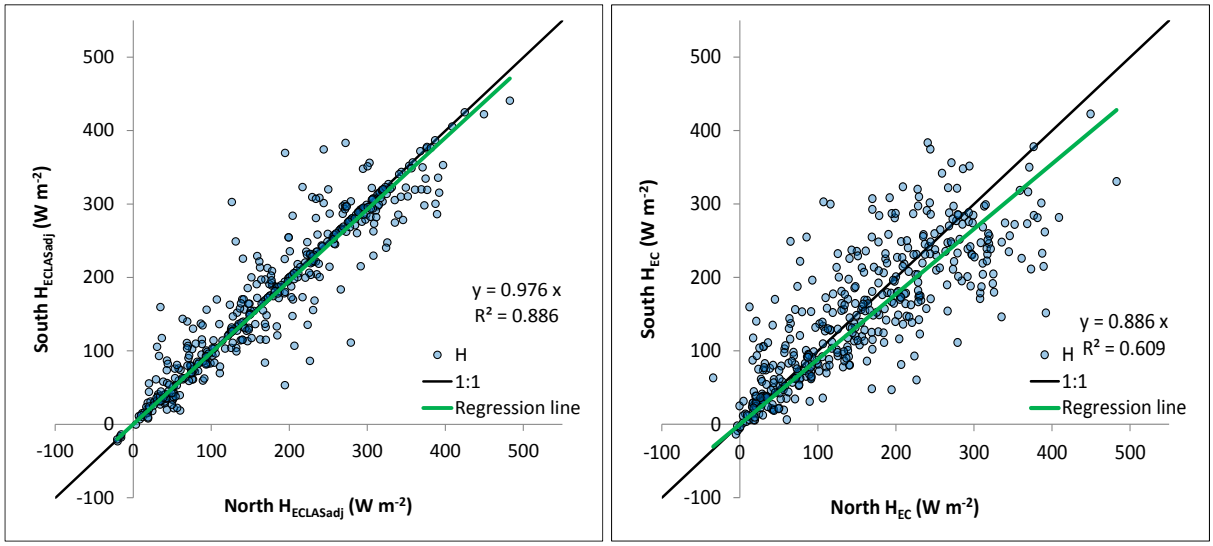

Figure 5-5. Regression plot of H north vs H south. The graph on the left uses LAS adjusted data, while the graph on the right uses original EC data. June 2011, n = 420.

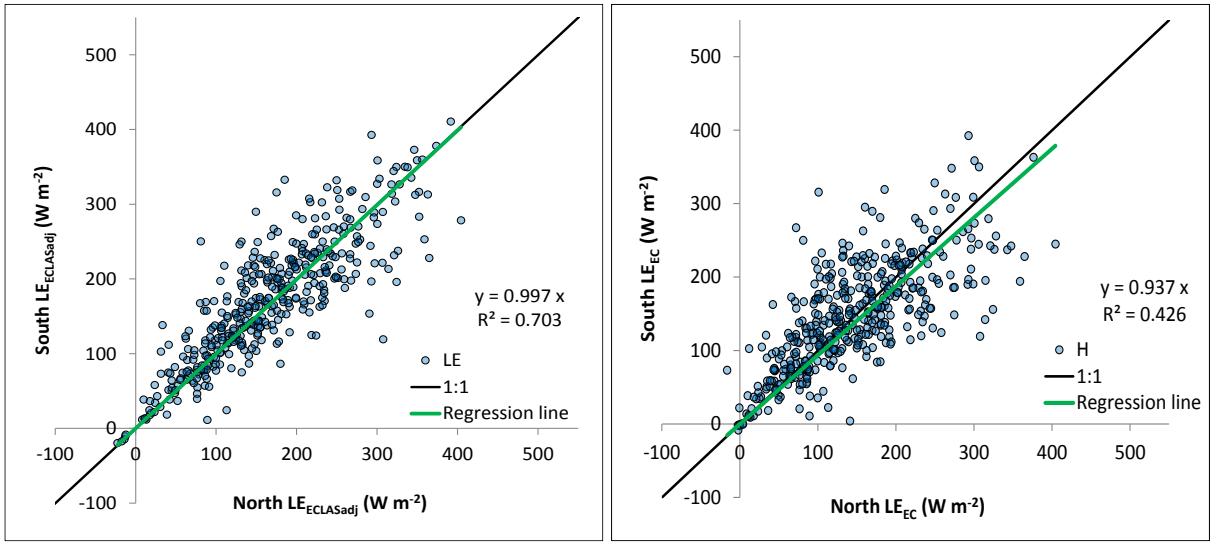

Figure 5-6. Regression plot of LE north vs LE south. The graph on the left uses LAS-adjusted data, while the graph on the right uses original EC data. June 2011, n = 420.

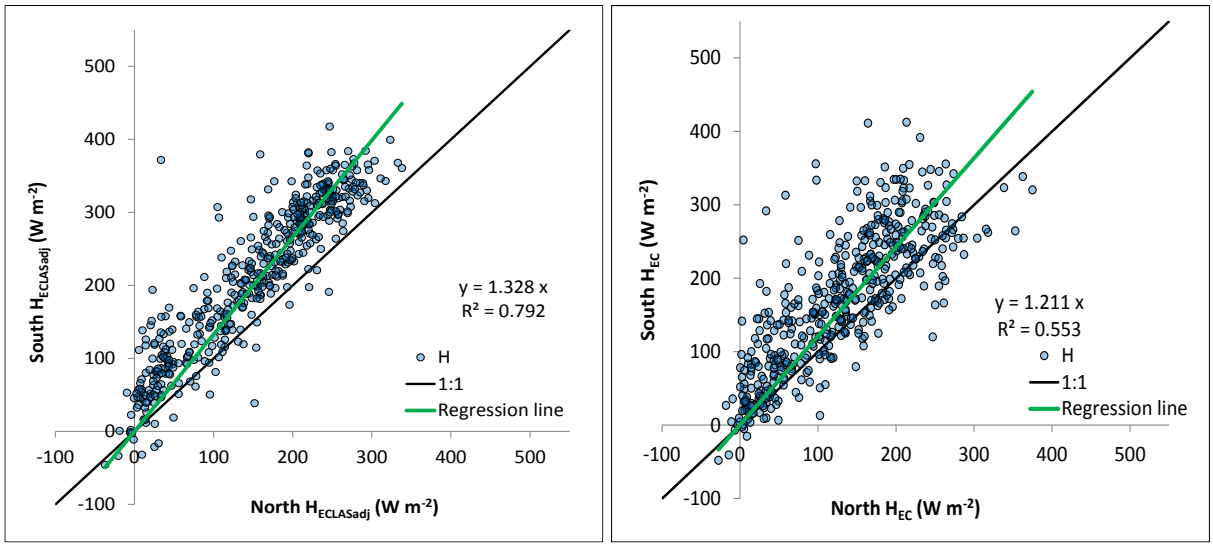

Figure 5-7. Regression plot of H north vs H south. The graph on the left uses LAS adjusted data, while the graph on the right uses original EC data. August 2011, n = 482.

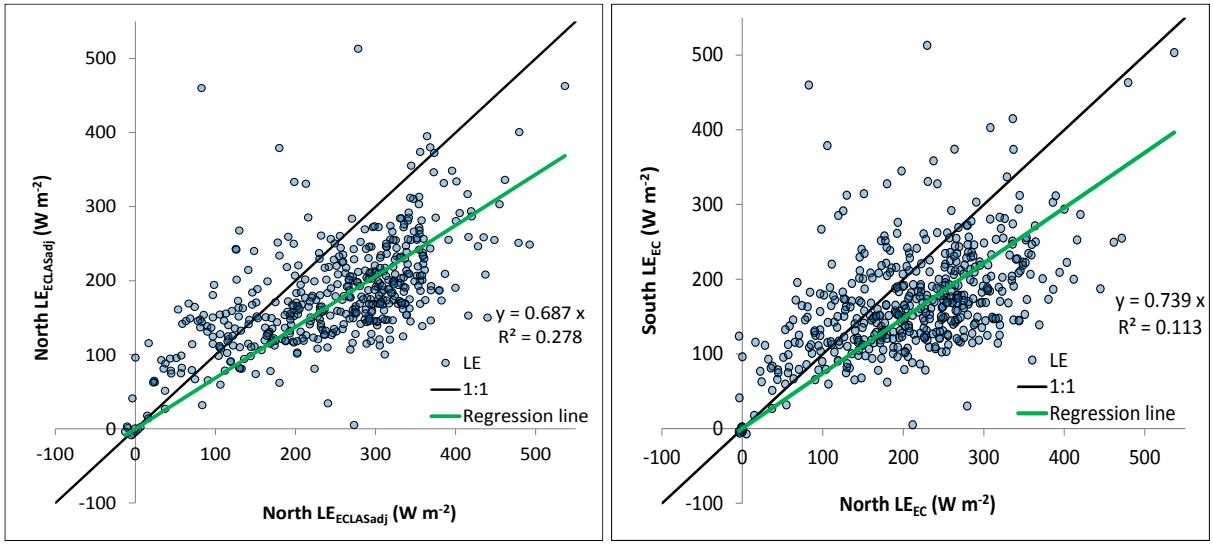

Figure 5-8. Regression plot of LE north vs LE south. The graph on the left uses LAS-adjusted data, while the graph on the right uses original EC data. August 2011, n = 482.

The timeframe when the delinking of the north and south turbulent fluxes occurs was the next question. Was July more like June or more like August, and was the September data more like August, or did it revert back to June-like behavior? The ANOVA results for July and September data are shown in Table 5-3. Figure 5-9 and Figure 5-10 show a graphical representation of the ANOVA. The ANOVA showed that for the July 2011 data set there was a not a statistically significant difference between LAS-adjusted north and south H ($p = 0.653$) and LAS-adjusted north and south LE ($p = 0.115$). However, for the September 2011 dataset, the ANOVA showed that there were

statistically significant differences between LAS-adjusted H north and south H (F(1, 938) = 54.181, p = 0.000) and LAS-adjusted H north and south LE (F(1, 938) = 214.327, p = 0.000).

Source	Type III SS	df	Mean Squares	F-ratio	p-value
JULY $H_{ECLASadj}$	437,136	1	437,136	39.723	0.000
Error	10,674,543	970	11,005		
JULY $LE_{ECLASadj}$	411,731	1	411,731	134.339	0.000
Error	2,972,917	970	3,065		
SEPT $H_{ECLASadj}$	623,385	1	623,385	54.181	0.000
Error	10,792,169	938	11,506		
SEPT $LE_{ECLASadj}$	754,156	1	754,156	214.327	0.000
Error	3,300558	938	3,519		

Table 5-3. ANOVA table showing the results for testing for statistically significant differences between for H north vs H South and LE north and LE south for the August 2011, n = 482, and September 2011, n = 485, datasets. H and LE were LAS adjusted data.

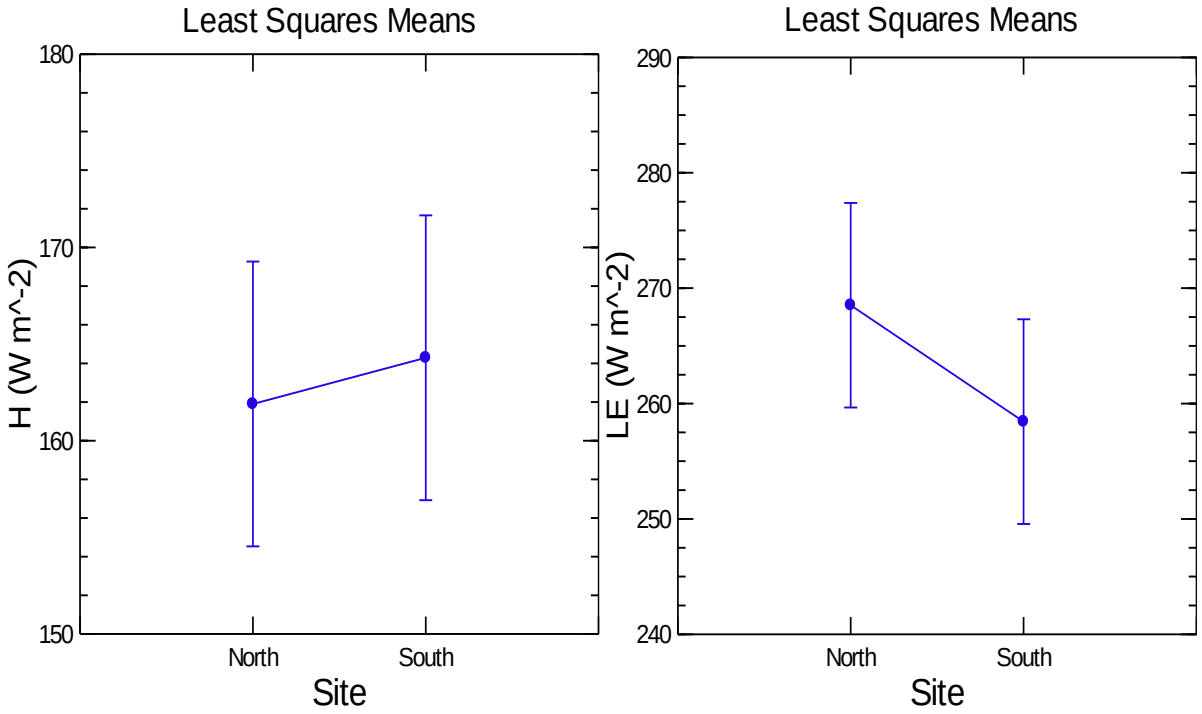

Figure 5-9. ANOVA for H north vs H south (left) and LE north vs LE South (right) using LAS-adjusted data. Data from July 2011, n = 506.

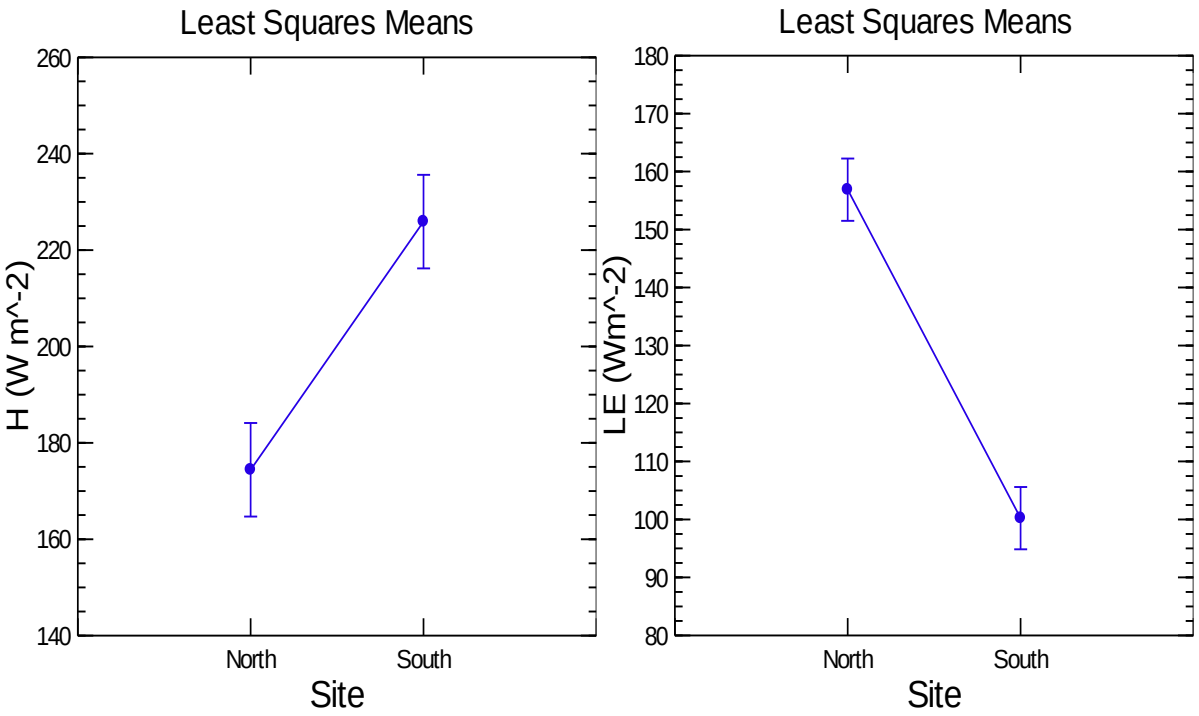

Figure 5-10. ANOVA for H north vs H south (left) and LE north vs LE south (right), using LAS-adjusted data. Data from Sept 2011, n = 485.

Several trends in the behavior of H and LE were apparent in the analysis, as illustrated in Figure 5-11. LAS-adjusted H was almost equal beginning in June between the north and south sites, but in subsequent months July, August and September, H at the south site was larger than at the north site. This difference was statistically significant in August and September. Through the July, August and September time frame, H increased each month and was highest in September. This was likely a function of a drying soil profile limiting the ET process.

LAS-adjusted LE showed the opposite trend. Beginning in June, LE was slightly larger at the south site, but this difference was not statistically significant. The relationship was reversed in July, August, and September, with LE becoming larger at the north site. The differences between the north and south site became statistically significant in August and September. In contrast to H, LE peaked in July, and then decreased in August and September. This pattern is thought to be a function of drying soil profiles resulting in less moisture available for the ET process, as well as shorter daytime periods when the plants were actively transpiring, and lower R_n values to drive the process.

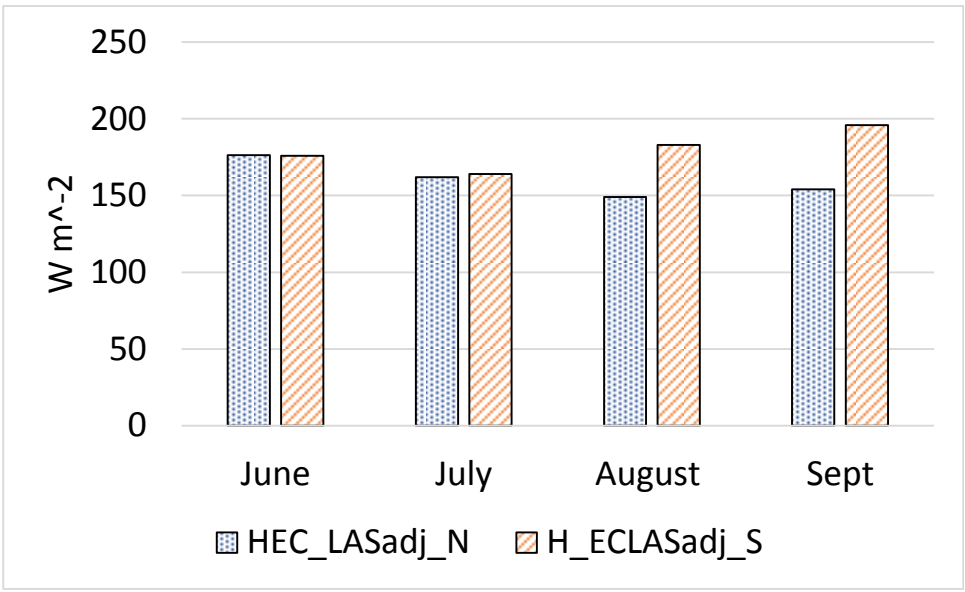

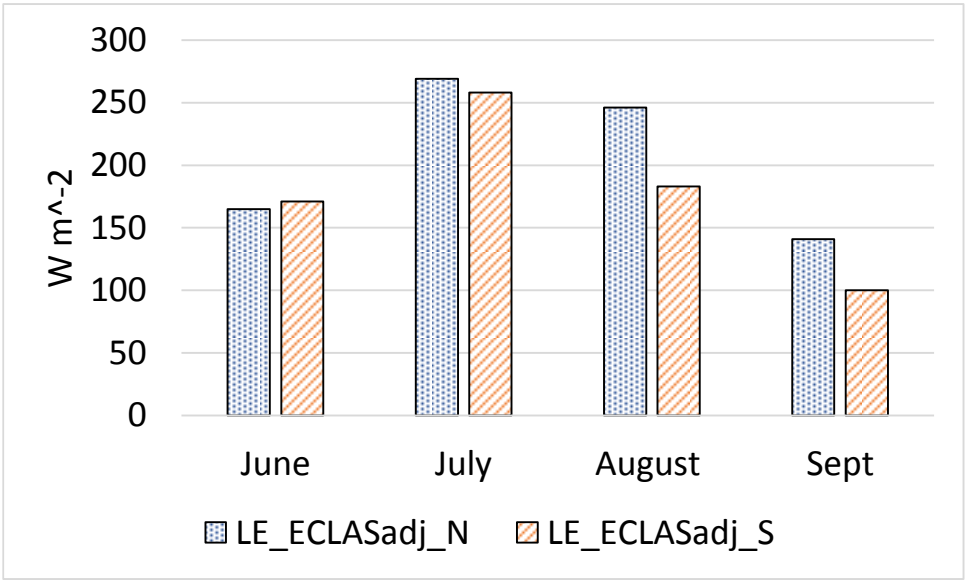

Figure 5-11. Comparison of monthly average (least square means) LE between the north (top) and south (bottom) sites for four months in 2011. All data include in the charts has been adjusted by the LAS adjustment.

Figure 5-12 shows the relationship between cumulative precipitation from rain gages in the Island Park area, LE from the north and south sites based on the original EC measurement (which is likely underestimated by 10 to 20 percent), expressed as mm of precipitation, and ET_r calculated from data from the Ashton AGRIMET station for 2011. Note that the ET is based on uncorrected LE flux estimates for the entire period. Thus it likely underestimates actual ET by 10 - 20 percent. Although the rain gages showed different amounts of precipitation due to local siting conditions, all showed similar trends in terms of when precipitation events occurred. The Island Park north tower rain gage

at 3 m height recorded less precipitation than the Island Park south tower rain gage at 22 m height. The difference in precipitation between the two island park rain gages could be due to siting conditions. The north tower rain gage was located on the ground in a small clearing near the north tower, where trees could have sheltered it and resulted in under-measurement of precipitation (it was moved to a larger clearing in the fall of 2014). However, even though the rain gages were only 1.7 km apart, the differences in precipitation could be real and a result of local weather patterns. However, the large differences shown are unlikely.

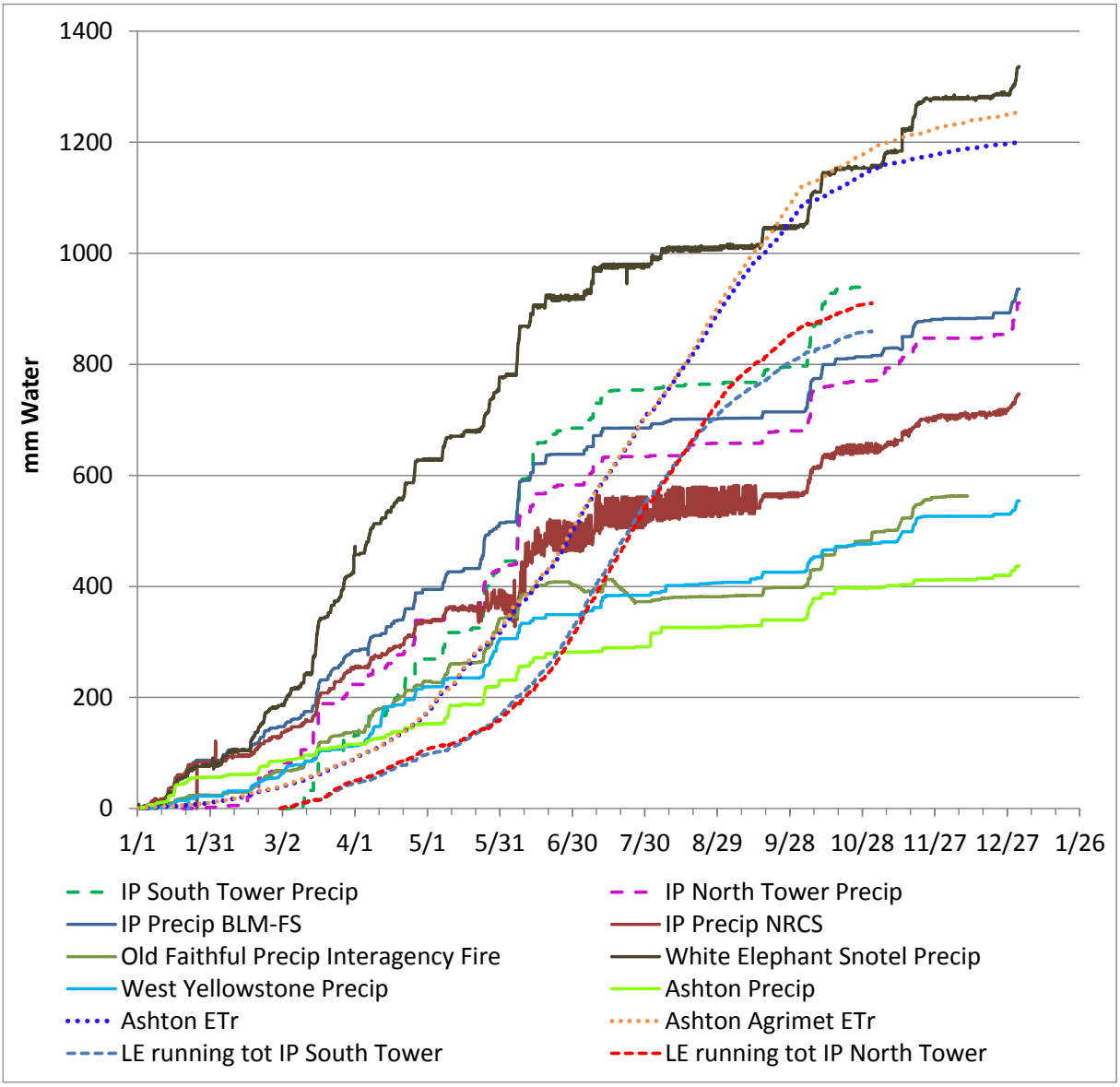

Figure 5-12. Cumulative analysis of precipitation from rain gauges in the Island Park area, LE from the Island Park north and south sites based on original EC data, and ET_r calculated from data from the Ashton AgriMet station.

A salient point for the cumulative ET and precipitation in Figure 5-12 is that the LE line from the Island Park north site crossed the Island Park south rain gage line on August 26. The LE line from the Island Park south site approached the south tower rain gage line a few days later on September 7. However additional precipitation received in that timeframe prevented the south tower LE from actually exceeding the precipitation until September 27, and then only for a 9-day period. Early October storms increased cumulative precipitation above LE for both sites. The August timeframe when cumulative LE was approaching cumulative precipitation was correlated with the trend of reduced LE in August and September, illustrated in Figure 5-11. Given that the graph shows under-estimated ET from unadjusted EC data, the timeframe when ET crossed the precipitation lines likely happened earlier. This discussion of timeframes is in the context of ET based on the original LE data from the EC systems. As a result, the timeframes noted above would shift to earlier dates due to the estimated 10 – 20 percent under-measurement of the LE by the EC system.

Figure 5-13 shows the average soil VWC for the north and south sites and precipitation measured by the rain gages at the north and south sites. The average soil VWC was based on 9 sensors at the north site and 15 sensors at the south site ranging in depth from a near the surface to approximately ½ meter in depth. Thus the north and south soil VWC lines in Figure 5-13 represent an average soil VWC for the upper ½ meter of soil profile that may supply most of the water consumed by transpiration. All sensors included in the average were reviewed to ensure they were performing well.

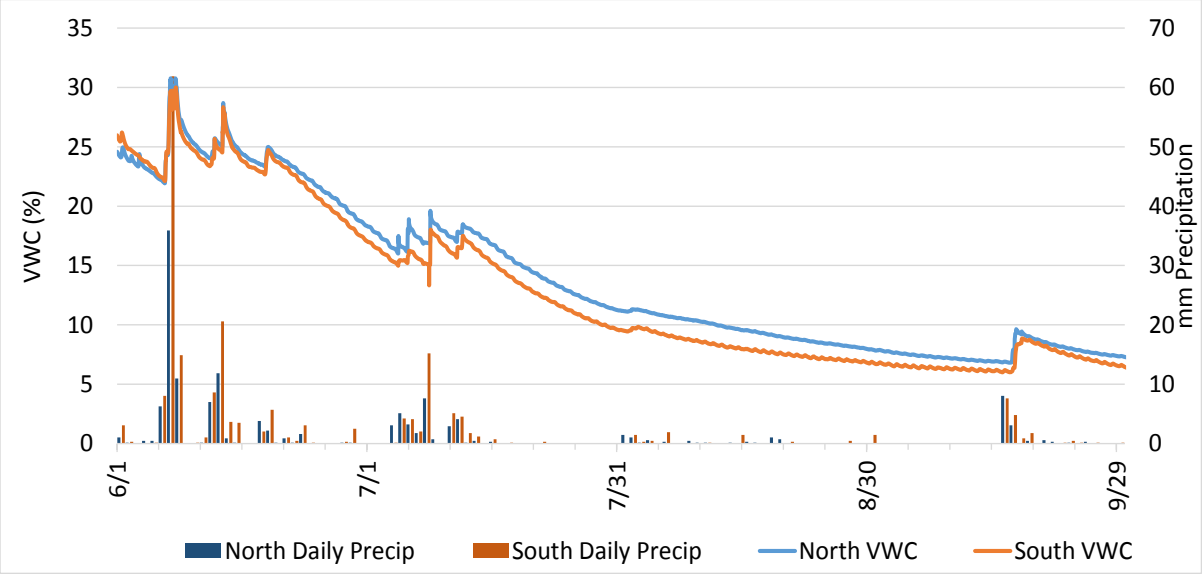

Figure 5-13. Graph of soil VWC and precipitation records for Island Park north and south sites for June, July, August, and September 2011.

The behavior of the soil VWC lines in Figure 5-13 indicate a drying soil profile as time progressed from snowmelt-out (mid to late May), through summer and early fall. Significant precipitation events were registered in the VWC lines as increases in the soil VWC. Initially the slope of the VWC line was relatively steep as the soil profile dried quickly in early summer. The slope became flatter in late July as the soil profile continued to dry more slowly and some abstraction of water may have occurred from below the sensors. The late July timeframe when the slope became less steep corresponded to the time periods when the turbulent fluxes at the north and south sites became delinked.

Figure 5-14 shows that after late June, the soil VWC at the north site was slightly higher than the soil VWC at the south site. This was in contrast to the higher LE at the north site which should dry the soil profile more quickly and result in a lower soil VWC. Alternatively, the north site may have been able to sustain higher LE throughout August and September due to a higher water storage capacity in the soil due to soil structure differences. Detailed soil data were not available to assess if soil porosity may have been a factor in the higher LE at the north tower. Precipitation at the north and south sites was fairly even through the summer.

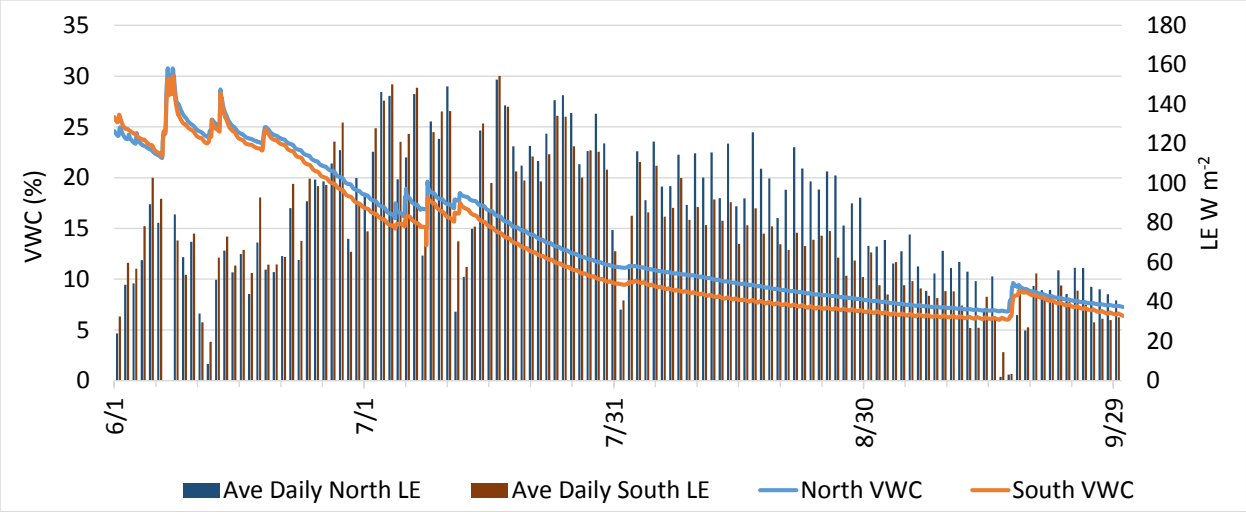

Figure 5-14. Graph of VWC and LE for the Island Park north and south sites for June, July, August, and September 2011.

Figure 5-14 suggests that soil VWC could be a factor affecting the relationship between LE and H at the north and south sites. Figure 5-15 shows a conceptual graph of the relationship between soil water tension and soil VWC. As soil VWC decreases, the water tension in the soil increases exponentially. Small changes in the soil VWC can result in large differences in the readily available water (RAW) for transpiration. The relatively small difference in soil VWC between the north and south sites seen in Figure 5-14 could be responsible for the differential in LE through the soil VWC-

soil water tension relationship. An ANCOVA (Analysis of Covariance- an ANOVA-type analysis which allows multiple continuous variables) model was run to test whether there was a statistically significant link between LE and soil VWC. These results are summarized in Table 5-4. Based on the ANCOVA results, the covariate, soil VWC, was not significantly related to LE in July ($p = 0.414$). However, the soil VWC was statistically significantly related to LE in June ($F(1, 839) = 205.109$, $p = 0.000$), August ($F(1, 963) = 9.273$, $p = 0.002$), and September ($F(1, 969) = 9.130$, $p = 0.003$).

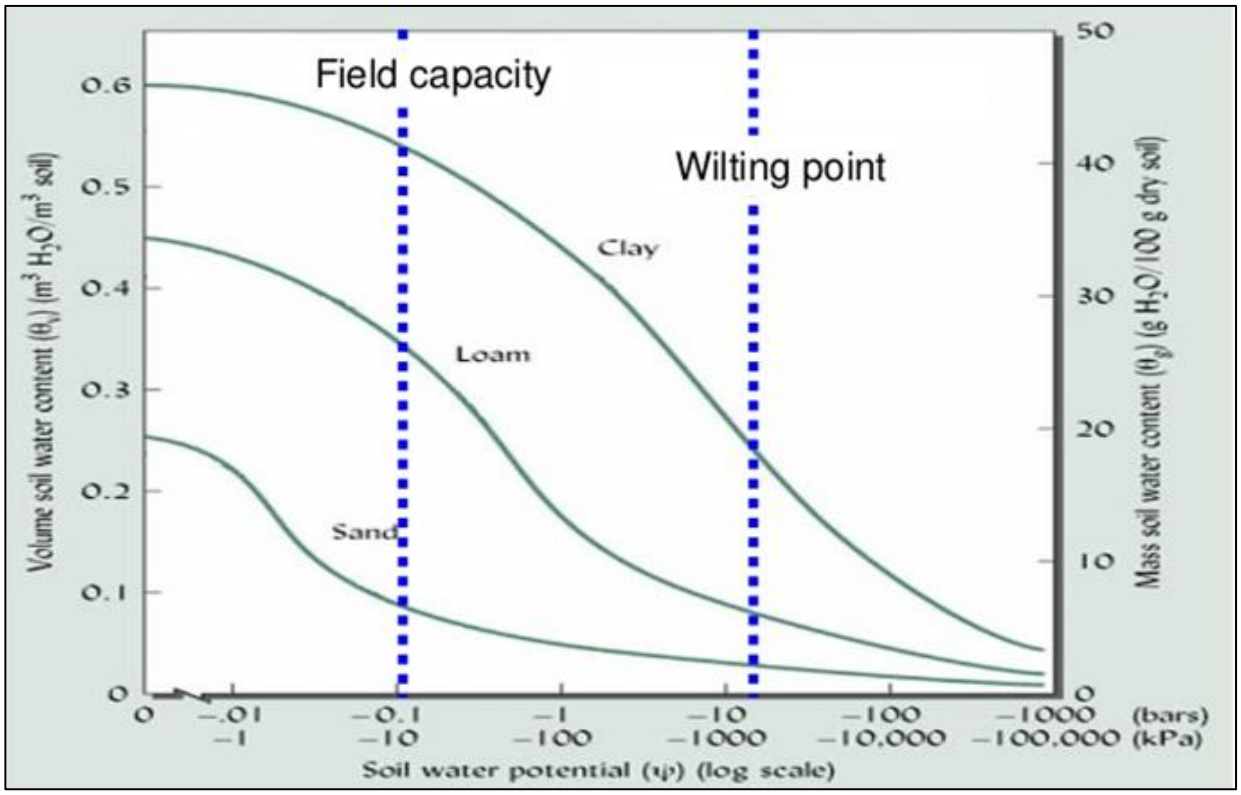

Figure 5-15. Graph showing soil water tension as a function of VWC. Source: Brady and Weil, 2002 (http://www.slideshare.net/jbgruver/understanding-soil-water)

The apparent ability of the soils at the north site to support higher LE throughout the period of analysis while at the same time maintaining a higher VWC would suggest that the soil at the north site must constitute a larger "reservoir" from which to sustain the LE. This could be due to a deeper soil profile and/or a soil texture class with a higher water holding capacity. The Web Soil Survey (http://websoilsurvey.sc.egov.usda.gov/App/WebSoilSurvey.aspx) was consulted to determine which soils occurred in the Island Park research area. It showed the area where both the north and south sites are located were mapped as a soil complex (1700—ABLA/VASC, CARU Koffgo, 4 to 15 percent slopes) with a typical profile described as:

- Oi - 0 to 1 inches: slightly decomposed plant material
- A - 1 to 5 inches: ashy silt loam
- Bw - 5 to 19 inches: gravelly silt loam
- BC - 19 to 51 inches: extremely cobbly sandy loam
- C - 51 to 60 inches: cobbles

	Source	Type III SS	df	Mean Squares	F-ratio	p-value
June	Site	1,668	1	1,668	0.298	0.585
	VWC	1,148,310	1	1,148,310	205.109	0.000
	Error	4,697,177	839	5,599		
July	Site	1,6396	1	16,396	1.583	0.209
	VWC	6,928	1	6,928	0.669	0.414
	Error	10,470,877	1011	10,357		
August	Site	355,504	1	355,504	**49.053**	**0.000**
	VWC	67,202	1	67,202	**9.273**	**0.002**
	Error	6,979,148	963	7,247		
Sept	Site	190,737	1	190,737	**62.755**	**0.000**
	VWC	27,750	1	27,750	**9.130**	**0.003**
	Error	2,945,167	969	3,039		

Table 5-4. ANCOVA table showing the results of a series of analysis testing the significance of VWC as a variable in the difference in LE between the north and south sites. LE was the dependent variable, site was the independent variable, and VWC was the covariant. Data from 2011; June n = 420, July n = 506, August n = 482, September n = 485.

While the soil complex provides a general indication of the soil at the north and south sites, it is not specific enough to determine whether there are difference in the soil type at the sites that could account for the increased available water at the north site. Photos taken of the exaction of the holes for the power poles are consistent with a cobbly sandy loam soil type (Figure 5-16 and Figure 5-17).

Summary

The analysis in this section found that there was a statistically significant difference between the turbulent fluxes at the north and south towers in August and September, but not in June and July for the 2011 dataset. Soil VWC was investigated as a possible factor for the delinking of the fluxes from the north and south sites. ANCOVA indicated that soil VWC is significantly correlated with LE in June, August, and September. A graphical analysis of soil VWC, precipitation, and LE support the ANCOVA results that there was a significant relationship between soil VWC and LE between the north and south sites, possibly through the soil VWC-soil water tension function. Additional analysis with data from other years is needed to determine if the delinking of the turbulent fluxes between the north and south towers occurs each year.

Figure 5-16. Photo taking during the excavation of the holes for the power poles that support the Island Park south site observation tower showing the soil texture. Note the presence of rocks in the soil profile.

Figure 5-17. Photo taken during the excavation of the holes for the power poles that support the Island Park north site observation tower. Note the presence of large cobbles.

5.2. Exploration of Wind Behavior Patterns and their effect on Turbulent Fluxes and EBCE

The Island Park north and south sites are approximately 1.7 km apart. One question is whether these sites experience similar wind behavior in terms of wind direction, wind speed, and time-of-day, and how these variables might relate to differences in LE and EBCE behavior at the two sites. Particularly of interest is if these variables may play in the delinking of the turbulent fluxes at the north and south sites. Wind behavior may affect turbulent fluxes and EBCE, and if differential wind behavior was present at the north and south sites, these patterns may have been involved in the delinking of the turbulent fluxes, as described in Section 4.2. This section explores these questions.

A preliminary visual analysis of wind behavior and EB closure ratio indicated that generally the EB closure ratio approached 1.0 as the afternoon winds shifted to the southwest and wind velocity increased. This wind pattern was correlated with improving EB closure as wind speeds increased in the afternoon. Figure 5-18 and Figure 5-19 present a graphical analysis of the relationship of EB closure ratio, H, and LE to wind speed and direction. EBCE appeared to be more variable on days with a variable wind, on days with less wind, and on days with non-typical wind patterns. Night-time wind patterns were usually from the east and velocities were typically less than in the day. Night-time EB closure ratio generally decreased to less than 50 percent and experienced spikes. At night, when equilibrium boundary layer conditions tended to be stable and wind speed was relatively calm, it was common for density-driven gravity drainage of air to transport fluxes horizontally through tree canopies beneath the level of the H and LE flux measurements (Baldocchi, et al. 2000, Wilson et al. 2002, Froelich et al. 2005). This air movement can transport heat, LE and CO_2 fluxes horizontally on even slightly sloping terrain beneath the EC system and are therefore these fluxes may not be captured by the flux measurement system and can be a reason of poor EB closure at night. There did not appear to be an obvious, consistent correlation between wind patterns and flux behavior at the sites.

Others have found wind to be correlated with EBCE. Researchers in Hawaii (Anderson 2014) studied paired eddy covariance sites with identical crop and cultivation practices and similar climate, but with the notable exception of wind. One tower was located in an area with funneled trade winds, the other in a leeward setting with less wind. They found that closure improved with turbulence, and that turbulent conditions as indicated by u* were more common at the windy site. Wilson et al. (2002) reviewed the closure pattern at a number of FLUXNET sites and found that closure improved

with increasing turbulent intensity. This section details a more rigorous statistical-based analysis of the relationship between wind behavior and the fluxes.

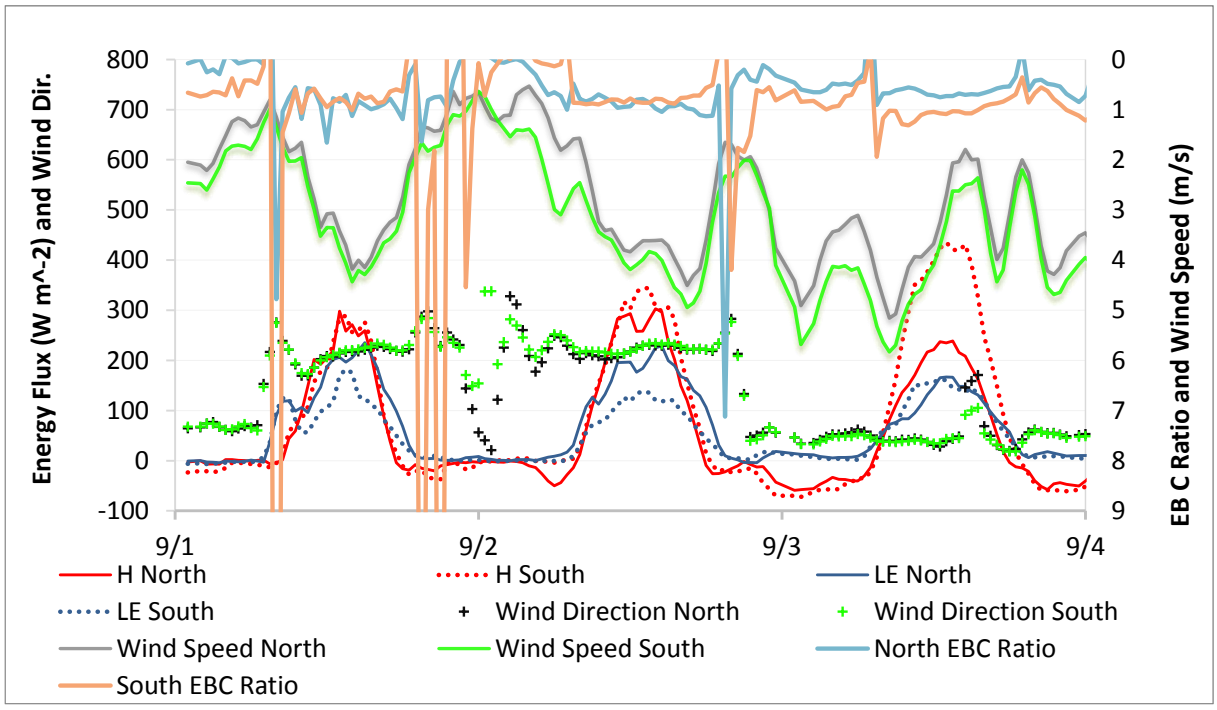

Figure 5-18. Graphical analysis of the relationship between H and LE and wind behavior for the Island Park north and south sites. Data from the July 2011 dataset.

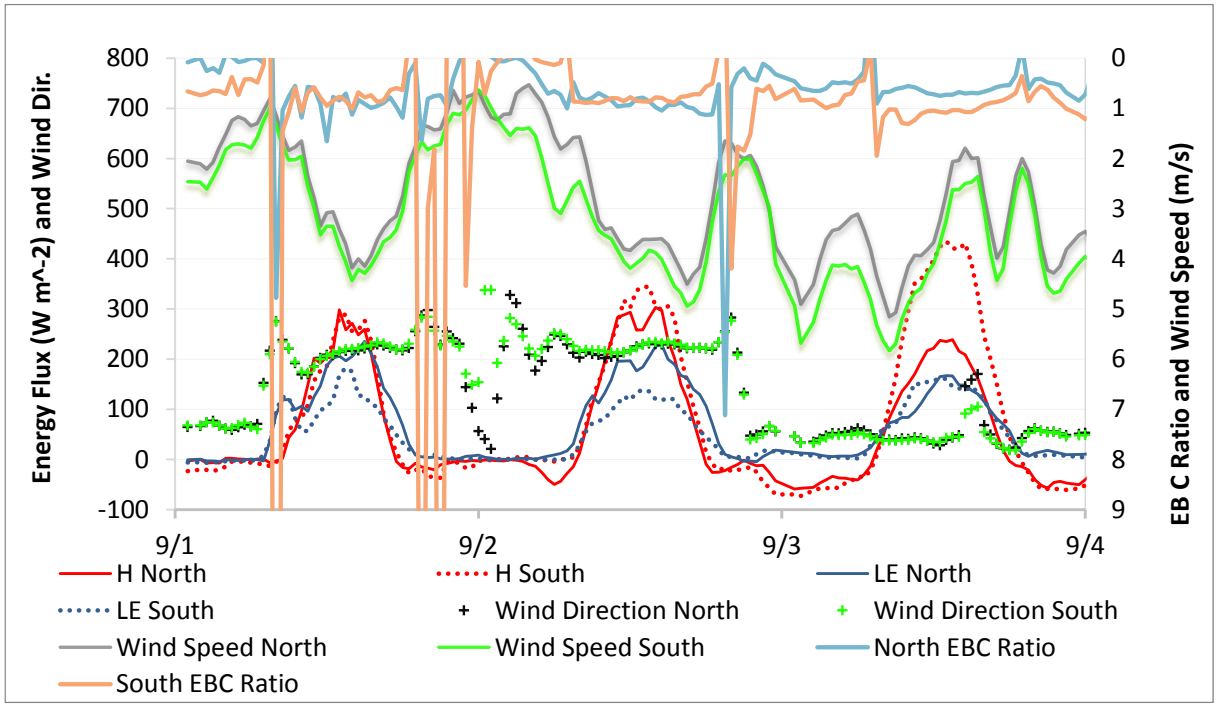

Figure 5-19. Graphical analysis of the relationship between H and LE and wind behavior for the Island Park north and south sites. Data from the September 2011 dataset.

5.2.1 Methodology

Bar graphs were prepared to summarize wind behavior patterns in a general sense. These graphs show how common a particular wind direction or speed is relative to a particular time of day and provide context for interpreting subsequent ANOVA. ANOVA was used to explore the similarity of wind patterns at the north and south sites, and whether the wind patterns were correlated with LE. The ANOVA used wind speed and LE as dependent variables. Site, time of day, and wind direction were independent variables. Wind direction was a categorical variable developed by dividing the compass in to 8 quadrants of 45 degrees each, beginning with 0, north. Time of day was also a categorical variable consisting of four time codes of 6 hours each, beginning with midnight. The data from LAS-adjusted time steps was used in the analysis.

ANOVA was used to test for statistically significant correlation between LE as the dependent variable and wind direction, time of day, and wind speed as independent variables. Wind speed was also transformed into a categorical variable by creating wind speed categories from 0 to the maximum wind speed in 1 m/s increments.

This analysis used the Island Park 2011 data. The ANOVA for wind speed and LE parameters were initially implemented using the June and August datasets. The June 2011 dataset represented a time frame when the turbulent fluxes from the north and south site were linked, i.e., there were no statistically significant differences between H and LE values at the north and south sites. The August 2011 dataset represented the time frame when the H and LE from the north and south sites were not linked. The results of the ANOVA runs from June and August 2011 were compared to identify differences in wind behavior between the sites that could affect LE and help explain why the north and south sites became delinked in August. The July (turbulent fluxes linked) and September (turbulent fluxes not linked) datasets were analyzed to investigate if the same patterns were present.

EBCE Residual and wind behavior was also analyzed using ANOVA. EBCE residual was set as the dependent variable, and site, wind speed categories, and wind direction were used as independent variables.

5.2.2 Results

June 2011 Wind

The bar graphs in Figure 5-20 and Figure 5-21 illustrate the number of time steps in a particular wind speed category. A.m. winds tended to be lighter than p.m. winds. The north and south sites had a

similar wind pattern of stronger p.m. winds, with the north site tending to experience higher wind velocities. Winds tended to be either still or at 5 - 6 m/s.

The bar graphs in Figure 5-22 and Figure 5-23 compare the number of time steps with a particular wind direction. Both the north and south sites again experienced similar patterns. Wind direction 5, corresponding to SSW, was the most common a.m. wind direction. Wind direction 6, corresponding to WSW, was the most common p.m. wind direction.

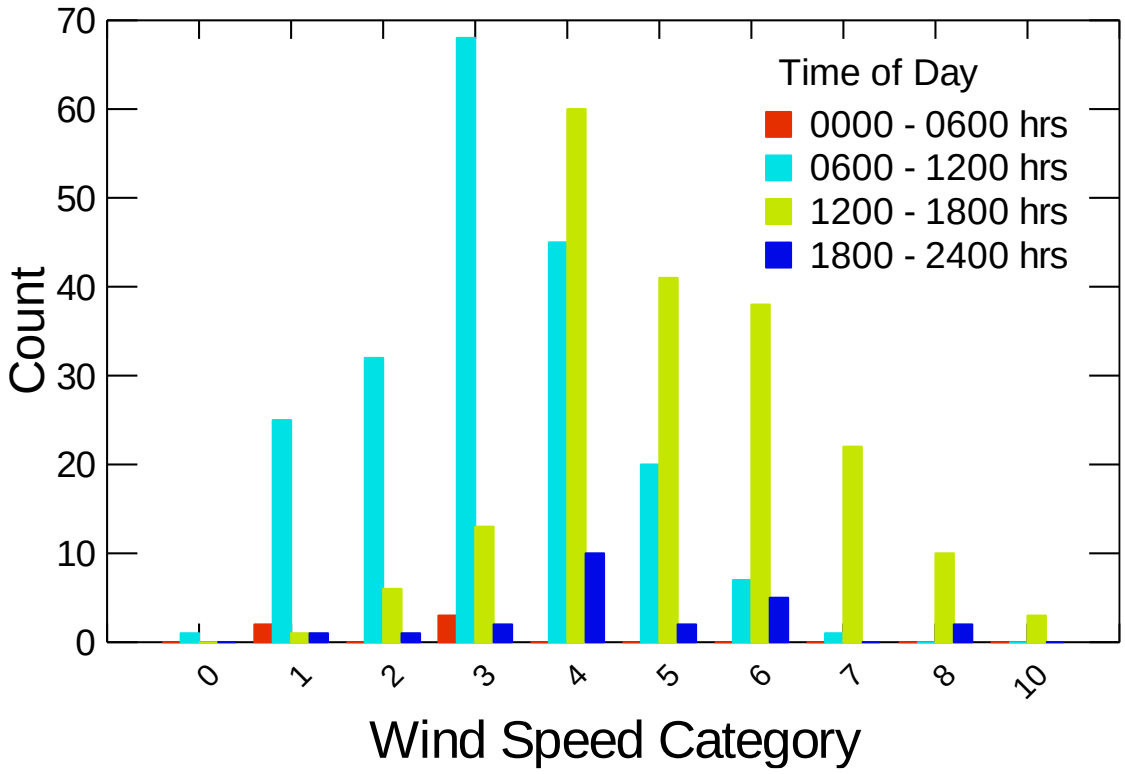

Figure 5-20. Graph of number of time steps having a particular wind speed. North site. Data from June 2011. Wind speed categories are in m/s.

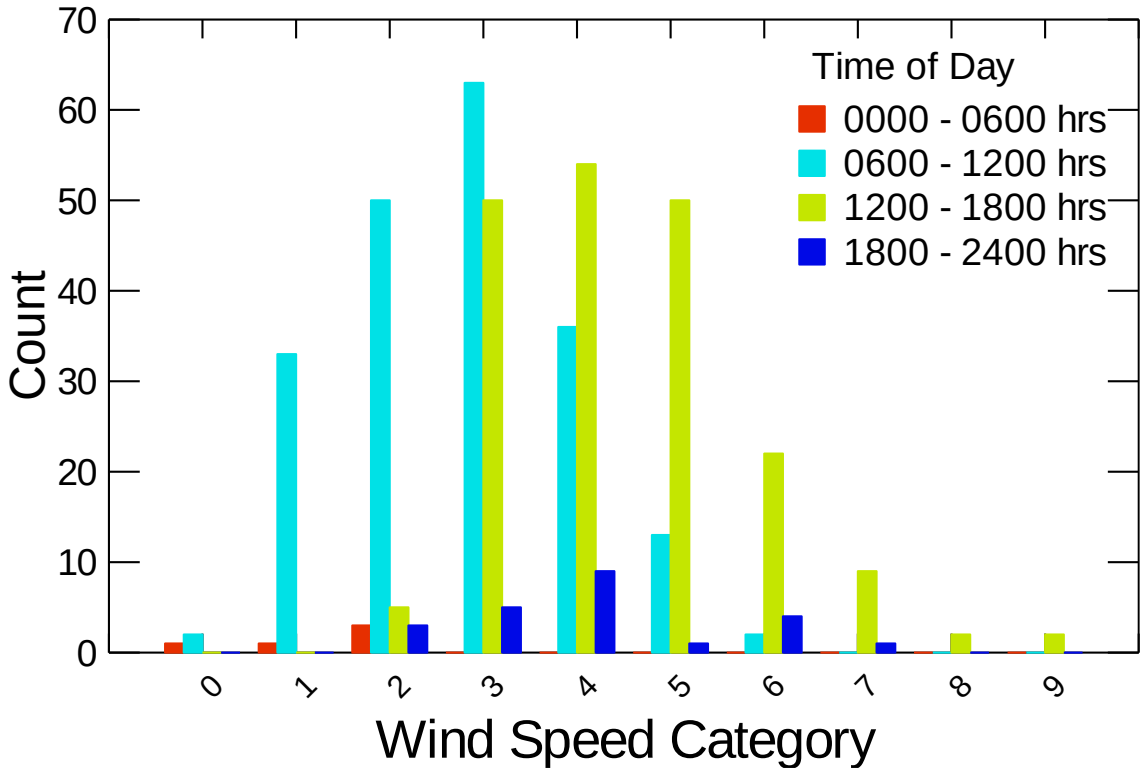

Figure 5-21. Graph of number of time steps having a particular wind speed. South site. Data from June 2011. Wind speed categories are in m/s.

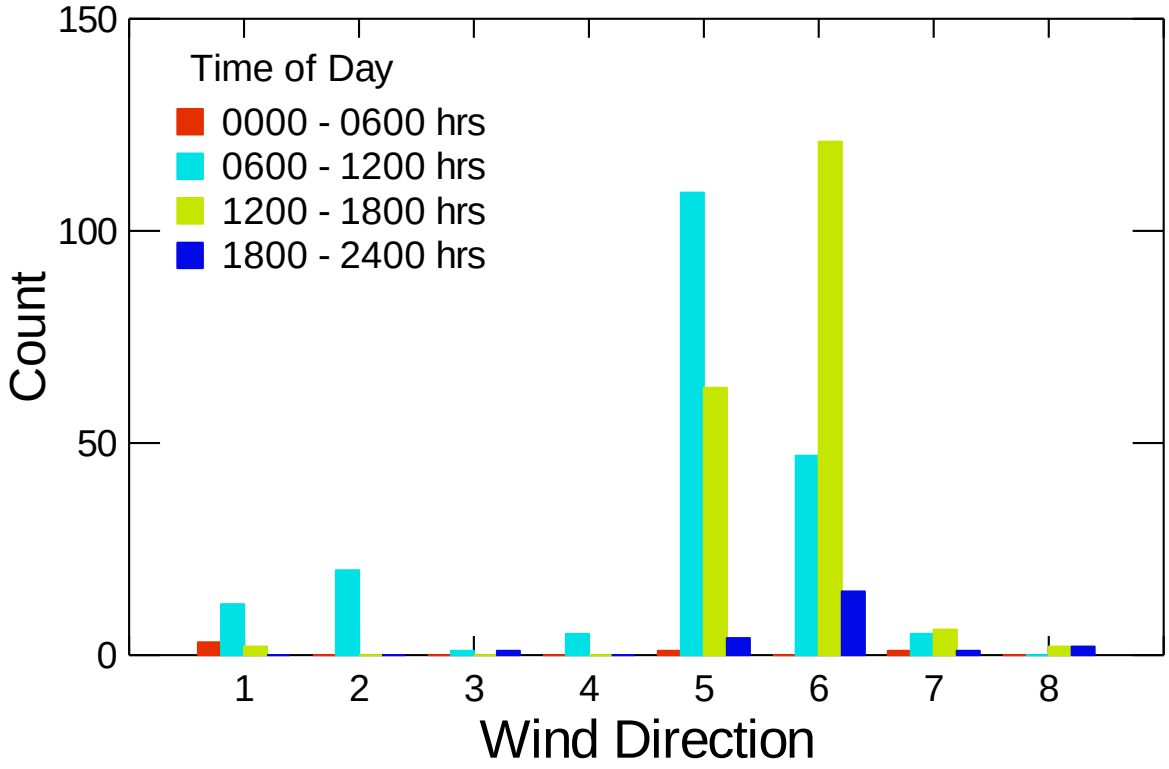

Figure 5-22. Graph of number of time steps with a particular wind direction. North Site. Data from June 2011. Wind direction categories: 1 = NNE, 2 = ENE, 3 = ESE, 4 = SSE, 5 = SSW, 6 = WSW, 7 = WNW, 8 = NNW.

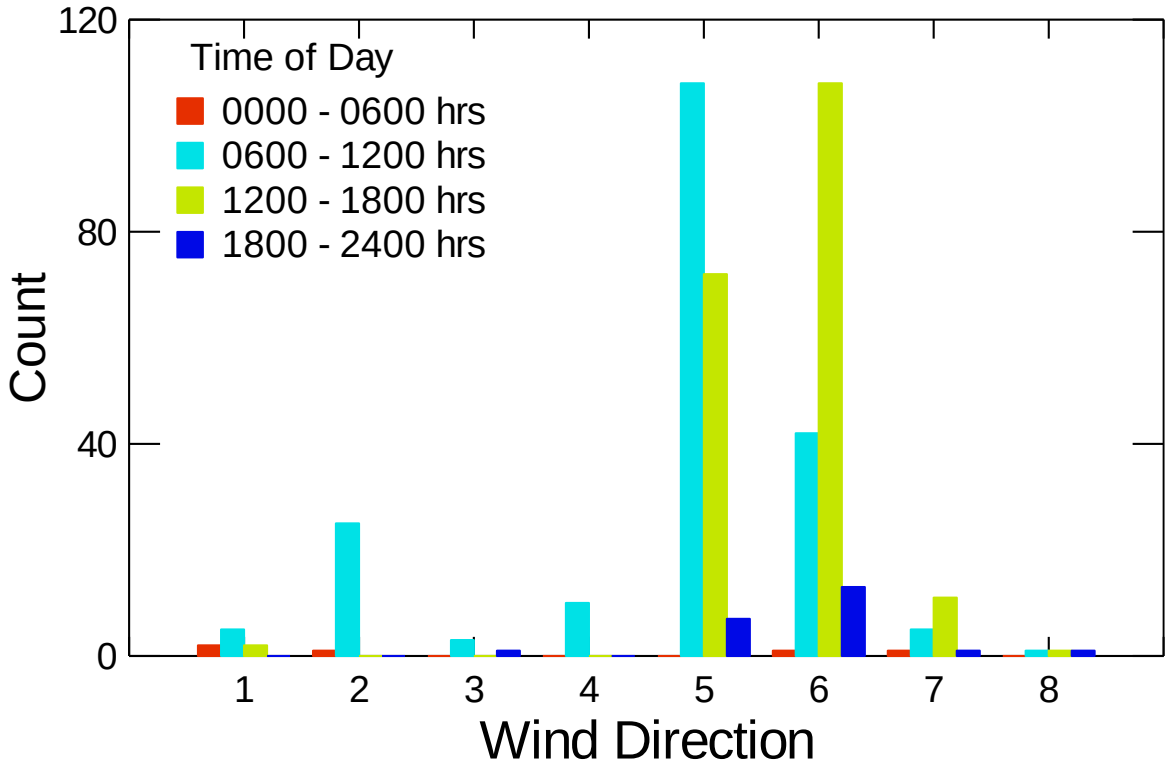

Figure 5-23. Graph of number of time steps with a particular wind direction. North Site. Data from June 2011. Wind direction categories: 1 = NNE, 2 = ENE, 3 = ESE, 4 = SSE, 5 = SSW, 6 = WSW, 7 = WNW, 8 = NNW.

Graphical analysis can assist in understanding the general wind behavior, but statistically methods allow conclusions to be drawn regarding parameters that have statistically significant interactions. ANOVA testing the similarity of wind patterns in the June 2011 dataset between the north and south sites showed that the differences in mean wind velocity between the north and south sites was statistically significant ($F(1, 840) = 23.194$, $p = 0.000$) (Table 5-5). The least-squared mean wind speed at the north site was 0.5 m/s higher than at the south site.

Source	Type III SS	df	Mean Squares	F-ratio	p-value
Site	62	1	62	**23.184**	0.000
Error	2,251	840	3		

Table 5-5. ANOVA table for wind speed vs site. Data from June 2011, n = 420.

Two-way ANOVA between dependent variable wind speed and independent factors site and time of day showed that the interaction between site and time of day was not statistically significant ($p = 0.561$). However, there was statistically significant difference in mean wind speeds between the north and south sites ($F(1, 834) = 6.811$, $p = 0.009$) and mean wind speed and time of day: $F(3, 834)$, 136.780, $p = 0.000$) (Table 5-6). Figure 5-24 graphically depicts the wind behavior at the north and

south sites, respectively, as a function of time of day. Both sites showed a trend of increasing wind from morning to afternoon, then decreasing wind speeds in the evening and night. Wind speeds were higher at the north site, particularly in daytime periods B and C.

Source	Type III SS	df	Mean Squares	F-ratio	p-value
Site	12	1	12	**6.811**	0.009
Time of Day	741	3	247	**136.780**	0.000
Site*Time Code	4	3	1	0.685	0.561
Error	1,506	834	2		

Table 5-6. ANOVA table for wind speed vs site and time of day. Data from June 2011, n = 420.

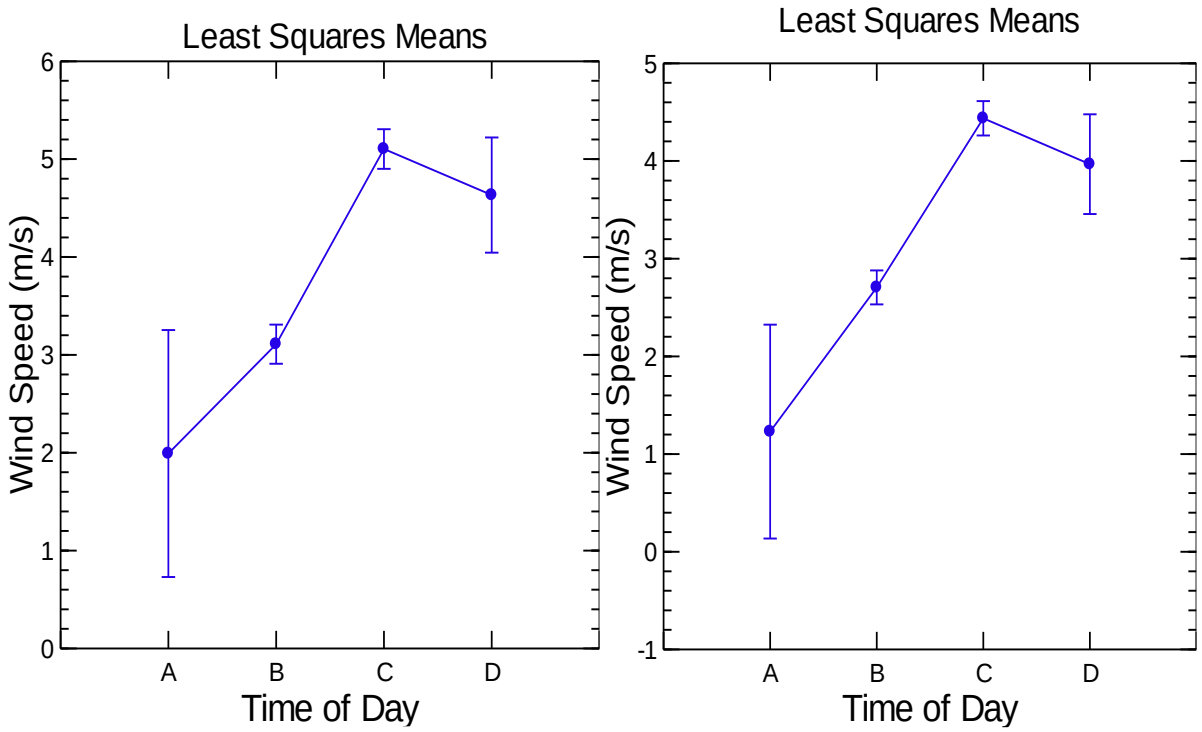

Figure 5-24. Wind speed vs Time of Day, north site (left) and south site (right), June 2011, n = 420. Time of day code: A = 0000 – 0600 hrs, B = 0600 – 1200 hrs, C = 1200 – 1800 hrs, D = 1800 – 2400 hrs.

Two-way ANOVA between dependent variable wind speed and independent factors site and wind direction showed that the interaction between site and wind direction was not statistically significant ($p = 0.133$) (Table 5-7). There was no statistically significant difference in mean wind speed between sites ($p = 0.487$). However, there was a statistically significant difference in mean wind speeds and wind directions ($F(7, 862) = 20.147$, $p = 0.000$). Figure 5-25 shows that the strongest winds at the north and south sites came from wind directions 5 and 6, corresponding to 180 to 270 degrees. This was the predominant wind direction during the daytime for both the north and south sites.

Source	Type III SS	df	Mean Squares	F-ratio	p-value
Site	1	1	1	0.483	0.487
Wind Dir	323	7	46	**20.147**	0.000
Site*Wind Dir	26	7	4	1.597	0.133
Error	1,891	826	2		

Table 5-7. ANOVA table for wind speed vs site and wind direction. Data from June 2011, n = 420.

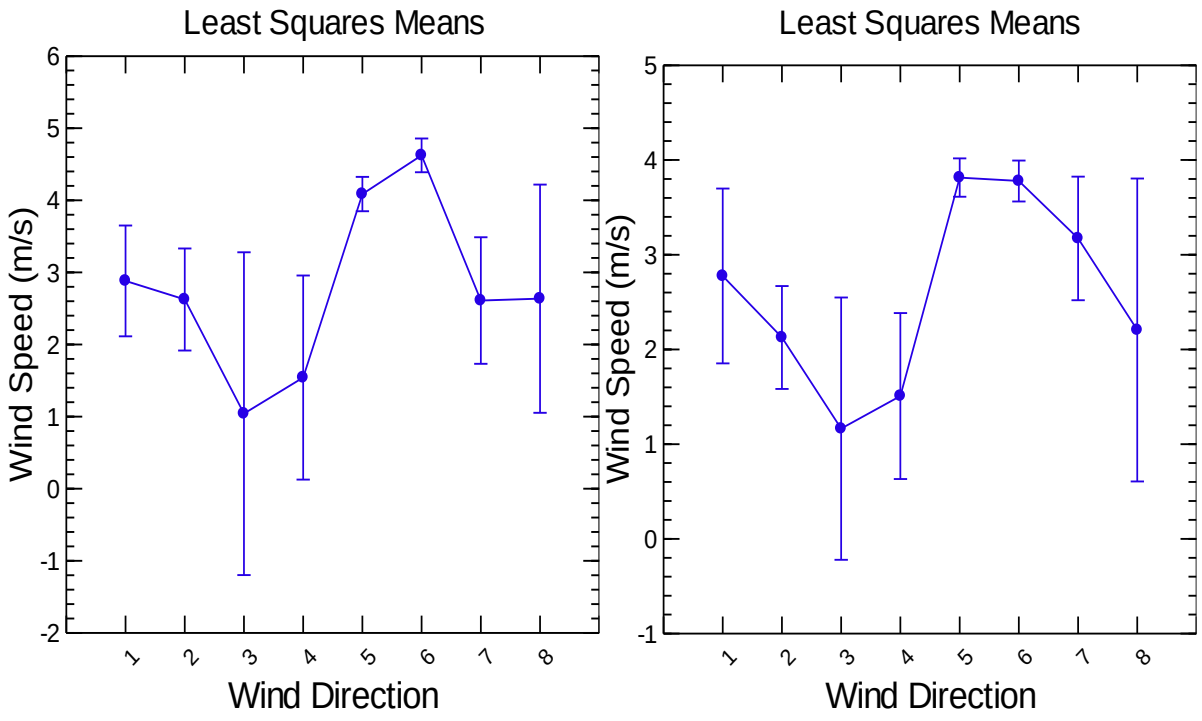

Figure 5-25. Wind speed vs wind direction, north site (left) and south site (right), June 2011, n = 420. Wind direction categories: 1 = NNE, 2 = ENE, 3 = ESE, 4 = SSE, 5 = SSW, 6 = WSW, 7 = WNW, 8 = NNW.

In summary regarding wind behavior, the mean wind speed at the north site was statistically significantly higher than the south site. Time of day and wind direction were statistically significant predictors of wind speed. Wind speed and wind direction were not combined in the same ANOVA because they violate assumptions of multicollinearity. Increasing wind speeds were strongly correlated with wind directions 5 and 6. Differences between these factors at the north and south sites may have contributed to the delinking of LE between the north and south sites in August and September.

June 2011 LE

Two-way ANOVA between dependent variable LE and independent factors site and wind direction showed that the interaction between site and wind direction was not statistically significant (p = 0.452) (Table 5-8). There was no statistically significant difference in mean LE between the north and

south sites (p = 0.930) (see section 4.2). However, wind direction had a statistically significant effect on mean LE (F(7, 826) = 6.544, p = 0.000).

Source	Type III SS	df	Mean Squares	F-ratio	p-value
Site	51	1	51	0.008	0.930
Wind Dir	304,749	7	43,536	**6.544**	0.000
Wind Dir*Site	21,070	7	3,010	0.452	0.869
Error	5,495,557	826	6,653		

Table 5-8. ANOVA table for LE vs site and wind direction. Data from June 2011, n = 420.

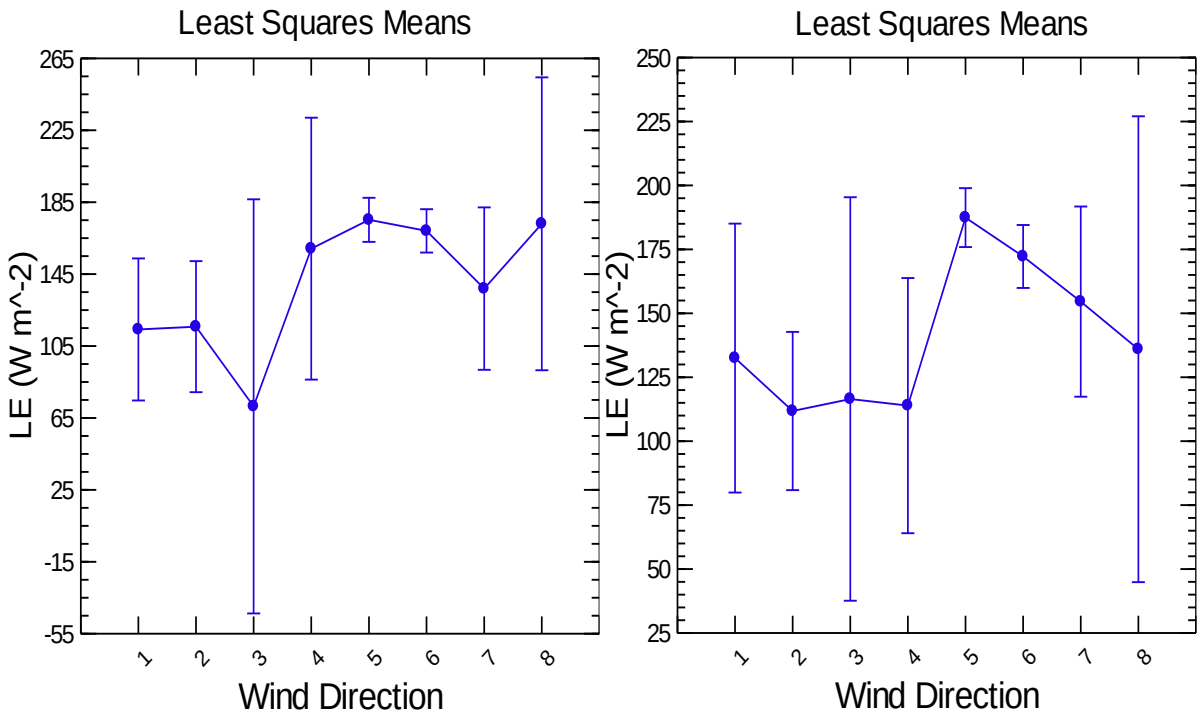

Figure 5-26. LE vs wind direction, north site (left) and south site (right). June 2011, n = 420. Wind direction categories: 1 = NNE, 2 = ENE, 3 = ESE, 4 = SSE, 5 = SSW, 6 = WSW, 7 = WNW, 8 = NNW.

Figure 5-26 shows the relationship between LE and wind direction at the north and south sites. The strongest LE signal was associated with wind directions 5 and 6. These wind directions corresponded to the predominant south westerly wind patterns that were present in the majority of the June 2011 dataset time steps (Figure 5-20 and Figure 5-21). The statistically significant effect of wind direction on mean LE was limited to between direction 1 and directions 5 and 6 and direction 2 and directions 5 and 6 at the north site and direction 2 and directions 4 and 6 and direction 4 and direction 5 at the south site. There was not a statistically significant difference in LE between wind directions 5 and 6, the most common wind directions. Directions 1 and 2 were more common in the early morning or

the late evening, so statistically significant differences detected by the ANOVA may be more directly related to higher mid-day and afternoon R_n rather than being a product of the wind direction per se.

Two-way ANOVA between dependent variable LE and independent factors site and wind speed categories showed that the interaction between site and wind speed category was not statistically significant ($p = 0.353$) (Table 5-9**Error! Reference source not found.**). There was no statistically significant difference in mean LE between the north and south sites ($p = 0.279$) (see section 4.2). However, wind speed category had statistically significant effect on mean LE ($F(8, 819) = 30.928$, $p = 0.000$). Figure 5-27 graphically depicts the relationship between LE and wind speed categories. LE was positively correlated with increasing wind speed. At the north site this relationship was consistent for wind speed categories 2 - 7. At the south site the positive relationship was not as consistent. However, higher LE in the afternoon is linked to higher R_n, and increased wind speed associated with afternoon heating is likely a secondary factor (see Figure 5-24).

Source	Type III SS	df	Mean Squares	F-ratio	p-value
Site	6,207	1	6,207	1.174	0.279
Wind Speed Category	1,308,003	8	163,500	**30.928**	0.000
Site*Wind Speed Category	46,993	8	5,874	1.111	0.353
Error	4,329,565	819	5,286		

Table 5-9. ANOVA table for LE vs site and wind speed. Data from June 2011, n = 420.

August 2011 Wind Speed

The bar graphs in Figure 5-28 and Figure 5-29 illustrate the number of time steps in a particular wind speed category. Similar to the patterns seen in June, a.m. winds tended to be lighter than p.m. winds. The north and south sites had a similar wind pattern of stronger p.m. winds, with the north site tending to experience higher wind velocities. Winds tended be 2 – 3 m/s in the morning and 4 – 6 m/s in the afternoon.

The bar graphs in Figure 5-30 and Figure 5-31 compare the number of time steps with a particular wind direction. Both the north and south sites again experienced similar patterns. Wind direction 5, corresponding to SSW, was again the most common a.m. wind direction. Winds form direction 1 and 2, corresponding to NNE and NEN, were also common in the a.m. Wind direction 6, corresponding to WSW, was the most common p.m. wind direction.

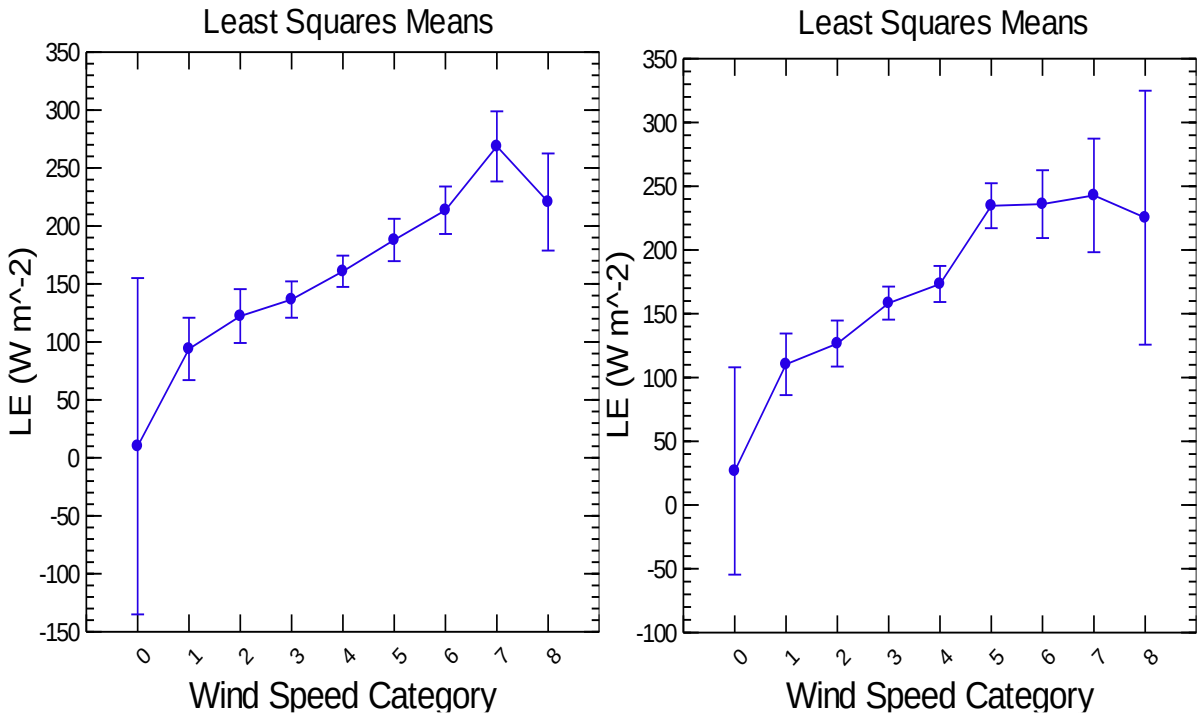

Figure 5-27. LE vs wind speed category, north site (left) and south site (right). June 2011, n = 420. Wind speed categories are in m/s.

ANOVA between dependent variable wind speed and independent factor site showed there was a statistically significant difference in mean wind velocity between the north and south sites ($F(1, 964) = 34.773$, $p = 0.000$) (Table 5-10). The north site again had higher wind velocities. The least-squared mean wind speed and the north site was 0.5 m s^{-2} higher than at the south site. This was the same difference in wind speed between sites observed in the June 2011 dataset. Some of the difference may have been due to differences in heights of the sonic anemometers above mean canopy height, where the north tower was at 24 m and the south tower was at 22 m above the ground surface. The north tower is also near a ridgeline that separates a break north toward the Henrys Fork of the Snake River and south toward the south tower. Siting near the ridgeline may have influenced wind speeds and direction.

Source	Type III SS	df	Mean Squares	F-ratio	p-value
Site	72	1	71	**34.773**	0.000
Error	1985	964	2		

Table 5-10. ANOVA table for wind speed vs site. Data from August 2011, n = 482.

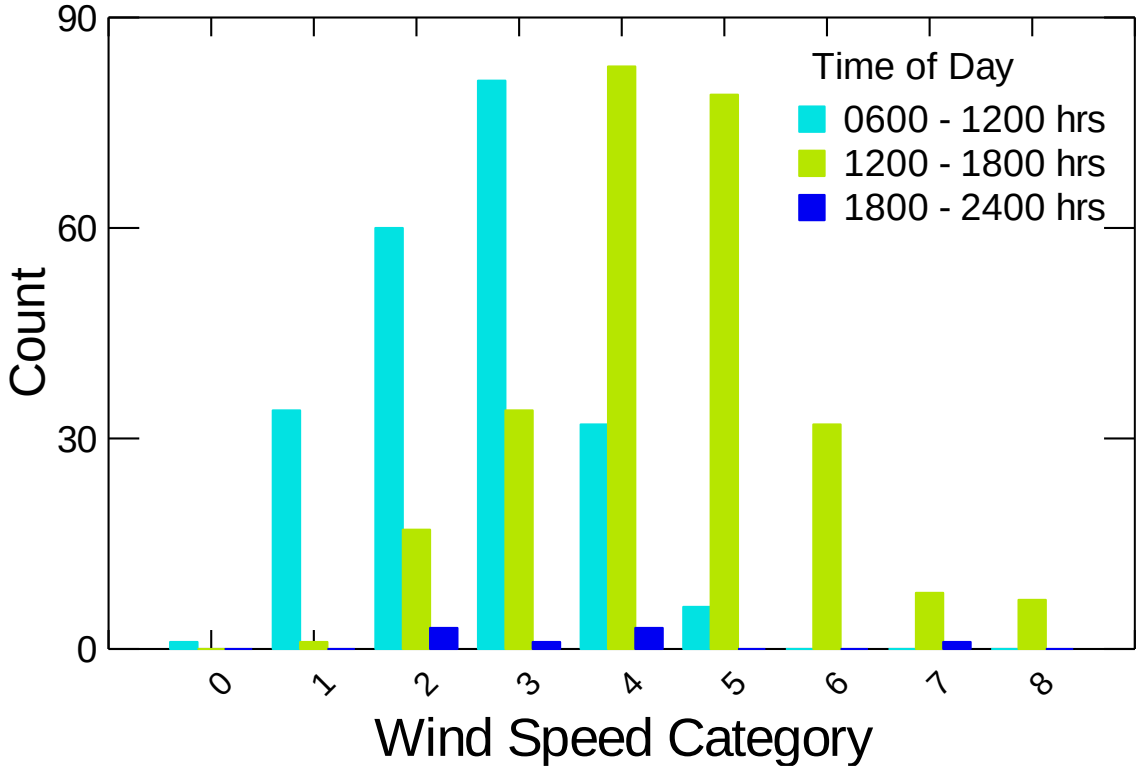

Figure 5-28. Wind Speed category count, north site. August 2011. Wind speed categories are in m/s.

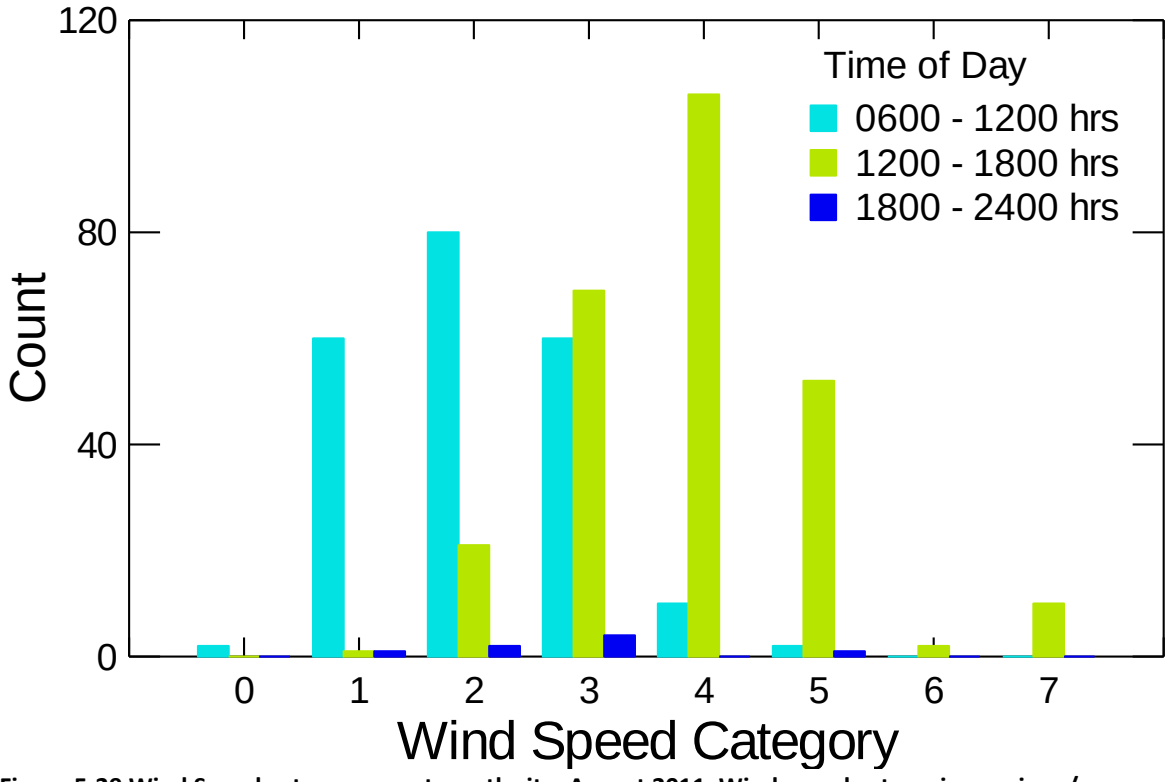

Figure 5-29 Wind Speed category count, south site. August 2011. Wind speed categories are in m/s.

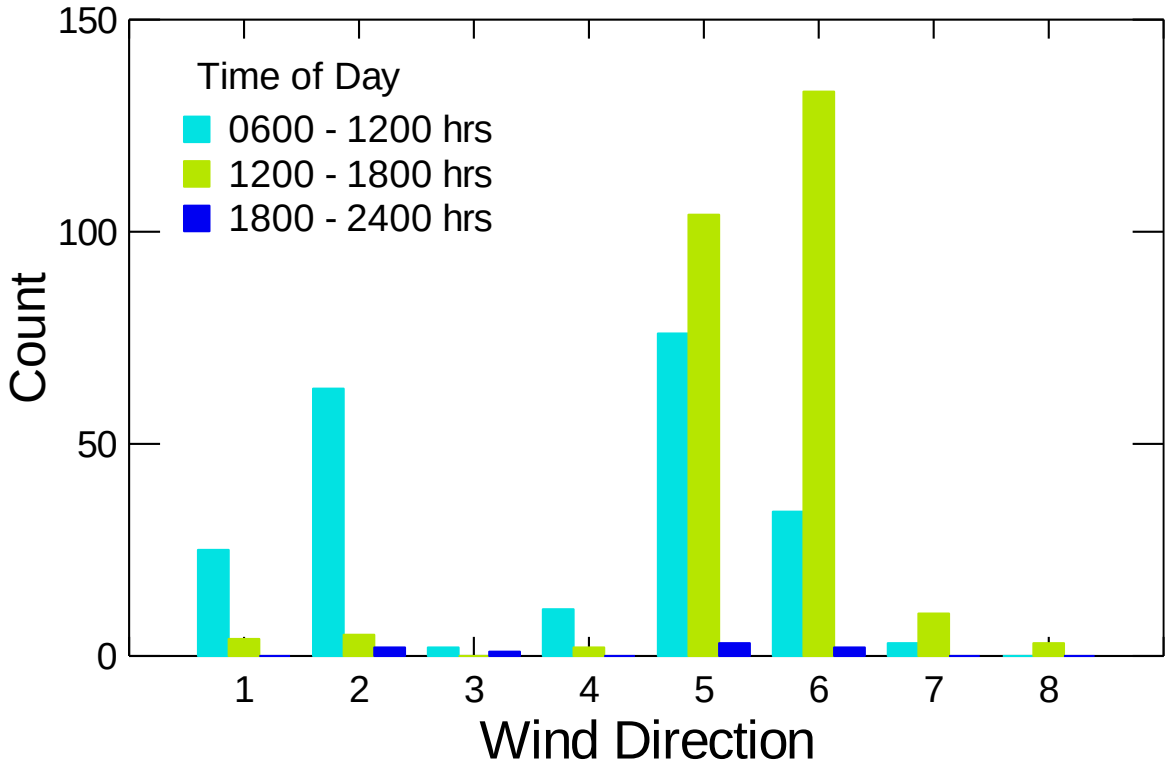

Figure 5-30. Wind direction count, north site. August 2011. Wind direction categories: 1 = NNE, 2 = ENE, 3 = ESE, 4 = SSE, 5 = SSW, 6 = WSW, 7 = WNW, 8 = NNW.

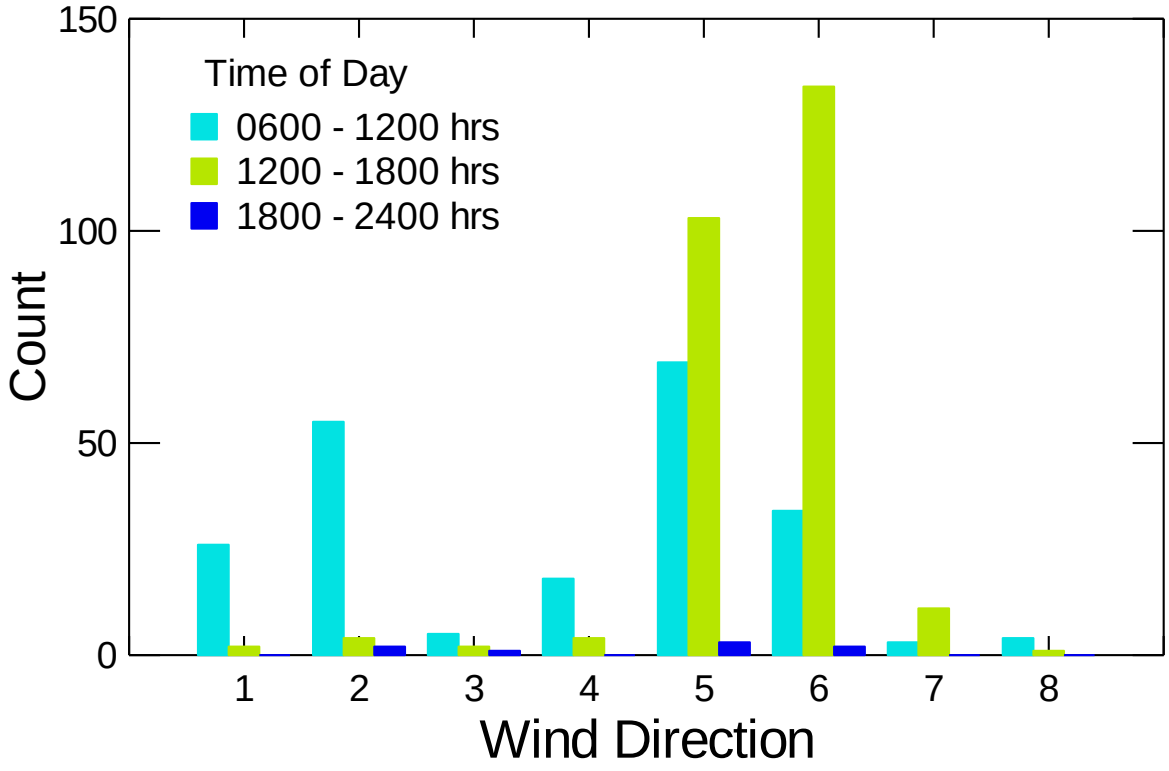

Figure 5-31. Wind direction count, south site. August 2011. Wind direction categories: 1 = NNE, 2 = ENE, 3 = ESE, 4 = SSE, 5 = SSW, 6 = WSW, 7 = WNW, 8 = NNW.

Two-way ANOVA between dependent variable wind speed and independent factors site and time of day showed that the interaction between sites for wind vs time of day was not statistically significant ($p = 0.765$) (Table 5-11). However, there was statistically significant difference in mean wind speeds between site ($F(1, 960) = 10.033$, $p = 0.002$) and mean wind speed and time of day ($F(2, 960)$, 319.772, $p = 0.000$). Figure 5-32 graphically depicts the wind behavior at each site as a function of time of day. Both sites showed a trend of increasing wind from morning to afternoon, then decreasing wind speeds in the evening and night. This pattern was similar to the pattern observed in the June 2011 dataset (Figure 5-24).

Source	Type III SS	df	Mean Squares	F-ratio	p-value
Site	12	1	12	**10.033**	0.002
Time of Day	793	2	397	**319.772**	0.000
Site*Time of Day	0.7	2	0.3	0.269	0.765
Error	1,191	960	1		

Table 5-11. ANOVA table for wind speed vs site and time of day. Data from August 2011, n = 482.

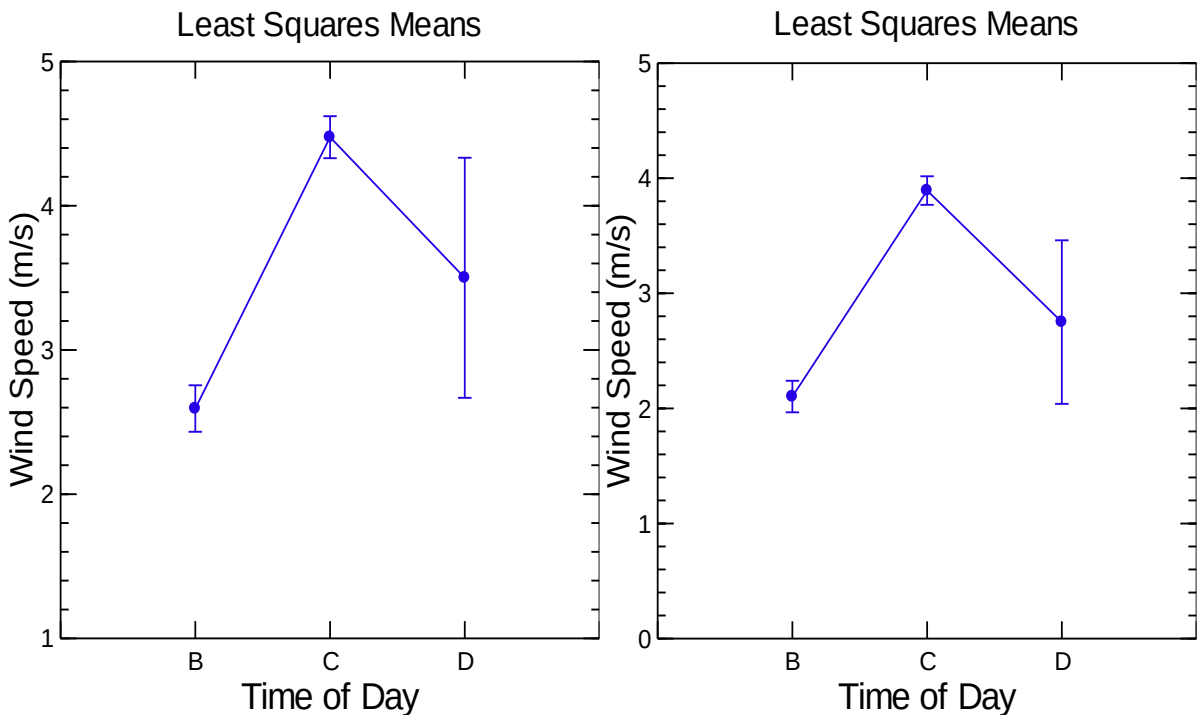

Figure 5-32. Wind speed vs time of day, north site (left) and south site (right). August 2016, n = 482. Time of day code: A = 0000 – 0600 hrs, B = 0600 – 1200 hrs, C = 1200 – 1800 hrs, D = 1800 – 2400 hrs. No data from time code A was available due to shortening of the day length in August.

Two-way ANOVA between dependent variable wind speed and independent factors site and wind direction site showed that the interaction between site and wind direction was not statistically significant (p = 1.151) (Table 5-12). There was statistically significant difference in mean wind speed between sites (F(1, 950) = 6.528, p = 0.011) and mean wind speeds and wind directions (F(7, 950) = 40.687, p = 0.000). Figure 5-33 shows that the strongest winds at the north and south sites come from wind directions 5 and 6, corresponding to 180 to 270 degrees, which was the most prevalent wind direction during the daytime. This pattern was also similar to the pattern observed in the June 2011 dataset (Figure 5-25).

Source	Type III SS	df	Mean Squares	F-ratio	p-value
Site	10	1	10	**6.528**	0.011
Wind Dir	454	7	65	**40.687**	0.000
Site*Wind Dir	13	7	2	1.151	0.329
Error	1,514	950	2		

Table 5-12. ANOVA table for wind speed vs site and wind direction. Data from August 2011, n = 482.

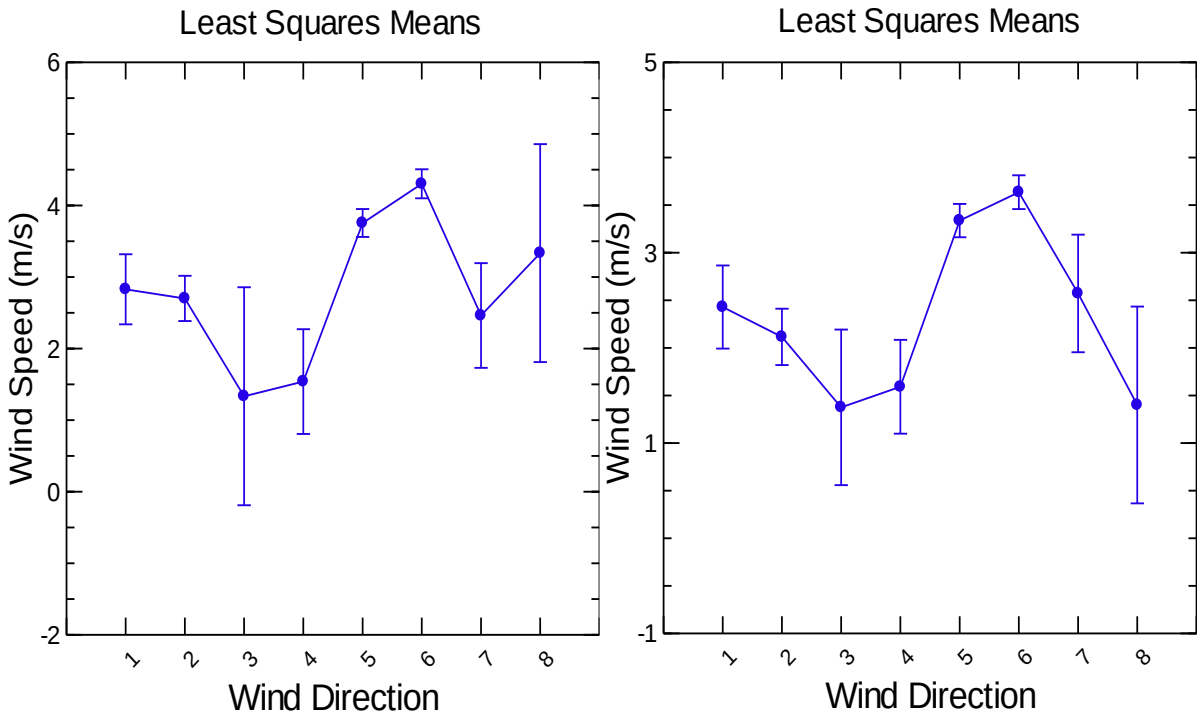

Figure 5-33. Wind speed vs wind direction, north site (left) and south site (right). August 2011, n = 482. Wind direction categories: 1 = NNE, 2 = ENE, 3 = ESE, 4 = SSE, 5 = SSW, 6 = WSW, 7 = WNW, 8 = NNW.

August 2011 LE

Two-way ANOVA between dependent variable LE and independent factors site and wind direction showed that the interaction between site and wind direction was statistically significant ($F(7, 950) = 9.280$, $p = 0.000$) (Table 5-13). The statistically significant interaction between site and wind direction was not present in the June 2011 dataset. There was statistically significant difference in mean LE between the north and south sites ($F(1, 950) = 12.639$, $p = 0.000$) (see section 4.2) and in mean LE and wind direction ($F(7, 950) = 37.100$, $p = 0.000$).

Source	Type III SS	df	Mean Squares	F-ratio	p-value
Site	76,856	1	76,856	**12.639**	0.000
Wind Direction	1,579,211	7	225,602	**37.100**	0.000
Site*Wind Direction	395,014	7	56,431	**9.280**	0.000
Error	5,776,931	950	6,081		

Table 5-13. ANOVA table for LE vs site and wind direction. Data from August 2011, n = 482.

Figure 5-34 shows the relationship between LE and wind direction at the north and south sites. The strongest LE signal was associated with wind directions 5 and 6, the most prevalent day-time wind direction (Figure 5-30 and Figure 5-31). The statistically significant effect on mean LE from wind direction was restricted to between direction 1 and directions 5, 6, and 7 and direction 2 and directions 4, 5, 6 and 7. The difference between mean LE and directions 5 and 6 were not statistically significant. Directions 1 and 2 were more common in the early morning or the late evening, so statistically significant differences detected by the ANOVA may be more related to higher mid-day and afternoon R_n and energy availability rather than being a product of the wind direction per se.

Two-way ANOVA between dependent variable LE and independent factor site and wind speed categories showed the interaction between site and wind speed category was statistically significant ($F(6, 942) = 9.844$, $p = 0.000$) (Table 5-14). There was statistically significant difference in mean LE between the north and south sites ($F(1, 942) = 24.399$, $p = 0.000$) (see section 4.2) and in mean LE and wind speed ($F(6, 942) = 16.754$, $p = 0.000$). Figure 5-35 graphically depicts the relationship between LE and wind speed categories. A pattern of increasing LE with increasing wind speed was observed at the north site. However at the south site, LE initially increased and then was relatively stable with higher wind speeds. The overall magnitude of LE was also lower at the south site than at the north site. This was in contrast to the June 2011 data set when the turbulent fluxes at the north and south sites were linked: LE was positively correlated with increasing wind speed at both the

north and south sites, and LE was similar in terms of magnitude (see Figure 5-27). It appears that the differential relationship between wind speed and LE between the north and south site could be correlated with the delinking of the LE at the north and south towers in August 2011.

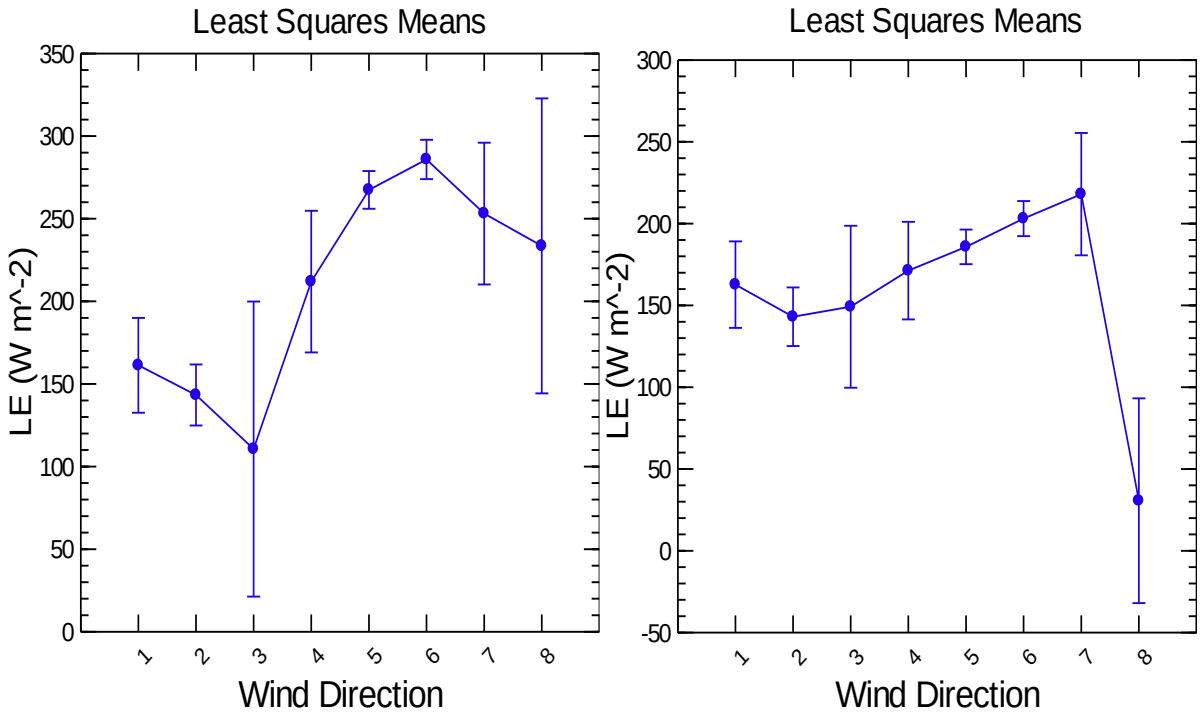

Figure 5-34. LE vs wind direction, north site (left) and south site (right). August 2011, n = 482. Wind direction categories: 1 = NNE, 2 = ENE, 3 = ESE, 4 = SSE, 5 = SSW, 6 = WSW, 7 = WNW, 8 = NNW.

Source	Type III SS	df	Mean Squares	F-ratio	p-value
Site	172,034	1	172,03	**24.399**	0.000
Wind Speed Category	708,766	6	118,128	**16.754**	0.000
Site*Wind Speed Category	289,552	6	48,259	**6.844**	0.000
Error	6,641,813	942	7,051		

Table 5-14. ANOVA table for LE vs site and wind speed. Data from August 2016, n = 482.

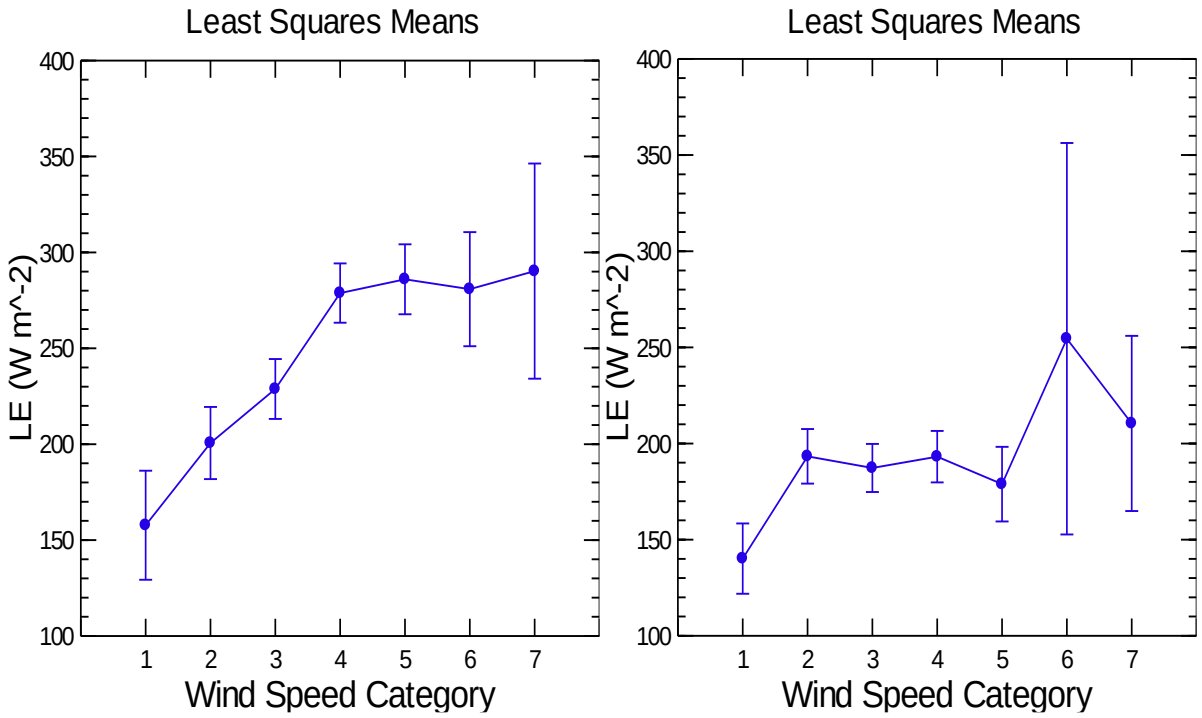

Figure 5-35. LE vs wind speed categories, north site (left) and south site (right). August 2011, n = 482. Wind speed categories are in m/s.

To explore whether this pattern holds more broadly, the data from July 2011, when the turbulent fluxes at the north and south tower were linked, and September 2011 when the fluxes were not linked were analyzed. Graphs of LE vs wind speed categories are presented in Figure 5-36 and Figure 5-37 for July and September, respectively. Graphs of LE vs wind direction are presented in Figure 5-38 and Figure 5-39 for July and September, respectively.

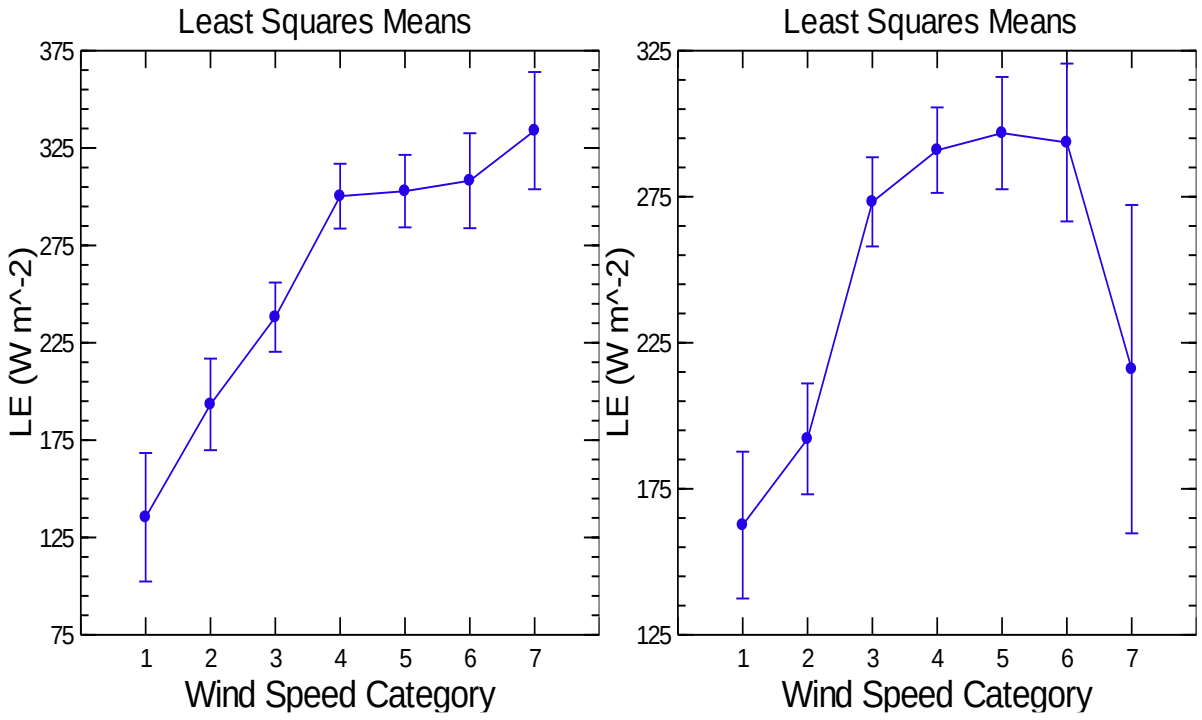

Figure 5-36. LE vs wind speed categories, north site (left) and south site (right). July 2011, n = 506. Wind speed categories are in m/s.

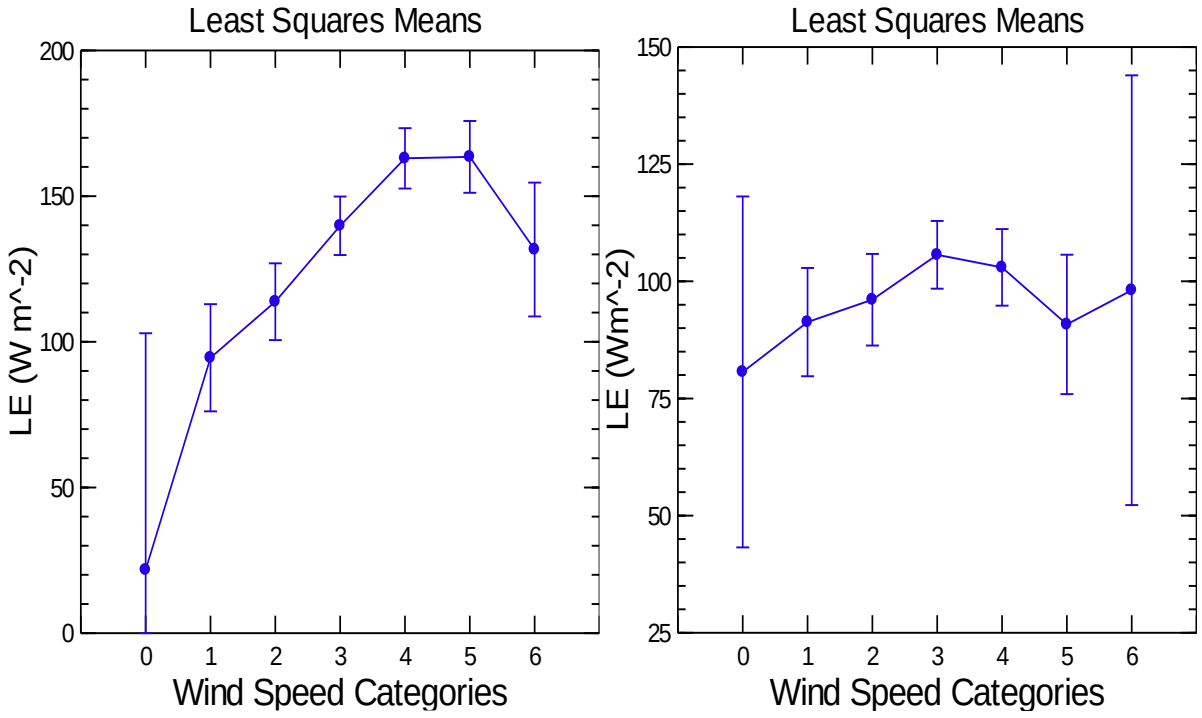

Figure 5-37. LE vs wind speed categories, north site (left) and south site (right). September 2011, n = 485. Wind speed categories are in m/s.

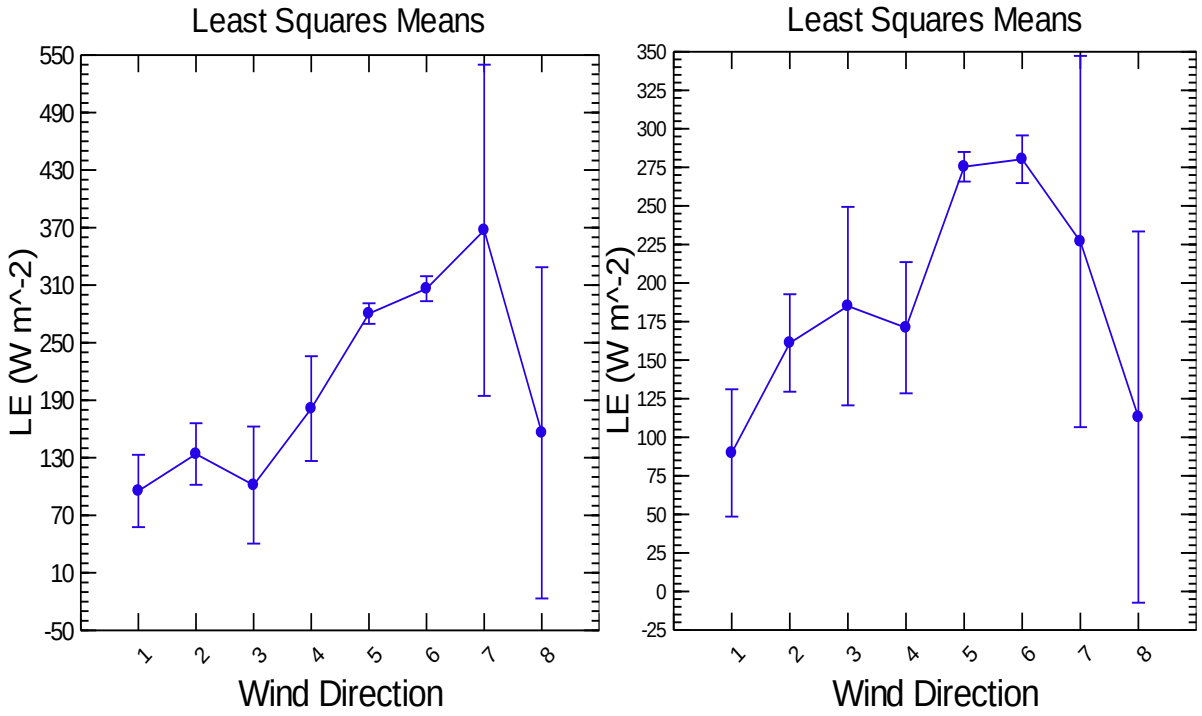

Figure 5-38. LE vs wind direction, north site (left) and south site (right). July 2011, n = 506. Wind direction categories: 1 = NNE, 2 = ENE, 3 = ESE, 4 = SSE, 5 = SSW, 6 = WSW, 7 = WNW, 8 = NNW.

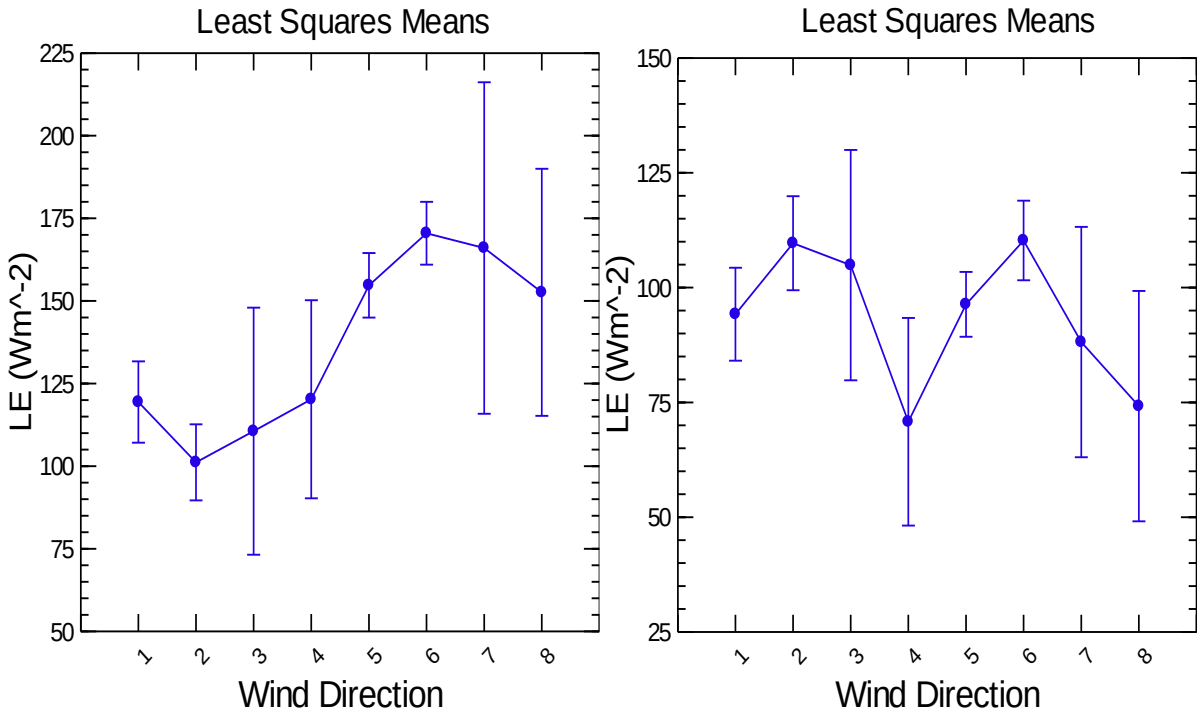

Figure 5-39. LE vs wind direction, north site (left) and south site (right). September 2011, n = 485. Wind direction categories: 1 = NNE, 2 = ENE, 3 = ESE, 4 = SSE, 5 = SSW, 6 = WSW, 7 = WNW, 8 = NNW.

The north site had a consistent relationship between increasing LE and increasing wind speed during the four-month time period. However, the relationship between wind speed and LE at the south site was less consistent. In June there was a strong positive relationship between increasing wind speed and LE. In August and September when the LE at the north and south sites was not linked, increasing wind speed was correlated with higher LE at the north site. In contrast, increasing wind speeds were not well correlated with higher LE at the south site. July, when LE at the north and south sites was linked, appeared to be a transitional month between the June pattern and the August-September pattern. LE was still positively correlated with increasing wind speed, but less strongly so than it was in June.

The mechanism behind the change in behavior between wind speed and LE is not readily apparent. Winds at the north site were a little stronger than at the south site. Higher wind speed would tend increase LE by removing the conditioned boundary layer adjacent to an evaporating or transpiring surface more quickly, increasing vapor pressure deficit and thereby increasing ET. Increasing wind speeds could have opposing effects on LE at the north and south sites if increasing winds introduced differentially-preconditioned air mass over the sites. This behavior would require a more moist area, such as a water body or a lush vegetated area, or drier surface, such as a barren area, in the upwind area of one of the sites, but such an area was apparently absent from the vicinity of either site. Shallower soil depth or more coarse soil at the south site or less dense trees may have played a role. Detailed spatial information on tree density and soils was not available to this study.

The pattern of higher wind speeds at the north site could be a factor in the delinking of the sites. However, it is not clear why the effect would become more pronounced in August and September since the differential wind speed pattern between the north and south sites was present in the June and July datasets as well. It is also possible that the relationship between wind velocity and LE is more correlational than causal.

Another variable that could explain the difference in ET between the north and south sites and their corresponding ET_c are differences in the forest communities. (See Figure 1-1 and Figure 1-2 showing close-up aerial images of the forest community surrounding the north and south sites). The community around the south site appears to be comprised of more open, non-forested areas with forbs and grasses. The rooting structure of the forbs and grasses would generally be shallower than the trees. The implication is that as the upper layers of the soil dried out more quickly than the deeper soil, the more shallowly-rooted forbs and grasses would have had less RAW, which would

have reduced transpiration rates. Figure 3-41 illustrates how Soil VWC changes with soil depth. Deeper soil layers tended to have higher VWC.

EBCE Residual and Wind Behavior

The ANOVA for June, July, August, and September between dependent variable EBCE residual and independent factor site indicated that there was not a statistically significant difference in the north and south site residuals for June, August, and September (June: p = 0.111, August: p = 0.138, September: = 0.123) (Table 5-15). However, the residual between the north and south sites for July 2011 was statistically significant (p = 0.004).

Source	Type III SS	df	Mean Squares	F-ratio	p-value
June					
Site	6,740	1	6,740	2.541	0.111
Error	2,227,861	840	2,652		
July					
Site	15,016.313	1	15,016.313	**8.271**	0.004
Error	1,837,377	1,012	1,815.589		
August					
Site	5,111.265	1	5,111.265	2.208	0.138
Error	2,231,347	964	2,314.675		
September					
Site	6,222.615	1	6,222.615	2.389	0.123
Error	2,442,858	938	2,604.326		
ANOVA results for residuals vs site. 2011 data.					

Table 5-15. ANOVA table for EBCE residual vs site for June, n = 420, July, n = 506, August, n =482, and September, n = 485, 2011 datasets. Statistically significant F-ratio values are in bold font.

Two-way ANOVA between dependent variable EBCE residual and independent factors site and wind speed categories found statistically significant interaction between site and wind speed category for July ($F(6, 985) = 3.660$, $p = 0.001$) , August ($F(6, 942) = 18.465$, $p = 0.000$), and September ($F(5, 918) = 6.979$, $p = 0.000$) (Table 5-16). The interaction between site and wind speed category was not statistically significant for June ($F(8, 819) = 1.176$, $p = 0.310$). There was statistically significant differences between residual and wind speed category for June ($F(8, 819) = 3.957$, $p = 0.000$), August ($F(6, 942) = 16.144$, $p = 0.000$), and September ($F(5, 918) = 5.017$, $p = 0.000$), but not for July ($F(6, 985) = 1.738$, $p = 0.109$).

Source	Type III SS	df	Mean Squares	F-ratio	p-value
June					
Site	83	1	83	0.033	0.857
Wind Speed Category	80,363	8	10,045	**3.957**	0.000
Site*Wind Spd Cat	23,891	8	2,986	1.176	0.310
Error	2,079,150	819	2,539		
July					
Site	10,573	1	10,573	**5.942**	0.015
Wind Speed Category	18,557	6	3,093	1.738	0.109
Site*Wind Spd Cat	39,070	6	6,512	**3.660**	0.001
Error	1,752,519	985	1,779		
August					
Site	579	1	579	0.301	0.583
Wind Speed Category	186,313	6	31,052	**16.144**	0.000
Site*Wind Spd Cat	213,096	6	35,516	**18.465**	0.000
Error	1,811,863	942	1,923		
September					
Site	14	1	14	0.005	0.941
Wind Speed Category	62,071	5	12,414	**5.017**	0.000
Site*Wind Spd Cat	86,349	5	17,270	**6.979**	0.000
Error	2,271,545	918	2,474.450		

Table 5-16. ANOVA table for residual vs site and wind speed category for June, n = 420, July, n = 506, August, n = 482, and September, n = 485, 2011 datasets. Statistically significant F-ratios are in bold font.

Graphs of the relationship between residual and wind speed categories were useful in interpreting the ANOVA findings and further exploring the relationship between EBCE residual and wind velocity. The graphs for the north and south site from the June dataset did not show a consistent relationship between increasing wind velocity and EBCE for either site (Figure 5-40). The graphs for July (Figure 5-41), August (Figure 5-42), and September (Figure 5-43) showed a pattern of decreasing EBCE with increasing wind velocity at the north site, while the south site showed an inconsistent correlation between EBCE and wind velocity. This relationship may be associated with the previously-noted correlation between increased wind velocity and increased LE at the north site. The correlation between increased wind speed and increased LE was less consistent at the south site, particularly in August and September (see Section 4.2).

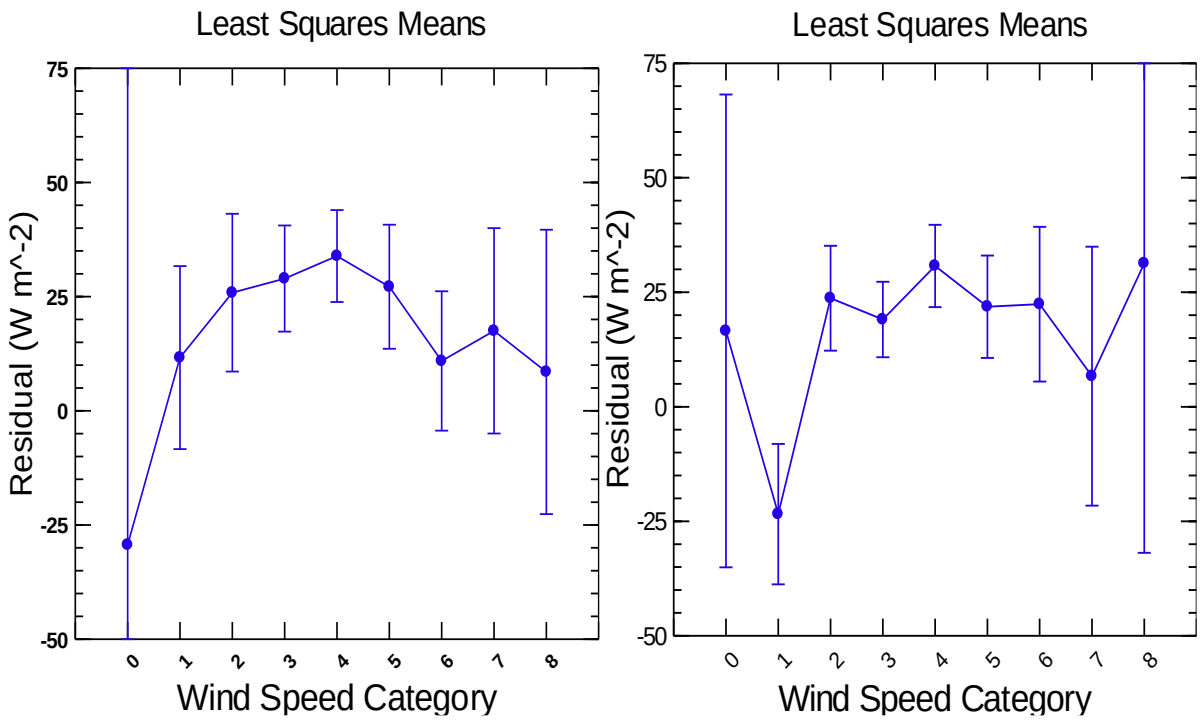

Figure 5-40. EBCE residual vs wind speed category (m/s), north site (left) and south site (right). June 2011, n = 420.

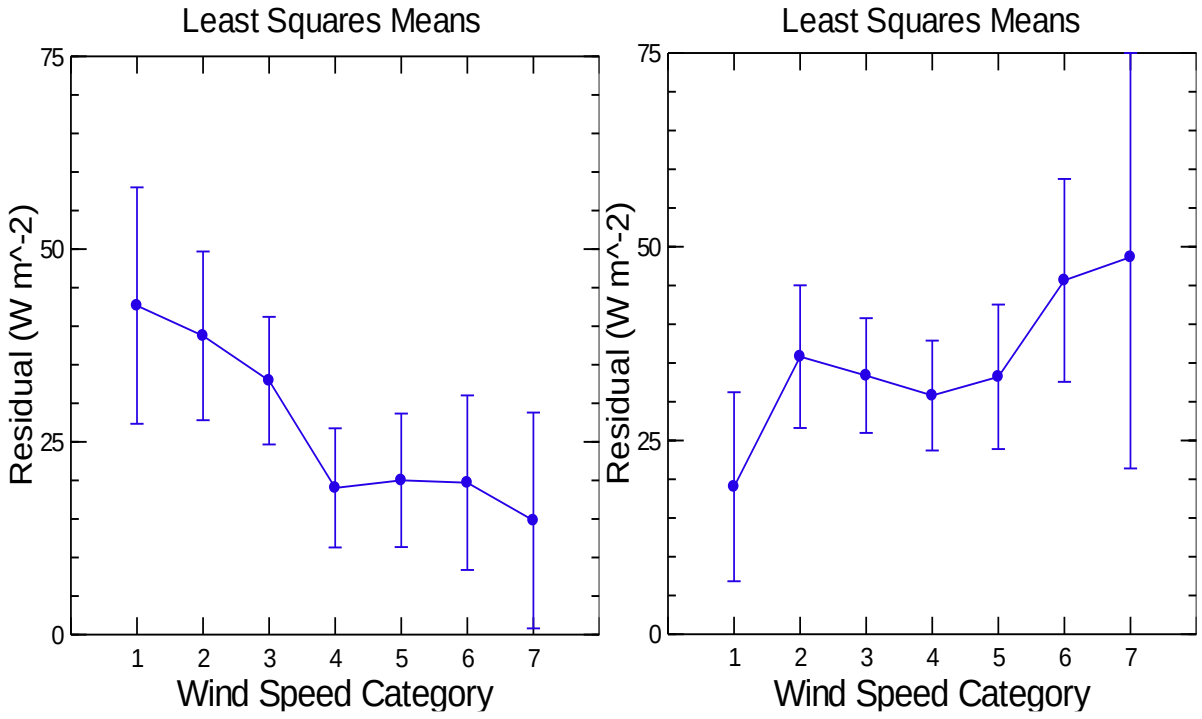

Figure 5-41. EBCE residual vs wind speed category (m/s), north site (left) and south site (right). July 2011, n = 506.

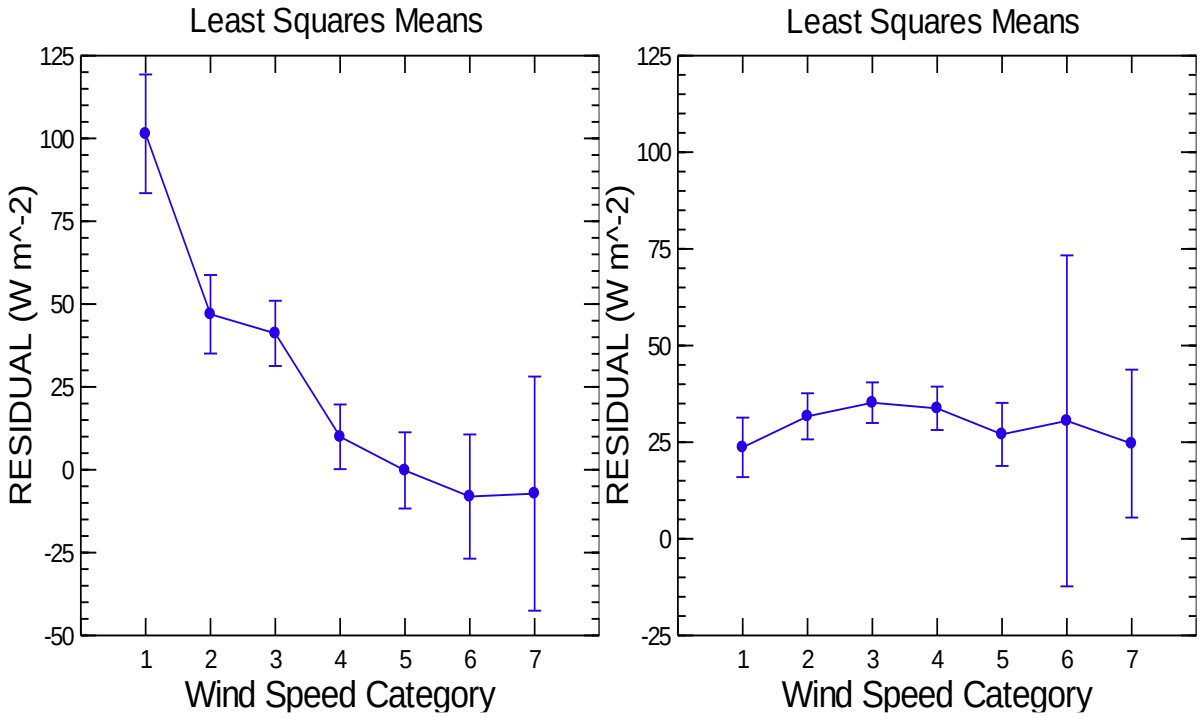

Figure 5-42. EBCE residual vs wind speed category (m/s), north site (left) and south site (right). August 2011, n = 482.

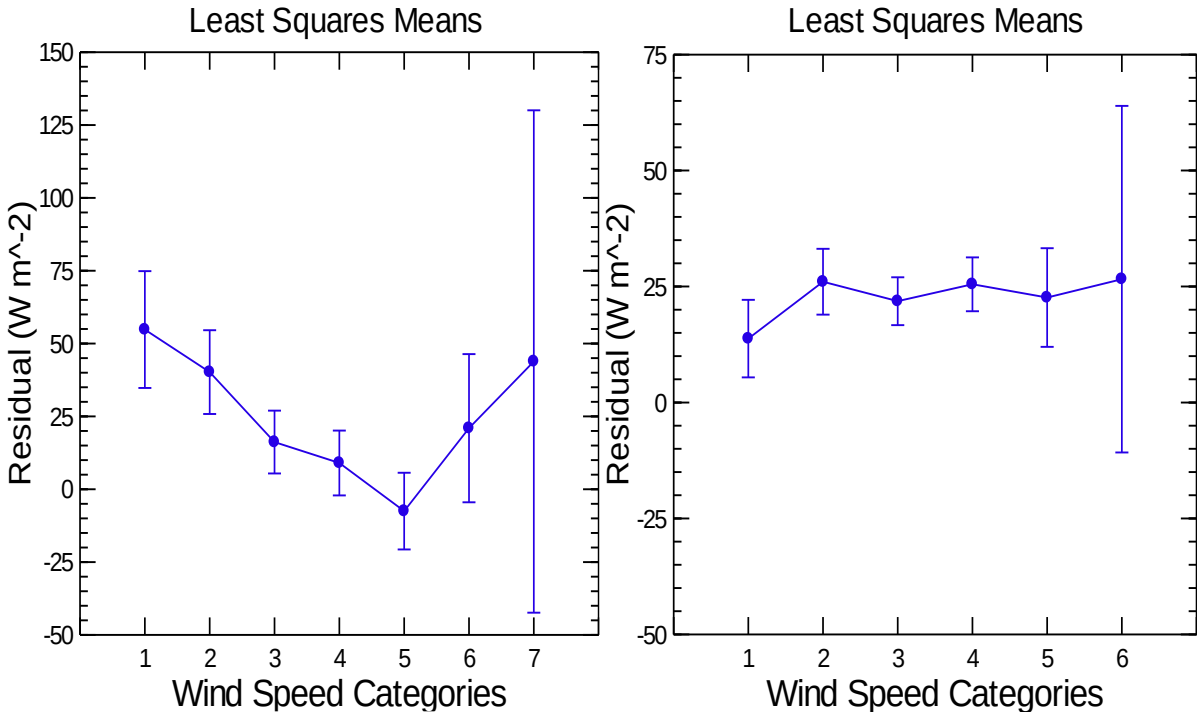

Figure 5-43. EBCE residual vs wind speed category (m/s), north site (left) and south site (right). September 2011, n = 485.

Two-way ANOVA between dependent variable EBCE residual and independent factors site and wind direction category found statistically significant interaction between site and wind direction category for all months: June ($F(7, 821) = 2.097$, $p = 0.042$), July ($F(7, 983) = 5.590$, $p = 0.000$) , August ($F(7, 950) = 19.929$, $p = 0.000$), and September ($F(7, 924) = 38.125$, $p = 0.000$) (Table 5-17). There was statistically significant differences between residual and wind direction category for June ($F(7, 821) = 5.266$, $p = 0.000$), August ($F(7, 950) = 6.592$, $p = 0.000$), and September ($F(7, 924) = 8.295$, $p = 0.000$), but not for July ($F(7, 983) = 1.555$, $p = 0.145$).

Source	Type III SS	df	Mean Squares	F-ratio	p-value
June					
Site	439	1	439	0.176	0.675
Wind Direction	92,246	7	13,178	**5.266**	0.000
Site*Wind Direction	36,732	7	5,247	**2.097**	0.042
Error	2,054,456	821	2,502		
July					
Site	3,720	1	3,720	2.120	0.146
Wind Direction	19,097	7	2,728	1.555	0.145
Site*Wind Direction	68,669	7	9,810	**5.590**	0.000
Error	1,724,954	983	1,755		
August					
Site	34,711	1	34,711	**17.660**	0.000
Wind Direction	90,692	7	12,956	**6.592**	0.000
Site*Wind Direction	274,189	7	39,170	**19.929**	0.000
Error	1,867,231	950	1,966		
September					
Site	3,833	1	3,833	1.982	0.160
Wind Direction	112,297	7	16,042	**8.295**	0.000
Site*Wind Direction	516,156	7	73,736	**38.125**	0.000
Error	1,787,066	924	1,934		

Table 5-17. ANOVA table for residual vs site and wind direction categories June, n = 420, July, n = 506, August, n =482, and September, n = 485, 2011 datasets. Statistically significant F-ratios are in bold font.

Graphs of the relationship between residual and wind direction categories are useful in interpreting the relationship between EBCE residual and wind direction. The wind direction - residual interaction for the north site showed a pattern of decreasing EBCE residual with wind direction 5 and 6, which

were the prevalent wind directions during the day-time period for July, August, and September (Figure 5-45, Figure 5-46 and Figure 5-47). June was in contrast to this pattern, with EBCE residual increasing with the prevalent wind directions 5 and 6 (Figure 5-44). The wind direction - residual interaction for the south site showed an opposing relationship between EBCE residual and wind direction. EBCE residual increased with wind direction 5 and 6 for the months of June, July, and September In contrast, the EBCE residual decreased with wind directions 5 and 6 in. While these relationships are interesting, the opposing behavior north and south site between EBCE residual and wind direction is perplexing, particularly given that LE increased with wind directions 5 and 6. It is possible that the relationship between EBCE residual and wind direction may also be more correlational rather than causal.

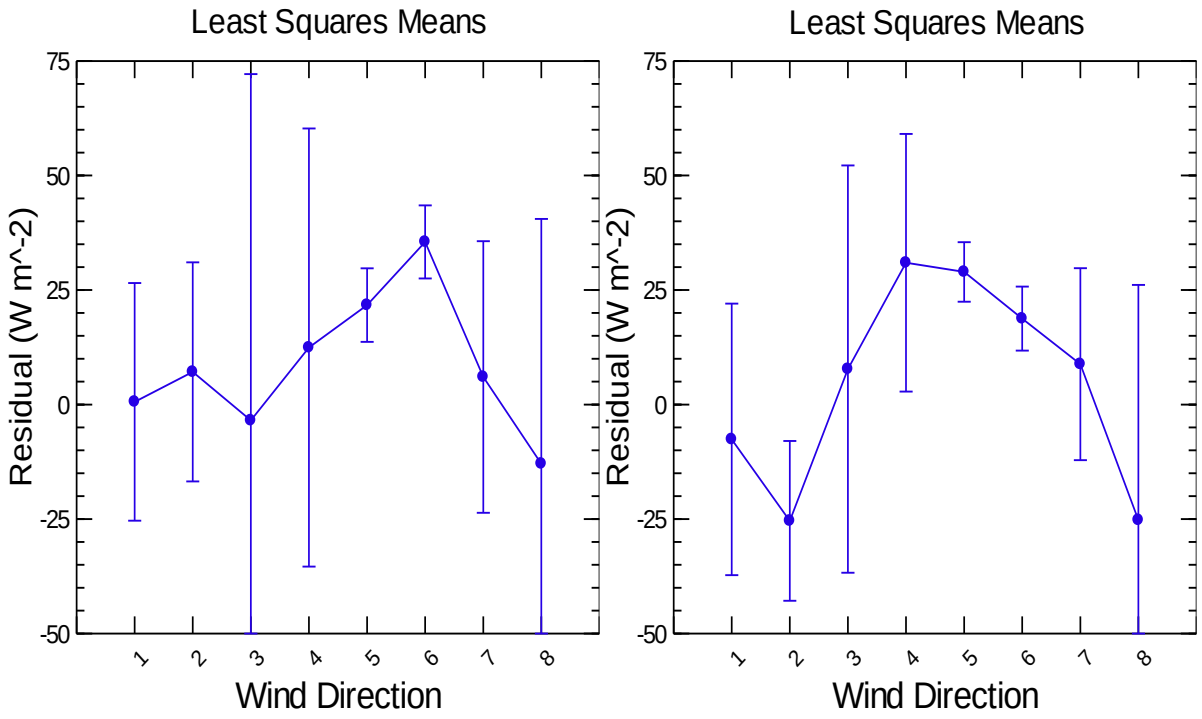

Figure 5-44. EBCE residual vs wind direction, north site (left) and south site (right). June 2011, n = 420. Wind direction categories: 1 = NNE, 2 = ENE, 3 = ESE, 4 = SSE, 5 = SSW, 6 = WSW, 7 = WNW, 8 = NNW.

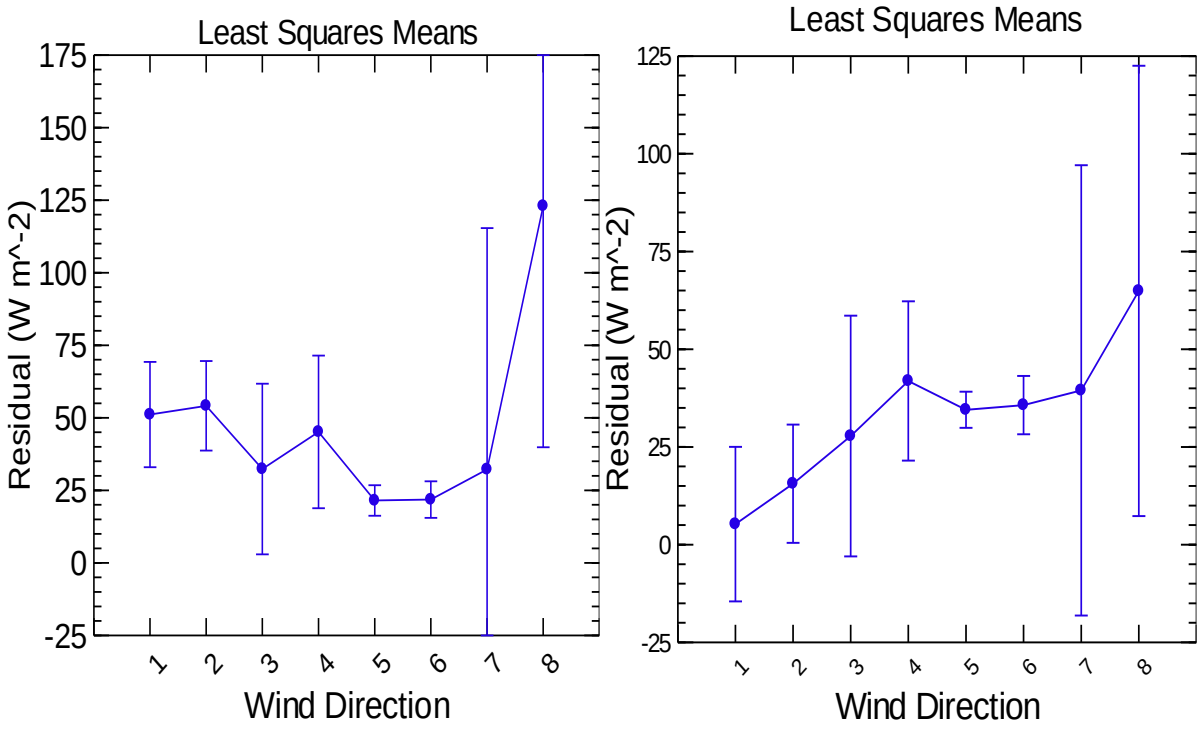

Figure 5-45. EBCE residual vs wind direction, north site (left) and south site (right). July 2011, n = 506. Wind direction categories: 1 = NNE, 2 = ENE, 3 = ESE, 4 = SSE, 5 = SSW, 6 = WSW, 7 = WNW, 8 = NNW.

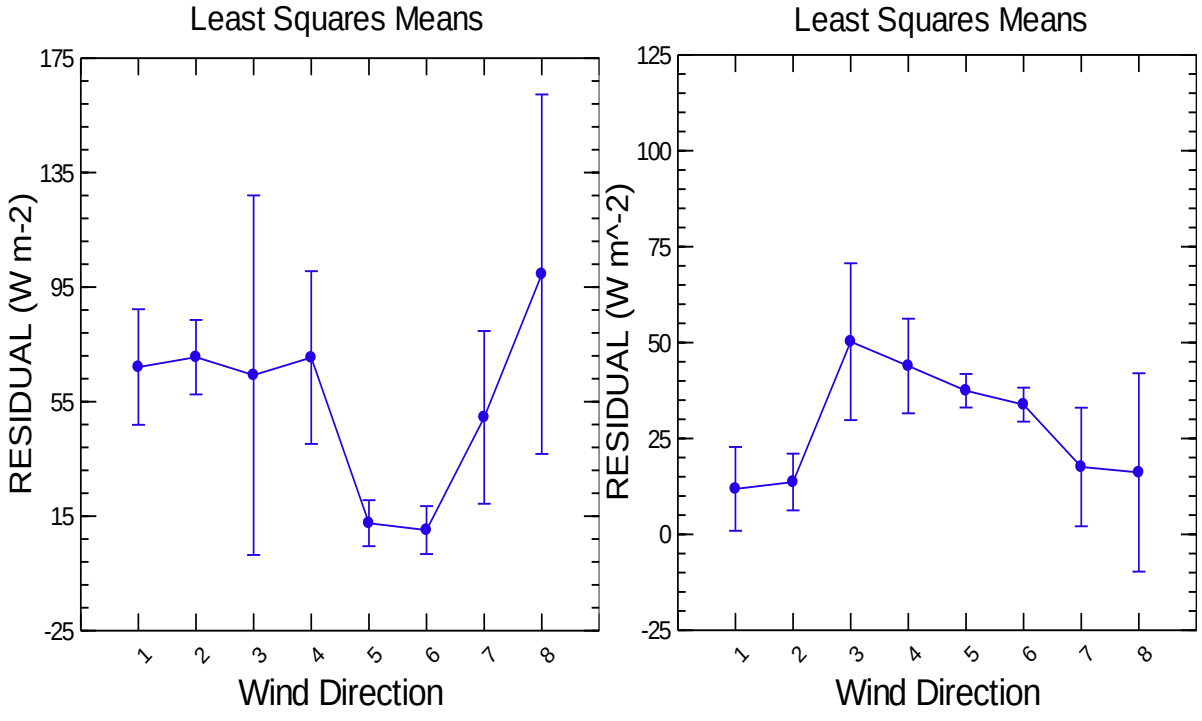

Figure 5-46. EBCE residual vs wind direction, north site (left) and south site (right). August 2011, n = 482. Wind direction categories: 1 = NNE, 2 = ENE, 3 = ESE, 4 = SSE, 5 = SSW, 6 = WSW, 7 = WNW, 8 = NNW.

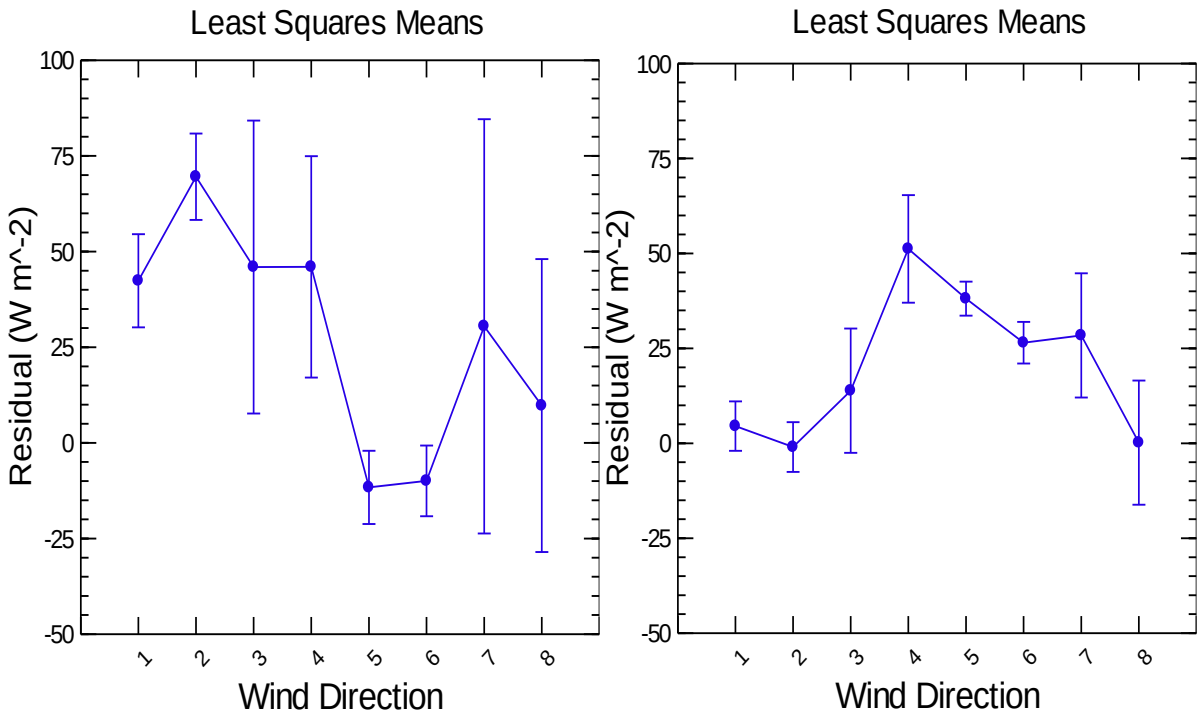

Figure 5-47. EBCE residual vs wind direction, north site (left) and south site (right). September 2011, n = 485. Wind direction categories: 1 = NNE, 2 = ENE, 3 = ESE, 4 = SSE, 5 = SSW, 6 = WSW, 7 = WNW, 8 = NNW.

Chapter 6 Calculation of Cover ET Coefficient (ET_c) Values for the Island Park Lodgepole Pine Forest Community

This section addresses the development of crop coefficient (K_c) (Allen et al. 2005) for the Island Park lodgepole pine forest based on the ET measured by the EC systems at the north and south sites. The concept of K_c is usually applied to a specific crop. The Island Park lodgepole pine forest is comprised of a complex mix of tree overstory and grass and forbs understory. Although the concept is the same as explained in Allen et al. (2005), K_c will be referred to here as a Cover ET coefficient (ET_c) to emphasize the broader inclusion of ET from the forest ecosystem. In this application, ET_c includes the effects of water stress on the ET values.

6.1 Methodology

Daily Cover ET coefficient (ET_c) valued were calculated for the Island Park forests based on the LE from the Island Park 2011 dataset for the north and south sites for the months of June, July, August, and September. The purpose of the ET_c calculation was to 1) determine if ET_c is relatively constant and predictable with time of season and therefore 2) ET_c can be used as a means for estimating ET in an operational mode.

REF ET (Allen 2016) was used to calculate reference ET_r using weather data from the RAWS Island Park weather station (IPF11) for the same period. This station was located approximately 5.8 km south of the south site and 7.6 km south of the north sites, at an elevation of 1,932 m in a small clearing approximately 50 m from the nearest trees. The coordinates for the Island Park RAWS are 44°25'13.8" N, 111°22'02.8" W. Figure 6-1 shows a close-up aerial image of the weather station. Prior to using the Island Park RAWS to calculate ET_r, the climatic characteristics of the station were evaluated to determine if the conditions were appropriate for such use. One tool in this evaluation is the parameter K_o. K_o is used to estimate dew point when it is not available for computing reference ET (Allen and Robison 2007). K_o is an index for evaluating the aridity of a weather station and is calculated as:

$$K_o = T_{min} - T_{dew},$$

where T_{min} is the minimum daily temperature and T_{dew} is the average daily dew point.

Figure 6-1. Close up aerial image showing the Island Park RAWS.

For weather stations in agricultural settings in semiarid and arid climates, the typical K_o value is 2 - 5 degrees. K_o can be used as an indicator of station aridity. Daily K_o values were calculated for the Island Park RAWS station (Figure 6-2). Table 6-1 lists the monthly K_o values for the Island Park RAWS site, the Ashton, Idaho, AgriMet site, and the Average K_o values for Idaho reported in ETIdaho (Allen and Robison 2007). Negative values indicate that the minimum daily temperature fell below the average daily dew point. The K_o values for the Island Park RAWS indicated that it was within the range other weather stations presented in ETIdaho (Allen and Robison 2007).

	K_o Island Park RAWS	K_o Ashton, ID, Agrimet	Mean K_o ET Idaho
June	0.04	1.14	1.5
July	-1.85	-0.65	1.5
August	-0.77	1.16	1.5
September	-0.53	2.82	1.5

Table 6-1. Table of monthly K_o values for the Island Park RAWS, Ashton AgriMet, and the mean monthly K_o values for weather stations in ET Idaho. K_o value for Idaho are also shown from ET Idaho.

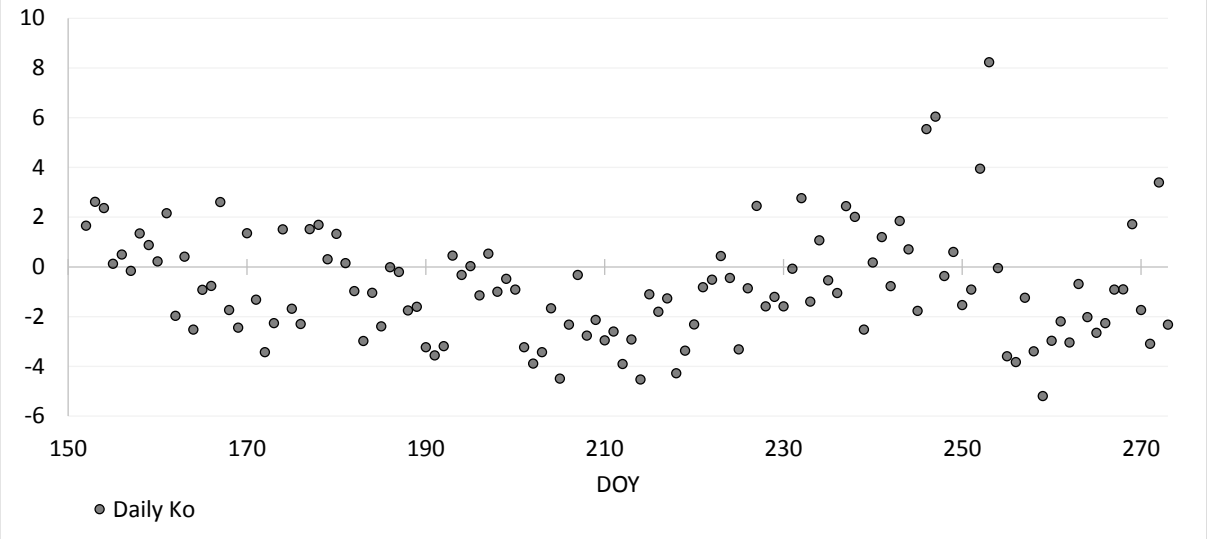

Figure 6-2. Daily K_o values for the Island Park RAWS weather station.

The Island Park RAWS station provided air temperature, relative humidity, winds speed, and dew point as observations taken approximately 6 minutes before the top of the hour. Solar radiation was not available from the RAWS station in 2011. A short wave global radiation (R_s) dataset corresponding to each observation in the RAWS dataset for the time period of interest was developed from the Island Park data. The Island Park data were reported as a half-hourly averages for each 30 minute time step, making each data point representative of a single observation 15

minutes into the period. Since the RAWS data observation was taken near the top of the hour, an estimate of R_s corresponding to the RAWS observation was calculated from the Island Park dataset by averaging R_s from the half-hour period of the RAWS observation and R_s of the half-hour period following the RAWS observation. Each half-hour R_s estimate was an average of three Island Park radiometers, namely the NR01 at the north site and the NR01 and the CNR1 at the south site.

The RAWS data were used as an input file for REF ET. REF ET performed additional QA/QC review of the weather station data. The QA/QC routine consisted of graphically comparing the R_s data to R_{so}, graphically evaluating the behavior of air temperature vs dew point, and graphically evaluating the relative humidity and wind data. If problems were observed with the R_s data, REF ET would make an adjustment to correct the data in the case of R_s. No adjustment was required for the RAWS Island Park dataset. Hourly ET_r in mm/hr was calculated by REF ET.

Three different LE datasets from the Island Park dataset were used to derive ET_c. The first dataset was comprised of only data that were corrected by the LAS-based adjustment. Daily ET_c from this data set was only calculated for days with complete data from 1000 to 1800 hours. These days represented the best data from the dataset. Approximately 85 percent of the total ET_r for the day occurred during this time period. The second dataset used all LAS data regardless of the number of time steps for a particular day. The number of hourly time steps ranged from 2 time steps to 13 time steps covering the period of 600 to 1800 hours. When fewer than 13 time steps were available, they could occur anytime during the day. The dataset corresponding to the extended data set was important because dew, which usually represents a water loss to the system, is evaporated in the early morning periods. ET_c values calculated from early morning periods tend to be higher than later in the day, even though the total ET, in mm/hr, from these periods was low. For the first two datasets, ET_c was calculated for both the north and south sites utilizing the ET (LE) from each site. The LE data from the top of the hour (i.e., time step hours 300, 400, not 330, 430, etc.,) were paired with the RAWS ET_r data and used to calculate ET_c because they spanned the time when the RAWS observations, which were point data recorded approximately 6 minutes before the hour, were taken.

The third data set used all Island Park data that did not have error flags. LAS-adjusted data were used if they were available. If LAS adjusted data were not available, then unadjusted LE from the EC system was used. LAS adjusted data were available for approximately 59 percent of the time steps. The LAS adjustment on average increased data by 10 to 15 percent, however, the unadjusted data was also included to evaluate the effect of including a complete dataset between 700 and 1800

hours for the calculation of ET_c. The third dataset also differed from the first two in that the Island Park ET estimate that was paired with the ET_r estimate from the RAWS data was the average of the ET from the ½ hour time step within which the RAWS observation was taken (i.e., 200, 300, 400, etc.) and the ½ hour time step following the observation (i.e., 230, 330, 430, etc.), resulting in an estimate representative of ET at the top of the hour.

LE in W m^{-2} was converted to ET in mm per ½ hour period using the following conversion sequence:

$$\frac{W}{m^2} = \frac{J}{s\ m^2} * 0.0018\ \frac{MJ}{m^2\ 30min}\ * 0.0408\ \frac{mm}{MJ\ 30\ min}$$

ET was then converted to mm/hr by multiplying by 2.

ET_c was calculated for both the north and south sites utilizing the ET (LE) from each site. The data from the top of the hour (i.e., time step hours 300, 400, not 330, 430, etc.,) were used to calculate ET_c because they spanned the time when the weather station observations that were used to calculate ET_r were taken. Daily ET_c was calculated by summing ET and ET_r for each day, and dividing the period sum ET by period sum ET_r:

$$K_c = \frac{\sum ET_{site}}{\sum ET_r}$$

where ET_{site} is the ET from the area of interest and ET_r is the reference ET.

6.2 Results

The QA/QC plots for a sample period of days are shown in Figure 6-3, Figure 6-4, Figure 6-5, and Figure 6-6. The hourly R_s data points were nearly coincident with the R_{so} curve on clear-sky days, indicating that the R_s data were well-behaved and did not include a systematic bias from a dirty or out-of-level sensor, or a sensor with a calibration error (Figure 6-3). The dew point approached the air temperature during the night time, suggesting these data were reliable and representative of a relatively moderate ET condition (Figure 6-4) (EWRI 2005). Relative humidity data demonstrated appropriate patterns and magnitude throughout the day (Figure 6-5). Wind speed data were within reasonable ranges and were consistent with general patterns observed in the Island Park data (Figure 6-6).

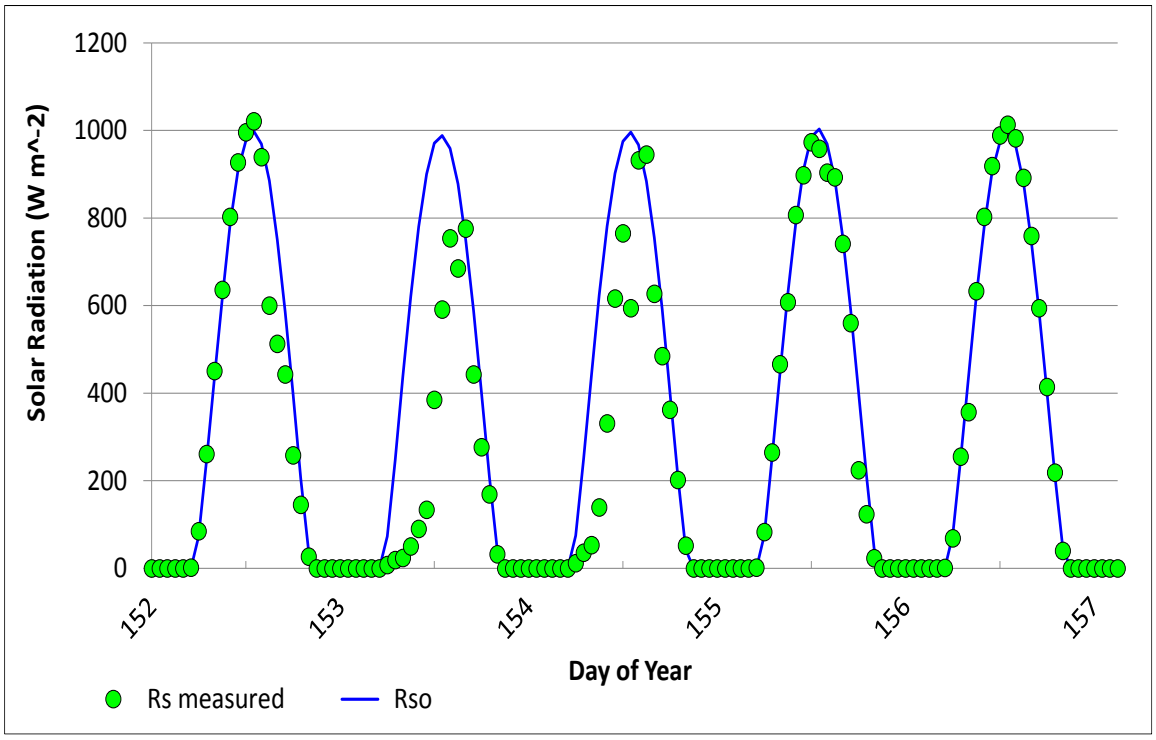

Figure 6-3. Graph from REF ET QA/QC showing the relationship of measured R_s to R_{so} for a sample periods.

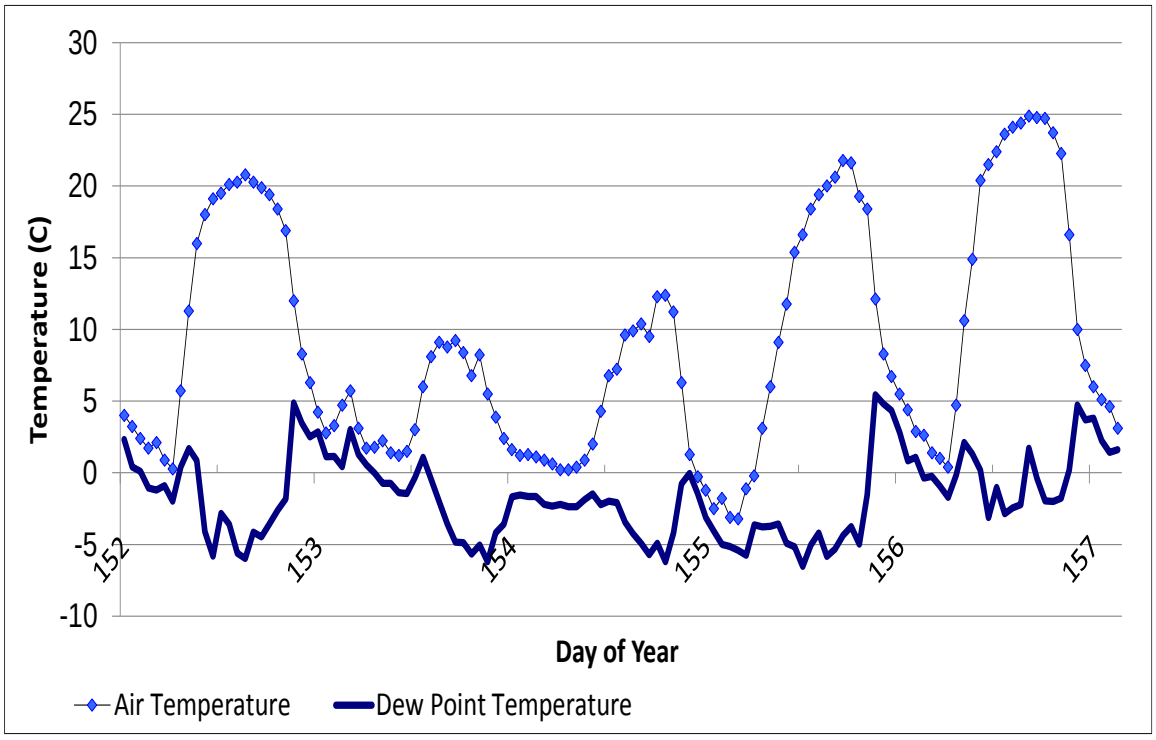

Figure 6-4. . Graph from REF ET QA/QC showing the relationship between air temperature and dew point temperature for a typical sample period.

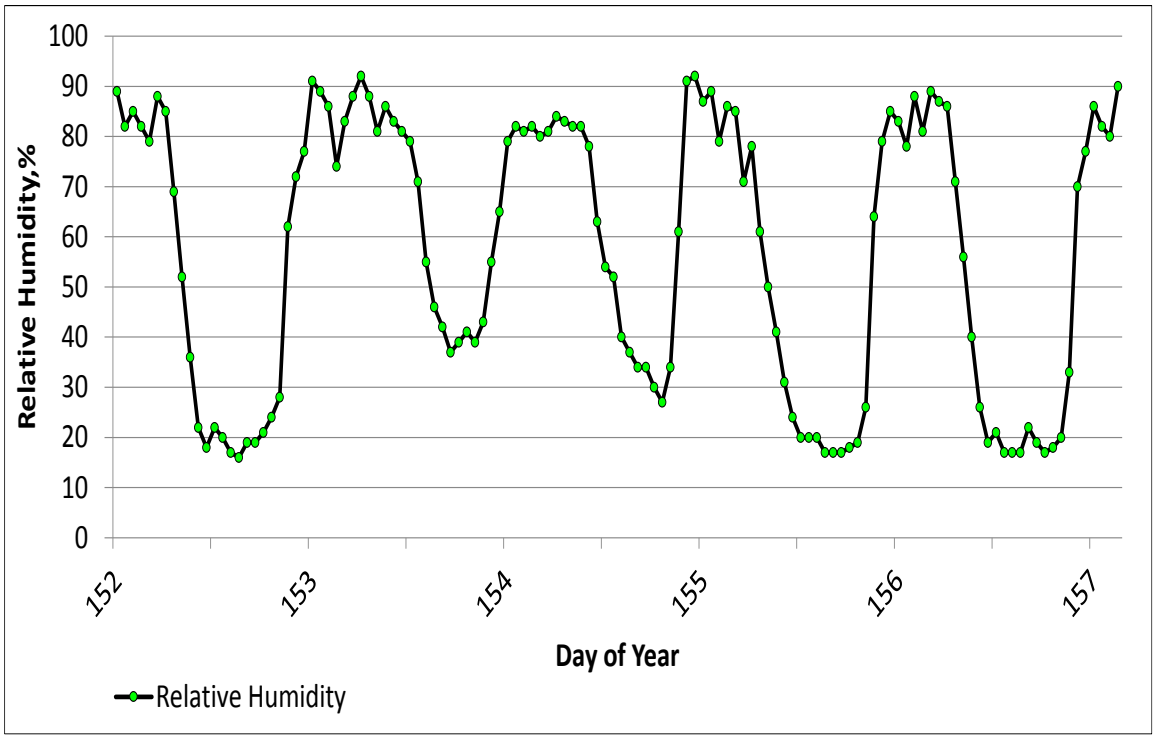

Figure 6-5. Graph from REF ET QA/QC showing the behavior of relative humidity for a sample period for data from the IP RAWS station.

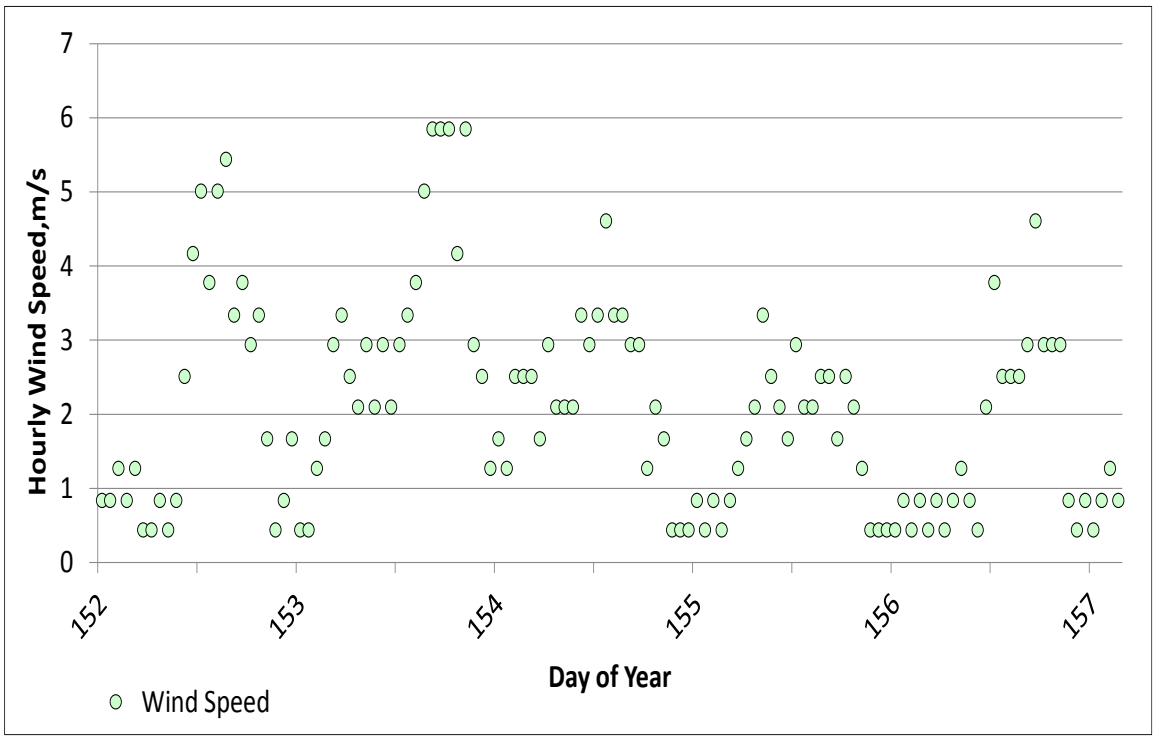

Figure 6-6. Graph from REF ET QA/QC showing the behavior of wind speed for a sample period for data from the IP RAWS station.

Figure 6-7 shows a graph of the daily ET_c values for the June through September period calculated with LAS-adjusted data with data restricted to the 1000 to 1800 hour period (the "first" dataset) and ET_c calculated with all LAS-adjusted data (the "second" dataset). As detailed above, the ET_c values for the 1000 to 1800 hours dataset only included those days for which a complete dataset of LAS-adjusted data for that time period were available. In contrast, the second data set based on the all LAS-adjusted data included all the days during the period regardless of the number of time steps present for a given day. ET_c calculated from the data corresponding the 1000 to 1800 hour period ranged from about 0.8 in June to 0.5 for the north site in September and 0.25 for the south site in September. ET_c calculated for all LAS-adjusted data ranged from about 1.2 in early and mid-summer to 0.5 for the north site in September and 0.25 for the south site in September. The high values are about 50 percent higher for the data set using all LAS adjusted data, whereas the low values are about the same.

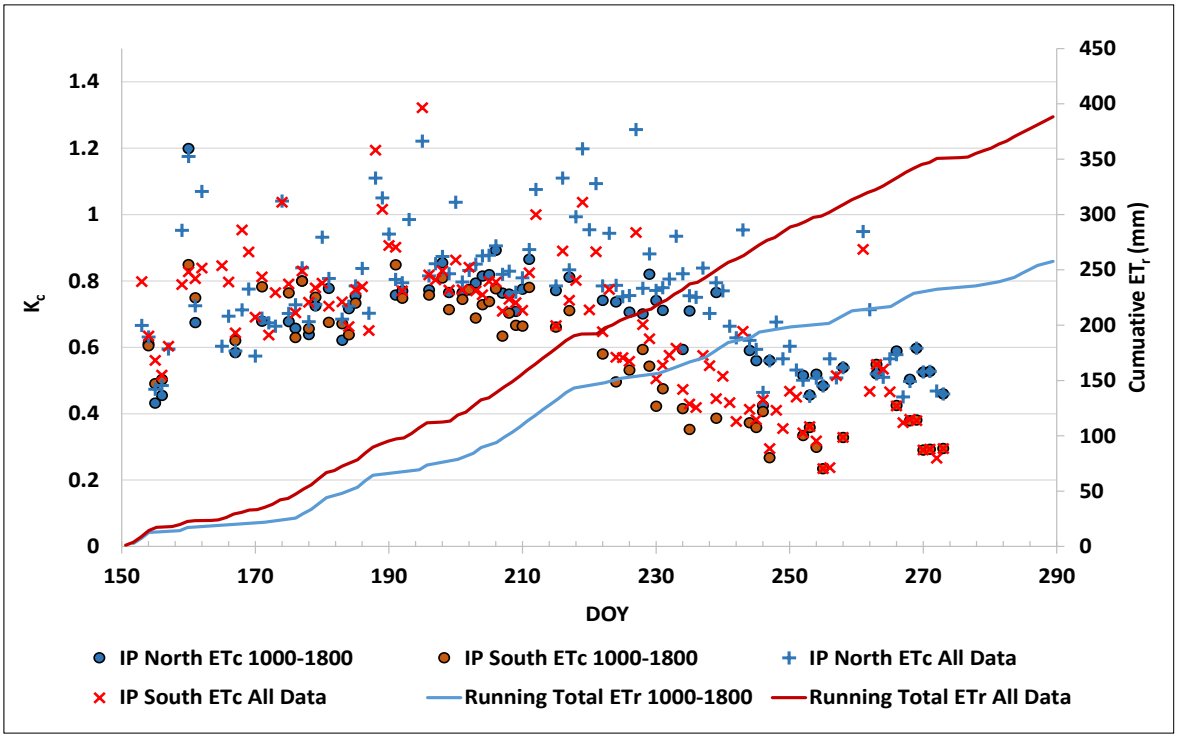

Figure 6-7. Graph of daily ET_c vales calculated from the Island Park dataset using LAS-adjusted data. Also shown is the cumulative Island Park RAWS ET_r used for each ET_c. This graph compares ET_c values calculated using data restricted to 1000-1800 with ET_c values calclated using all LAS-adjusted data.

The inclusion of the early morning time steps (hours 0600-900) in the second dataset tended to increase ET_c because the early morning time steps transformed additional energy flux into LE associated with evaporation of dew and possibly more open plant stomates. The dew formation and evaporation process is an important component of the overall water budget of the forest system so

the ET_c values calculated from the full range of data are of interest. The second dataset also represented higher ET from periods following precipitation that were not included in the first data set due to an incomplete data set. The ET_c values from the second dataset displayed more variability because of the early morning evaporation of the dew and higher ET following precipitation.

Figure 6-7 also shows that ET_c values were similar for the north and south sites at the start of the period but became progressively more distinct as time progressed. The north site maintained a higher ET_c later in the summer and fall. These differences reflected the patterns observed in LE between the two sites in Section 5.1.

The number of hourly time steps and their distribution throughout the day varied for daily ET_c calculated with all LAS-adjusted data on any given day (the second dataset). The effect of the number of hourly periods used to calculate ET_c on the magnitude of ET_c was evaluated graphically (Figure 6-8). With the exception of daily ET_c calculated with two time steps, the magnitude of ET_c calculated with different numbers of hourly time steps fell within a similar range of values. An examination of the data associated with ET_c calculated with two time steps found that that the high ET_c values were from days with only early morning periods when LE was particularly high, probably due to evaporation of dew. Therefore, these values are likely real, but not reflective of a daily ET_c value. While it appears from Figure 6-8 that a reasonable range of ET_c values were obtained regardless of the number of hourly time steps available for a particular day (with the exception of two time steps), ET_c should be calculated using time steps representative of the variation of the ET process throughout the day. If ET_c is to be calculated with data from a limited number of time steps, care should be taken to ensure that ET_c is representative of the daily process.

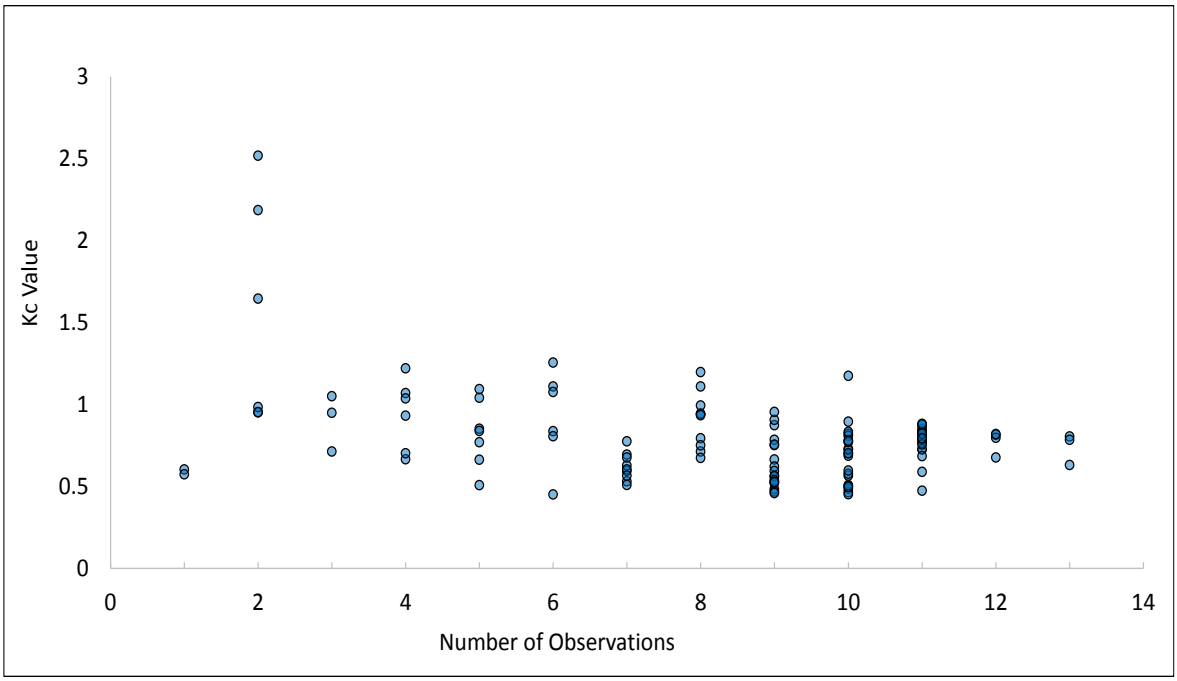

Figure 6-8. Graph comparing the distribution of ET_c values calculated with all LAS-adjusted data based on the number of hourly periods per day included in the ET_c calculation for June-September 2011.

Figure 6-9 shows a graph comparing LE from the Island Park north and south sites and ET_r from the Island Park RAWS for a five-day period in July 2011. This graph shows the relationship of the data that comprises ET_c.

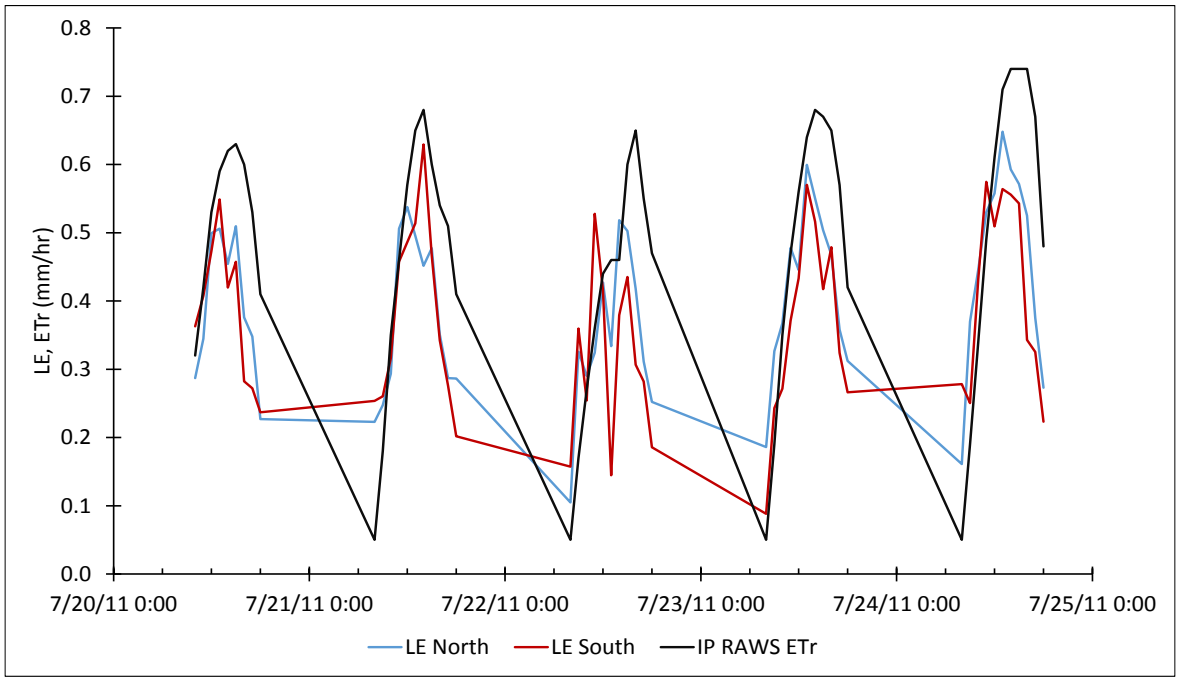

Figure 6-9. Graph comparing hourly ET in mm for the Island Park north and south sites and the Island Park RAWS for a five day period in July, 2011.

The overall patterns and magnitude of the ET_c curves in Figure 6-10, Figure 6-11, Figure 6-12, and Figure 6-13 seems reasonable for a natural forest community. Some ET_c values approached 1 early in the season when water was not limiting to ET, and the values declined as the season progressed and the soil profile dried out. Variability in the curve is probably real and not surprising for ET_c calculated with data from a single season. The variability could probably be reduced by expanding the calculation of ET_c to utilize data from additional years. The use of data from addition years would also increase the confidence in the ET_c values.

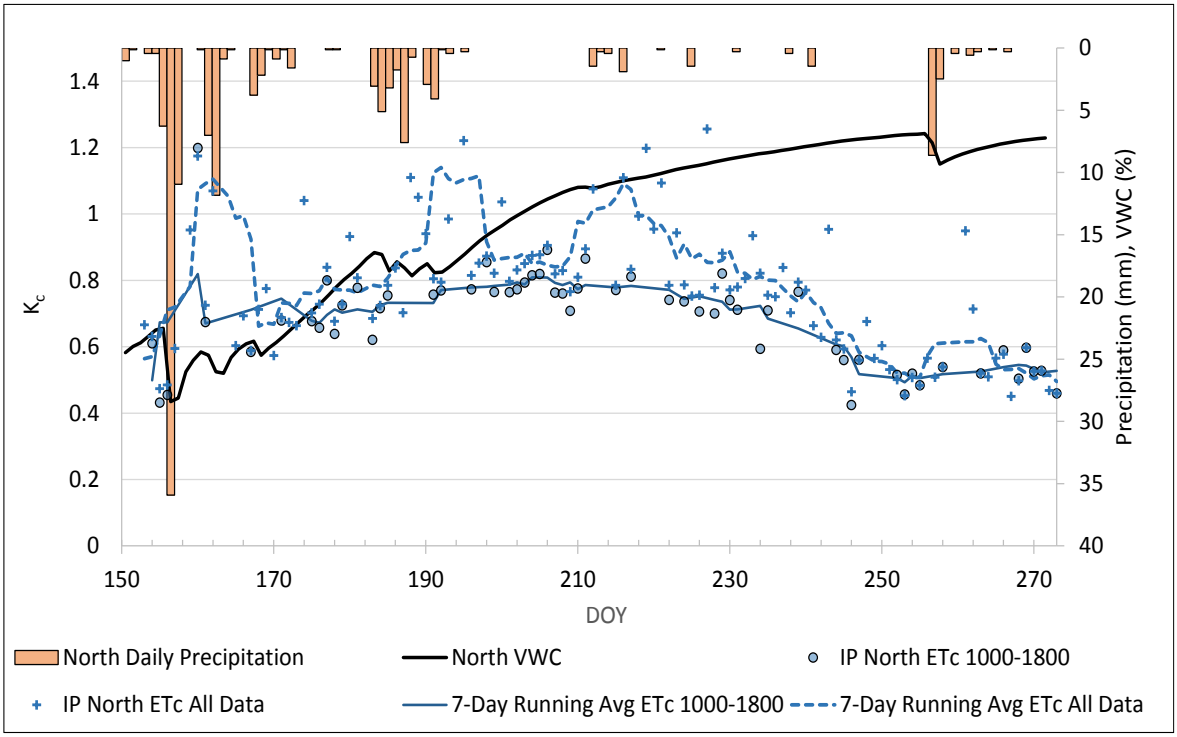

Figure 6-10. Graph comparing daily ET_c values calculated with LAS-adjusted data restricted to 1000-1800 vs all available LAS-adjusted data for the north site for June-September 2011. This graph also compares the 7-day running average for both groups and shows corresponding precipitation and VWC.

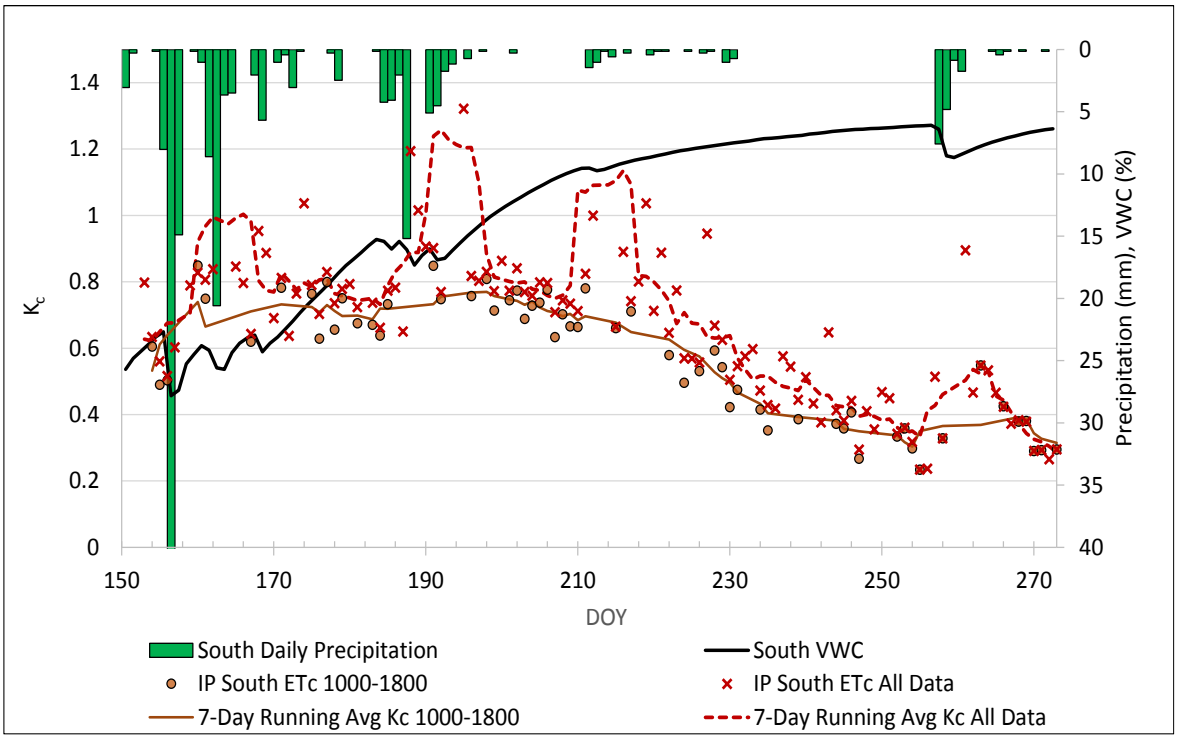

Figure 6-11. Graph comparing daily ET_c values calculated with LAS-adjusted data restricted to 1000-1800 vs all available LAS-adjusted data for the south site for June-September 2011. This graph also compares the 7-day running average for both groups and shows corresponding precipitation and VWC.

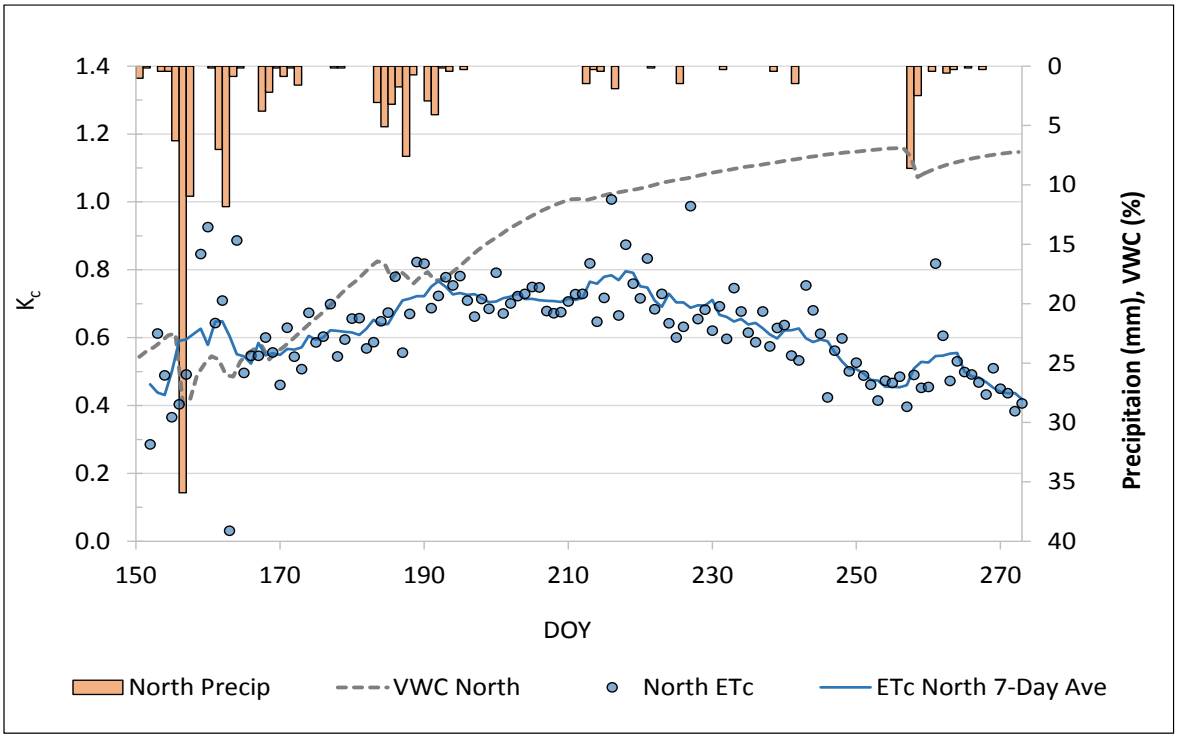

Figure 6-12. Graph showing the daily ET_c for the north site calculated with LAS-adjusted data when available and non-LAS-adjusted data when the former was not available. A line showing the 7-day running average ET_c along with corresponding precipitation and VWC for June-September 2011 is also shown.

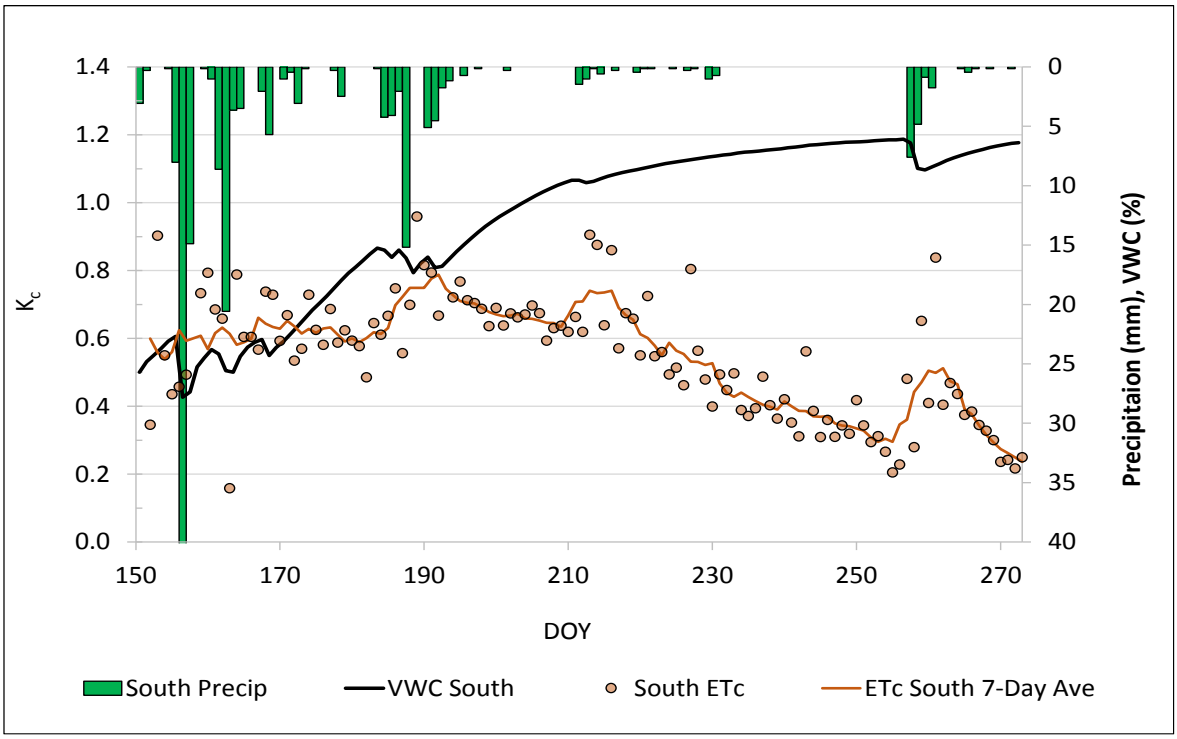

Figure 6-13. Graph showing the daily ET_c for the south site calculated with LAS-adjusted data when available and non-LAS-adjusted data when the former was not available. A line showing the 7-day running average ET_c along with corresponding precipitation and VWC for June-September 2011 is also shown.

Riekerk (1982) studied ET in slash pine tree (*Pinus elliottii*) in Florida using a weighing lysimeter. He measured evapotranspiration to calculated potential evaporation (ET_c). Although the author found considerable variability in the ET_c values based on climatic conditions and available soil water, he reported ET_c values of 0.92 for the autumn months, 0.44 for the winter months, and 0.89 for the spring months. Values were not reported for the summer months due to equipment challenges. Notwithstanding that the Riekerk (1982) work was in a substantially different system, the ET_c rates he found are similar to the Island Park values.

Figure 6-10 and Figure 6-11 compare the daily ET_c values for the north and south site for the first and second datasets. The higher average value of ET_c from the all-LAS adjusted data was apparent for both the north and south sites. The seven-day running average ET_c for the two datasets, which was centered on the day for which the calculation was being made, emphasized the greater magnitude of the all-LAS adjusted data. The higher variability of this dataset noted previously was also evident in the running mean ET_c line.

Figure 6-14 shows a graph of the ET_c values calculated with the third data set for the north and south sites. ET_c ranges from a high of approximately 1 for both the north and south sites, to a low of 0.4 for

the north site and 0.2 for the south site. The higher ET_c values for the north site and the increasing divergence of the ET_c values as time progresses was evident in this data set well,. Overall the ET_c values were in a similar range as those calculated previously with the more limited datasets.

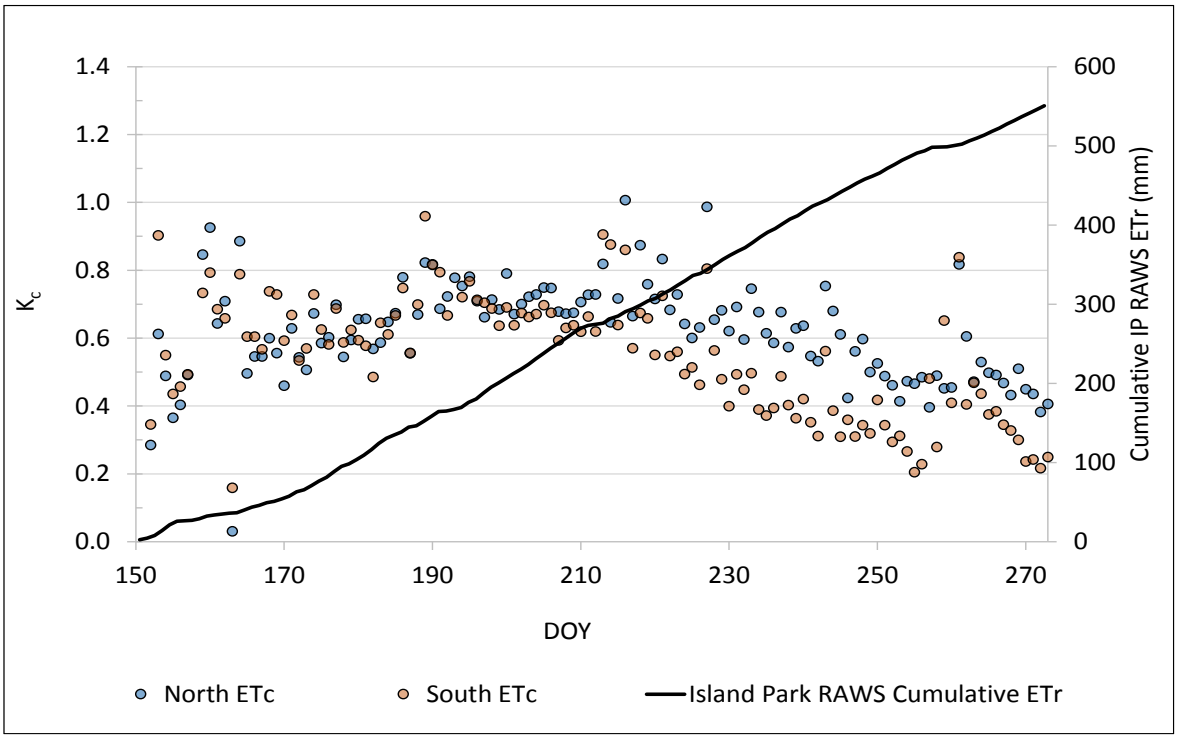

Figure 6-14. Graph comparing daily ET_c values calculated with LAS-adjusted data when available and non-LAS-adjusted data when the former was not available for the Island Park north and south sites for June-September 2011. Also shown is the cumulative Island Park RAWS ET_r used in the calculation of ET_c.

The 7-day running average for the third dataset, shown in Figure 6-12 and Figure 6-13, was less variable as well. The full set of hourly steps in the calculation of daily ET_c reduced the variability of the estimates.

The effect of precipitation can be seen in the ET_c values and the ET_c curves. In the early season when the soils were wet from snowmelt and precipitation, soil water availability was less limiting to ET and additional precipitation had little effect on ET_c. Soil VWC dropped from approximately 30 percent in early June to approximately 15 percent by early July. Precipitation in July, August, and September tended to be reflected in the ET_c values.

The decreasing ET_c as the season progressed was probably due to the soil profile drying out, reducing the RAW, as explained in section 5.1.2. It appears that precipitation primary affected ET_c through surface evaporation, given that elevated ET_c following precipitation was short-lived. However, the

precipitation that fell on about DOY 260 was sufficient to wet the soil profile enough to elevate ET_c for a few days and was also reflected in the soil VWC lines.

Summary

Daily ET_c for the Island Park site reflects the consumptive water loss through evaporation and transpiration relative to ET_r. Daily ET_c calculated from three data sets were compared: the first data set used only LAS-adjusted LE from days when a completed data series was available from 1000 to 1800 hours. The second dataset used all LAS-adjusted ET regardless of the number of time steps available during the day. The third dataset used ET from all time steps that were not removed during QA/QC. If LAS-adjusted ET was available for a time step, it was used; if not ET based on the original LE from the EC system was used, recognizing that it may be 10 – 20 percent low. The daily ET_c from the third dataset is preferred because it best represents the temporal range of the ET process throughout the day. It is recommended that future calculations apply an adjustment to the data that were not LAS-adjusted to correct for the 10 – 20 under-measurement.

Chapter 7 Summary and Conclusions

Surface energy balance for a lodgepole pine forest in eastern Idaho was evaluated using flux measurements from two research measurement sites, north and south, at Island Park, Idaho. R_n was measured with 4-way radiometers. Turbulent fluxes were measured with EC systems. G was estimated from data collected by soil heat flux plates, thermocouples, and volumetric water content probes. CS was estimated using measurements of canopy temperature using an IRT. A error flagging system that accompanied the data was found to be very useful in the data QA/QC process.

EBCE analysis indicated approximately 20 percent closure error for the system. Each component of the EB equation was analyzed to investigate the closure error. The primary contributing factor to the EBCE was determined to be the under-measurement of turbulent fluxes by the EC systems. This finding is consistent with the literature (Wilson et al. 2002, Finnigan et al. 2003, Twine et al. 2000, Foken 2008, Stoy et al. 2013). Reasons for under-measurement of turbulent flux reported in the literature include large eddies and regional advection due to landscape heterogeneity. Recent research also indicates that sonic anemometer design may also result in under-measurement of eddy velocities due to shadowing of the anemometer and result in under-estimation of the fluxes (Frank et al. 2015).

A novel approach to adjust under-measured turbulent fluxes using corresponding H form a LAS was developed and tested with the data from the flux sites. The LAS adjustment increased the EB closure ratio to approximately 95 percent, compared to approximately 80 percent for unadjusted data.

Methodology for estimating G in a complex forest environment were also explored. Each research site included six G subsites selected to represent the variation in solar exposure, vegetation, ground cover of the forest. The subsites were instrumented to collect the data necessary to estimate G for each setting. In addition, instruments at each subsite were placed a two different depths below the soil surface. The combination of subsites and sensor depths was used to explore the number of subsites necessary to develop a representative G and the best depth for sensor placement. The data showed that on a 24-hour basis G tended to 0 regardless of the relative solar exposure and the least squared means difference between G from all subsites was less than 6 W m^{-2}. However, on shorter time steps, such as the half hourly time steps, the solar exposure of the soil subsites became important. Soil subsites with more solar exposure during the day had higher maximums and minimums that those located in shady settings. When considered on 6-hour time intervals, the least

squared mean difference in G between the subsites was as large as 75 W m^{-2}. These findings suggest that the number of sensor sites and their relative solar exposure would be less important for daily or longer energy balance considerations. However, it is recommended that a sufficient number of measurement sites be used to be representative of the diversity of the study area and to provide independent confirmation of G.

In terms of depth of sensor placement to estimate G at the surface, there was no statistically significant difference between the 6 and 12 cm depths. Therefore, it was concluded that sensor depth was not important if the sensors were installed well and the soil properties correctly characterized.

G was found to vary by season. In terms of month-by-month regression assessment of the EB equation, G had a bigger coefficient in June. The coefficient decreased in mid-summer, but increased again in the fall. Regression indicated that G was under-represented in the June and September relative to mid-summer. Reasons for the stronger representation of G in mid-summer may include higher solar angles and less shading of the ground surface.

The Island Park north and south flux sites were approximately 1700 m apart in lodgepole pine forests. The research explored whether these sites measured the same energy flux system, or if they were different. Statistical analysis of the turbulent fluxes on a month by month basis found that there were no statistically significant differences between the turbulent fluxes measured at the two sites in June and July. However, the sites were statistically different in August and September.

Statistical analyses were conducted to explore whether the turbulent fluxes and EBCE were affected by wind speed, wind direction, and time of day. Typical patterns were observed in the data with statistically significant relationship to the turbulent fluxes and EBCE. However, it was likely that these relationships were more correlational than causal. VMC between the two sites followed similar patterns. However, at the north site the VWC was a few percent higher than at the south site. The primary variable in the delinking of the fluxes between the two sites was most likely VWC. The difference in VWC between the two sites was likely enough to reduce LE due to associated differences in soil water potential as the south site has a lower VWC than the north site.

ET derived from the LAS-adjusted LE was used to characterize daily water use for the lodgepole pine forest. ET_r was calculated using meteorological data from a nearby weather station. A ET_c curve was developed for the 4-month period of June, July, August, and September. ET_c values peaked at around

0.8 in late June, corresponding to high R_n and adequate soil moisture. Subsequently ET_c values declined as the season progressed. The south site was characterized by lower ET_c values than the north site in August and September. This declined appeared to be driven by drying soil conditions, as noted above. Although there were differences in the vegetation composition surrounding the north and south sites (the south site had more small meadow-like openings that could contribute to lower ET due to shallower root system), it was hypothesized that the diverging VWC between the north and south site was the primary driving factor responsible for lower k_c values at the south site as time progressed. Precipitation during the summer was sufficient to cause short-term increases in the ET_c rates, but ET_c returned quickly to the previous levels and resumed the long-term trend.

Based on this work, additional research needs include the following:

- Investigation to determine why the VWC decreases more quickly at the south site than the north site. Is the divergence of the VWC real, and if so is the difference due to differences in consumptive water use between the sites related to differences in the forest and understory composition and root structure. Alternatively, soil structural differences between the two sites could result in more moisture being stored in the soil at the north site, and there be able to support higher ET rates.
- Related investigations to understand why LE is higher at the north site than at the south site. Researchers have noted that turbulent fluxes are linked to atmospheric turbulence and u*. Are there differences in these parameters between the north and south sites that contribute to or drive the differences in LE?
- Analysis of data from additional years to verify findings from the 2011 dataset:
    - The relationship between the turbulent fluxes at the north and south towers. Analysis of data from additional years would confirm if the delinking of the turbulent fluxes between the north and south sites follows a similar pattern each year.
    - The application of the LAS adjustment to turbulent flux data from additional years would confirm that the method is robust and applicable across years.
    - The calculation of the ET_c value for additional years. This would increase the robustness and confidence in the ET_c values.
- Approaches to tighten up the error flagging in the original data. This could include the use of a moisture detection plate rather than the rain gauge to determine when precipitation was present.

Limitation of the analysis and the results include the use of the ET_c values for other years and forests. The values presented in this document are from a single year and additional years should be evaluated before the ET_c values are more widely used.

Literature Cited

Alfieri, J. G., & Blanken, P. D. (2012). How representative is a point? The spatial variability of surface energy fluxes across short distances in a sand-sagebrush ecosystem. *Journal of Arid Environments, 87*, 42-49. doi:10.1016/j.jaridenv.2012.04.010

Alfieri, J. G., Kustas, W. P., Prueger, J. H., Hipps, L. E., Evett, S. R., Basara, J. B., . . . Howell, T. A. (2012). On the discrepancy between eddy covariance and lysimetry-based surface flux measurements under strongly advective conditions. *Advances in Water Resources, 50*, 62-78. doi:10.1016/j.advwatres.2012.07.008

Allen, R. (2008). Quality Assessment of Weather Data and Micrometeorological Flux- Impacts of Evapotranspiration Calculation (Vol. 64, pp. 191-204). Journal of Agricultural Meteorology: Society of Agricultural Meteorology of Japan.

Allen, R. G., Pereira, L. S., Raes, D., & Smith, M. (1998). Crop evapotranspiration: Guidelines for computing crop requirements. (pp. 300). Rome, Italy: FAO.

Allen, R. G., Pereira, L. S., Smith, M., Raes, D., & Wright, J. L. (2005). FAO-56 dual crop coefficient method for estimating evaporation from soil and application extensions. *Journal of Irrigation and Drainage Engineering-Asce, 131*(1), 2-13. doi:10.1061/(asce)0733-9437(2005)131:1(2)

Allen, R. G., Pruitt, W. O., Wright, J. L., Howell, T. A., Ventura, F., Snyder, R., . . . Elliott, R. (2006). A recommendation on standardized surface resistance for hourly calculation of reference ETO by the FAO56 Penman-Monteith method. *Agricultural Water Management, 81*(1-2), 1-22. doi:10.1016/j.agwat.2005.03.007

Allen, R. G., Robison, C.W. (2007). Evapotranspiration and consumptive irrigation water requirements for Idaho. Technical Report prepared by the University of Idaho Research and Extension Center, Kimberly, Idaho. Prepared for Idaho Department of Water Resources, Boise, Idaho.

Anderson, R. G., & Wang, D. (2014). Energy budget closure observed in paired Eddy Covariance towers with increased and continuous daily turbulence. *Agricultural and Forest Meteorology, 184*, 204-209. doi:10.1016/j.agrformet.2013.09.012

Baldocchi, D., Finnigan, J., Wilson, K., Paw U, K. T., & Falge, E. (2000). On measuring net ecosystem carbon exchange over tall vegetation on complex terrain. *Boundary-Layer Meteorology, 96*(1-2), 257-291. doi:10.1023/a:1002497616547

Barr, A. G., Morgenstern, K., Black, T. A., McCaughey, J. H., & Nesic, Z. (2006). Surface energy balance closure by the eddy-covariance method above three boreal forest stands and implications for the measurement of the CO2 flux. *Agricultural and Forest Meteorology, 140*(1-4), 322-337. doi:10.1016/j.agrformet.2006.08.007

Blonquist, J. M., Tanner, B. D., & Bugbee, B. (2009). Evaluation of measurement accuracy and comparison of two new and three traditional net radiometers. *Agricultural and Forest Meteorology, 149*(10), 1709-1721. doi:10.1016/j.agrformet.2009.05.015

Brotzge, J. A., & Duchon, C. E. (2000). A field comparison among a domeless net radiometer, two four-component net radiometers, and a domed net radiometer. *Journal of Atmospheric and Oceanic Technology, 17*(12), 1569-1582. doi:10.1175/1520-0426(2000)017<1569:afcaad>2.0.co;2

Burba, G. (2005). Eddy Covariance Method for Scientific, Industrial, Agricultural, and Regulatory Applications. LI-COR Biosciences, Lincoln, Nebaska.

Doorenbos, J., & Pruitt, W. O. (1977). Crop water requirements (Vol. Irrigation and Drainage Paper No.24 (rev.)). Rome, Italy: FAO.

EWRI. (2005). The ASCE Standardized Reference Evapotranspiration Equation. Report of the Task Committee on Standardization of Reference Evapotranspiration, Environmental and Water Resources. Institute of the American Society of Civil Engineers.

Facchi, A., Gharsallah, O., Corbari, C., Masseroni, D., Mancini, M., & Gandolfi, C. (2013). Determination of maize crop coefficients in humid climate regime using the eddy covariance technique. *Agricultural Water Management, 130*, 131-141. doi:10.1016/j.agwat.2013.08.014

Finnigan, J. J., Clement, R., Malhi, Y., Leuning, R., & Cleugh, H. A. (2003). A re-evaluation of long-term flux measurement techniques - Part I: Averaging and coordinate rotation. *Boundary-Layer Meteorology, 107*(1), 1-48. doi:10.1023/a:1021554900225

Foken, T. (2008). The energy balance closure problem: An overview. *Ecological Applications, 18*(6), 1351-1367. doi:10.1890/06-0922.1

Foken, T., Wimmer, F., Mauder, M., Thomas, C., & Liebethal, C. (2006). Some aspects of the energy balance closure problem. *Atmospheric Chemistry and Physics, 6*, 4395-4402.

Franssen, H. J. H., Stockli, R., Lehner, I., Rotenberg, E., & Seneviratne, S. I. (2010). Energy balance closure of eddy-covariance data: A multisite analysis for European FLUXNET stations. *Agricultural and Forest Meteorology, 150*(12), 1553-1567. doi:10.1016/j.agrformet.2010.08.005

Froelich, N. J., Schmid, H. P., Grimmond, C. S. B., Su, H. B., & Oliphant, A. J. (2005). Flow divergence and density flows above and below a deciduous forest. Part I. Non-zero mean vertical wind above canopy. *Agricultural and Forest Meteorology, 133*(1-4), 140-152. doi:10.1016/j.agrformet.2005.09.005

Garai, A., Kleissl, J., & Smith, S. G. L. (2010). Estimation of Biomass Heat Storage Using Thermal Infrared Imagery: Application to a Walnut Orchard. *Boundary-Layer Meteorology, 137*(2), 333-342. doi:10.1007/s10546-010-9524-x

Ghamarnia, H., Miri, E., & Ghobadei, M. (2014). Determination of water requirement, single and dual crop coefficients of black cumin (Nigella sativa L.) in a semi-arid climate. *Irrigation Science, 32*(1), 67-76. doi:10.1007/s00271-013-0412-2

Gharsallah, O., Facchi, A., & Gandolfi, C. (2013). Comparison of six evapotranspiration models for a surface irrigated maize agro-ecosystem in Northern Italy. *Agricultural Water Management, 130*, 119-130. doi:10.1016/j.agwat.2013.08.009

Greth, J. (2013). An EPSCoR evapotranspiration and energy balance flux site in southern idaho in support of remote sensing and hydroclimate modeling. Maters Thesis. University of Idaho, Moscow, ID.

Haverd, V., Cuntz, M., Leuning, R., & Keith, H. (2007). Air and biomass heat storage fluxes in a forest canopy: Calculation within a soil vegetation atmosphere transfer model. *Agricultural and Forest Meteorology, 147*(3-4), 125-139. doi:10.1016/j.agrformet.2007.07.006

Heusinkveld, B. G., Jacobs, A. F. G., Holtslag, A. A. M., Berkowicz, S. M., & Ams. (2002). *The surface energy balance over a desert, and the relevance of soil heat flux measurements*.

Higgins, C. W. (2012). A-posteriori analysis of surface energy budget closure to determine missed energy pathways. *Geophysical Research Letters, 39*, 5. doi:10.1029/2012gl052918

Hoedjes, J. C. B., Zuurbier, R. M., & Watts, C. J. (2002). Large aperture scintillometer used over a homogeneous irrigated area, partly affected by regional advection. *Boundary-Layer Meteorology, 105*(1), 99-117. doi:10.1023/a:1019644420081

Hsieh, C. I., Huang, C. W., & Kiely, G. (2009). Long-term estimation of soil heat flux by single layer soil temperature. *International Journal of Biometeorology, 53*(1), 113-123. doi:10.1007/s00484-008-0198-8

Kessomkiat, W., Franssen, H. J. H., Graf, A., & Vereecken, H. (2013). Estimating random errors of eddy covariance data: An extended two-tower approach. *Agricultural and Forest Meteorology, 171*, 203-219. doi:10.1016/j.agrformet.2012.11.019

Kjaersgaard, J. H., Cuenca, R. H., Martinez-Cob, A., Gavilan, P., Plauborg, F., Mollerup, M., & Hansen, S. (2009). Comparison of the performance of net radiation calculation models. *Theoretical and Applied Climatology, 98*(1-2), 57-66. doi:10.1007/s00704-008-0091-8

Kohsiek, W., Liebethal, C., Foken, T., Vogt, R., Oncley, S. P., Bernhofer, C., & Debruin, H. A. R. (2007). The energy balance experiment EBEX-2000. Part III: Behaviour and quality of the radiation measurements. *Boundary-Layer Meteorology, 123*(1), 55-75. doi:10.1007/s10546-006-9135-8

Liu, Y. B., Hiyama, T., Yasunari, T., & Tanaka, H. (2012). A nonparametric approach to estimating terrestrial evaporation: Validation in eddy covariance sites. *Agricultural and Forest Meteorology, 157*, 49-59. doi:10.1016/j.agrformet.2012.01.012

Massman, W. J., & Lee, X. (2002). Eddy covariance flux corrections and uncertainties in long-term studies of carbon and energy exchanges. *Agricultural and Forest Meteorology, 113*(1-4), 121-144. doi:10.1016/s0168-1923(02)00105-3

Michel, D., Philipona, R., Ruckstuhl, C., Vogt, R., & Vuilleumier, L. (2008). Performance and uncertainty of CNR1 net radiometers during a one-year field comparison. *Journal of Atmospheric and Oceanic Technology, 25*(3), 442-451. doi:10.1175/2007jtecha973.1

Michiles, A. A. D., & Gielow, R. (2008). Above-ground thermal energy storage rates, trunk heat fluxes and surface energy balance in a central Amazonian rainforest. *Agricultural and Forest Meteorology, 148*(6-7), 917-930. doi:10.1016/j.agrformet.2008.01.001

Moderow, U., Aubinet, M., Feigenwinter, C., Kolle, O., Lindroth, A., Molder, M., . . . Bernhofer, C. (2009). Available energy and energy balance closure at four coniferous forest sites across Europe. *Theoretical and Applied Climatology, 98*(3-4), 397-412. doi:10.1007/s00704-009-0175-0

Moderow, U., Feigenwinter, C., & Bernhofer, C. (2007). Estimating the components of the sensible heat budget of a tall forest canopy in complex terrain. *Boundary-Layer Meteorology, 123*(1), 99-120. doi:10.1007/s10546-006-9136-7

Ogee, J., Lamaud, E., Brunet, Y., Berbigier, P., & Bonnefond, J. M. (2001). A long-term study of soil heat flux under a forest canopy. *Agricultural and Forest Meteorology, 106*(3), 173-186. doi:10.1016/s0168-1923(00)00214-8

Oliphant, A. J., Grimmond, C. S. B., Zutter, H. N., Schmid, H. P., Su, H. B., Scott, S. L., . . . Ehman, J. (2004). Heat storage and energy balance fluxes for a temperate deciduous forest. *Agricultural and Forest Meteorology, 126*(3-4), 185-201. doi:10.1016/j.agrformet.2004.07.003

Oncley, S. P., Foken, T., Vogt, R., Kohsiek, W., DeBruin, H. A. R., Bernhofer, C., . . . Weidinger, T. (2007). The Energy Balance Experiment EBEX-2000. Part I: Overview and energy balance. *Boundary-Layer Meteorology, 123*(1), 1-28. doi:10.1007/s10546-007-9161-1

Panin, G. N., & Bernhofer, C. (2008). Parametrization of Turbulent Fluxes over Inhomogeneous Landscapes. *Izvestiya Atmospheric and Oceanic Physics, 44*(6), 701-716. doi:10.1134/s0001433808060030

Papale, D., Reichstein, M., Aubinet, M., Canfora, E., Bernhofer, C., Kutsch, W., . . . Yakir, D. (2006). Towards a standardized processing of Net Ecosystem Exchange measured with eddy covariance technique: algorithms and uncertainty estimation. *Biogeosciences, 3*(4), 571-583.

Riekerk, H. (1982). Pine tree evapotranspiration. Research Center Research Project Technical Completion Report OWRT Project Number A-039-FLA. Publication No. 62 Florida Water Resources March 24. Retrieved from http://wrrc.essie.ufl.edu/common/info/pdf/62_pine_tree_evapotranspiration.pdf on Nov 25, 2016.

Stoy, P. C., Mauder, M., Foken, T., Marcolla, B., Boegh, E., Ibrom, A., . . . Varlagin, A. (2013). A data-driven analysis of energy balance closure across FLUXNET research sites: The role of

landscape scale heterogeneity. *Agricultural and Forest Meteorology, 171*, 137-152. doi:10.1016/j.agrformet.2012.11.004

Twine, T. E., Kustas, W. P., Norman, J. M., Cook, D. R., Houser, P. R., Meyers, T. P., . . . Wesely, M. L. (2000). Correcting eddy-covariance flux underestimates over a grassland. *Agricultural and Forest Meteorology, 103*(3), 279-300. doi:10.1016/s0168-1923(00)00123-4

Webb, E. K., Pearman, G. I., & Leuning, R. (1980). CORRECTION OF FLUX MEASUREMENTS FOR DENSITY EFFECTS DUE TO HEAT AND WATER-VAPOR TRANSFER. *Quarterly Journal of the Royal Meteorological Society, 106*(447), 85-100. doi:10.1002/qj.49710644707

Wilson, K., Goldstein, A., Falge, E., Aubinet, M., Baldocchi, D., Berbigier, P., . . . Verma, S. (2002). Energy balance closure at FLUXNET sites. *Agricultural and Forest Meteorology, 113*(1-4), 223-243. doi:10.1016/s0168-1923(02)00109-0

Wright, J. L. (1982). NEW EVAPO-TRANSPIRATION CROP COEFFICIENTS. *Journal of the Irrigation and Drainage Division-Asce, 108*(1), 57-74.

Zeri, M., & Sa, L. D. A. (2010). The impact of data gaps and quality control filtering on the balances of energy and carbon for a Southwest Amazon forest. *Agricultural and Forest Meteorology, 150*(12), 1543-1552. doi:10.1016/j.agrformet.2010.08.004

Zhao, W., Allen, R. G., & Stewart, J. W. (2014). Report on Longwave Radiation Calibration in Island Park. Kimberly, Idaho: Unpublished report.

Zhu, G. F., Su, Y. H., Li, X., Zhang, K., Li, C. B., & Ning, N. (2014). Modelling evapotranspiration in an alpine grassland ecosystem on Qinghai-Tibetan plateau. *Hydrological Processes, 28*(3), 610-619. doi:10.1002/hyp.9597

Appendices

Appendix A. Maps and List of Instrumentation at the Island Park North and South Sites

Island Park North Site

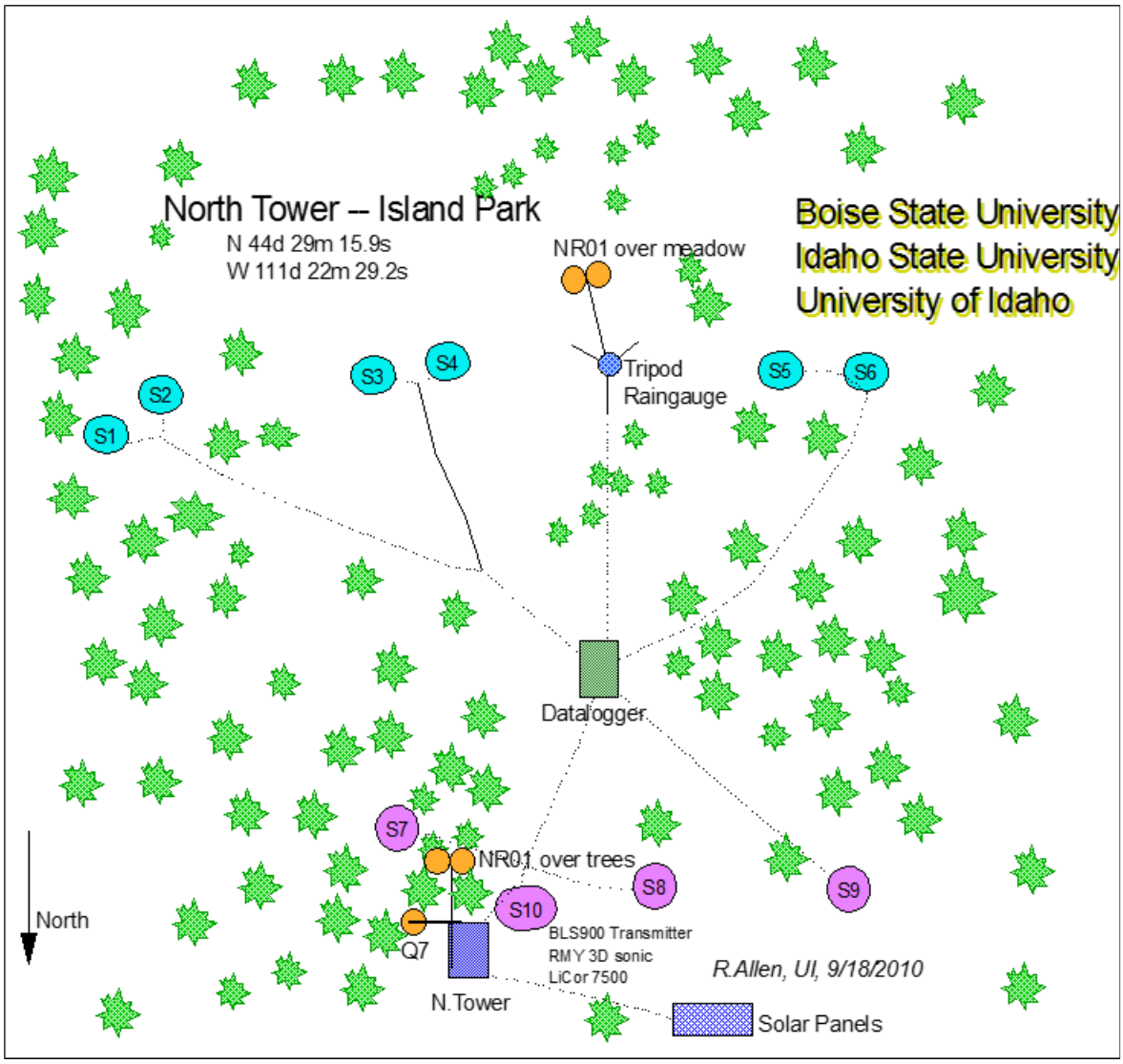

Figure A-1. Schematic of the Island Park north site (Allen, 2011, Island Park site description (http://www.kimberly.uidaho.edu/epscor/IslandPark/Island_Park_Site_Description.pdf).

Table A-1. List of sensors at the Island Park north site.		
Location	**Device**	**Depth or Height**
Instruments on North Tower		
	NR01 4-way Radiometer	22 m over trees to South
	Q7 Net Radiometer	5 m over meadow to West
	BLS900 Scintec Transmitter	24 m looking south
	RM Young 3D sonic	25 m SW corner of tower
	LiCor 7500 Hygrometer	25 m SW corner of tower
	Apogee Pyranometer	24.5 m SW corner of tower
	Apogee IRT	22 m NE corner of tower looking toward NE at 25 deg from Nadir at tree canopy
	CR1000 datalogger	4 m on tower
	Vaisalla RH/T	4 m on tower
	motion-detection camera	
Instruments at the North Soil Sensor Site		
	CR1000 datalogger and 3 multiplexors	
	Vaisalla RH/T	2 m on datalogger mast
	NR01 4-way Rad.	3.5 m over understory in open meadow, some shade at times
	Tipping bucket rain gauge	3.5 m on NR01 tripod
Instrument at Soil Heat Flux Sites		
N1 *Mostly-shaded, grasses and forbs* *Relatively 'lush' understory* *~0-2 cm are old needle mulch*	Rebs Soil Heat Flux Plate	6 cm
	Rebs Soil Heat Flux Plate	12 cm
	Thermocouple	2 cm
	Thermocouple	4 cm
	Thermocouple	9 cm
	Thermocouple	14 cm
	Campbell Scientific CS616 soil water content	0-12 cm (at an angle)
N2 *Mostly-shaded, grasses and forbs* *Relatively 'lush' understory* *~0-2 cm are old needle mulch*	Rebs Soil Heat Flux Plate	6 cm
	Rebs Soil Heat Flux Plate	12 cm
	Hukseflux Self-Calibrating Soil Heat Flux Plate	12 cm
	Thermocouple	2 cm
	Thermocouple	4 cm
	Thermocouple	9 cm
	Thermocouple	14 cm
	Campbell Scientific CS616 soil water content	0-12 cm (at an angle)
N3 *Mostly Open Meadow, grasses and forbs, some shade*	Rebs Soil Heat Flux Plate	6 cm
	Rebs Soil Heat Flux Plate	12 cm
	Thermocouple	2 cm

~0-1 cm are old needle mulch	Thermocouple	4 cm
	Thermocouple	9 cm
	Thermocouple	14 cm
	Campbell Scientific CS616 soil water content	0-12 cm (at an angle)
N4 *Mostly Open Meadow, grasses and forbs, some shade* *~0-1 cm are old needle mulch*	Rebs Soil Heat Flux Plate	6 cm
	Rebs Soil Heat Flux Plate	12 cm
	Thermocouple	2 cm
	Thermocouple	4 cm
	Thermocouple	9 cm
	Thermocouple	14 cm
	Campbell Scientific CS616 soil water content	0-12 cm (at an angle)
N5 *Open/Shaded over time, grasses and forbs* *~0-2 cm are old needle mulch*	Rebs Soil Heat Flux Plate	6 cm
	Rebs Soil Heat Flux Plate	12 cm
	Thermocouple	2 cm
	Thermocouple	4 cm
	Thermocouple	9 cm
	Thermocouple	14 cm
	Decagon Echo 5 soil moisture sensor	2-6 cm (near vertical)
	Campbell Scientific CS616 soil water content	0-12 cm (at an angle)
N6 *Open/Shaded over time* *Open/Shaded over time* *~0-3 cm are old needle mulch*	Rebs Soil Heat Flux Plate	6 cm
	Rebs Soil Heat Flux Plate	12 cm
	Thermocouple	2 cm
	Thermocouple	4 cm
	Thermocouple	9 cm
	Thermocouple	14 cm
	Campbell Scientific CS616 soil water content	0-12 cm (at an angle)
Deeper Soil Water Content Sites		
N7 *Shaded (in patch of trees), grasses and forbs* *Relatively 'lush' understory*	Campbell Scientific CS616 soil water content	12-42 cm
	Campbell Scientific CS616 soil water content	42–72 cm
	Campbell Scientific CS616 soil water content	70-100 cm
	Decagon Echo 5 soil moisture sensor	100-105 cm
N8 *Open, grasses and forbs, occasional shade*	Campbell Scientific CS616 soil water content	12-42 cm
	Campbell Scientific CS616 soil water content	42-72 cm
	Campbell Scientific CS616 soil water content	12-42 cm Not listed

	Decagon Echo 5 soil moisture sensor	100-105 cm
N9 *Open, grasses and forbs, occasional shade*	Campbell Scientific CS616 soil water content	12-42 cm
	Campbell Scientific CS616 soil water content	42-72 cm
	Campbell Scientific CS616 soil water content	60-90 cm cm over frac. rock
	Decagon Echo 5 soil moisture sensor	100-105 cm
N10 *In South Power Pole trench at North Tower, buried in bottom of hole, in shad of trees and tower*	Campbell Scientific CS616 soil water content	2.4 m (8 ft) placed horizontally in disturbed soil alongside and above frac. rock

Table A-1. List of sensors at the Island Park north site (adapted from Allen, 2011, Island Park Site Description http://www.kimberly.uidaho.edu/epscor/IslandPark/Island_Park_Site_Description.pdf).

Island Park South Site

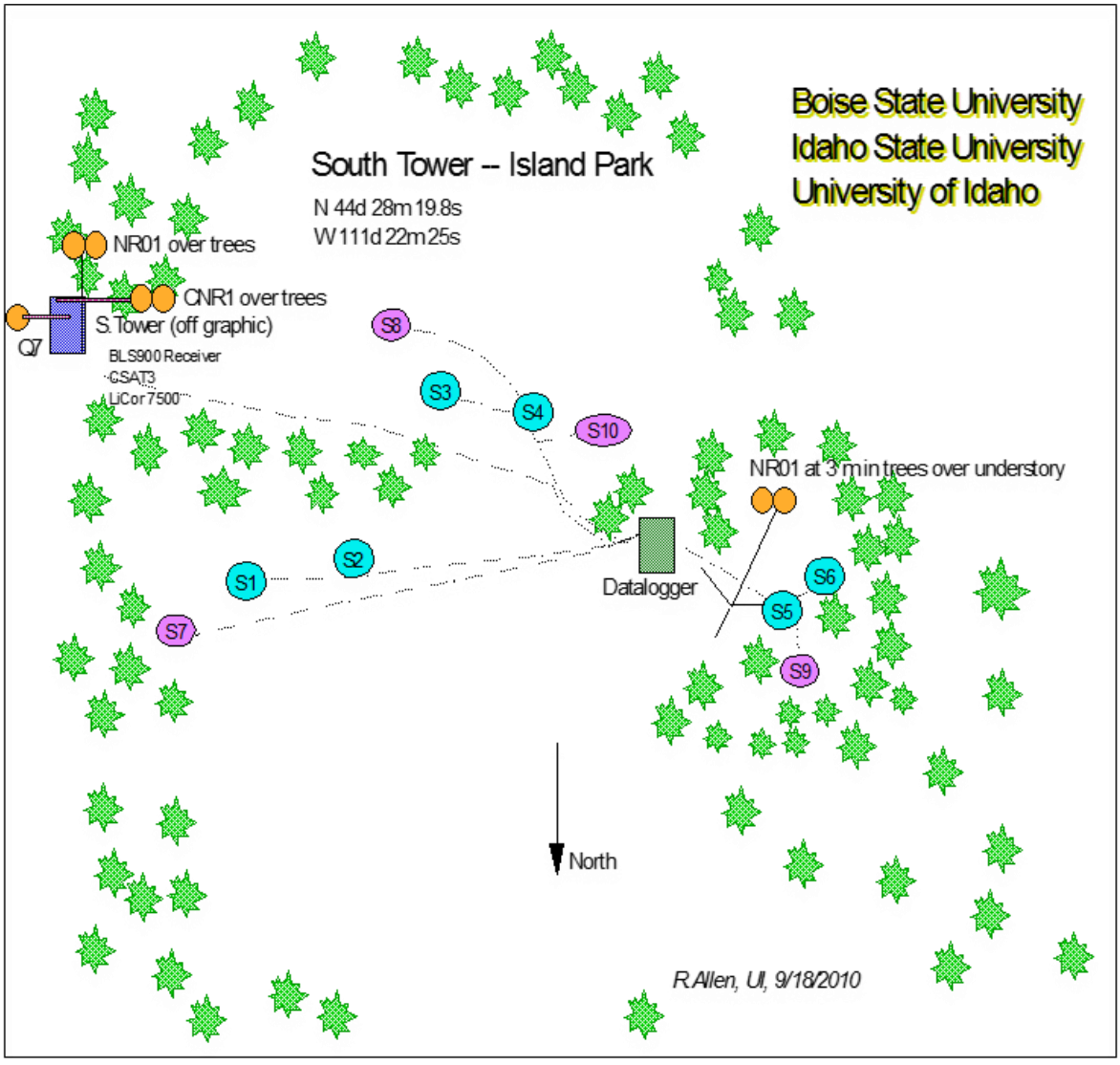

Figure A-2. Schematic of the Island Park south site (Allen, 2011, Island Park site description, http://www.kimberly.uidaho.edu/epscor/IslandPark/Island_Park_Site_Description.pdf)

Table A-2. List of sensors at the Island Park south site.		
Location	**Device**	**Depth or Height**
Instruments on the South Tower		
	NR01 4-way Radiometer	20 m over trees to South
	CNR1 4-way Radiometer	20 m over trees to West
	Q7 Net Radiometer	5 m over meadow to East
	BLS900 Scintec Receiver	22 m looking north
	CSAT3 3D sonic	23 m SW corner of tower
	LiCor 7500 Hygrometer	23 m SW corner of tower
	Eppley PSP Pyranometer	22.5 m SW corner of tower
	Tipping bucket with antifreeze	22.5 m W side of tower
	Apogee IRT	22 m NW corner of tower looking toward north at 25 deg from Nadir at tree canopy
	CR1000 datalogger	4 m on tower
	Vaisalla Relative Humidity/Temperature	4 m on tower
	motion-detection camera	
Instruments at the South Soil Sensor Site		
	CR1000 datalogger and 3 multiplexors	
	Vaisalla RH/T	2 m on datalogger mast
	NR01 4-way Rad.	3.5 m over understory in mostly shade
Soil Heat Flux Locations		
S1 *Semi-shaded, grasses and forbs* *Relatively 'lush' understory*	REBS Soil Heat Flux Plate	6 cm
	Rebs Soil Heat Flux Plate	12 cm
	Thermocouple	1.5 cm
	Thermocouple	3.0 cm
	Thermocouple	4.5 cm
	Thermocouple	9.0 cm
	Decagon Echo 5 soil moisture sensor	1-5 cm (near vertical)
	Campbell Scientific CS616 soil water content	0-12 cm (at an angle)
S2 *Semi-shaded, grasses and forbs* *Relatively 'lush' understory*	Rebs Soil Heat Flux Plate	6 cm
	Rebs Soil Heat Flux Plate	12 cm
	Hukseflux Self-Calibrating Soil Heat Flux Plate	12 cm
	Thermocouple	1.5 cm
	Thermocouple	3.0 cm
	Thermocouple	4.5 cm
	Thermocouple	9.0 cm
	Campbell Scientific CS616 soil water content	0-12 cm (at an angle)

S3 *Open Meadow, grasses and forbs* *Thinner, drier environment than S1,S2*	Rebs Soil Heat Flux Plate	6 cm
	Rebs Soil Heat Flux Plate	12 cm
	Thermocouple	1.5 cm
	Thermocouple	3.0 cm
	Thermocouple	4.5 cm
	Thermocouple	9.0 cm
	Decagon Echo 5 soil moisture sensor	1-5 cm (near vertical)
	Campbell Scientific CS616 soil water content	0-12 cm (at an angle)
S4 *Open Meadow, grasses and forbs* *Thinner, drier environment than S1,S2*	Rebs Soil Heat Flux Plate	6 cm
	Rebs Soil Heat Flux Plate	12 cm
	Thermocouple	1.5 cm
	Thermocouple	3.0 cm
	Thermocouple	4.5 cm
	Thermocouple	9.0 cm
	Campbell Scientific CS616 soil water content	0-12 cm (at an angle)
S5 *Shaded, grasses and forbs* *Relatively 'lush' understory*	Rebs Soil Heat Flux Plate	6 cm
	Rebs Soil Heat Flux Plate	12 cm
	Thermocouple	1.5 cm
	Thermocouple	3.0 cm
	Thermocouple	4.5 cm
	Thermocouple	9.0 cm
	Decagon Echo 5 soil moisture sensor	1-5 cm (near vertical)
	Campbell Scientific CS616 soil water content	0-12 cm (at an angle)
S6 *Shaded, grasses and forbs* *Relatively 'lush' understory*	Rebs Soil Heat Flux Plate	6 cm
	Rebs Soil Heat Flux Plate	12 cm
	Thermocouple	1.5 cm
	Thermocouple	3.0 cm
	Thermocouple	4.5 cm
	Thermocouple	9.0 cm
	Campbell Scientific CS616 soil water content	0-12 cm (at an angle)
Deeper Soil Water Content Sites		
S7 *Semi-shaded, grasses and forbs* *Relatively 'lush' understory*	Campbell Scientific CS616 soil water content	12-42 cm
	Campbell Scientific CS616 soil water content	42-72 cm
	Campbell Scientific CS616 soil water content	70-100 cm Not listed
	Decagon Echo 5 soil moisture sensor	1-5 cm

	Decagon Echo 5 soil moisture sensor	75 cm
	Decagon Echo 5 soil moisture sensor	100-105
S8 *Open Meadow, grasses and forbs* *Thinner, drier environment than S7*	Campbell Scientific CS616 soil water content	12-42 cm
	Campbell Scientific CS616 soil water content	42-72 cm
	Campbell Scientific CS616 soil water content	100-105 cm Not listed
	Decagon Echo 5 soil moisture sensor	12 cm
	Decagon Echo 5 soil moisture sensor	12 cm
	Decagon Echo 5 soil moisture sensor	12 cm
S9 *Shaded, grasses and forbs* *Relatively 'lush' understory*	Campbell Scientific CS616 soil water content	12-42 cm
	Campbell Scientific CS616 soil water content	42-72 cm
	Campbell Scientific CS616 soil water content	70-100 cm
	Decagon Echo 5 soil moisture sensor	12 cm
	Decagon Echo 5 soil moisture sensor	12 cm
	Decagon Echo 5 soil moisture sensor	12 cm
S10 *Open Meadow, grasses and forbs* *Thinner, drier environment than S7* *Trees to west*	Campbell Scientific CS616 soil water content	12-42 cm
	Campbell Scientific CS616 soil water content	42-72 cm
	Campbell Scientific CS616 soil water content	70 – 100 cm
	Decagon Echo 5 soil moisture sensor	12 cm
	Decagon Echo 5 soil moisture sensor	12 cm
	Decagon Echo 5 soil moisture sensor	12 cm
S11 *In North Power Pole hole at South Tower, embedded in side of hole, in shad of trees and tower*	Campbell Scientific CS616 soil water content	12-42 cm
	Campbell Scientific CS616 soil water content	206 m
	Campbell Scientific CS616 soil water content	70 – 100 cm

	Decagon Echo 5 soil moisture sensor	12 cm
	Decagon Echo 5 soil moisture sensor	12 cm
	Decagon Echo 5 soil moisture sensor	12 cm

Table A-2. List of sensors at the Island Park south site (adapted from Allen, 2011, Island Park Site Description http://www.kimberly.uidaho.edu/epscor/IslandPark/Island_Park_Site_Description.pdf).

Appendix B. Calculation of G

The following is based analysis of data processing spreadsheets provided by Dr. Wenguang Zhao, University of Idaho-Kimberly, 2016. For the Island Park data set, G is calculated as

$$G_{sur} = G_{plate} + \Delta H_{Storage}$$

(From Soil_heat_Flux, Column BA)

Where G_{sur} is the soil heat flux at the soil surface, G_{plate} heat flux measured by the soil heat flux plate and the depth where it is installed, and $H_{Storage}$ is calculated one of two ways. The default calculation uses a polynomial fit based on the equation from Soil_heat_Flux, column AN: [=IF(Parameters!$J$36=0,AA9,Polyn_fit_4T!BL10)]

First, Soil storage by mineral soil is calculated on the Parameters sheet in Column C as:

$$H_{min} = 100 * 100 * C25(C16 - C17 * C22) * \frac{C18}{\$C\$3 * 60}$$

Which becomes:

$$H_{min} = \frac{100cm}{1m} * \frac{100cm}{1m} * 6cm * \left(1.12\frac{g}{cm^3} - 13\% * 1.3\frac{g}{cm^3}\right) * 0.87\frac{J}{gK} * \frac{1}{1800s}$$
$$= 27.579\frac{W}{m^2K}$$

The unit analysis is: $\frac{cm^3}{m^2} * \frac{g}{cm^3} * \frac{J}{gK} * \frac{1}{s} = \frac{J}{m^2sK} = \frac{W}{m^2K}$

$H_{Storage}$ is calculated as:

=(Parameters!$C$26+Parameters!$C$27+Parameters!$C$28*S_Soil!BR8)*(AY10-AY8)/2/Parameters!$C$25*BL$3
(eq. from Poly_fit_4T, column BL)
Which gives:

$$H_{Storage} = (H_{min} + H_{OM} + H_{water} * \%\, water\ content) \times \left(\frac{T_{after} - T_{before}}{2}{depth}\right) \times depth$$

The units are: $\frac{W}{m^2 * K} * \frac{\frac{K}{1}}{\frac{cm}{1}} * cm = \frac{W}{m^2}$

T_{after} and T_{before} are calculated through a 2nd degree polynomial regression equation to extend the temperature to the surface. Mean temperature for each soil slab above the plate was determined from the regression equation:

=((AA11*AY$3+AB11/2*AY$3^2+AC11/3*AY$3^3)-(AA11*AY$2+AB11/2*AY$2^2+AC11/3*AY$2^3))/(AY$3-AY$2)
(eq. from Poly_fit_4T, column AY)

Which gives

$$T = \frac{\left((Pit\#1c0 \times depthL) + \left(\frac{Pit\#1c1}{2} \times depthL^2\right) + \left(\frac{Pit\#1c2}{3} \times depthL^3\right)\right) - \left((Pit\#1c0 \times depthU) + \left(\frac{Pit\#1c1}{2} \times depthU^2\right) + \left(\frac{Pit\#1c2}{3} \times depthU^3\right)\right)}{Depth_L - depth_U}$$

And Pit#c0, c1, and c2 are given by: INDEX(LINEST(J8:M8,(J$1:M$2),TRUE,FALSE),1,3)

The variables depthL and depthU refer to the lower and upper depths.

If the switch from the parameters page is 0, then

$$H_{Storage} = (H_{min} + H_{OM} + H_{water} \times \%\, watercontent)(\Delta T)$$

(eq from column AA)
And ΔT is calculated as $\Delta T = \frac{T_{A1.5-2.25} - T_{B1.5-2.25} + T_{A4.5-20.25} - T_{B4.5-20.25}}{4}$
(from Soil_heat_Flux, column O)

Appendix C. Data Processing

Description of Standard Correction Included in the Processing of the Eddy Covariance Data

The EC method requires a number of corrections to the raw flux values since flux measurements are imperfect due to assumptions, instrument problems, physical phenomena, and specifics of the particular terrain (Burba 2005). The table above shows the most common corrections, affected fluxes, and very approximate mid-day warm-season ranges of these corrections in relation to the flux in an unstressed mid-latitude green vegetative ecosystem. The bolded corrections have been applied to the Island Park data (W. Zhao personal communication, November 22, 2016).

Procedure	Affected fluxes	Effect	Range
Spike removal	all	depends	0-15%
Coordinate rotation	all	depends	0-25%
Time delay adjustment	mostly closed path	increases flux	0-50%
Webb-Pearman-Leuning terms	any gas	depends	0-50%
Frequency response corrections	all	increases flux	0-50%
Angle of attack correction	all	depends	0-25%
Sonic heat flux correction	sensible heat flux	depends	0-10%
Spectroscopic effects for LASERs	any gas	depends	0-25%

Table C-1. List of corrections for the eddy covariance method. Adapted from Burba 2005.

Description of the QA/QC Processing Using the Error Flags

Three new worksheets were added to the monthly Excel files that contain the Island Park data. The first sheet was “Ana_Data”. A macro copied relevant data for Rn, H, LE, and G from the corresponding worksheets into the “Ana_Data” worksheet. All data was pasted with links to the original data so that it could be traced more easily to the source, and updated/revised in a single place if revisions to the data were made. The data were displayed graphically for the entire month.

The data quality flagging was also displayed in a second graph, which is aligned below the data graph. The data quality evaluation combined a visual review of the data behavior with the data quality flagging. "Good" data to be retained for the regression analysis was coded with a 1 based on the error flagging; data with an error code indicating it was problematic (error code 4 or greater) was coded with a 0.

The data were then manually copied into the second worksheet "Sorted_Data". Data coded with a 1 was sorted to the top and displayed in the graph; data coded with a 0 was left at the bottom of the worksheet but was not included in the graph. The graph gives an overview of the data that will be used in subsequent analysis.

Data coded with a 1 corresponding to daytime periods are then copied into the third worksheet "Daytime_Only" and displayed on a graph.

Step-by-step processing of the flux data:

1. Insert Ana_Data template; use template with the latest date.
2. Run Macro1 to import data. This macro also checks the error coding for the H and LE data and adds a 1 in the last column if the error code is less than 4 and a 0 if the error code is greater than or equal to 4.
3. Run Macro2 to update data graph.
4. Run Macro3 to update flagging graph.
5. Evaluate data quality and flag data that is problematic (this is now done by the macro based on the error coding).
6. Copy Ana_Data to Sorted_Data- PASTE LINKS.
    - Insert a blank worksheet and rename it Sorted_Data
    - Select and copy by hand the data from Ana_Data
    - Paste the data to Sorted_Data manually
7. Sort data manually based on flagging, 0 to bottom.
8. Insert blank row after last row of good data and insert "EndGoodData" in column A.
9. Run Macro4 to update data graph.
10. Run macro5 to export Daylight_Only data.
11. Run Macro6 to update day time only data graph.

Description of how to apply the LAS adjustment.

1. Insert a blank page.
2. Copy desired row heading from master, “Const LAS Corr”.
3. Copy the formulas for the first cells. Formulas will populate the cells with the data and implement the LAS adjustment.
4. Verify that the formulas point to the correct cells copy the cells down.